Comparison of Constitutive Relationships based on Kinetic Theory of Granular Gas for Three Dimensional Vibrofluidized Beds

By

Nadeem Ahmed Sheikh

A Doctoral Thesis submitted in partial fulfilment of the requirements for the award of Doctor of Philosophy of Loughborough University

2011

DEDICATED TO MY DEAR PARENTS AND FAMILY MEMBERS

Abstract

Granular materials exist in many forms in nature ranging from space debris to sand dunes and from breakfast cereals to pharmaceutical tablets. They can behave like a solid or a viscous fluid or a gas. The gas-like nature of granular materials in rapid flows allows the use of models based on kinetic theory thus revealing in depth complex physics and phenomena. However unlike conventional fluids here the energy balance requires additional dissipation terms as a consequence of inelasticity. The complexity of their interaction and diversity in application has led to numerous studies using experimental methods and numerical simulations in order to determine the most appropriate constitutive relationships for granular gases. With large dissipation the form of the constitutive relationship becomes particularly important, especially in the presence of non-equipartition and anisotropy. This thesis is focused on constitutive models of simple granular flows. A vibrated bed is often used as an idealisation of granular flows, providing a convenient approximation to the simplest type of flow: binary and instantaneous collisions with no rotations. Using finite element method (FE) based COMSOL modules we solve conservation of mass, momentum and energy resulting from granular kinetic theory in axi-symmetric form to generate time and spatial resolved solutions of packing fraction, velocity and granular temperature and compare the predictions to numerical simulation and experiment.

At first we show the comparison for two closure sets, one based on a simple near elastic approach while the second based on revised Enskog theory for dense inelastic flows. The results for the second approach show good agreement with the results of previously validated near elastic models and experimental results. The observed differences between the two closure sets are small except for the observation of temperature upturn in a dilute region of the cell away from base. One cause of this is the presence of additional constitutive terms in the balance equations and are a consequence of inelasticity.

The models also consider time varying effects at low frequency of excitation. These solutions show existence of wave-like effects in the cell with associated temperature upturn within the hydrodynamic applicability region. Presence of instantaneous cyclic rolling is also seen in both approaches. Evidence from MD simulations and experiments qualitatively support the findings of hydrodynamic models in phase resolved as well as time average behaviour.

Subsequently, the frequency of vibration was varied to unlink the wave motion from the bulk temperature. Lack of agreement between experiment and the model predictions are shown to be due to lack of separation of time scale between the grain-base interaction and the base frequency. A sharp decrease of heat flux is measured showing that the energy input is frequency dependent. Analysis of the bulk behaviour shows that at high frequency, hard sphere based models are able to capture the steady state behaviour reasonably well. Further investigations that modulate the driving with a low frequency amplitude change revealed the dynamic nature of flow with the low frequency component. No significant influence of high frequency signal is noted except the reduction of base heat flux. Independent analysis of bulk behaviour for modulated wave excitation using MD simulations and hydrodynamic models showed wave motion in a pattern similar to non-modulated low frequency vibration.

A one-dimensional inviscid model was used to determine the underlying scaling relationships for near elastic granular flows. A form of non-dimensionalisation predicts scaling behaviour for the granular flow. The predictions show good results for the dilute flows using hard sphere MD simulations. Results from MD simulations confirm dilute limit scaling of base temperature, packing fractions and heat flux coefficients. At higher inelasticity and loading condition the model fails to capture the real physics suggesting the need for a more accurate model. This simplified model does, however, set the basis for describing the main scalings for vibrofluidized granular beds, and in the future we anticipate that effects of further inelasticity and enhanced density could be incorporated.

Keywords: Kinetic theory model, vibrofluidized bed, finite element methods, constitutive relationships, revised Enskog theory, MD simulations.

Acknowledgement

First of all I am greatly thankful to my Lord ALLAH Almighty for blessing me with the wealth of knowledge, health, wisdom and patience.

I would like to express my deepest gratitude to my principal supervisor Dr. Ricky Wildman for introducing me to this exciting field of granular flows. This research work would not have materialized without his continuous guidance, motivation and patience throughout the research period.

I am also grateful to Professor Jonathan Huntley, my second supervisor, for his remarkable guidance, help and trenchant scrutiny throughout my research work. Special thanks to Dr. V. Kumaran for his invaluable support and useful discussion especially on the constitutive relationships and Dr. Julian Talbot for his motivation and help to undertake granular motor project.

I am thankful to Wolfson School of Mechanical and Manufacturing Engineering, Loughborough University, for providing the financial assistance during this research work.

Nadeem Ahmed Sheikh

Loughborough University

Table of Contents

List of figures

List of tables

List of Symbols

A	Cross section area of granular cell (m^2)
a	Acceleration (ms^{-2})
a_0	Base amplitude (m)
c	Speed of sound in granular media (m/s)
C_ϕ	Constant relating base heat flux
d	Particle diameter (m)
e	Particle-particle coefficient of restitution
e_b	Particle-base coefficient of restitution
e_w	Particle-wall coefficient of restitution
Fr	Froude number
g	Acceleration due to gravity (ms^{-2})
g_o	Radial distribution function
I	Unit tensor
I_e	Energy transfer integral (m^4/s^4)
J	Heat flux (W/m^2)
J_b	Heat flux at the base (W/m^2)
$\mathrm{K_{dv}}$	Bulk viscosity($kgm^{-1}s^{-1}$)
K_{dv}^*	Reduced coefficient for Bulk viscosity
L	Height of the vibrated cell (m)
m	Particle mass (kg)
n	Number density (m^{-3})
n	Normal component
N_g	Number of grains
N	Number of particles per unit area (m^{-2})
N^*	$Nd^2\sqrt{1-e^2}$
p	Pressure (Pa)
p'	Pressure scaled by mass ($m^{-1}s^{-2}$)
Q	Heat sink/source
	$\left\{\begin{matrix}\frac{kg}{ms^3} \text{ sec 7.2} \\ \frac{1}{ms^3} \text{ all other sections}\end{matrix}\right\}$
R	Radius of vibrated cell (m)
r	Radial direction (m)
S	Integral of intensity velocity (m/s)
T	Granular temperature scaled by mass (m^2/s^2)
T_c	Contact duration between grains (s)
T_o	Granular temperature at the base (m^2/s^2)
T_∞	Granular temperature at the asymptotic limit(m^2/s^2)
T'	Granular temperature (kgm^2/s^2)
TE	Echo time (s)
t	Time (s)
t	Tangential component
u	Velocity vector (m/s)
u	Radial component of velocity (m/s)
V_b	Base velocity (m/s)

$<v^2>$	Ensemble average speed (m^2/s^2)
V_p	Volume of particles (m^{-3})
V_T	Total volume (m^{-3})
v	Vertical component of velocity (m/s)
v_x	Components of velocity in x direction (m/s)
v_y	Components of velocity in y direction (m/s)
v_z	Components of velocity in z direction (m/s)
x, y, z	Cartesian coordinate system (m)
z_{max}	Maximum packing fraction position (m)
ρ	Mass density ($kg\ m^{-3}$)
η	Packing fraction
η_b	Base packing fraction
η_{max}	Maximum packing fraction
v_0	Characteristic collision frequency ($1/s$)
κ	Thermal conductivity $\begin{Bmatrix} 1/ms \text{ sec } 7.2 \\ \frac{kg}{ms} \text{ all other sections} \end{Bmatrix}$
κ^*	Dimensionless Coefficient of thermal conductivity
κ_0	Elastic limit of thermal conductivity ($kgm^{-1}s^{-1}$)
μ	Inelastic contribution to heat flux (kgs^{-3})
ζ	Shear viscosity ($kgm^{-1}s^{-1}$)
ζ^*	Dimensionless coefficient for shear viscosity
ϕ	Phase angle of base (rad)
δ	Deflection (m)
γ_n	Damping coefficient
χ	Pair distribution function
v_η	Collision frequency due to viscous transport ($1/s$)
$\gamma^{(0)}$	Zero order dissipation rate dimensionless coefficient ($kgm^{-1}s^{-2}$)
$\gamma^{(1)}$	First order dissipation rate dimensionless coefficient ($kgm^{-1}s^{-2}$)
κ^k	Dimensionless kinetic component of thermal conductivity
v_k	Collision frequency due to kinetic transport ($1/s$)
μ^k	Dimensionless Kinetic inelastic collisional contribution to heat flux
ω	Base frequency (rad/s)
Ω	Angular velocity ($1/s$)
η_0	Elastic limit of shear viscosity ($kgm^{-1}s^{-1}$)
γ	Dissipation ($m^{-1}s^{-3}$)
γ_1	Cooling rate (s^{-1})
γ^*	Reduced coefficient for Dissipation rate ($kgm^{-1}s^{-2}$)
$\tilde{k}_n$	Stiffness of grain ($N\ m^{-3/2}$)

Relationship between the dimensional and dimensionless variables

Dimensionless Variable	Dimensional Relationship
T^*	T/gd
p^*	$p\pi d^2/6mg$
$\mathbf{u}^*$	$\mathbf{u}/\sqrt{(gd)}$
$V_b{}^*$	$V_b/\sqrt{(gd)}$
z^*	z/d
r^*	r/d
Ω^*	$\Omega/\sqrt{(g/d)}$
a_0*	a_0 / d
τ^*	$t/\sqrt{\frac{d}{g}}$
I_e^*	$I_e/(gd)^2$

Chapter 1 Introduction to Granular Flows

1.1 Introduction

Granular materials are found in a wide range of applications in industry, including food, pharmaceutical manufacturing, agriculture and mining processes. These materials are often defined as a collection of large number of discrete solid particles (Duran 2000). Granular materials are involved in many interesting problems in the fields of civil engineering, soil mechanics, earthquake engineering, manufacturing engineering and physics where granules need to be stored, transported, and processed. These materials occur abundantly in nature in various forms. They are diverse in their shapes and sizes ranging from micron sized washing powders to few meters sized rocks forming Saturn's planetary rings. They are so common in our daily life that they sometimes go unnoticed. Food products like rice, corn, and breakfast cereal flakes, building materials such as sand, gravel, and soil, chemicals such as coal, plastics, and pharmaceuticals, and landslides of boulders and debris are few amongst many examples of granular materials. Relatively little is known, however, about their behaviour. In most processes they can be controlled reasonably well, but the reasons why are not always clear. Our basic understanding of granular flows is limited and most designs rely on empirical guidelines for their behaviour.

1.2 Granular flows

Granular materials exhibit a range of behaviour from elastic solids to rapid fluid-like flow depending on the local stress conditions (Evesque 1992). In the form when granular media behaves like elastic materials, it can support large loads supported through the frictional bonds amongst the particles (Duran 2000). When the loading overcomes the frictional bonding the system fails and particles begin to flow. In slowly moving dense grains the interaction amongst themselves is friction dominated and they move relative to one another. This phenomenon of deformation is referred to as the 'quasi-static' regime of granular flows (Evesque 1992, Farkas, Tegzes et al. 1999). When forced to higher accelerations, the inertia of the grains dominate and interaction between them is relatively instantaneous compared to the mean free time. This fluidic behaviour is known as 'rapid granular flows' (Duran 2000, Evesque 1992, Bug & Berne 1987). In all sorts of fluidic motion the velocity of each particle can be described as a sum of two components. One corresponds to the mean velocity of the bulk material and the second velocity component corresponds to the particle motion relative to mean bulk motion (Chapman, Cowling 1991,

Serero, Goldhirsch et al. 2006, Wildman, Huntley et al. 2001, Ramrez R., Soto R. 2003). The space between the flowing particles is generally filled with fluid like air and technically speaking their flow is a multiphase process. For reasonably dense systems, the effects of the interstitial fluid is generally small and can be ignored as the particles are the main contributors for transport phenomena especially when the interstitial fluid has relatively low density (Goldhirsch 2003).

Although granular flows are complex and exhibit phenomena that cannot be described using classical ideas of fluid flows as they stand, an obvious analogy exists between random motion of granular particles and agitated motion of dense gases (Lun, Savage et al. 1984, Haff 1983, Jenkins, Richman 1985b, Kumaran 2000a, Montanero, Garzo et al. 2000). However, there are at least two important differences one cannot neglect; firstly the granular interaction is inelastic and secondly typical granular flows involve larger flow gradients than their corresponding molecular counterparts (Montanero, Garzo et al. 2000). Even though empirical predictions of granular flows are reasonably effective for specific applications, without understanding of these flows from first principles it is difficult to predict granular behaviour when implementing changes in design geometry and operating inputs.

1.3 Motivations for studying granular flows

The most interesting feature of the granular flows is the interacting behaviour of the grains, which can be diverse, ranging from collisional to frictional and/or electrostatic, leading to a variety of complex patterns (Alain, Emmanuel et al. 2005). Collective motion of grains is of particular importance in predicting natural phenomena as well as for industrial applications such as process design and power generation (Sunthar 2001). According to some estimates, granular materials contribute to $100 billion in the USA economy in different forms in the chemical and process industries (Duran 2000, Sunthar 2001) and a major part of the electrical power generation production specially through coal processing is linked with these materials.

Granular flows can be hazardous in industries with hopper failure, storage tank bursts as well as naturally occurring phenomena such as landslides causing damage to property, business and mankind as well (Evesque 1992). Poor understanding of the physics of these materials is the main concern in devising methods to avoid such incidents. Most of the first hand knowledge of the particulate materials is empirical and general mathematical

approaches are limited to simpler systems. Over the past few decades a number of theoretical and experimental efforts have been made in order to comprehensively understand them (Lun et al. 1984, Garzo et al. 2007, Jenkins, Savage 1983). In the recent past computer simulations (Hrenya et al. 2008, Luding, Clement et al. 1996) as well as high tech experimental facilities such as high speed cameras (Wildman et al. 1999), nuclear magnetic resonance imaging (NMR) (Huntley et al. 2007) and positron emission particle tracking (PEPT) (Wildman et al. 2005) have revealed the in depth physics of these materials. Extensive theoretical frameworks have been proposed by theoreticians that broadly describe the physics in many of the observed cases. Still there are grey areas which are of particular importance in our complete understanding particularly when these materials are made to flow at high speeds. Areas such as anisotropic behaviour (Sela, Goldhirsch 1998), time varying behaviour (Huan et al. 2004), scaling characterization (Kumaran 2008), unsteady effects (Huntley et al. 2007), pattern formation (Makse et al. 1998) and clustering (Falcon et al. 1999) are few amongst many which hinder our complete know how. These challenges are posed by the inherent dissipative nature of these flow which sometimes leads to some of the spectacular phenomenon such as ratchet effects (Farkas et al. 1999).

The investigation of the exact form of constitutive relationships for energy and momentum transport fascinates many technologist and theoreticians (Garzo et al. 2007) but at the same time poses a great deal of difficulty while simulating them. Use of different hydrodynamics descriptions is still an open issue. Time variations, anisotropy, non-equilibrium effects, inelasticity, boundary conditions, constitutive relationships and mechanisms of heat transfer are some of the challenges while simulating them with solution methods are equally testing due to the non-linearity and complexities of the models (Goldshtein, Shapiro 2006, Goldshtein et al. 2006, Wildman et al. 2008). Theoreticians are actively researching for scaling behaviours and higher order effects in these flows (Hrenya et al. 2008). A number of efforts in simulating these models have been reported but limited to steady state nature of monodisperse granular physics (Viswanathan et al. 2006) and often reduced to one dimensional (Huntley et al. 2007, Wildman et al. 2008, Martin, Huntley et al. 2005). There is still a bridge to be made between the theoretical framework and a real time tool for use in practical industrial scale granular systems. Building such a workbench can be useful in design and analysis for problems involving granular flow. Commercial design packages usually do not include granular material sections and the few who claim to be able to describe these systems (e.g., Fluent) are not well equipped to describe the true

physics. It is indeed important to develop modelling and simulation procedures for granular materials within the frameworks of currently available methods which can be accommodated in commercial packages. This research is a stepping stone to be used in an effort to formulate such tools. As part of this research, using currently available simulations methods, complex non-linear, time varying mathematical models are developed and solved for real time problems concerning monodisperse granular systems.

Using hydrodynamic methods, an effort has also been made in this research work, to investigate some interesting phenomena in these flows. Influences of boundary condition, characterization of scaling trends, performance of constitutive relationships under various loading conditions are investigated and compared against the results using experimental methods and particle level descriptions. These interesting yet challenging areas are amongst the prime motivators for this research work.

1.4 Understanding granular physics

Transport is of particular importance in granular media. Many industrial processes such as drying, cooling, agglomeration, granulation, and coating involve transportation of mass, momentum and energy. Conventional methods used for fluids involve balances of these quantities but for granular flows there are some fundamental differences. In order to understand granular flows a common method is to explore a simplified system that allows us to deduce the key physics, including for example, shear cells, rotating drum and fluidized cells. A number of experimental methods such as NMR (Xiaoyu Yang, Candela 2000) and high speed photography (Warr, Huntley et al. 1995), particle level molecular dynamics simulations (Ramirez, Risso et al. 2000) as well as bulk hydrodynamic models (Goldshtein, Kamenetsky et al. 2002, Bougie, Moon et al. 2002) have explored systems that use these geometries to test and analyze granular physics.

Vibration is very helpful for fluidizing materials that have a high irregularity of shapes and sizes. It is especially helpful with those materials which fluidise poorly due to a broad particle size distribution. In simple dry vibrofluidized beds vibration is the only mode which fluidises the bed. In such a system, one observes that the behaviour of the fluidized material is strongly dependent on both the strength and type of shaking. Typically, the particles are set into motion via interaction with the boundary of the system, usually in a vertical position. When the boundary acceleration exceeds that due to gravity the particles are able to move ballistically, setting the system into a fluidized state. The motion of

particles in such a state resembles the classical picture of a molecular gas and a number of successful models have built upon this analogy over the past three decades (Lun, Savage et al. 1984, Jenkins, Richman 1985b). As the principal difference between a classical and a granular fluid is the inelasticity of particle-particle and particle wall collisions (Liu, Nagel 1992, Nedderman R. M. 1992) a rational description requires considerations of factors such as the anisotropy, roughness of particles (which couples translational and rotational degrees of freedom), soft-particle interactions (which mean that particles deform during collisions) (Goldshtein, Kamenetsky et al. 2002) alongside the inherent transient nature of shaken beds. In addition, the coefficient of restitution is a function of collisional velocity and realistic particles tend to consist of varying sizes and shapes (poly-disperse) (A.Goldshtein, et al., 2002).

It would be very difficult, however, to develop a hydrodynamic model with constitutive relations explicitly dependent on all of the above factors. With the exceptions of some attempts to approximately include friction and the use of a collisional model with a velocity-dependent restitution coefficient (A.Goldshtein, et al., 2002), to our knowledge most of these factors have not been incorporated to date. Besides this most of the work has been limited to steady state physics and often reduced to one dimensional models for monodisperse systems utilizing constitutive relationships applicable to near elastic systems (Martin, Huntley et al. 2005, Bougie, Moon et al. 2002, Serna, Marquina 2005). It is important, therefore, to test whether the available models capture the three dimensional time-dependent behaviour of granular flows.

In this research work we use monodisperse vibrated beds as a tool to investigate the effects of different types of constitutive models for granular physics. For comparison and further investigation molecular dynamics simulations and experimentation are also carried out using the same test geometry.

1.5 Aims and Objectives

The main aim is to develop understanding of the physics of these flows by studying them in a realizable environment of dry vibrated cells by the means of experimentation methods such as NMR, particle level molecular dynamics simulations and bulk hydrodynamic models. With the focus on implementation using the commercially available resources of hydrodynamic methods on real time system, all the hydrodynamic simulations in this study are carried out using commercial package COMSOL with user defined methods.

Objectives for this work are outlined as follows:

- To develop a viscous hydrodynamic model resolving time dependent behaviour of a vibrated granular bed in an axi-symmetric geometry incorporating different forms of the constitutive relationships.
- To investigate the behaviour of the boundary conditions, constitutive relationships and the predicted scaling relationships under different loading conditions, vibrating frequencies and driving velocities.

1.6 Summary

The thesis is sectioned into eight chapters. The first one introduces the area by highlighting the importance and usefulness of granular materials followed by the aim and objectives of this research work. The second chapter summarizes the extensive literature particularly useful for the areas addressed in this research. The third chapter details the model development and the solution framework of the axi-symmetric hydrodynamic model with its validation for steady state case followed with time dependent solution and comparison of results with MD simulations and experiments at low frequencies in chapter four. In chapter five tests of these models to the limits of high frequency are included. Time varying effect of modulation in vibration amplitude of the base is studied in chapter six. Chapter seven focuses on the parametric characterization and tests of constitutive relationship predictions. This is followed with conclusion and future recommendations in the last chapter.

Chapter 2 Literature Survey

In this chapter we survey the literature and background on granular flows in general and granular physics in dry vibrated beds in particular. An introduction to the terminologies often used in this area is also provided for the ease of readers. We revisit the standard theories used over the past few decades to understand the physics of these complex flows. Particulate level modelling using molecular dynamics simulations and continuum level hydrodynamics modelling is also included in this section. This is followed by an overview of experimental methods used in characterizing granular flows. At the end we highlight some of the areas which are of prime focus in current research on granular flows.

2.1 Description of Granular flow behavior

Granular gases are grains in a fluidized state caused by sufficiently strong forcing that leads to the stage when particles interact by nearly instantaneous collisions compared to the mean free time or time between collision (Nedderman R. M. 1992). Granular systems can be considered analogous to molecular gases, but there is obviously a disparity between the size of the molecules of a gas and the macroscopic particles. This does not pose any mathematical or physical issue. Most classical molecular gases are realized at macroscopic scale obeying the same laws as in microscopic scale. Thus all granular gases can be thought of macroscopic realizations of classical molecular gases obeying the same laws of motion. The major change or disparity lies in the kind of interaction these macroscopic particulates undergo. Macroscopic descriptions in classical gases interact elastically while inelasticity is the major implication concerning the behaviour of the collection of grains. The inelasticity results in the loss of kinetic energy upon impact.

One method that has proved successful in describing granular flows is the kinetic theory of granular media (Lun, Savage et al. 1984, Jenkins, Richman 1985b, Kumaran 2000a, Montanero, Garzo et al. 2000). The kinetic theory of gases provides us with a useful ground to develop a continuum (hydrodynamic) model on an analogy basis (Haff 1983, Goldshtein, Kamenetsky et al. 2002, Jenkins, Richman 1985a, Ding, Gidaspow 1990). For this one needs to develop constitutive relations for closure of the continuity, momentum and energy balance equations (Ramrez R., Soto R. 2003, Garzo, Dufty et al. 2007, Kumaran 2004, Sela, Goldhirsch 2000, Garzo, Dufty 1999). A successful hydrodynamic description strongly depends on the correctness of these constitutive relationships. In the most recent theories and experiments, a common hypothesis employed for granular gases

is that of a gathering of uniform, smooth hard spheres in three dimensions; in two dimension disks are considered. Further simplification of collision characterization includes the fixed coefficient of normal restitution, denoted by e.

Kinetic theory provides the basic framework on the basis of which the general continuum equations for rapid granular flows can be derived through the conservation of mass, momentum and energy where the energy conservation equation includes the sink terms due to inelasticity. The closure of these equations can be provided with the kinetic theory giving the constitutive relations and the state law. At high speeds and dilute conditions the number of collisions between the particles is reduced and the time between the collisions becomes significantly large. At this stage the time scale attached to a given collision becomes negligible as compared to the time attached between collisions (Goldhirsch 2003). This state leads to some of the approximations that helps in reducing the complexities of these flows. By assuming the collisions to be instantaneous and binary helps in defining pair distribution functions and collision integrals with relatively less mathematical complexity which are fundamental in describing the very basic continuum models.

Continuum models relate the state variables in a balanced form producing the complete picture of the flow. In order to understand granular gases, state variables such as temperature and packing fraction carry significant importance due to their definition and use. Although they are defined in similar fashion as in molecular gases but carry significant physical aspects in granular mechanics. Detailed definitions and their importance are discussed in next section.

a) Granular Temperature

As in the case of molecular gases, one can define the macroscopic fields for granular gases, such as granular temperature, velocity and mass density (or number density). Granular temperature is generally defined in terms of square of the velocity fluctuation about its mean in any given direction (Evesque 1992, Goldhirsch 2003). Mathematically it is given by

$$T' = \frac{1}{3} m < v^2 > \qquad \textbf{(2.1)}$$

Where m is the mass of particle, $\langle v^2 \rangle$ is the ensemble average speed of the particle about its mean velocity.

Granular temperature is analogous to the temperature associated with thermal motion but temperature is purely a thermodynamic phenomenon and accounts for the internal energy, whereas granular temperature requires external agitation. This is a consequence of the inelasticity of the collisions between the macroscopic solid particles and the total internal energy possessed by the grains associated with the granular temperature is always released/dissipated due to inter-particle collisions and/or collisions with the container. Thus in order to maintain the granular temperature continuous input of energy needs to be supplied to balance the energy lost in dissipative collisions. However, there is a key point about the granular temperature from the perspective of kinetic theory.

In granular systems equipartition does not necessarily exist and granular temperature may vary in orthogonal directions (Wildman, Parker 2002). Non-equipartition can be a significant contributor in processes such as mixing and segregation of poly-dispersed granular flows (Galvin, Dahl et al. 2005). In a Cartesian reference system the directional components of granular temperature are given by

$$T_x \propto m < v_x^2 > \quad \textbf{(2.2)}$$

$$T_y \propto m < v_y^2 > \quad \textbf{(2.3)}$$

$$T_z \propto m < v_z^2 > \quad \textbf{(2.4)}$$

where v_x, v_y and v_z are the fluctuating components of the velocity in the respective x, y and z directions.

b) Packing Fraction

Another key variable in describing the state of a granular flow is the packing fraction also commonly known as the solid fraction. This is a dimensionless quantity and is equal to the fraction of a unit volume (or unit area in two dimensions) that is occupied by the solid/granular material (Nedderman R. M. 1992, Carnahan, Starling 1969), such that

$$\eta = \frac{V_p}{V_T} \quad \textbf{(2.5)}$$

where V_p is the volume of the particles and V_T is the total volume. Number density n is related to the packing fraction η through

$$n = \frac{6\eta}{\pi d^3} \quad \textbf{(2.6)}$$

where d is the diameter of the particles.

c) Driving hydrodynamic models and constitutive relationships

In the past few decades efforts have been made to model the behaviour of granular flows using the continuum hypothesis. One of the first models was proposed by Haff in 1983 (Haff 1983). Haff proposed to model the energy dissipation by considering the particle collision details. The leading order velocity distribution involving these dissipative collisions was assumed to be that of Maxwellian (Maxwell-Boltzmann distribution); such an argument is valid for nearly elastic systems. With increase of inelasticity such approximations tends to fail. The constitutive relationships were largely developed through the scaling arguments in Haff's model. Using Maxwellian distributions Jenkins and Savage further developed a theory of uniform smooth near to elastic particles (Jenkins, Richman 1985b, Jenkins, Savage 1983). By taking the general forms of the probability distribution of a single particle velocity and for the case of binary collisions, the expressions for continuity, linear momentum and fluctuation of kinetic energy and the energy dissipation were derived (Montanero, Garzo et al. 2000, Brey, Dufty et al. 1999).

Further developments in the formulation of hydrodynamic models utilize the method of moments by integrating Boltzmann-Enskog kinetic equation with various weight functions to obtain transport equations. This method requires ad hoc approximations for the singlet distribution function (SDF) appearing in the Boltzmann-Enskog equation. Different approximations of the SDF have been used (Lun, Savage et al. 1984, Jenkins, Richman 1985b, Jenkins, Richman 1985a, Ding, Gidaspow 1990, Richman M.W., Martin R.E. 1992) in problems dealing with rapid granular flows. Another continuum description for a vibrofluidized granular bed is based on considering momentum conservation in the vertical direction and the energy conservation equation to describe the dynamics of the bed (Richman M.W., Martin R.E. 1992). In this analysis, asymptotic techniques were used to calculate the velocity distribution function. The description includes the transport of momentum and energy due to viscous and thermal effects in contrast to the Euler-type equations obtained from Goldshtein, et al. (Goldshtein, Shapiro et al. 2006). Recently

transport theory for classical gases has been extended to the granular gases to obtain Navier-Stokes order equations and transport coefficients in terms of inelasticity. Such methods are also known as Chapman-Enskog solutions of the Boltzmann equation and have been applied to low density systems (Brey, Dufty et al. 1998). A kinetic theory description specific to vibrated beds is developed by Kumaran (Kumaran 2000a) by using asymptotic analysis to calculate velocity distribution functions in the limit of maximum base velocity being small compared to the root mean square particle velocity. In the limit of a nearly elastic system, the transport coefficients for momentum and energy were derived.

Generalization of both Boltzmann and Enskog kinetic equations allow inelastic collisions to provide a basis for granular media. The Revised Enskog theory (RET) for elastic collisions is a well known accurate kinetic theory for conventional fluids (Garzo, Hrenya et al. 2007) which covers the entire fluid domain. It can also describe the crystallization phase as well which is of relevance for granular media undergoing clustering and dense pattern formations (Garzo, Dufty et al. 2007). The difference between standard Enskog theory (SET) and revised Enskog theory (RET) traces to the choice of pair correlation function. RET treats the pair correlation as a function of local concentration as well as its gradient while SET neglects the gradients (Montanero, Santos et al. 2007). Brey et al. proposed models based on RET for dilute and dense regimes for inelastic gas of particles (Brey, Dufty et al. 1999). By expanding the field gradients about homogeneous cooling state (HCS), hydrodynamic equations were developed for time-dependent velocity distribution function and temperature. Exact results for the distribution function and transport coefficients in terms of the linear integral equation solution have been developed by Garzo and Dufty (Garzo, Dufty 1999) for the mono-disperse case. This model is particularly useful since it describes the system over a wide range of fluidic density and dissipation. This has been lately extended to poly-disperse media (Garzo, Dufty et al. 2007, Garzo, Hrenya et al. 2007).

2.2 Molecular Dynamics Simulations on Granular Flows

Molecular dynamics provides an insight into the behaviour of macroscopic particles for systems ranging from dilute to dense regime depending upon the computational resources. It acts as a virtual experimental setup although restricted due to some of the physical and computational limitations. Molecular dynamics simulation models are particle level models describing the nature of particle and its interaction physics when it comes to terms with

neighbours. Molecular dynamics is by far the closest replica of the experimental setups and an handful tool in studies involving statistical mechanics. By utilizing the laws of physics relating particle motion and interaction (Shäfer, Dippel et al. 1996, Stevens, Hrenya 2005) in a typical MD simulation the coordinates of each of the simulated particles are known at all instances. This helps in revealing the insight of the granular behaviour which is difficult to capture in experimental methods. MD simulations are also flexible allowing us to introduce variations such as different natures of particle interactions (Shen, Hopkins 1988), introduction of shape and surface roughness (Kumaran 2006a, Kumaran 2006b) and poly-dispersion (Wildman, Parker 2002, Paolotti, Barrat et al. 2004).

Through ensemble averaging of the respective locations and velocities the hydrodynamic scale physics can be generated detailing the temporal and spatial fluctuations of hydrodynamic quantities (Ramrez R., Soto R. 2003, Sunthar 2001). MD simulations have been used in a number of research works highlighting, validating and explaining granular physics. Phenomenon such as convective rolling (Ramrez R., Soto R. 2003, Wildman, Martin et al. 2005), energy scaling (Warr, Huntley 1995), dynamic wave propagation (Alain, Emmanuel et al. 2005, Bougie, Moon et al. 2002), clustering and stationary waves (Paolotti, Barrat et al. 2004, Sunthar, Kumaran 2001) are a few of the findings demonstrated by MD simulations. Apart from their versatile applications and benefits, these models are still computer simulations having limitations such as excessive computational requirements, round off errors and truncation errors. Despite that, these methods are frequently used to test the hydrodynamic models, in following sections we summarize a few commonly used methods for particle level simulations.

a) Cellular Automata

Cellular automata uses a lattice or grid to map the domain. Each cell state describes the physics depending upon its neighbouring cells and the transport law/rule. The properties of each cell within the lattice at time *t* is related only to the properties of that cell and its neighbours at *t-1*. This method is particularly helpful in studying pattern formations in high density beds. In real flows, large scale features have been reported with considerable accuracy (Baxter, Behringer 1990).

b) Particle dynamics modeling

Particle order dynamics modelling simulations are amongst the most regularly used and widely accepted methods for granular media. Due to their accuracy with lesser computational requirements, many granular systems have been studied with these techniques such as (Marshall 2009), showing great deal of agreement between simulations and experiments.

This is an iterative method with simple algorithm working along the lines of the general steps summarized below:

- The position and velocity of each grain is identified at time instant t_1.
- Based on grain positions, collision is detected amongst the grains and or boundaries of the container.
- Post collision velocities are obtained from the collision rules.
- Velocities and positions of each of the grains are updated for the next time or the collision depending on the kind of sphere model selected.

The iterative loop runs till the number of collisions or the simulation time criteria is met. Depending upon the detail of the interaction between the particles two methods have been commonly used in literature. Details of these two models are included in the following sections.

c) Distinct Element modeling

In distinct element modeling (DEM) the interaction of the participating particles involve consideration of grain elastic nature. The simulation solves for the new value of position and velocity for each time step calculated through the basic equations of motion.

$$z(t + \Delta t) = z(t) + v(t)\Delta t + \frac{1}{2}a(t)\Delta t^2 \quad \textbf{(2.7)}$$

$$v(t + \Delta t) = v(t) + a(t)\Delta t \quad \textbf{(2.8)}$$

The simulation depends on the interaction physics of the grain, namely the soft sphere model. In the soft sphere case the dynamics of each collision is examined in detail. The deformation of the sphere is accounted during the collision. It allows grains to interact for long time durations with multiple contacts specially applicable for slow dense flows. However, this detail description is at the cost of high computational requirements as well

as input data for the complex input parameters modelling the softness of the sphere. Through those parameters and the force law of interaction (Shäfer, Dippel et al. 1996, Marshall 2009) the time varying deformation in the grains during collision is estimated and the net acceleration is calculated for each grain. DEM is amongst the accurate tools used in the molecular dynamics.

d) Event driven simulations

As in a rapid granular flow the grains interact with each other by instantaneous collisions. The forces act only when there is a collision and the particles usually move in a uniform gravitational field between collisions. The Event Driven (ED) simulation takes advantage of the fact that under gravity, particles travel in parabolic paths between successive collisions, and the time required for the next collision can be explicitly calculated from a knowledge of the particle positions and velocities (Duran 2000). The ED simulation technique proceeds by calculating the time required for the next collision, and advancing all the particles' positions to their positions at the next collision. The colliding particles are allowed to interact by a collision rule giving a set of post collision velocities for the particles. The simulation then advances to the next collision event. In contrast to the soft sphere simulation, the time advancement in the ED simulation is in steps of collisions rather than in time steps. Since in this method only binary collisions are considered, the collision times of the particles can be easily calculated. The change in momentum of the wall is neglected because its mass is large compared to that of the particle and the wall is assumed to affect only the normal component of the particle's velocity.

Based on inelastic hard sphere models, MD simulation accelerates the particles by calculating the time between instantaneous binary collision. These collisions conserve linear momentum, but dissipate energy (Sunthar 2001). The equations describing the dynamics for the particle wall and particle-particle collisions are given as

$$\hat{v}_i' = \hat{v}_i - (1+e_w)(\hat{v}_i \cdot \hat{n}_i)\hat{n}_i \qquad \textbf{(2.9)}$$

$$\hat{v}_{i,j}' = \hat{v}_{i,j} \pm \left(\frac{1+e}{2}\right)\left[(\hat{v}_j - \hat{v}_i)\cdot \hat{n}\right]\hat{n} \qquad \textbf{(2.10)}$$

where e is the coefficient of restitution for particle-particle collision and e_w is the coefficient of restitution for particle wall collision. $\hat{v}_i$ is the velocity vector of particle i, $\hat{n}_i$

is the unit normal vector that points from the centre of particle *i* to the point of contact with the wall and $\hat{n}$ is the unit centre to centre vector between the colliding pair *i* and *j*. For all of our work using event driven simulations in this thesis the particle interactions are modelled with constant value of coefficient of restitution *e*.

2.3 Testing hydrodynamic models

Although there have been considerable advances in our theoretical understanding of granular flows, validation of these models is challenging. Continuum equations of Euler and Navier-Stokes orders using Kinetic theory have been developed for granular medium (Lun, Savage et al. 1984, Jenkins, Richman 1985b, Richman M.W., Martin R.E. 1992) with certain simplifications. Such as these models usually assume inelastic hard-sphere binary collision as the base to simplify collision integrals. Previously these models have been tested with idealized scenarios which are difficult to achieve in a lab environment. More recently these equations have been put to work on experimentally realizable granular systems such as shear cells, rotating drums and fluidized beds for viability (Hrenya, Galvin et al. 2008, Huan, Yang et al. 2004, Wildman, Martin et al. 2008).

But granular materials in general are notorious to observe especially for the difficulties they pose to the experimenter. Granular gases in particular been most difficult to observe but at the same time show a wide range of phenomena which needs investigation and visualization. Amongst the most widest range of non-linear phenomena observed in granular flows only a handful of them have been understood completely. Thus by comparing the predictions of numerical simulations against the experimental findings, much of the underlying physics could be understood. In this section first we introduce and review some of the experimental techniques used for analyzing and validating the mechanics of granular flows.

a) Experiments on Granular Flows

Over the last decade technological advancements have enabled experimentalists to track and follow the motions of the grains, thus enabling direct experimental tests of theoretical predictions. A wide variety of experiments ranging from the ‘bucket method’ for collecting grains that fall off the chute in order to find the flow rate (Johnson, Nott et al. 1990) to sophisticated optical and radioactivity tracking techniques have been employed in this field. These techniques include high-speed photography (Warr, Huntley et al. 1995, Warr,

Huntley 1995) and—in three dimensions—positron emission particle tracking (PEPT) (Wildman, Huntley et al. 2001) and nuclear magnetic resonance (NMR) (Huntley, Martin et al. 2007, Huan, Yang et al. 2004, Xiaoyu Yang, Candela 2000, Serna, Marquina 2005, Hill, Caprihan et al. 1997). The techniques give an insight into granular behaviour by allowing the tracking of single particles or high resolution measurement of the hydrodynamic fields, thereby enabling the models of granular flow to be tested in detail. Here we detail the working principle and advantages of two advance techniques, PEPT and NMR, successfully used for analyzing dry granular flows.

The PEPT technique involves labelling a tracer particle with radioactive nuclei in a granular bed. With time the nuclei decay by emitting a positron which rapidly annihilates with a local electron, producing two gamma rays travelling in opposite directions. Two position sensitive detectors placed either side of the system detect the gamma rays. A line can later be drawn between the two positions, along which the emitting particle must have lain. PEPT can typically locate the tracer particle up to 500 times per second, with an accuracy of 1-2 mm when the particle is travelling at 1 ms^{-1}. With the tracer particle used in PEPT is identical to all the others in granular flow, apart from its radioactivity, the trajectory obtained is representative of all the particles, and can be used to calculate the system distributions. Each location of tracer is attributed a coordinate in space and time (x,y,z,t). Then the grain is followed for some time with the square of the displacement being recorded for every subsequent location event. Once this has been completed for every grain location in each segment, the mean squared displacement is binned according to the time of location, and the ensemble average is calculated. The mean square speed and thus the granular temperature is extracted from the data through fitting. This technique has been recently used successfully to study highly fluidized dry granular beds (Wildman, Martin et al. 2005, Martin, Huntley et al. 2005) with results capturing the presence of convection rolls.

NMR (nuclear magnetic resonance) imaging is one method which has shown great promise for observing time resolved behaviour of grains in three dimensions. The system detects the liquid base of the moving particles and thus such granular materials can only be used which can help generate detectable signal for NMR. NMR methods have been recently used to measure short-time three dimensional displacement of naturally occurring grains in a system of mustard seeds vibrated vertically (Huntley, Martin et al. 2007). This technique obtains time averaging of the granular motion over a specific time interval. In this interval

the grains can move ballistically thus a direct measurement of granular temperature profile is made possible. Using specially designed sequence most of the particles in a chamber/cell can be traced with high level of accuracy. It can resolve data in a three dimensional frame but at the cost of time resolution. NMR is used for some of the experimental work carried out in this research. In forthcoming chapters further details are included on the setup and processing of the technique.

b) Vibrofluidized bed

Amongst many apparatuses vibrofluidized bed has been used as an idealised and simple system in which the granular behaviour is relatively simplified and can be a testing ground for models of granular flows. The mechanism consists of a vessel that undergoes high-frequency agitation of sufficient amplitude to fluidize the granular medium contained within it (Fig. 2.1). The energy input into the bed is through collisions between the moving lower boundary and the particles. A number of experimental techniques such as high-speed photography (Warr, Huntley et al. 1995), positron emission particle tracking (PEPT) (Wildman, Huntley et al. 2001), nuclear magnetic resonance (NMR) (Huntley, Martin et al. 2007, Xiaoyu Yang, Candela 2000, Hill, Caprihan et al. 1997) have been used to study granular flows in vibrated beds.

Vibrating method of fluidization has been found to yield standing wave pattern formation (Pak, Behringer 1993), convection (Wildman, Huntley et al. 2001), clustering (Duran 2000), steady-state flow fields far from the plate (Viswanathan, Wildman et al. 2006) and shocks (Bougie, Moon et al. 2002). In particular, vibrations result in sound propagation in dense vibrated beds with low amplitude, leading to phenomena such as convection rolls, heaping, standing waves and travelling waves (Liu, Nagel 1992, Pak, Behringer 1993, Liu, Nagel 1993). At high base velocities the particles are highly energetic and the bed becomes dilated. In this regime, the time of contact between the particles during a collision is small compared to the time between collisions, and momentum and energy are transmitted primarily due to instantaneous collisions between the particles. No sustained frictional contact can be maintained between particles, phenomena such as liquid-like streaming motion, wave propagation, gas like density variations and shock waves as a result of fluidization of the particles are observed (Alain, Emmanuel et al. 2005, Luding, Clement et al. 1996, Huntley, Martin et al. 2007, Wildman, Martin et al. 2005, Pak, Behringer 1993, Warr, Hansen 1996).

Despite simple system of vibrated bed, the nature of granular materials is inherently complex. For example in the case of classical gases or simply elastic spheres in the state of thermal equilibrium, the velocity distribution function is a Maxwellian. On the contrary for simple inelastic flow systems, the velocity distribution deviates from a Maxwellian even for the case of smooth spherical particles as there is no such state of thermal equilibrium (Farkas, Tegzes et al. 1999, Warr, Hansen 1996, McNamara, Luding 1998). The simplest possible state for the case when the collisions are inelastic is that of steady, homogeneous cooling. As the flow gets denser the pair distribution function for a colliding pair, consisting of product of velocity distribution function and radial distribution function, g_0 (Evesque 1992), becomes significant. This incorporates the effects of the volume occupied by the spheres on their collision frequency. However the functional form of the radial distribution function g_0 already exists (Carnahan, Starling 1969). Using the assumption that the error proportional to the square of the quantities are small, the velocity distribution function obtained for these flows can be approximated to that of elastic systems. Thus similar expressions for the pressure tensor and the energy flux vector are calculated by using the velocity distribution function and Enskog's extension of the assumption of molecular chaos (Garzo, Dufty 1999, Garzo, Dufty et al. 2007).

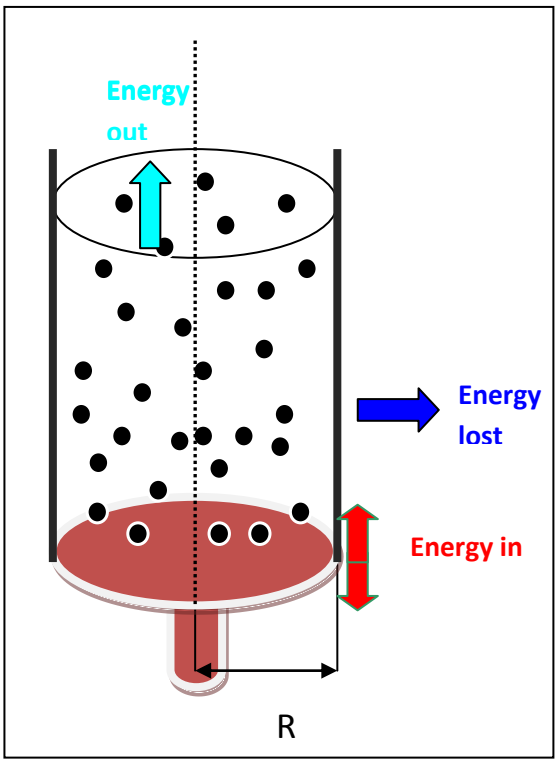

Figure 2-1: Schematic sketch of a vibrofluidized bed.

Some of the other simplifications for the solution of vibrated beds consider the amplitude of vibrating surface to be small compared to the succeeding collisions of the particles and the frequency of vibration is assumed to be large compared to the frequency of the collisions of the particles. This ensures that the velocity of the particles colliding with the vibrating surface is uncorrelated with the velocity of the surface itself. It is important to mention here that the dynamics of such a system then only depends on the mean square velocity in the limit where the velocity of the surface is small compared to the fluctuating velocity of the particles in the bed. These simplified models have been tested with idealized scenarios, and more recently these models have been put to work on experimentally realizable, time-dependent granular systems for viability, where Navier-Stokes order continuum equations are simulated to investigate the strongly temporal and spatial properties of vertically oscillated granular bed (Hrenya, Galvin et al. 2008, Huntley, Martin et al. 2007, Kumaran 2008). Still there is evidence of even higher order effects which has suggested the need of reviewing the form of constitutive relationships (Hrenya, Galvin et al. 2008).

Besides bulk behaviour the boundary motion in vibrated bed is of particular interest as it is usually periodic and therefore a possible cause of time dependent effects in the bed properties. Evidence from experimental findings, molecular dynamics simulations and hydrodynamic modelling by Bougie et al. (Bougie, Moon et al. 2002) and Huntley et al. (Huntley, Martin et al. 2007) has shown that time dependent effects cannot always be neglected. Nevertheless, the dynamic behaviour of a fluidized granular material shows some striking similarities with the behaviour of a fluid in thermal equilibrium, e.g. in its microscopic structure (Warr, Hansen 1996), self-diffusion properties (Wildman, Huntley et al. 1999) and convection behaviour (Wildman, Huntley et al. 2001). In the following section a detailed review of the vibrating base boundary is provided with its influence on the modelling and boundary conditions for granular flow.

c) Boundary Conditions for vibrated bed flows

The nature of the boundary conditions strongly influences the physics of granular materials specially the vibrating base in case of vibrated beds. Generally viscous classical fluids have no slip boundary conditions for momentum transfer with a wall which allow independent specification of the material properties to that of the flow field. The effect of wall is mostly felt in local regions in conventional fluids unless compressible fluids at high speed interact.

This is opposite to what we observe in granular flows. Here the flow behaviour at or due to the solid or free surface is an integral part of the solution for the entire flow field.

Considerable efforts have been made to understand their influence both experimentally and analytically. The experimental work of Savage & Sayed (Savage, Sayed 1984) shows the effect of rough walls. Profound effects of boundaries on the granular flow properties have been reported (Richman M.W., Martin R.E. 1992, Warr, Huntley 1995, Richman 1993, Jenkins, Louge 1997) which indicate that the drive surfaces are equally important as the granular material itself in determining the results of the test.

Boundary conditions are modelled from the first principles of momentum and energy balances at the surface (Jenkins, Richman 2006). Thus by satisfying the expressions for the balance of momentum and energy such granular boundary effect could be studied. We find considerable work on modelling the wall as rough particles which can be treated as granular materials principally and at high speeds the effects of shear can be neglected due to slip even leading to instantaneous collision (Warr, Huntley 1995, Richman 1993, Jenkins, Louge 1997). Through various methods of averaging, conditions have been obtained that apply to two dimensional systems of identical disks or three dimensional systems of identical spheres that interact with smooth bumpy boundaries (Jenkins, Louge 1997).

d) Comparison of methods for heat flux predictions at vibrating boundary

Calculations shown by Richman (Richman 1993) quantified the heat and momentum flux for the rapid granular flows of identical smooth spheres that interact with bumpy boundaries through inelastic collisions. The boundaries were considered to be non-stationary as well and could translate randomly with given specific mean velocities along with deviations about the mean with specified fluctuation velocities. Richman produced expressions for mean energy transfer in all the three orthogonal directions moving with a mean square velocity of $3V^2$ (V^2 for each of the direction) with V being the mean velocity of the base. The relationship includes addition and removal terms scaling with the square of base velocity and granular temperature. The basis of these calculations were upon the Maxwellian velocity distribution functions that relate and describe the velocities of both the flow particles and the boundaries. The rate of exchange was also calculated for the case

of linear momentum and kinetic energy between the granular particle and wall particle for a nearly flat surface.

Later Warr and Huntley showed detailed calculation for a triangular waveform inputting energy (Warr, Huntley 1995). A detailed analysis considering all possible combinations of impacts with possible speeds and positions of a particle upon a vibrating base is provided by Warr & Huntley. The energy was calculated using the mean change in velocity squared of the particles due to collision and it was evaluated numerically through an Energy integral I_e for a given base velocity magnitude. For these calculations the requirement is on the vibration period which should be much shorter than the mean time between successive collisions made by a given particle and the base. This analysis showed how the energy integral varies with the speed of the incident particles and the velocity of the base while taking into account the coefficient of restitution between the particle and the base. Remarkably it is shown that high incoming speeds of particles do not necessarily guarantee high energy inputs for small base velocities. In fact it is also possible for incident particles to lose energy on the average during an impact. This allowed direct comparison to the work of Richman for the mean square velocity of base ($3V^2$) and allowed a calculation of heat flux in a one dimensional system with flat boundaries. Kumaran also proposed energy input expressions for vibrated beds (Kumaran 1998). It gives an energy input proportional to the mean square speed of the bed. Although it is easy to implement, it does not allow for the possibility of energy extraction from the bed, nor does it take into account the coefficient of restitution between the particle and the base.

All the formulations rely on the continuum level description of granular temperature and base densities. For flow in the Knudsen regime, such description of continuum level state variables are not necessary accurate (Galvin, Hrenya et al. 2007). In the case of Warr and Huntley, the separation of time scales at the base can often become unclear and the assumption of Warr and Huntley is likely to break down in such regions. On the other hand, if the base time period reduces significantly as compared to mean free time, the assumption of instantaneous collisions also become susceptible and the current forms of boundary conditions need to be analyzed in such a scenario. In this thesis detailed discussions on these issue are covered in the forthcoming chapters. Interestingly in all the cases, the heat flux predicted by the above mentioned formulations provide a steady state expression and cannot be directly employed to study time varying behaviour. The phase

resolved behaviour of energy input and removal is calculated for the solution of time varying granular hydrodynamic model introduced in this thesis.

2.4 Open Issues

As summarized in the previous sections, research and development over the past few decades have revealed many of the complex and critical aspects of granular flows but still a number of characteristics remain poorly understood. Anisotropy, non-equipartition, nonlinear time dependent behaviours, unsteady pattern formations, temperature inversion, burnett order effects, non-equilibrium ratchet motions and scaling behaviour are few amongst many of the observed and expected phenomena in a dry granular vibrated bed.

Not only that most of these phenomena are non-linear but also are interlinked in complex fashion and the different formulations of constitutive relationships need critical analysis for application and validation. As the loading and dissipation increases even the near to idealized testing equipment produces highly non-linear phenomena requiring studies of phase transitions, super burnett order effects in bulk and near the boundaries to understand the complexities.

a) Polydisperse granular flows

An aspect of real life rapid granular flows is the variations of shape and sizes. Controlling the mixing/de-mixing of granular flows containing more than one species (a polydisperse system) is a problem faced by a wide range of industries. Often one likes to enhance the mixing (e.g., blending of pharmaceutical powders), but at other times one might want to force species segregation (e.g., separation of mined ores). Unfortunately, the physical mechanisms that govern mixing are not well understood, and industry faces considerable difficulties when trying to predict and control mixing/separation processes (Paolotti, Barrat et al. 2004). To be able improve these particle processing techniques, one requires significant control and a deep understanding of the physics of granular flows. When there is more than one size or mass phase within the system, the difficulties in predicting the bulk behaviour are considerably increased. Variations in shape and size also introduced problems such as non-equipartition and anisotropic effects (Wildman, Parker 2002).

Most of the computational hydrodynamics descriptions and constitutive relationships have been limited to steady state monodisperse granular flows. The recent developments in the theoretical modelling of polydisperse granular flows and their constitutive relationships

(Garzo, Dufty et al. 2007, Garzo, Hrenya et al. 2007) have raised opportunity for researchers to analyze and test the predictions for such flows. On the other hand testing and validation of different constitutive relationships for dense, time-varying, mono-dispersed granular flow still remains an open question. In this dissertation we only aim at the development of computational models for mono-disperse flows only using different forms of constitutive relationships. However we expect that the methodology used in this thesis can be extended to incorporate bidisperse and polydisperse flows with necessary modifications.

b) Form of constitutive relationships

With developments in the theoretical understanding of granular flows, different formulations of constitutive relationships have been proposed for different categories of monodisperse granular flows such as dense (Garzo, Dufty 1999), dilute (Jenkins, Savage 1983), smooth (Sela, Goldhirsch 2000), near elastic (Lun, Savage et al. 1984, Jenkins, Richman 1985b) and friction dominated (Kumaran 2008, Garzo, Hrenya et al. 2007). But only a handfull of these models has been tested for validation against experimental findings and amongst them near elastic models have found much appreciation (Hrenya, Galvin et al. 2008, Viswanathan, Wildman et al. 2006, Martin, Huntley et al. 2005). Therefore it is necessary to incorporate and validate the dense inelastic granular flow formulations with comparison against the established models and experimental findings. Especially with the fact that these formulations introduce additional constitutive relationships owing to inelasticity of the granular materials. In this dissertation we explore two types of constitutive formulations for monodisperse medium of granular flows covering dense highly dissipative mono-dispersed granular flows.

c) Time variant effects in granular gas

Most of the theoretical framework of granular flows has focused on the steady-state nature. Granular physics is unsteady by nature when subjected to flow. When subjected to vibration granular materials exhibit a variety of phenomena which are not only non-uniform in time but also in space. Unsteady flow patterns such as convection have already been reported in the literature, for instance (Sunthar 2001, Bougie, Moon et al. 2002, Rericha, Bizon et al. 2001, Khain, Meerson 2003) while axial dynamic wave propagation is explored experimentally and through hydrodynamic simulations (Bougie, Moon et al. 2002). Alongside temporal effect spatial variations in three dimensions are also observed

to be linked with the side wall dissipation and input base parameters (Wildman, Martin et al. 2005). Thus suggesting some link between the radial variations and base dynamics on the granular bed physics.

A one dimensional time-resolved hydrodynamic simulation revealed the axial dynamic fluctuations (Huntley, Martin et al. 2007) but is incapable of simulating the effect of radial variations under the influence of dissipative side wall. A three dimensional time varying picture with appropriate dissipative side wall conditions is the way to investigate the variations of granular cell. In this thesis an introduction of time varying axi-symmetric hydrodynamic model and its implementation and validation is included.

d) Testing Navier-Stokes order effects

Evidence of higher than Navier-stokes order effects has been reported in granular flows (Hrenya, Galvin et al. 2008). The exact form of the dissipation, stress tensor and the variations of bulk parameters are likely to induce Burnett and super Burnett order effects (Galvin, Hrenya et al. 2007, Van der Weele 2008). By analyzing the variations of Navier-Stokes order characteristic parameters a strong hint about the nature and order of flow and their gradients in the bulk granular dynamics can be studied.

By characterizing bulk flow parameters and their scalings in the asymptotic limits, it is expected to explain bulk physics in detail at least for steady state configuration and some of the analytical models of V. Kumaran have shown promise (Kumaran 2000a, Kumaran 2000b). Such developed non-dimensional parameters help in our understanding of granular flows and can lead to the ways to model them.

In our collaboration with V. Kumaran (personal communication), new parameters using the kinetic theory of granular gas were proposed which scale the nature of granular flow in a dry granular bed. This research work explores the predicted parameters, their related constitutive relationships and the scalings using an hydrodynamic model and molecular dynamics simulation.

2.5 Summary

A comprehensive survey of research work on granular flows is presented summarizing the kinetic theory, hydrodynamic modelling, molecular dynamics and experimental methods used over the past decades. The literature survey highlights a number of aspects in granular

physics with some of them still requiring further understanding. A summary of the grey areas is also included which are the subjects of research in present work. In the forthcoming sections the focus will be on dry granular flows in vibrated beds with the hydrodynamic models in three dimensions and temporal effects. Results are compared against molecular dynamics simulations and experimental findings using NMR and PEPT.

Chapter 3 Time varying axi-symmetric hydrodynamic model

3.1. Introduction

Modelling rapidly flowing granular flows is challenging. Broadly speaking, there are two levels of granular flow modelling, particle order and continuum order. One can take a particle level modelling approach such as that used in the discrete element method (DEM). This can be a powerful method, but it is computationally intensive which often becomes prohibitive with a large number of particles. An alternative is to use a continuum description of the system. A successful method for this has been in the development of closure through derivation of the constitutive relationships using the kinetic theory of granular gases. Relatively speaking, the continuum approach is far less computationally exhaustive than discrete elements modelling as the effects of loading conditions and packing fraction do not directly influence the solution time. With a set of governing equations, boundary conditions and closure fulfilment, it is much quicker to obtain the hydrodynamic level solutions than to perform particle level simulations. Although it is possible to develop programmes for solving hydrodynamic problems oneself, commercial software, such as Fluent and COMSOL, is available to solve these highly nonlinear problems numerically. With state of the art pre- and post-processors these commercial codes are also flexible in providing interfaces with user defined functions. In particular, COMSOL offers a user defined partial differential equation module in which implementation and modification of the equations and boundary conditions is relatively easy and accurate. In this Chapter we present a model for a vibrated three dimensional granular beds in which a numerical solution will be obtained by the Finite Elements approach (FE) as offered by COMSOL.

3.2. Hydrodynamics of vibrofluidized granular flow

In a granular flow, continuity and momentum are generally conserved, but kinetic energy is dissipated during collisions leading to a requirement of a continual input flux to balance the energy input rate with the dissipation rate and maintain the flow. This dissipation and time-dependent excitation highlights two problems that need investigation. Firstly, near-elastic models have been broadly successful in describing granular flows (Jenkins, Richman 1985b, Brey, Dufty et al. 1998, Lun, Savage et al. 1984), but it has become clear that as the system becomes more dissipative the weaker the description becomes and there is a need to re-evaluate the constitutive relations for granular flows to facilitate models

built for a larger range of coefficient of dissipation and packing fraction (Garzo, Dufty et al. 2007, Garzo, Dufty 1999). Secondly, up until recently, models for granular flow have not been experimentally tested in a transient or time dependent system. Evidence of the strong time dependent effects has been seen in wave motion at low frequency (Bougie, Moon et al. 2002), strong fluctuations over the course of vibration cycle (Huntley, Martin et al. 2007) and in the pattern formation seen in dense, highly periodic flows (Bizon, Shattuck et al. 1998). Therefore, the task here is twofold. Firstly, we look at the ways of implementing improved models based on the revised Enskog method (Goldhirsch 2003) in a realizable test system such as a vibrated bed. This requires restructuring the steady state viscous models of Vishwanathan (Viswanathan, Wildman et al. 2006) to undertake the work of Garzo and Dufty (Garzo, Dufty 1999). Secondly, we aim to develop a computationally friendly axi-symmetric hydrodynamic model using these constitutive relationships that includes the time dependent effects. We will address these tasks over the following chapters.

In this chapter we will describe the time varying hydrodynamic models in detail with two different forms of constitutive relationships and the numerical solution procedures and will present an initial validation through testing against steady state experimental results. In the subsequent chapters, analysis will be extended to a range of time-dependent systems to test the range of validity of our models in low frequency, high frequency and pulsed vibro-fluidised beds.

3.3. Hydrodynamic model

A granular flow must follow conservation laws of mass and momentum, and a balance relationship for energy. We give the governing relations for each below.

a. Non-Isothermal Flow

The generalized non-isothermal flow model is particularly useful for studies relating to heat transfer where there are variations in density and temperature. This form of the flow model is particularly helpful in implementing the constitutive relationships relating to temperature variations with slight compressibility effects (Chung 2002). These equations themselves arise from balances of mass and momentum. We consider the system to be compressible and therefore the stress tensor includes terms relating shear and normal strains to the stress. In our formulation, the momentum and mass balances are given by

$$\rho \frac{\partial \mathbf{u}}{\partial t} + \rho \mathbf{u}.\nabla \mathbf{u} = \nabla \left[-pI + \zeta(\nabla \mathbf{u} + (\nabla \mathbf{u})^T) - \left(2\frac{\zeta}{3} - K_{dv} \right) (\nabla.\mathbf{u}) I \right] + \boldsymbol{F} \quad \textbf{(3.1)}$$

$$\frac{\partial \rho}{\partial t} + \nabla.(\rho\, \mathbf{u}) = 0 \quad \textbf{(3.2)}$$

where ρ is the density; **u** is the velocity field; p is the pressure and ζ, K_{dv} are the shear and bulk viscosities respectively. Body forces are included in the momentum balance, $\boldsymbol{F}$, which can be due to, for example, gravity.

b. Convection Conduction Equation

The generalized energy balance equation is constructed by accounting for the conduction as well as convective heat transfer into a volume. For dissipative granular flows, extra terms appear in the energy balance accounting for the dissipation during inelastic particle-particle and particle-wall collisions. The heat balance within the system is described by

$$\rho \frac{\partial T}{\partial t} + \nabla.J = Q - \rho \mathbf{u}.\nabla T \quad \textbf{(3.3)}$$

where *T* is the granular temperature scaled by the mass of particle, *J* is the heat flux due to conductive part of heat transfer, *Q* is a sink or source term and *t* is time.

c. Constitutive Relationships

In order to close this nonlinear Navier-Stokes-like set of relations (Eq. 3.1, 3.2 and 3.3), one requires additional equations that describe the relationships between fluxes and gradients in the fields. The state law used for the model is given by

$$p = \rho T[1 + 2(1+e)G] \quad \textbf{(3.4)}$$

where G is given by $G = \eta g_o$ and $\eta = \frac{\pi \rho d^3}{6m}$ with *m* is the mass of a single particle and *d* is the particle diameter.

The radial distribution function at contact, g_o, accounts for the increase in collision rate over that predicted by Boltzmann at high densities due to volume effects and we use the approximation suggested by Carnahan (Carnahan, Starling 1969) and Torquato (Torquato 1995),

$$G = \begin{cases} \frac{2-\eta}{2\,(1-\eta)^3} & \eta < 0.49 \\ \frac{5.6916(0.64-0.49)}{0.64-\eta} & \eta > 0.49 \end{cases} \quad \textbf{(3.5)}$$

We used two sets of constitutive relationships for viscosity, thermal conductivity and dissipation, derived from the work of Jenkins on one hand, and on Garzo and Dufty on the other (Jenkins, Richman 1985b, Garzo, Dufty 1999). Firstly we introduce the Jenkins' formulation (Jenkins, Richman 1985b). It is developed from the expansion of Boltzmann equation for a nearly elastic system and has already shown promise for steady state cases (Viswanathan, Wildman et al. 2006).

The constitutive relationships for the bulk and shear viscosities are given by

$$K_{dv} = \frac{8\rho d\sqrt{\pi T}}{3\pi} G \quad \textbf{(3.6)}$$

and

$$\zeta = \frac{\rho d\sqrt{\pi T}}{6}\left[\frac{5}{16G} + 1 + \frac{4}{5}\left(1 + \frac{12}{\pi}\right) G\right]. \quad \textbf{(3.7)}$$

The heat flux, J, is given by $J = -\kappa \nabla T$ with the thermal conductivity κ as

$$\kappa = \frac{15\rho d\sqrt{\pi T}}{16}\left[\frac{5}{24G} + 1 + \frac{6}{5}\left(1 + \frac{32}{9\pi}\right) G\right]. \quad \textbf{(3.8)}$$

The dissipation is given by

$$Q = \frac{-12(1-e^2)}{d\sqrt{\pi}} \rho T^{3/2} G + \frac{2}{3}[-p(\nabla \boldsymbol{u}) + (K_{dv} + \frac{4}{3}\zeta)(\nabla \boldsymbol{u})^2] \quad \textbf{(3.9)}$$

where the first term on the right hand side is the energy dissipation rate due to particle-particle losses and the second term corresponds to pressure work and viscous heating.

The second formulation is based on the work of Garzo and Dufty. This presents constitutive relations that are more accurate and able to describe granular systems over all coefficients of restitution. However, it has not been rigorously tested and has yet to be considered within a time varying system. Based on the revised Enskog approach (see Chapter 2) it proposes corrections for the transport relationships at Navier-Stokes order with additional terms appearing for inelasticity and kinetic transfer. In the dilute limit these relationships agree well with Jenkins' formulation. The constitutive relationships and

coefficients as developed by Garzo and Dufty (Garzo, Dufty 1999) are reproduced below. The transport coefficients are reduced by $\kappa_0$and η_0 given by,

$$\kappa^* = {}^{\kappa}/_{\kappa_0} \quad \textbf{(3.10)}$$

$$K_{dv}{}^* = {}^{K_{dv}}/_{\eta_0} \quad \textbf{(3.11)}$$

$$\zeta^* = {}^{\zeta}/_{\eta_0} \quad \textbf{(3.12)}$$

$$\mu^* = {}^{\eta\mu}/_{T\,\kappa_0} \quad \textbf{(3.13)}$$

where $\kappa_0 = \frac{15\,\eta_0}{4}$ and $\eta_0 = \frac{5m}{16d^2}\sqrt{\frac{T}{\pi}}$ are the dilute limit values of thermal conductivity and shear viscosity respectively. While the cooling rate γ_1 is reduced as $\gamma^* = \gamma_1/v_0$ where v_0 is the characteristic collision frequency given by

$$v_0 = \frac{nT}{\eta_0}. \quad \textbf{(3.14)}$$

The bulk and shear viscosity coefficients are given by

$$K_{dv}{}^* = \frac{32}{45}\pi\eta G(1+e)\left(1-\frac{1}{32}c^*\right) \quad \textbf{(3.15)}$$

and

$$\zeta^* = \zeta^k\left[1+\frac{2}{15}\pi G(1+e)\right]+\frac{3}{5}K_{dv}{}^* \quad \textbf{(3.16)}$$

where the kinetic parts, $\zeta^k$and c^* are given by

$$\zeta^k = \frac{1}{\left(v_\eta-\frac{1}{2}\gamma^{(0)}\right)}\left[1-\frac{1}{15}(1+e)(1-3e)\pi G\right] \quad \textbf{(3.17)}$$

with

$$v_\eta = \frac{2-\eta}{2(1-\eta)^3}\left[1-\frac{1}{4}(1-e)^2\right]\left[1-\frac{1}{64}c^*\right] \quad \textbf{(3.18)}$$

$$\gamma^{(0)} = \frac{5}{12}\,\frac{2-\eta}{2(1-\eta)^3}(1-e^2)\left(1+\frac{3}{32}c^*\right) \quad \textbf{(3.19)}$$

and

$$c^* = 32(1-e)(1-2e^2)[81-17e+30e^2(1-e)]^{-1} \quad \textbf{(3.20)}$$

In this derivation, the heat equation also includes a density gradient term, such that $J = -\kappa\nabla T - \mu\nabla\eta$. The constitutive coefficients for the κ and μ are given by

$$\kappa^* = \kappa^k\left[1+\tfrac{1}{5}\pi G(1+e)\right] + \tfrac{64}{225}\pi\,\eta\,G(1+e)\left(1+\tfrac{7}{32}c^*\right) \quad \textbf{(3.21)}$$

where $k^k$is given by

$$\kappa^k = \frac{2(1+\frac{1}{2}(1+p^\epsilon)c^*)}{3(v_k-2\gamma^{(0)})} + \frac{\pi G}{10}(1+e)^2\{2e-1+[\tfrac{1}{2}(1+e)-\tfrac{5}{3(1+e)}]c^*\} \quad \textbf{(3.22)}$$

and $p^\epsilon$and v_k are given by

$$p^\epsilon = 1+\tfrac{1+\alpha}{3}\pi G, \quad \textbf{(3.23)}$$

$$v_k = \tfrac{1}{3}(1+e)\tfrac{2-\eta}{2(1-\eta)^3}\left[1+\tfrac{33}{16}(1-e)+\tfrac{19-3e}{1024}c^*\right] \quad \textbf{(3.24)}$$

The inelastic transport coefficient is given by

$$\mu^* = \mu^k\left[1+\tfrac{1}{5}\pi G(1+e)\right] \quad \textbf{(3.25)}$$

where the kinetic part $\mu^k$is the given by

$$\mu^k = \frac{2}{(2v_k-3\gamma^{(0)})}\left\{\begin{matrix}\left(1+\eta\partial_\eta ln\, g_o\right)\gamma^{(0)}\kappa^k+\frac{p^\epsilon}{3}\left(1+\eta\partial_\eta lnp^\epsilon\right)c^*-\\ \tfrac{2}{15}\pi G\left(1+\tfrac{1}{2}\eta\partial_\eta lng_o\right)(1+e)\\ \left\{e(1-e)+\tfrac{1}{4}\left[\tfrac{4}{3}+e(1-e)\right]c^*\right\}\end{matrix}\right. \quad \textbf{(3.26)}$$

where g_o is given by G/η.The dissipation term $Q$is given by

$$Q = \rho T^{3/2}\gamma_1 + \tfrac{2}{3\rho}[-p(\nabla\boldsymbol{u})+(K_{dv}+\tfrac{4}{3}\zeta)(\nabla\boldsymbol{u})^2] \quad \textbf{(3.27)}$$

where $\gamma^* = \gamma^{(0)}+\gamma^{(1)}$, and $\gamma^{(1)}$ is given by

$$\gamma^{(1)} = \left[-\tfrac{1}{v_0}(1-e)(p^\varepsilon-1)+\tfrac{5}{32}(1-e^2)\left(1+\tfrac{3}{64}c^*\right)g_o c_D\right]\nabla.\boldsymbol{u} \quad \textbf{(3.28)}$$

and $c_D$is given by

$$c_D = \frac{1}{v_0}\left[\frac{1}{2}\gamma^{(0)} + v_r + \frac{5c^*}{64}\left(1 + \frac{3}{64}c^*\right) g_o(1 - e^2)\right]^{-1} \quad \textbf{(3.29)}$$

where v_r is given by

$$v_r = \frac{1+e}{48} g_o(128 - 96e + 15e^2 - 15e^3) + \frac{c^*}{64}(15e^3 - 15e^2 + 498e - 434) \quad \textbf{(3.30)}$$

3.4. Boundary conditions

The steady state and time dependent models employ different ways of treating the base boundary conditions due to the inbuilt nature of the two models. In our initial testing of the model using a steady state formulation, we use an effective time independent heat flux while the heat flux and momentum for the time dependent model are introduced separately in the next chapter. The boundary conditions for the steady state case are as follows.

The axial symmetry of the problem (Fig. 3.1) allows the gradients of the temperature and of the components of the mean velocity fields to be specified:

$$\frac{\partial T(0,z)}{\partial r} = 0 \quad \textbf{(3.31)}$$

$$\frac{\partial u(0,z)}{\partial r} = 0 \quad \textbf{(3.32)}$$

$$\frac{\partial v(0,z)}{\partial r} = 0 \quad \textbf{(3.33)}$$

where *u* and *v* are the radial and vertical components of velocity vector **u**.The base of the cell provides the energy input to the system however the inertial effect of the base is negligible over the course of a complete cycle. The validity of this assumption will be revisited in chapter 4 and 5 where we consider time-dependent simulations of this system. For steady state system one can describe the heat flux description at the base in the limit of flat wall by (Richman 1993)

$$J(r,0) = \left(\frac{2}{\pi}\right)^{1/2} P(r,0)\left[\frac{2\overline{V_b}^2}{(T+\overline{V_b}^2)^{1/2}} - (1 - e_b)(T + \overline{V_b}^2)^{1/2}\right] \quad \textbf{(3.34)}$$

where $\overline{V_b}^2$ is the root mean squared velocity of the vibrating base and e_b is the coefficient of restitution between grain and the base. In order to support total number of grains N_g in the cell base pressure $P(r,0)$ is specified as

$$P(r,0) = \frac{N_g mg}{\pi R^2} \quad \textbf{(3.35)}$$

The sidewall is treated in similar fashion to the base, such that

$$J(R,z) = \left(\frac{2}{\pi}\right)^{1/2} P(R,z)\left[\frac{2\overline{V_h}^2}{(T+\overline{V_h}^2)^{1/2}} - (1-e_W)(T+\overline{V_h}^2)^{1/2}\right] \quad \textbf{(3.36)}$$

where $\overline{V_h}^2$ is the out of plane root mean squared velocity component of the wall. The quantity e_w represents the particle-wall coefficients of restitution. $P(R,\mathrm{z})$ is the pressure, *p*, at the side wall calculated through Eq. 3.4.

At the top boundary the heat flux is set to zero,

$$J(R,L) = 0. \quad \textbf{(3.37)}$$

The base, side wall and upper boundaries are considered impenetrable and we use non-slip boundary conditions to specify the condition:

$$\mathbf{u} = 0 \quad \textbf{(3.38)}$$

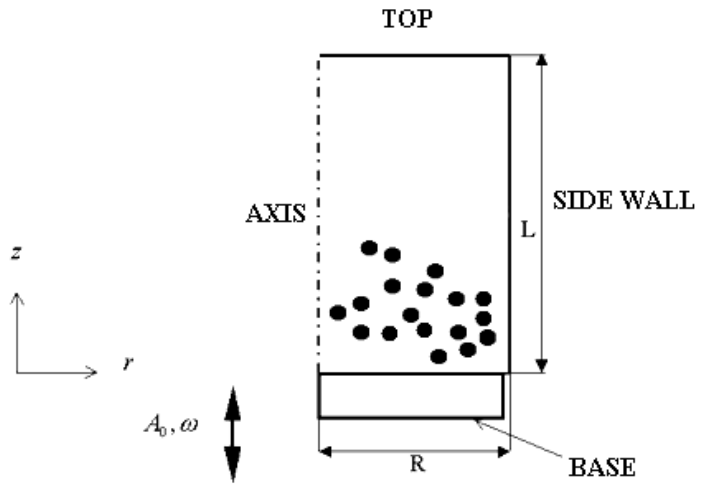

Figure 3-1: Axi-symmetric domain of vibrated granular bed.

3.5. Numerical solution and mesh independence

The solution of these Navier-Stokes-like equations requires techniques that are similar to those used for conventional fluids, but the boundary conditions leave profound effects not only on the stability of solution technique but the solution itself. This is the characteristic of granular flows as injection of heat and momentum through boundaries are critically important for the establishment of flow and usually evolve as a part of the solution. The coefficients of the constitutive relationships are functions of state variables such as density and temperature as in case of conventional fluids, but as the number density increases the dense gas effects are introduced through diverging form of radial distribution function which causes problem in attaining stability under very high packing fractions.

The finite element method has recently been used in granular flows with reasonable accuracy for instance (Viswanathan, Wildman et al. 2006). On the other hand finite difference scheme faced instabilities in convergence and implementation of heat flux at the base boundary poses problems which affects the bulk physics (Huntley, Martin et al. 2007). Here we employ a finite element package for steady state as well as time varying granular physics simulations.

In our system, the mass and momentum conservation equations (Eq. 3.1) and (Eq. 3.2) are implemented in the 'Non-Isothermal mode' of the Chemical Engineering-Momentum balance module, a supplementary module in COMSOL designed to facilitate the solution of heat and mass transfer problems. The energy equation (Eq. 3.3) is implemented in the 'Convection and Conduction mode' of the Chemical Engineering-Energy balance module with the equation of state (Eq. 3.4) implemented as an algebraic equation using the coefficient form of the user defined partial differential equation PDE module. We considered a cylindrical domain of radius R and height L shown in Fig. 3.1, containing N_g particles each with a diameter d and mass m. The granular bed is fluidized by a vertically vibrating the base of the system sinusoidally at an angular frequency ω and amplitude a_0. In our simulations we chose input parameters designed to match the details of experiments using PEPT (Wildman, Martin et al. 2005) detailed in Section 3.6.

The model is solved using different mesh densities varying through (a) 800 elements,10 boundary elements (b)1800 elements, 20 boundary elements, (c) 2500 elements, 25 boundary elements, and (d) 3300 elements, 30 boundary elements. It was observed that the numerical error was small (< 3%) with mesh quality changing from (a) to (b) and less than

1% from (c) to (d) and mesh quality (c) was selected for our computational domain. In comparison with experimental data the percentage error observed in the numerical solution was found reasonably small. However even with the mesh quality (d) the boundary layers near the side wall and base were not completely resolved. This requires significantly higher mesh densities in the close vicinity of the boundaries and was not performed due to the limited computational resources. For solution, a nonlinear solver is used based on the generalized mean residual (GMRES) solver and incomplete LU pre-conditioner with a drop tolerance of 10^{-6}. We used the 'Elimination' constraint handling method and 'Orthonormal' null-space function to obtain the solution.

3.6. Validation of Steady state hydrodynamic model with constitutive relationships

The hydrodynamic model and the two sets of constitutive relationships are compared with the experimental data obtained using PEPT and the hydrodynamic simulations of Viswanathan et al (Viswanathan, Wildman et al. 2006) in the limit of steady state case. Here a summary of the experimental setup is included for the sake of reference.

a. Experiments using Positron emission particle tracking

The detail working of PEPT technique has already been introduced in Chapter 2. Here for comparison we take the case using 700 glass beads each of 5 mm diameter placed in a 140 mm diameter polymethyl methacrylate (PMMA) container, of height 300 mm, fitted with a glass base. The coefficients of restitution were measured as 0.91 ± 0.02 for a glass-glass collision and 0.68 ± 0.04 for a glass-PMMA collision. The cylinder was attached to a Ling Dynamic Systems vibrator, which vibrated the system at a frequency of 50 Hz and amplitude of up to 1.54 mm with a sinusoidal waveform. In the system outlined here, PEPT typically locates the tracer particle up to 500 times per second, with an accuracy of 1-2 mm when the particle is travelling at 1 ms^{-1}. For further details on the setup and test procedures readers are referred to Wildman et al. (Wildman, Martin et al. 2005).

b. Results and discussion

Results are compared for Jenkins' (Jenkins, Richman 1985a) and Garzo's (Garzo, Dufty 1999) models for root mean squared base velocity of $V_b^* = 1.54$ where V_b^* is the non-dimensional base velocity. Both constitutive formulations, here abbreviated to SSM-Jenkins and SSM-Garzo for reference, are compared for the case of the dilute limit where

both models should produce similar results. Thus in Figs 3.2 and 3.3, a comparison of packing fraction and granular temperature show that both models compare reasonably well in the dilute regime with the experimental findings of PEPT (Wildman, Martin et al. 2005). In the case of SSM-Garzo, the granular temperature shows an increase in the region of the cell away from base (Fig. 3.3) and this is expected owing to the additional term appearing in the heat flux relationship relating density gradient, $J = -\kappa\nabla T - \mu\nabla\eta$. The effect of this additional term is consistent with previous results of Martin (Martin, Huntley et al. 2005) using constitutive relationships proposed by Brey et al (Brey, Dufty et al. 1998). The convective rolls and velocity patterns show agreement amongst the two models and the experimental findings of PEPT as shown in Fig 3.4. However due to limited computational resources the boundary layer near the side wall was not resolved completely. Still we can see from Fig. 3.2 and Fig 3.3 that below 5*d* there is good agreement between SSM-Garzo and SSM-Jenkins for the granular temperature. Above 5*d* we observe a difference in the temperature profiles that can be attributed to the second term in the heat flux.

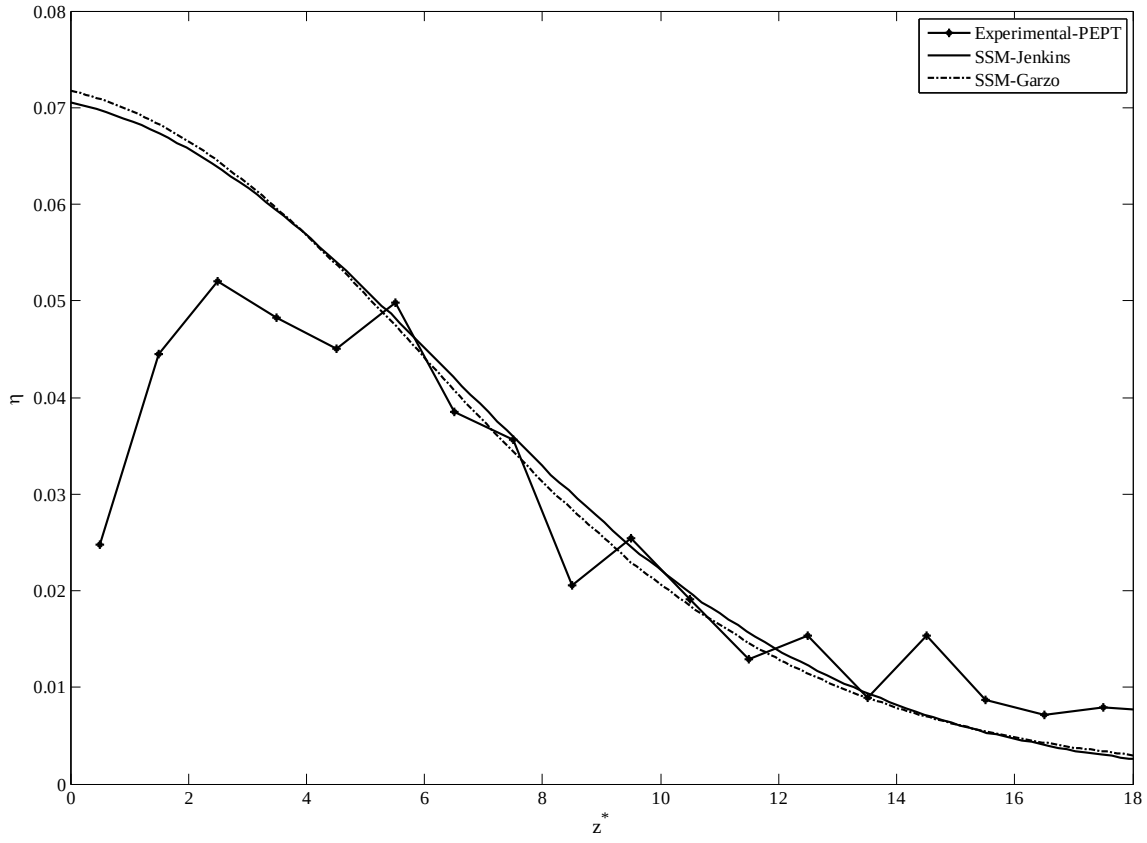

Figure 3-2: Packing fraction as a function of height for Steady state case at *r = 0.72 Data curves are labelled according to their nomenclature as given in body text.**

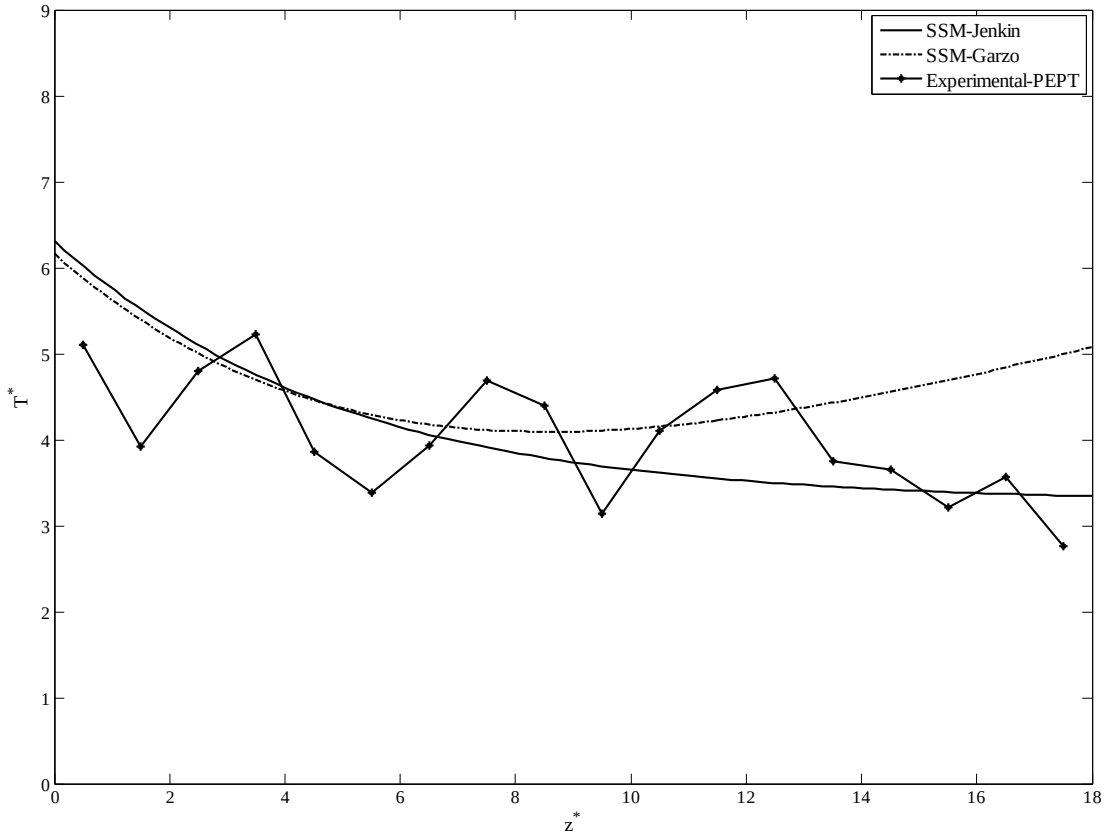

Figure 3-3: Granular temperature as a function of height for steady state case at *r = 0.72 Data curves are labelled according to their nomenclature as given in the body text.**

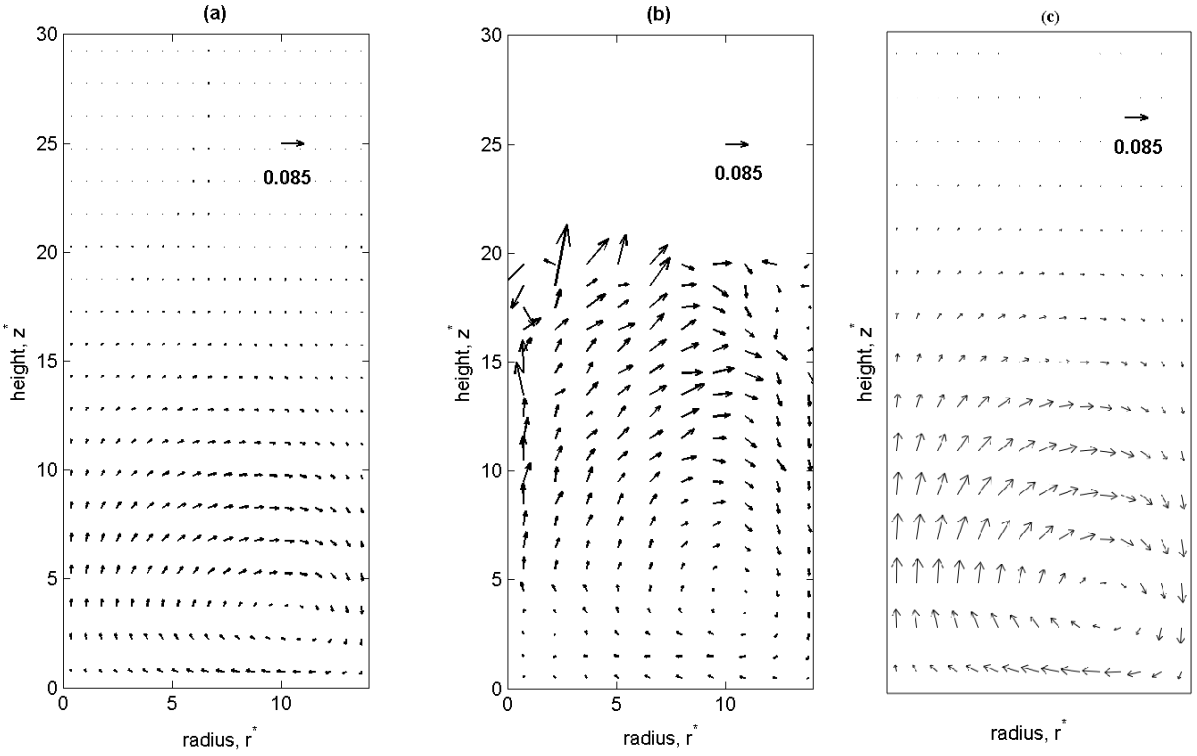

Figure 3-4: Velocity vectors in axi-symmetric case for the case of steady state model. (a) SSM-Jenkins, (b) experimental PEPT results and (c) SSM-Garzo.

SSM-Jenkins has been widely tested (Hrenya, Galvin et al. 2008, Wildman, Martin et al. 2008, Martin, Huntley et al. 2005) and as a consequence is commonly used for describing dry granular flows, despite the restriction in its derivation to near elastic particles. The use of these models in high dissipation flows raises questions regarding its applicability as it finds its roots for near elastic systems only. While SSM-Garzo has better mathematical foundations for providing solutions for larger ranges of packing fraction and inelasticity. To our knowledge, SSM-Garzo is a first attempt to use the complete model for realizable dense inelastic systems. In comparison with the results against the established SSM-Jenkins, it predicts the hydrodynamic behaviour reasonably well with the maximum difference between the predictions and experimental results lying within 15% for granular temperature predictions in major part of the cell particularly near the base ($z^* < 5$). SSM-Garzo seems to predict slightly higher packing fraction near to the base in comparison with SSM-Jenkins, and the packing fraction decays slightly earlier at higher altitudes of the cell owing to mass conservation. Near the side wall both models predict increased packing fractions at a height corresponding to that of the eye of the convection (not shown), whilst the SSM-Garzo predicts increased packing fractions consistently (see Fig. 3.5). However, these differences lie within the acceptable limits.

The presence of the eye of convection roll near the side wall is linked with the increased local density towards the side wall. Figure 3.5 shows the increased packing fractions near the wall at r^* = 13.5 compared to packing fraction predictions at the axis, r^* = 0. The increased region of local density means increased dissipation region leading to a reduction in the granular temperatures near the location of the eye of the convective roll. Both steady state models effectively indicate that the granular temperature fluctuations are strongly linked to the convective rolling (see Fig. 3.6). At r^* = 13.5 SSM-Jenkins shows a decrease in the granular temperature to its minimum between $4 < z^* < 10$ and the subsequent increase in temperature for $z^* > 10$. Otherwise a continuous decreasing trend is seen at the axis (r^*= 0) for SSM-Jenkins. Similarly SSM-Garzo also shows lower minimum temperatures at r^* =13.5 as compared to r^* = 0. Although SSM-Jenkins shows a localized temperature upturn away from the base. The temperature inversion is characteristic of SSM-Garzo due to appearance of the density gradient term in the constitutive relationships, something not present in SSM-Jenkins. It should also be noted that the rolling only appears when an inelastic wall is used, and has been confirmed in both models. The inelasticity of the wall links the viscous effects in the momentum and energy equations through an

enhanced density concentration appearing near the wall, which does not occur when the particle-wall collisions are elastic.

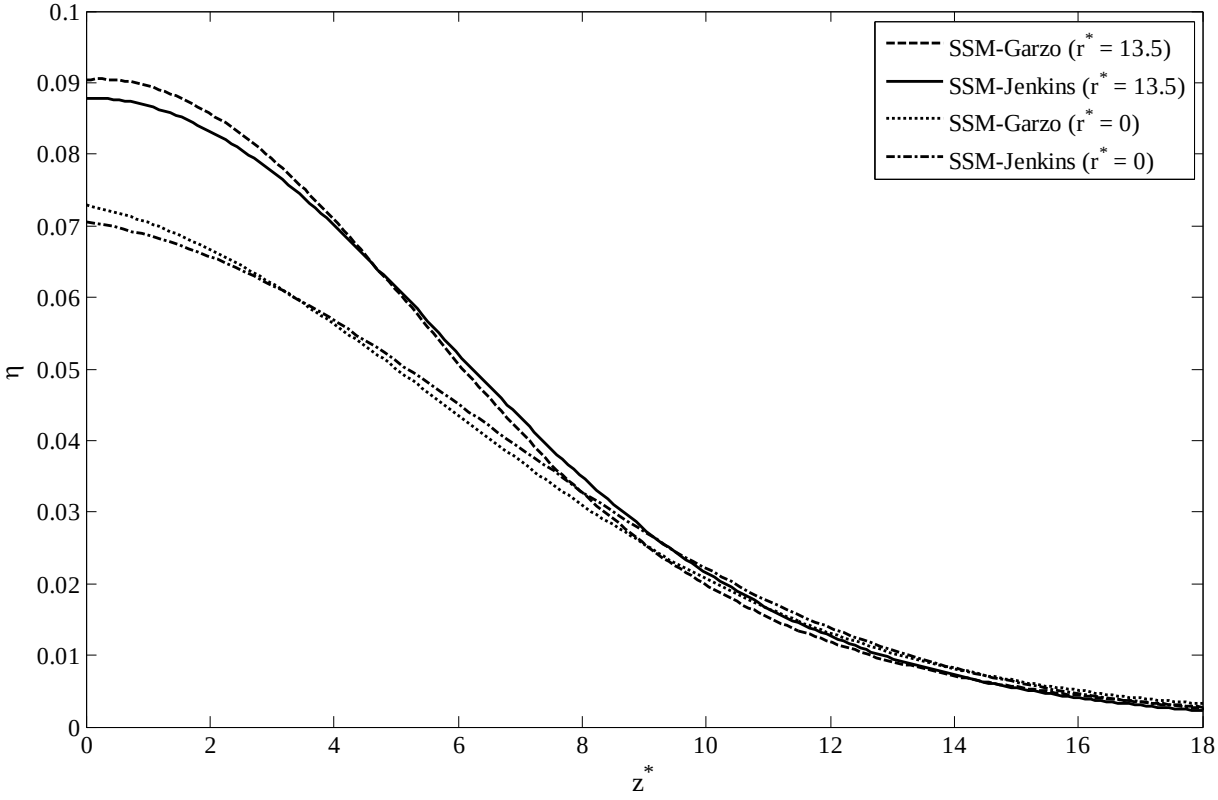

Figure 3-5: Packing fraction as a function of height at *r = 0 and 13.5 for n = 700 at $V_b^* = 1.54$.**

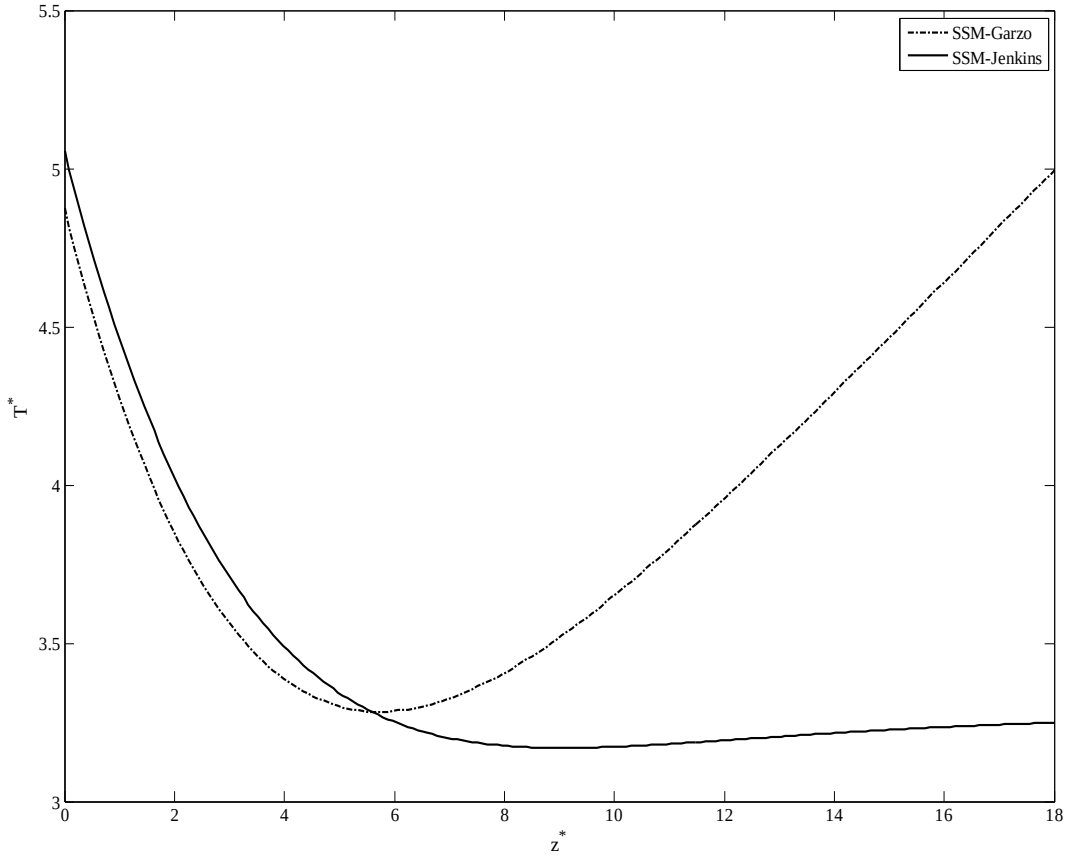

Figure 3-6: Granular temperature as a function of height at *r = 13.5 for n = 700 at $V_b^* = 1.54$.**

3.7. Summary

This chapter details the Navier-Stokes-like model for the steady state and time dependent granular motion in a vibrated axi-symmetric three dimensional granular bed. The model uses two types of constitutive formulations. Validation for the steady state case has been completed through comparison of the results for SSM-Garzo against those for SSM-Jenkins and PEPT experimental data, and show that SSM-Garzo agrees well with SSM-Jenkins model in the dilute regime. This agreement suggests that a time-dependent solution may be possible and in the forthcoming chapters we will develop these models further to the time dependent case with different loading conditions and frequencies of excitation.

Chapter 4 Low frequency vibro fluidized granular beds

4.1. Introduction

Time dependent physics for granular flows, in the recent past, started to have been investigated (Bougie, Moon et al. 2002). Evidence of generation of waves during low frequency vibration has been reported in the MD simulations of Bougie (Bougie, Moon et al. 2002) and the experimental findings and one dimensional modelling using Jenkins' formulation (Huntley, Martin et al. 2007) have both demonstrated strong time varying fluctuations in the mean velocity and granular temperature over the course of a typical vibration cycle. Previous investigations at similar base velocities, packing fraction and excitation frequency have previously confirmed a range of phenomena, including the presence of a convective rolling in the cell (Sunthar 2001, Bougie, Moon et al. 2002, Rericha, Bizon et al. 2001, Khain, Meerson 2003). In this Chapter we propose to extend these studies to time-dependant problems using a Navier-Stokes order axi-symmetric description. In particular we will look at the effect of radial variations on the dynamic nature of the cell during low frequency of excitation, thereby investigating a possible link between the steady state features (convection) and time varying effects (travelling waves). In this chapter we extend our analysis to include time dependent and phase resolved predictions of spatial variations of the temperature and velocity fields in a vibrofluidized granular bed. By simulating the model for the axi-symmetric geometry, it is possible to observe the transport of mass, momentum and granular temperature in both the axial and the radial directions as function of time.

In this chapter the time dependent hydrodynamic model introduced in Chapter 3 is solved. This chapter details the time varying treatment of vibrating boundary conditions, the solution procedure and the results for a granular bed vibrated at low frequencies. The results for the both constitutive formulations described in Chapter 3 are compared with the time varying behaviour of a dry granular flow in a vibrated bed obtained using molecular dynamics simulations and experimental results (Huntley, Martin et al. 2007). A summary of the experimental setup of the NMR apparatus is also included in this chapter for the sake of completeness.

4.2. Solving time dependent model

Here we solve both formulations introduced in Chapter 3 for the time varying case. In order to confirm the predictions of the models, hereby referred as ATD-Jenkins and ATD-Garzo, results are compared against phase-resolved findings of NMR experiments (Huntley, Martin et al. 2007) and hard sphere molecular dynamics simulations. All time/phase-resolved simulations are carried out for a total of 110 particles with mean diameter d = 2.04 mm with a base vibration frequency of 38.2 Hz, as per the parameters used in the experiments. The non-dimensional internal radius ($R^* = R/d$) of the domain was set as 4.4117 to match the cell in the experiments. Details of boundary conditions and solution checks for time dependent case are included in the following sections.

a. Boundary conditions for the time dependent model

Our time dependent model uses an axi-symmetric domain similar to that shown in Fig. 3.1, with the relevant boundaries as labelled. In order to obtain a complete description of the system thermal and momentum boundary conditions are required at each of the four edges of the system.

We solve the hydrodynamic model in the frame of the shaking cell which results in an additional momentum term in Eq. 3.1 of the form of $a_0\omega^2 cos(\omega\, t)$ (Huntley, Martin et al. 2007) where a_0 is the amplitude and ω is the frequency of the base. By solving in the frame of the shaking cell the base boundary effectively becomes motionless and is modelled as a static wall. For the heat flux at the base we adopt the relationship developed by Jenkins and Louge for static wall (Jenkins, Louge 1997),

$$J\,(r,0) = -p(3T)^{\frac{1}{2}}(\frac{\pi}{6})^{\frac{1}{2}}\{\frac{2}{\pi}(1-e_b)\} \qquad \textbf{(4.1)}$$

where e_b is the coefficient of restitution between particle and base and p is the pressure at base. The momentum boundary condition at the base is set to be a no-slip boundary as in the case of viscous fluids. The no-slip boundary condition eliminates all components of the velocity vector, such that $\mathbf{u} = 0$.

The top boundary of the domain is positioned high enough to avoid significant interaction of the granular material with the top whilst at the same time ensuring that the density does not fall so low that the continuum no longer exists. The continuum region limit is

calculated using the cut off packing fraction value based on the relationship $\eta = \frac{\sqrt{\pi}}{24T^*}$ (Martin, Huntley et al. 2005).

The calculated height varies from 6.2d to 8d during the course of a cycle but for the sake of simplicity the higher value of 8d is used for all simulations. The boundary condition consisted of a zero heat flux $J(r, L) = 0$. The momentum boundary condition at the top is taken as no-slip. Trial solutions were also made with stress-free boundary conditions but no discernable difference was observed.

The side wall is modelled as a static, dissipative boundary. The heat flux due to the inelastic particle side wall collisions is then given by

$$J\,(r, R) = -p(3T)^{\frac{1}{2}}(\frac{\pi}{6})^{\frac{1}{2}}\{\frac{2}{\pi}(1 - e_w)\} \qquad \textbf{(4.2)}$$

where e_w is the particle side wall coefficient of restitution.

At the axis of the cylinder, the axial symmetry of the problem requires that the gradient of the temperature in the radial direction $\frac{\partial T(0, z)}{\partial r}$ is zero.

b. Solver stability and necessary checks

Previously developed one dimension phase resolved hydrodynamic model in Huntley et al (Huntley, Martin et al. 2007) faced problems due to the stability of numerical scheme and the highly non-linear nature of the model. Using finite element scheme to solve equations in non-conservative form helps this model by not requiring artificial/additional stabilization techniques at any stage of the solution in spite of the presence of nonlinearity and steep gradients in the domain (COMSOL 2007). A number of checks are employed to test the validity of the solution, which includes a) ensuring the number of particles (N_g) remained constant throughout the simulation at any time and b) checking that the net energy gain over a cycle is zero. The number of grains in the cell is calculate using

$$N_g = A \int_0^R \int_o^L n\, dr\, dz \qquad \textbf{(4.3)}$$

where n is the number density and A is the cross-sectional area of cell.

Both conditions are plotted in Figs 4.1 and 4.2 to show the fluctuations in the integrated quantities, the number of grains and the domain energy integral. We can observe that the test quantities settle down quickly and the solutions acquires periodic steadiness after non-dimensional time $\tau^* = 6.0$.

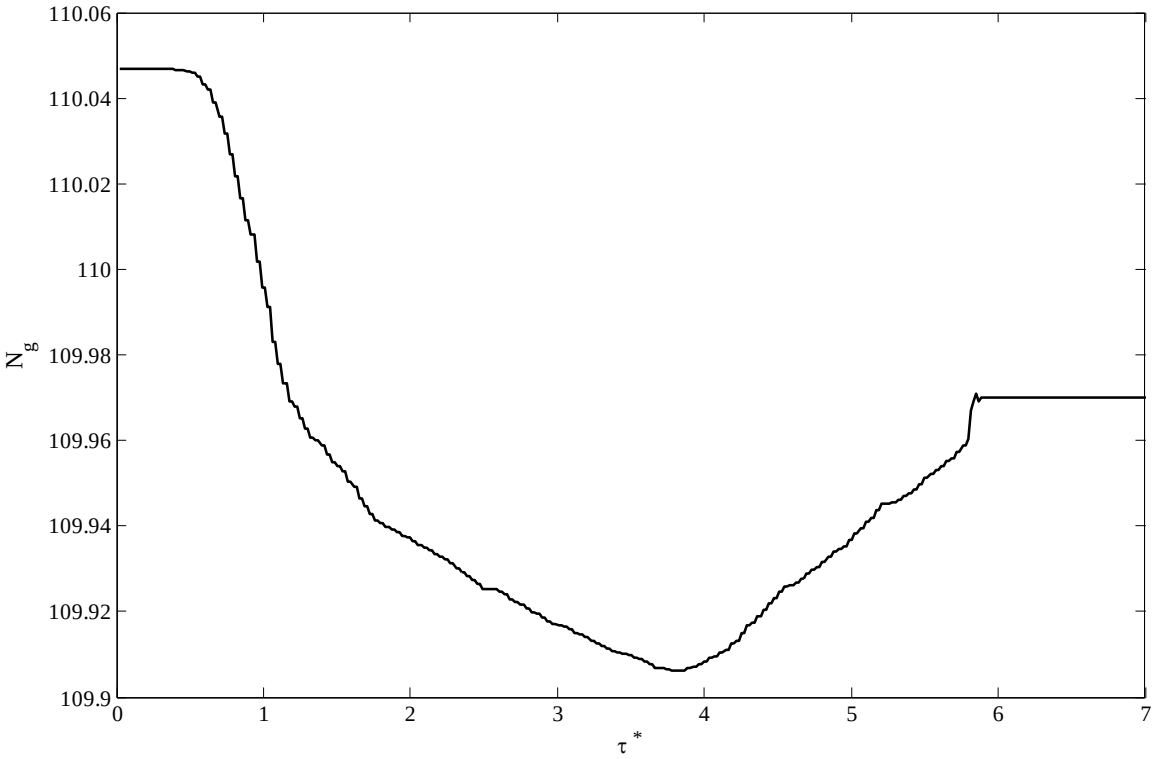

Figure 4-1: Number of grains N_g as a function of time for 110 grains vibrated at 38.2 Hz.

In the transient or time dependent problem a wave motion is a possibility. In order to ensure similarity with the experimental scenario, similarity parameter check of average speed of sound in the granular medium is also used. The speed of sound in a fluidized granular medium of spheres, in the dilute limit, can be calculated using $c = \sqrt{\frac{5T^*}{3}}$ (Huntley, Martin et al. 2007). The average speed based on the radially time averaged granular temperature is calculated as 1.17 and 1.21 for ATD-Jenkins and ATD-Garzo as compared to 1.1 observed in NMR experiments.

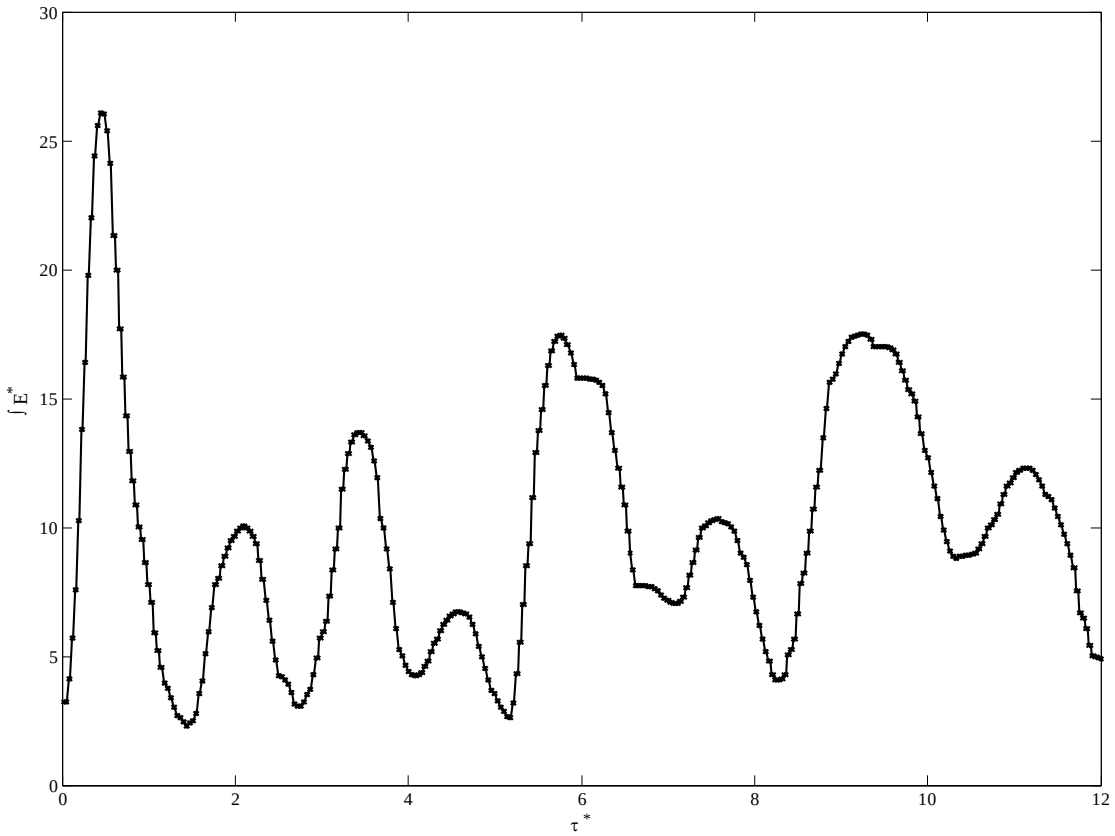

Figure 4-2: Integral of total energy E^* as the function of time showing the fluctuations acquiring steady pattern.

4.3. Testing the time dependent model

Results for the time dependent models using ATD-Jenkins and ATD-Garzo are compared against both MD simulations and the results of experiments performed using NMR. Brief details of both MD simulations and NMR experiments are included for reference.

a. Molecular dynamics simulations

Here an event driven MD simulation is used which models particles as inelastic hard spheres where collisions are instantaneous and binary, details of which can be found in Section 2.2. To generate the initial configuration particles are inserted sequentially and randomly in the cylinder without overlap. A preliminary run was performed typically for 10^6 total number of collisions in order to allow the system to reach a stationary non equilibrium state. To generate hydrodynamic scale trends using the molecular dynamics code, a virtual grid is generated to find the localized variations of granular temperature and packing fractions in the domain. The locations of the grains' centres in their local grid cells are noted and associated properties are stored. The results are averaged over the predefined period of time and/or number of collisions, thus generating temperature and packing

fraction readouts at all required instances at all places with in the domain of cells. For steady state the averaging is carried out for the total duration of the simulation while when obtaining phase-resolved data the averaging time is discretised into phase angle. To produce meaningful results the simulation is run for 10^6 collisions.

b. Nuclear magnetic resonance imaging

Detail on the NMR working and data acquisition can be found in Chapter 2. For our study, mustard seeds were used in a Bruker Biospin DMX 300 spectrometer operating at a frequency of 300.13 MHz (Huntley, Martin et al. 2007). The mean diameter of these grains was 2.04 mm with a 5.66 mg mass on average. The granular cell was machined from a permanently antistatic acetal co-polymer with a glass disc insert (thickness 1 mm) at the bottom. The bore of the NMR spectrometer constrained the external radius of cell and the effective internal diameter was 9 mm. The drive frequency was 38.2 Hz for the cell which was evacuated to reduce air drag on the grains. 110 grains (two monolayers at closed packed) of granular material (mustard seeds) were fluidized. Coefficients of restitution were measured using high-speed photography as follows: mustard–plastic, 0.60; mustard–glass, 0.58; mustard–mustard, 0.68. In order to obtain phase resolution of granular temperature and packing fractions, the NMR signal excitation was triggered at a fixed phase of the sample vibration with twelve increments in the vibration phase to complete a vibration cycle. In order to improve signal to noise ratio eight datasets were averaged. The setup, forms of the NMR signal sequence and results can be found in Huntley et al. (Huntley, Martin et al. 2007).

4.4. Results and discussion

Figures 4.3, 4.4 and 4.5, 4.6 show the non-dimensional granular temperature field, T^* and velocity field, $\mathbf{u}$ plotted for six parts of the cycle, with phase $\phi = 0, \pi/3, 2\pi/3, \pi, 4\pi/3 \,\&\, 5\pi/3$ for both the axi-symmetric time dependant models, ATD-Jenkins and ATD-Garzo. These results demonstrate that in certain parts of the cycle, the radial variation is significant, something which cannot be captured in a one dimensional model. For example, at $\phi = \pi$ in both models (Fig. 4.3 and 4.5), there is an increase in granular temperature at the axis, by a factor of ~1.4 over that observed at the wall. In addition there are significant temporal variations in the temperature field, not only in the axial direction, but also in the radial direction. A connection of base phase with the variation of cumulative granular temperature gradient in the radial direction is shown in

Fig. 4.7. The figure shows high temperature radial gradients at some of the phase locations of the base. These radial fluctuations are important since the energy loss at the wall is linked with the energy balance of the particles over the course of a cycle. In the axial direction both hydrodynamic models show wave propagation with a pulse of high temperature moving away from base. Additionally ATD-Garzo shows a rising granular temperature at large distances away from base. A detailed discussion on the heat wave movement and temperature variations in axial direction is included in the next section.

The velocity field also shows interesting variations. Figure 4.4 and 4.6 show how the velocity field changes over the course of a cycle. It is evident that direction reversal occurs with the formation of a roll at similar phase locations for example, phase $\phi = \pi$ where high radial gradients are also seen in granular temperature. The phase resolved velocity vectors show the presence of two dominant rolls at two points in time and location. One roll appears near to the base while the other appears higher in the cell. The presence of a roll and its direction can be correlated with the phase of the base. Figure 4.8 shows the variation of normalized mean Vorticity , $\Omega^* = \frac{1}{2}(\frac{\partial \mathrm{u}}{\partial \mathrm{z}} - \frac{\partial \mathrm{v}}{\partial \mathrm{r}})$, for the case of ATD-Jenkins and ATD-Garzo over the course of a typical base cycle. The normalization is made with peak angular velocity obtained using ATD-Jenkins. The highest and lowest points of the angular velocity indicate the points in the phase with strongest presence of rolling while the opposite gradients in the neighbourhood of both peaks show the opposite directions of rotation. The highest value indicates the roll formed away from the base while the second peak stands for the roll near the base.

Interestingly, we see that the radial gradients in granular temperature are at their strongest at the same phase location points where the velocity circulation is greatest, for example at $\pi/3 < \phi \leq \pi$, suggesting a strong coupling between the heat flux and the convection rolls. Both ATD-Jenkins and ATD-Garzo demonstrate the generation and presence of the rolls in the domain (see Fig. 4.3 (a, e) and 4.4 (a, e)) but in ATD-Garzo the location of the rolling pattern is slightly lower (~ 1 particle diameter) compared to ATD-Jenkins.

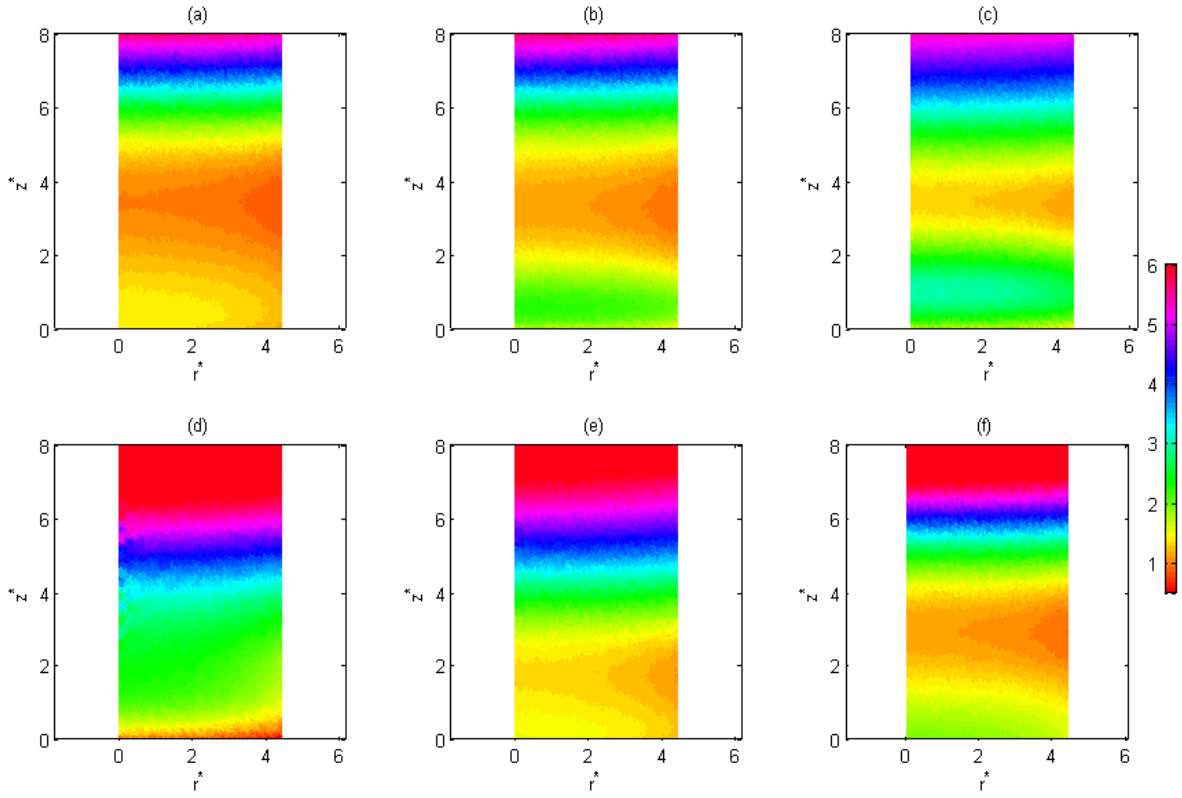

Figure 4-3: Surface plots of non-dimensional granular temperature T^* for ATD-Garzo during six stages of a vibration cycle starting from (a) to (f) at phase $\phi = 0, \pi/3, 2\pi/3, \pi, 4\pi/3 \& 5\pi/3$.

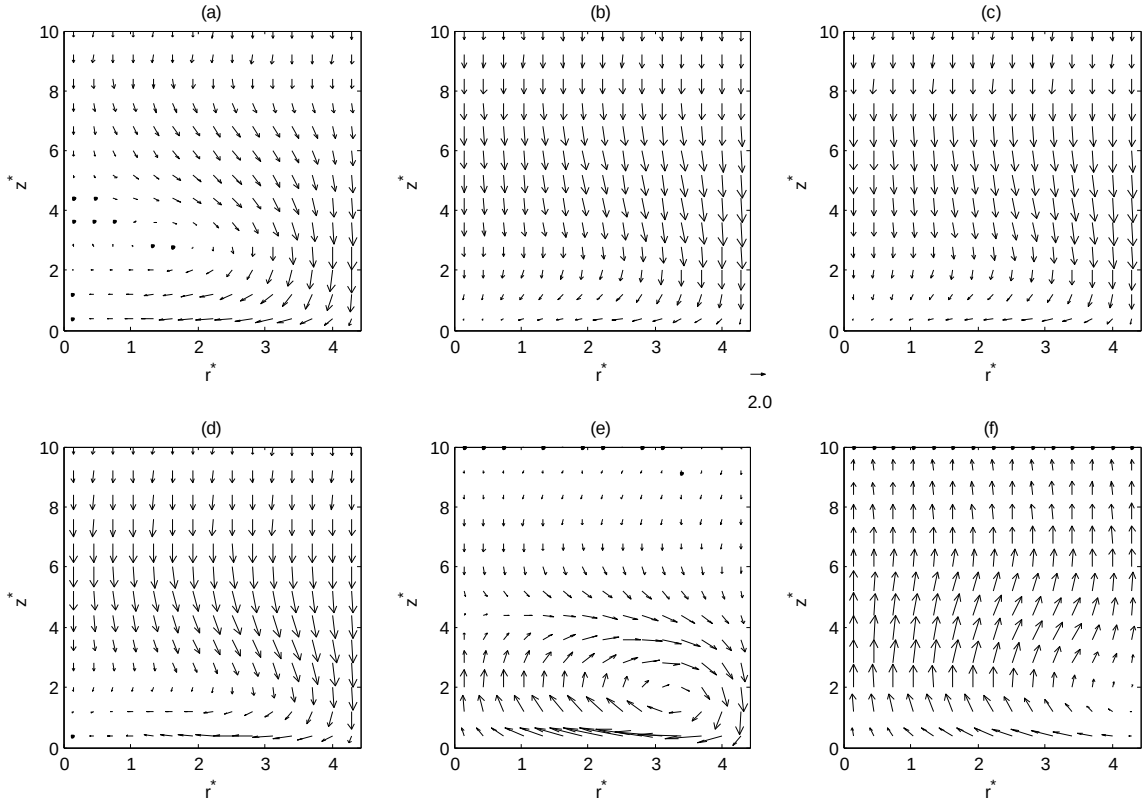

Figure 4-4 Vector plots of velocity u for ATD-Garzo during six stages of a vibration cycle starting from (a) to (f) at phase $\phi = 0, \pi/3, 2\pi/3, \pi, 4\pi/3 \& 5\pi/3$.

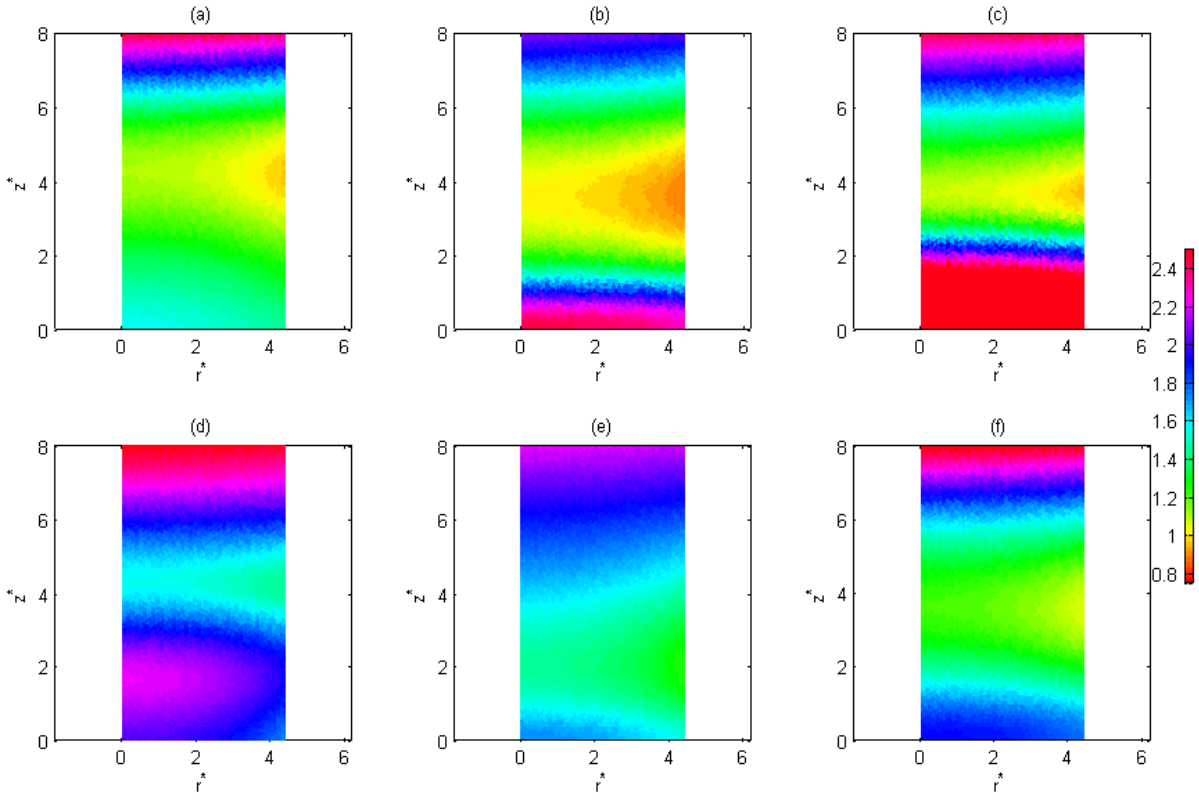

Figure 4-5: Surface plots of non-dimensional granular temperature T^* for ATD-Jenkins during six stages of a vibration cycle starting from (a) to (f) at phase $\phi = 0, \pi/3, 2\pi/3, \pi, 4\pi/3 \& 5\pi/3$.

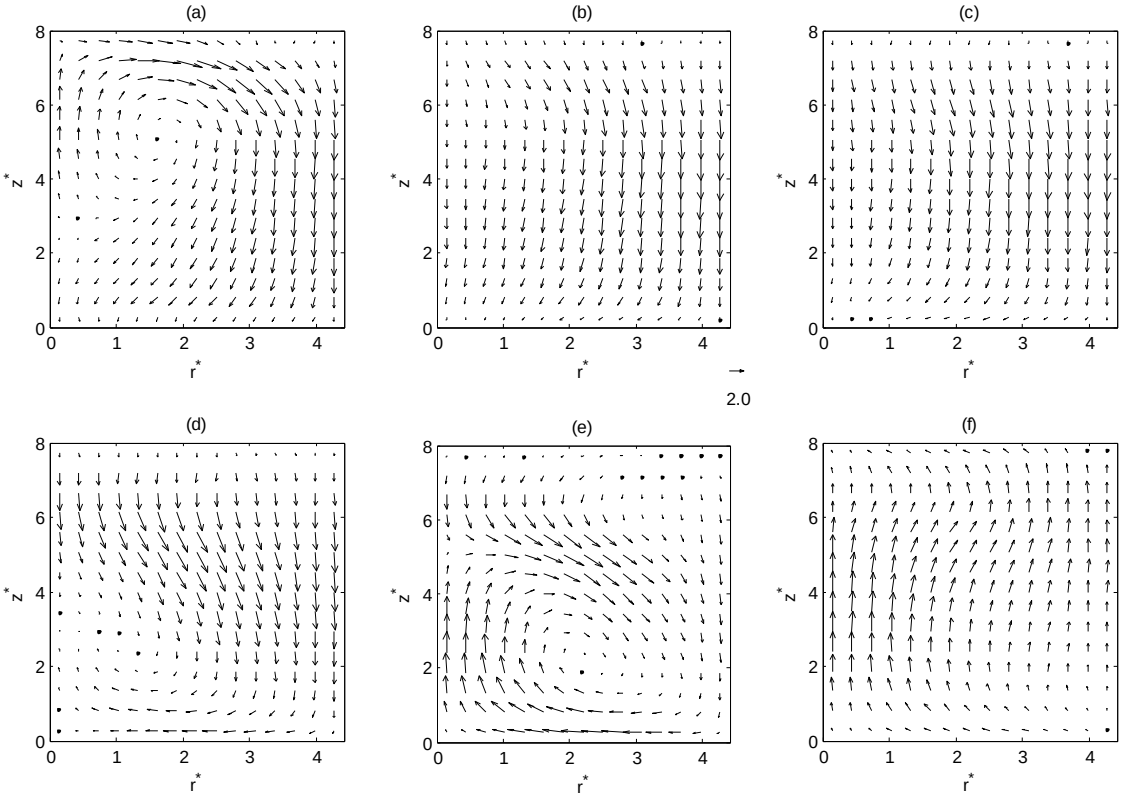

Figure 4-6: Vector plots of velocity u for ATD-Jenkins during six stages of a vibration cycle starting from (a) to (f) at phase $\phi = 0, \pi/3, 2\pi/3, \pi, 4\pi/3 \& 5\pi/3$.

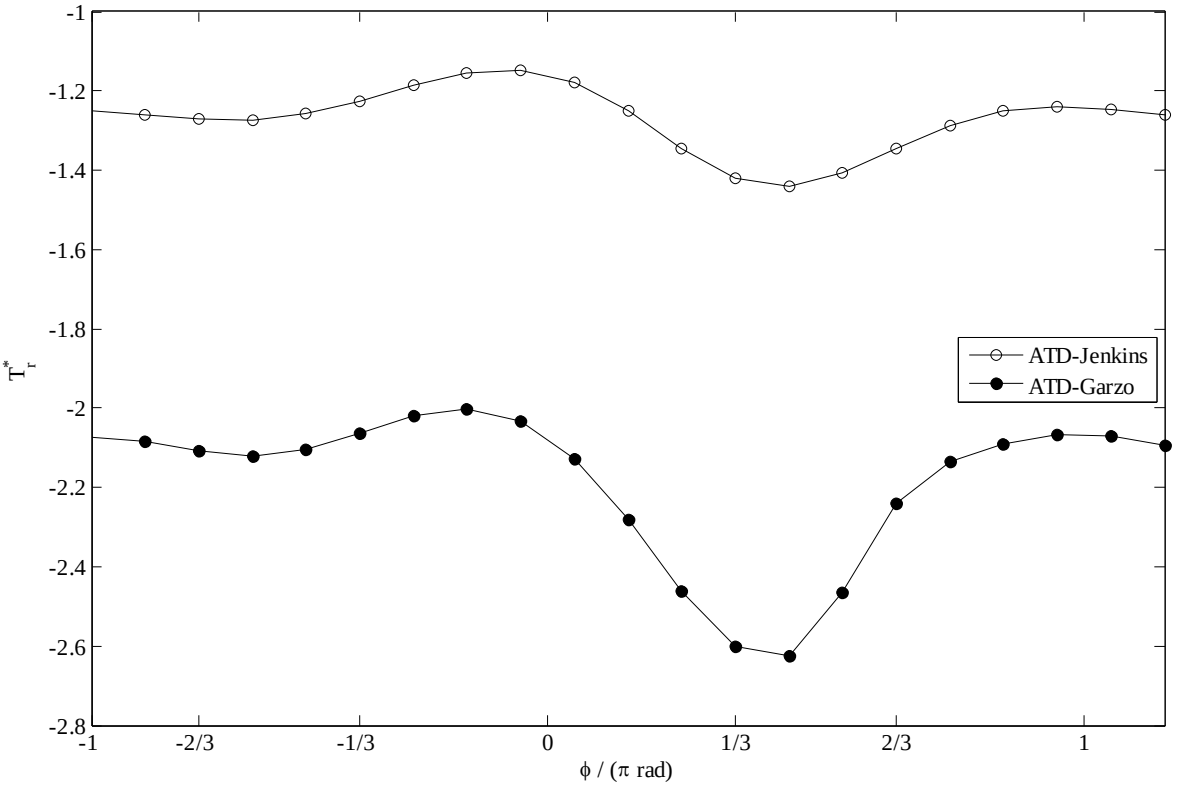

Figure 4-7: Radial cumulative temperature gradient variation during a typical cycle for the case of ATD-Jenkins and ATD-Garzo.

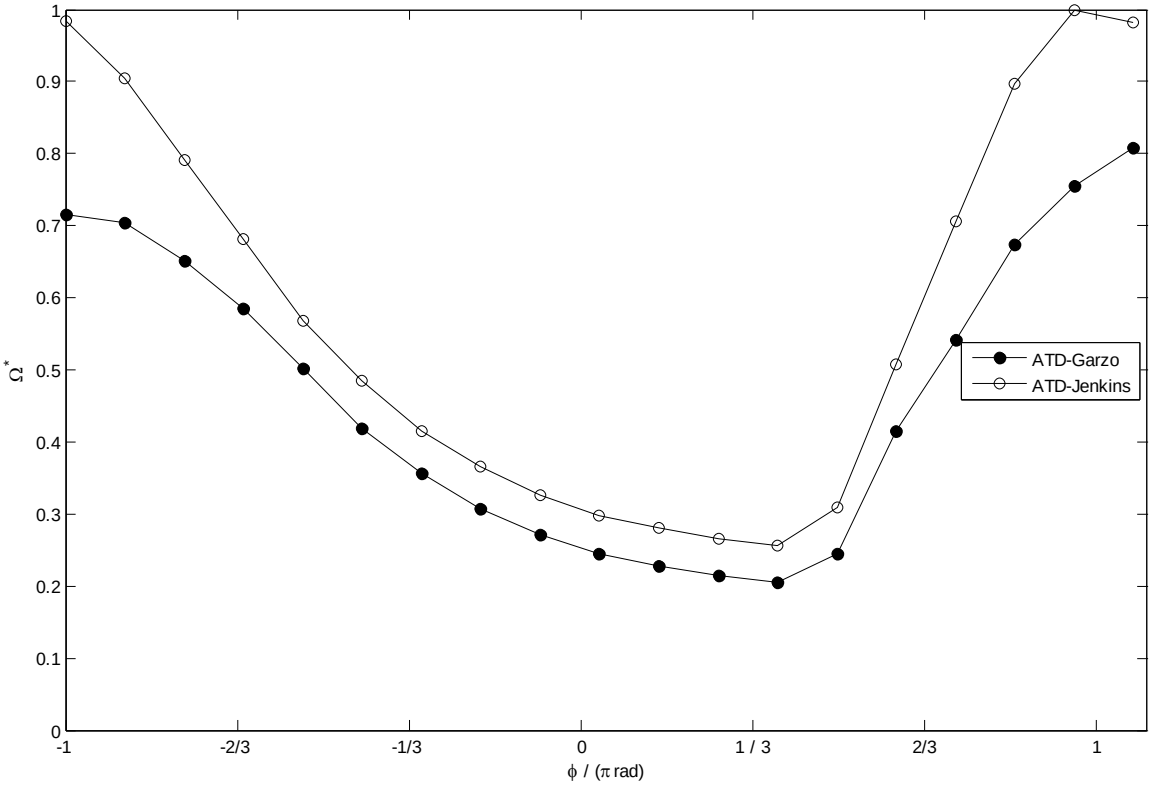

Figure 4-8: Normalized peak angular velocity variation during a typical cycle for the case of ATD-Jenkins and ATD-Garzo.

a. Transport mechanisms and viscous effects

During shaking, the particles leave the plate during a cycle when the maximum downwards acceleration of the plate is greater than gravity. When the layer is off the plate, it is cooled by inelastic collisions within the system and at the side wall, while the particles are simultaneously accelerated towards the plate by gravity leading to a large mean velocity. As the high velocity grains collide with the bottom plate a pressure pulse is formed. The development and propagation of this wave is attached to the cyclic motion of the base (Bougie, Moon et al. 2002).

When the amplitude of vibration is small compared to the particle diameter, the transfer of heat through the granular medium is mainly through conduction and the momentum wave is diffused through bulk viscosity (Alain, Emmanuel et al. 2005). When the base amplitude is increased and becomes comparable to the mean particle size, then the fluctuations in energies of some of the particles will be high compared to the mean energy of the surroundings at a given height. Those high energy grains move up in the cell and cool down through collisions at heights higher than before causing an expansion of bed. This 'thermal expansion' generates instability in the system as it overcomes the stabilizing feature of thermal conductivity and bulk viscosity. The high temperature particles cool and move back downwards to hit the base with higher velocity generating a stronger pulse. Such an effect is amplified due to the fact that a dissipative wall provides radial gradients in flow domain. With the side wall dissipation contribution the fluid tends to self organize in a cyclic pattern (Khain, Meerson 2003, Ramirez, Risso et al. 2000).

Transport through wave propagation and rolling motion, are both attributes of viscous effects which could only be observed in a complete hydrodynamic description when an appropriate Navier-Stokes order model is used in a three dimensional domain. In order to describe propagation of dynamic motion in the bed a time dependent model is required. Here the presented time dependent flow model allows slight allowance of compressibility in the flow as opposed to incompressible flow models developed previously (Viswanathan, Wildman et al. 2006, Martin, Huntley et al. 2005). For highly compressible flows even this formulation is inadequate and a transformation to conservative variables is required which is beyond the scope of this work and generally lesser applicable to granular physics.

The propagating disturbances due to the base play a significant role in the process of heat transfer, as seen by Huntley et al (Huntley, Martin et al. 2007) where it was observed that

the viscous damping of propagating waves led to higher temperature regions at the top of fluidized cells. The transient nature of the flow can be seen more strongly by plotting the radial-averaged granular temperature as a function of altitude (Fig. 4.9). The results show reasonable qualitative and quantitative agreement, between each of the models, and between the hydrodynamic models and the MD simulation and experimental results. At large altitudes there is a significant discrepancy between ATD-Garzo and the other results, but this is due to the system becoming increasingly more Knudsen like as the altitude increases, which is not captured by ATD-Garzo. At lower altitudes most of the key features are captured. Importantly we see evidence that a temperature wave propagates through the cell. Both models predict an increase of granular temperature away from base. Such wave motion and increase of temperature is expected as shown by Huntley et al. (Huntley, Martin et al. 2007). It can be noticed that ATD-Garzo predicts a much higher increase of temperature in all the frames shown in Fig. 4.9 and this is predominantly because of additional packing fraction gradient term in heat flux ($J = -\kappa\nabla T - \mu\nabla\eta$) along with the velocity variations especially during rolling contributing to the viscous component of the energy equation (Eq 3.9). This fact is discussed in the next section.

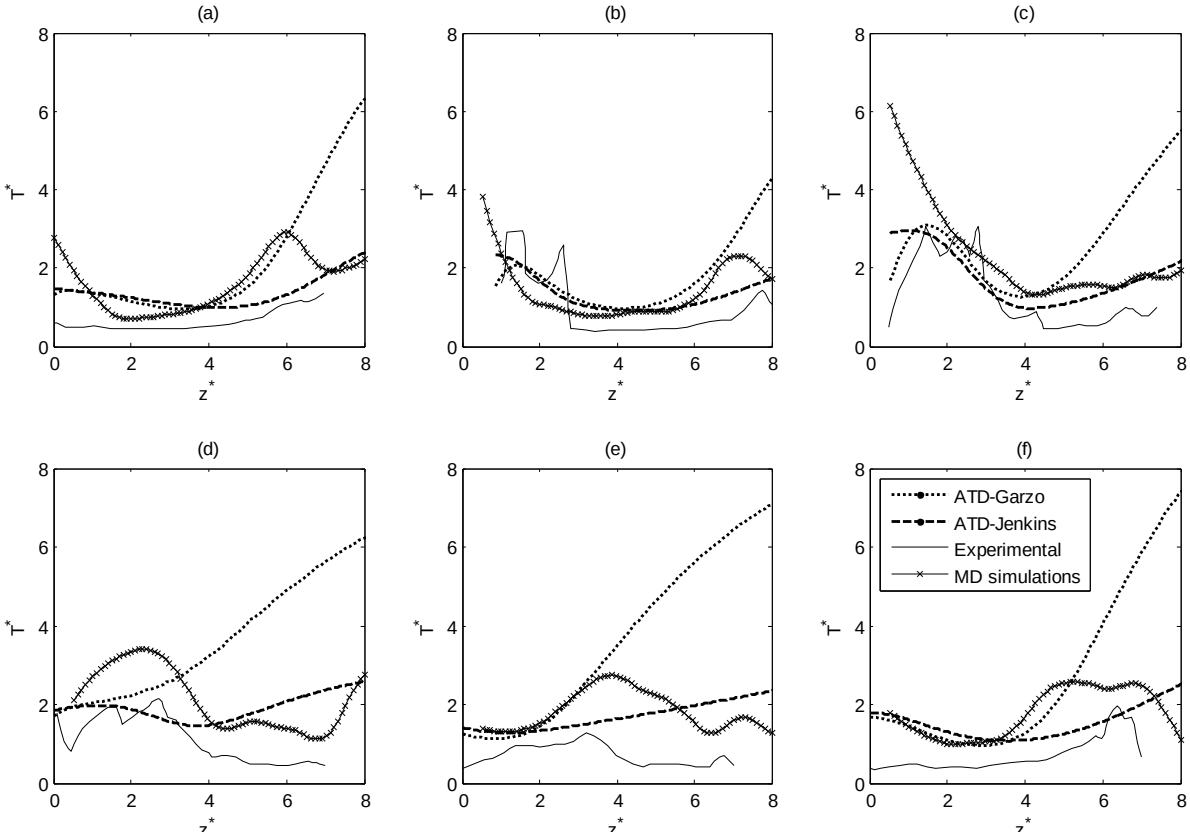

Figure 4-9: Radially-averaged granular temperature T^* showing the motion of the heat wave during 6 phases ((a) = 0 to (f) = 5π/3 in steps of π /3) of a vibration cycle.

b. Time averaged results

The time averaged results for the granular temperature for MD simulations, hydrodynamics models and experimental results are shown in Fig. 4.10. It shows that in some parts of cell (~5*d*) both the hydrodynamic models capture the behaviour observed in the molecular dynamics simulations and experiments. The FE solutions qualitatively reproduce the behaviour at higher altitude seen in the 1-D numerical results presented in Huntley et al (Huntley, Martin et al. 2007) but this is not evident in the experimental results. Both ATD-Garzo and ATD-Jenkins predict upturns of granular temperature with former showing significantly higher values, as would be expected due to the presence of the concentration gradient term in the heat flux. While the bulk behaviour show reasonable agreement with experimental results and MD simulations until ~5*d* above the base, after which ATD-Garzo curve starts to significantly deviate from the other results. Temperature increases in MD simulations results can also be seen but they are not as significant as those observed in the ATD-Garzo solution.

The upturn in time-averaged temperature predicted by both of the models (Fig. 4.10) requires investigation. It is expected with the ATD-Garzo model which includes an additional term related to the density gradient in the heat flux, $J = -\kappa\nabla T - \mu\nabla\eta$, along with conduction. In the last chapter we showed that this term results in generating temperature upturn for a steady state model (SSM-Garzo) leading to a substantial increase in granular temperature profile away from base with decreasing packing fraction. In SSM-Jenkins such a behaviour is not observed (see Fig. 3.3 and 3.6), but the time varying model shows significant increase of temperature away from base. Previously it was related to the viscous damping of heat wave in the bed (Huntley, Martin et al. 2007). At some phase locations in Fig. 4.9, an increase of the temperature at large distances from base can also be seen in experimental results and MD simulations (see Fig. 4.9). The contribution of viscous effects in the energy equation (Eq. 3.3) is related through $(\nabla\mathbf{u})^2$. Figure 4.10 shows an increase in its contribution in both models compared to the experimental results. Although qualitative predictions are similar in some parts of cell, quantitatively the ATD-Jenkins solution predicts significantly higher contribution than the ATD-Garzo method particular at heights of $z^* > 6$. In the presence of convection rolls the value of $(\nabla\mathbf{u})^2$ would be greater than without its presence due to increased variations in both radial and longitudinal components and an increase of viscous contributions between $4 < z^* < 6$ in the ATD-Garzo results can perhaps be linked to the regions of rolling (see Fig. 4.4 (a) near $z^* \sim 6$).

On the other hand ATD-Jenkins predicts higher viscous activity in the region $z^* > 6$ due to location of a roll in the higher regions of the cell (see Fig. 4.6 (a)). A corresponding temperature increase can also be observed for ATD-Jenkins at similar height as anticipated (Fig. 4.10) (Huntley, Martin et al. 2007).

Although the viscous component contributes to the temperature upturn in both models but ATD-Garzo has an additional contribution due to packing fraction gradient ($\mu\nabla\eta$) term in the energy equation. Here the packing fraction gradient term together with the viscous contributions produces the resultant temperature profile higher for ATD-Garzo as compared to ATD-Jenkins at $z^* > 5$. The MD simulations also show a small temperature upturn, of degree more similar to ATD-Jenkins that ATD-Garzo, but again the relative diluteness of the upper regions of the cell make conclusive comparisons difficult in these regions.

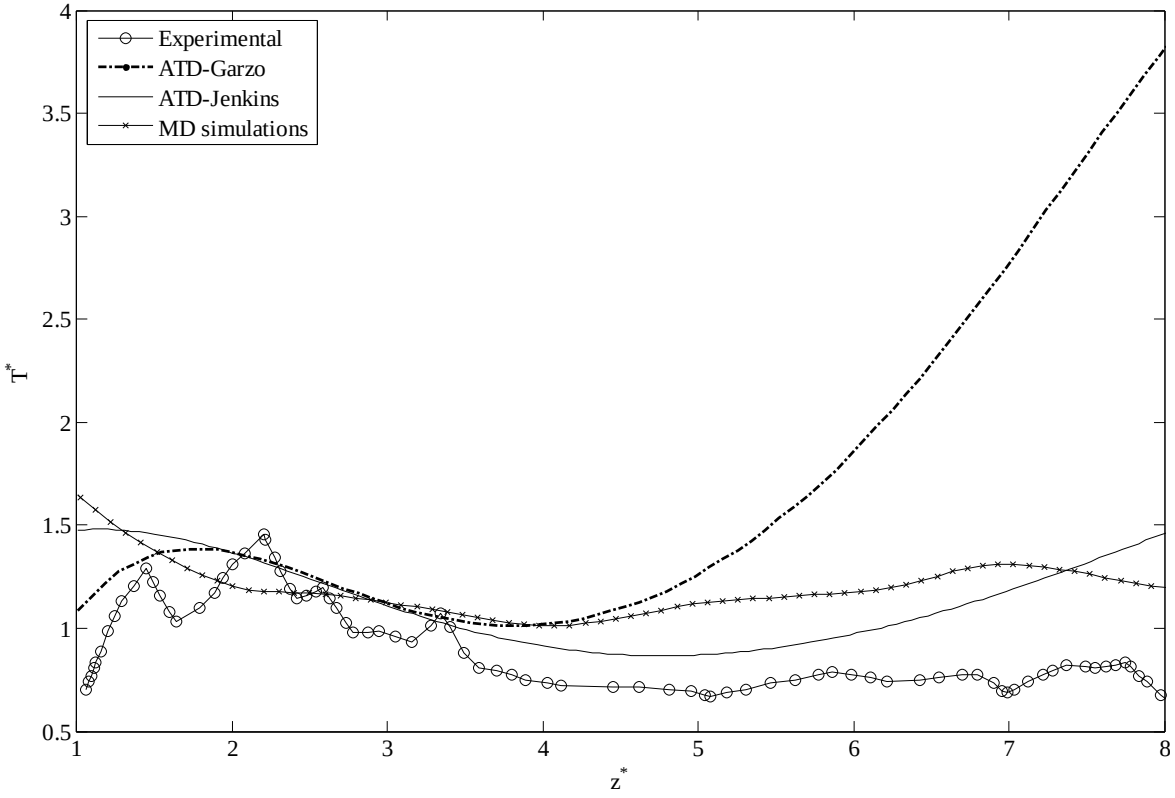

Figure 4-10: Radially time-averaged (over one cycle) granular temperature variations for ATD-Jenkin and ATD-Garzo compared with NMR and MD results.

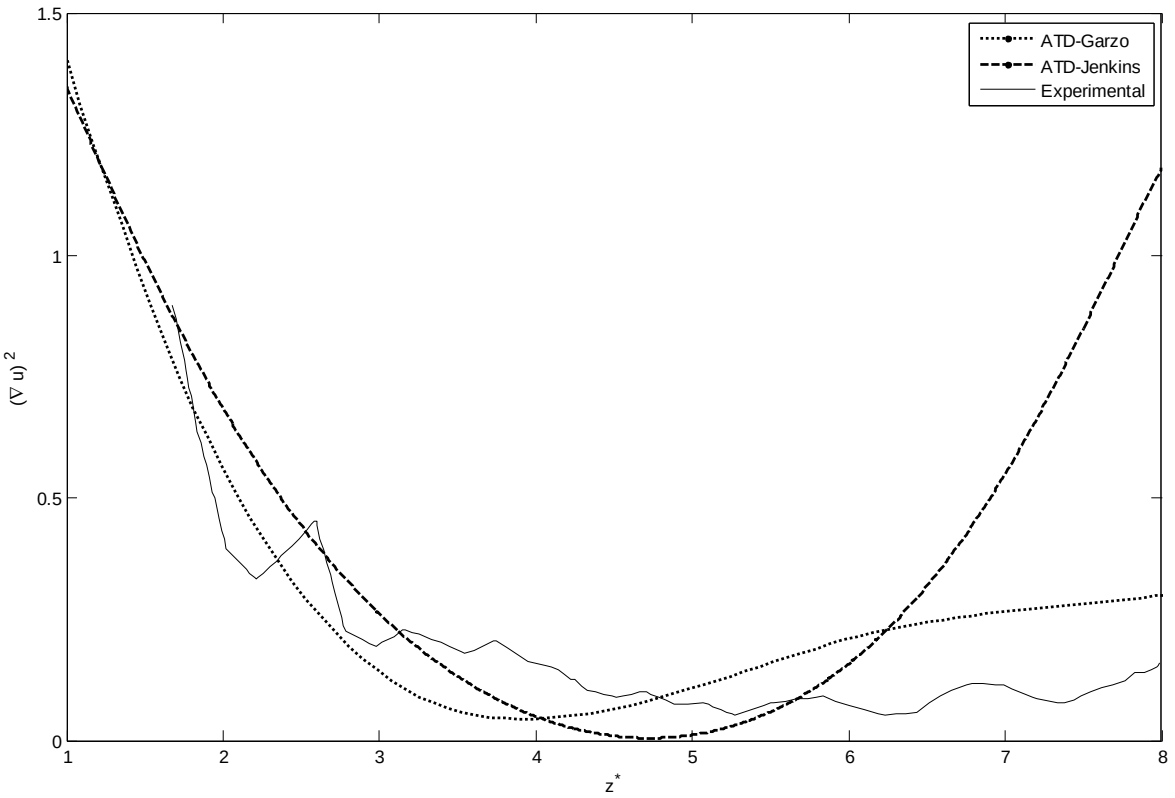

Figure 4-11: Plot of cycle-averaged square of velocity gradient for ATD-Jenkins and ATD-Garzo models with experimental results.

4.5. Summary

This chapter details the time dependent solution of the Navier-Stokes-like model for low frequency excited granular motion in a vibrated axi-symmetrical dry granular bed. Two models, ATD-Jenkins and ATD-Garzo, are solved using the FE method with two different closure forms. Both models have been used to describe the time averaged nature of a vibrofluidized bed, and compare reasonably well with MD and experimental results. We observed the appearance of strong rolling and wave propagation and showed a link between the cyclic increase in the granular temperature with the viscous effects. The hydrodynamic results especially for ATD-Garzo show a reasonable match with the MD simulations as a function of time. A qualitative matching behaviour is also seen with the experimental results. For time averaged behaviour hydrodynamic models and MD simulations show similar trends. An extension of this methodology to different loading and operating conditions is described in the following chapters.

Chapter 5 High frequency vibro fluidized granular beds

5.1. Introduction

In the last chapter we observed the behaviour of a granular bed fluidised with a low frequency excitation. The phase resolved dynamics of the granular flow revealed that the momentum and energy transport in the cell associates with the base phase. At higher frequencies of excitation one expects in the first instance, that the nature of bed will be similar to that observed in the steady state (Sunthar, Kumaran 2001, Soto, Mareschal et al. 1999), since with near to ultrasonic frequency and low amplitudes the effect of base motion and its frequency can be assumed to be small (Sunthar 2001, Rericha, Bizon et al. 2001). However, at these frequencies in the laboratory, the time scales of the vibration are close to the time scales associated with the collisions. This is potentially significant since steady state theoretical predictions of the heat flux at the vibrating base are independent of the frequency of vibration (Richman 1993). Therefore it is necessary to explore the validity of our modelling tools at high frequency and to propose methods to describe vibro-fluidised beds operating at high frequency. In this chapter we aim to study the physics of granular bed at near to ultrasonic frequencies using a combination of experimental methods, hydrodynamics models and MD simulations. We will compare the predictions of hydrodynamic models and with experimental observations and test the assumptions used for developing the models using soft sphere MD simulations.

5.2. Nuclear Magnetic Resonance Experimental Setup

Experiments at high frequency (~11-17.5 kHz) with low amplitude (~10-100 μm) were carried out using an ultrasonic actuator placed within a NMR spectroscope. A brief detail on the experimental setup is included in following sections.

a. Setup

The testing rig consisted of an actuator with waveguide, amplifier (MF300 having range from 1 kHz to 100 kHz), signal generator (Farnell Function Generator FG1) and the granular cell. The ultra-sonic actuator was used to fluidise a bed of mustard seeds (details given below) at a range of frequencies and amplitudes. The setup used in the tests is shown in the Fig. 5.1. The velocity of the base was monitored using a laser vibrometer (Polytech OFV512 class two fibre interferometer). The laser from the vibrometer was directed down through the top of the granular cell whilst in the NMR spectroscope using the mirror

positioned at the top. The reflected beam returning from the cell bottom surface was then directed back to the vibrometer through the same mirror (Fig. 5.2). Figure 5.2 shows the sonotrode/horn with the waveguide and CAD model for the setup used with the NMR spectroscope. The upper part of the waveguide with the cell on top is inserted into the spectroscope bore, while the rest rested on the base (Fig. 5.1). The external diameter of the granular cell was limited due to the size of the bore in the spectroscope, and thus a cell of 7 mm in radius was used. The cell was machined from Polyether ether ketone (PEEK) material, which avoided the generation of any interference with the magnetic field of the spectroscope, whilst creating a cell with high stiffness and coefficient of restitution.

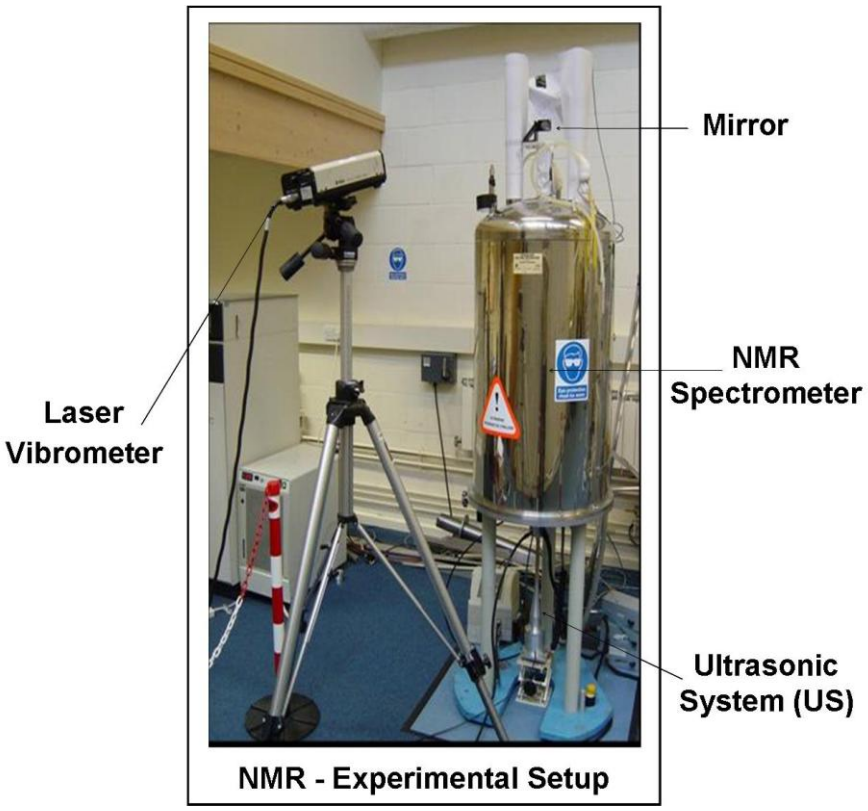

Figure 5-1: NMR setup at Cambridge university.

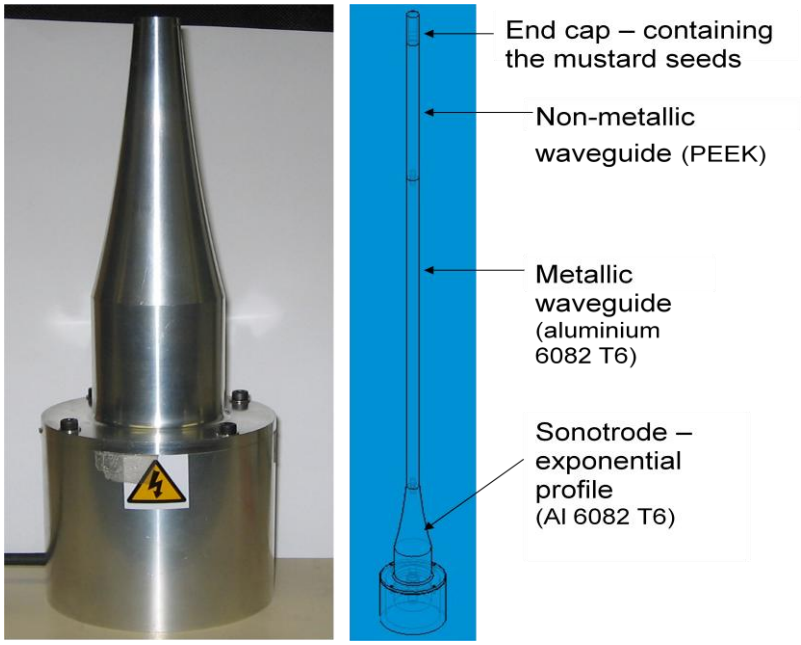

Figure 5-2: Left, Actual Sonotrode with exponential profile. Right, CAD model of the actuator assembly with wave guides and vibrating cell.

Table 5-1: Summary of experimental runs conducted.

Sr.	Base Frequency (kHz)	Peak to peak Base velocity ($m\ s^{-1}$)	No. of seeds
1	11.11	1.0	40
2	17.68	1.0	40
3	11.11	0.5	40
4	11.11	0.74	40
5	11.11	0.33	40
6	20.2	0.74	20
7	17.68	0.74	20
8	11.11	0.74	20
9	20.2	0.74	10
10	17.68	0.74	10
11	11.11	0.74	60
12	11.11	0.74	80

b. NMR spectroscope

For most NMR acquisitions, a liquid phase within the sample/granular material is the source for signal generation, and for this experimental study, mustard seeds were used in a Bruker Biospin DMX 300 spectrometer operating at a ^{1}H frequency of 300.13 MHz. The time averaged signal for the mean velocity was measured using a specially designed spin echo pulse signal (Huntley et al. 2007). A 25mm ^{1}H birdcage resonator was used to excite and detect the magnetization from the mustard seeds with the pulse length of 32 ms. The total echo time, TE, was 2.46 ms. Eight scans, at a recycle time of 365 ms, were averaged to obtain a sufficient signal-to-noise ratio. The acquired raw data were zero filled to 256 data points in the velocity encode dimension, and then a two-dimensional Fourier transform was applied to give spatially encoded, velocity profiles, denoted here by S (v, z). These parameters enable determination of velocities within a range -0.85 to 0.85 m s^{-1} and with a resolution of 0.007 m s^{-1}. Only the vertical velocity component (v) was measured since the granular temperature is normally highest in this direction, and the measured signal was integrated through the thickness of the cell to get radially averaged distributions. At this time, obtaining the velocity fluctuations in all directions simultaneously is not possible, but in future developments in this field it may become feasible. The field of view in the *z*-direction was 40.0 mm and the number of data points acquired were 128, giving an axial pixel resolution of 312 μm/pixel.

c. Granular material specifications

Mustard seeds were used in all the experiments. These had a mean diameter of d = 2.3 ±0.2 mm and an average mass of 6.47 mg. A typical layer of mustard seeds consisted of 40 grains. The coefficients of restitution were measured using high speed photography, from which we identified average values of 0.66 ± 0.09 for grain-grain collisions, 0.74 ± 0.08 for grain-side wall collisions and 0.7 ± 0.07 for grain-base collisions.

d. Limitations

One limitation arises because of the finite time taken by the NMR spectrometer to non-intrusively probe the granular dynamics. At ultrasonic frequencies, the NMR data acquisition time is of the order of the time period of the base, and thus phase resolved observation was not possible. As a consequence, only time averaged data was acquired for these experiments.

The strength of the ultrasonic actuation and height of fluidization decreased with an increase of the number of layers. As would be expected, bed height reduced significantly as the number of seeds were increased from 20 to 80 (one layer of beads = 40 particles) and above this number, fluidization was no longer observed: this set an upper limit for our experiments. With less than 20 seeds, signal to noise ratio was not high enough to achieve adequate spatial resolution and thus, experiments were limited to no fewer than 20 particles.

The ultrasonic actuator was designed to excite at 20 kHz, but a range of frequencies was explored. Other modes were found giving a range of resonating frequencies from 11.11 kHz to 26.5 kHz with an achievable peak velocity of 0.91m/s.

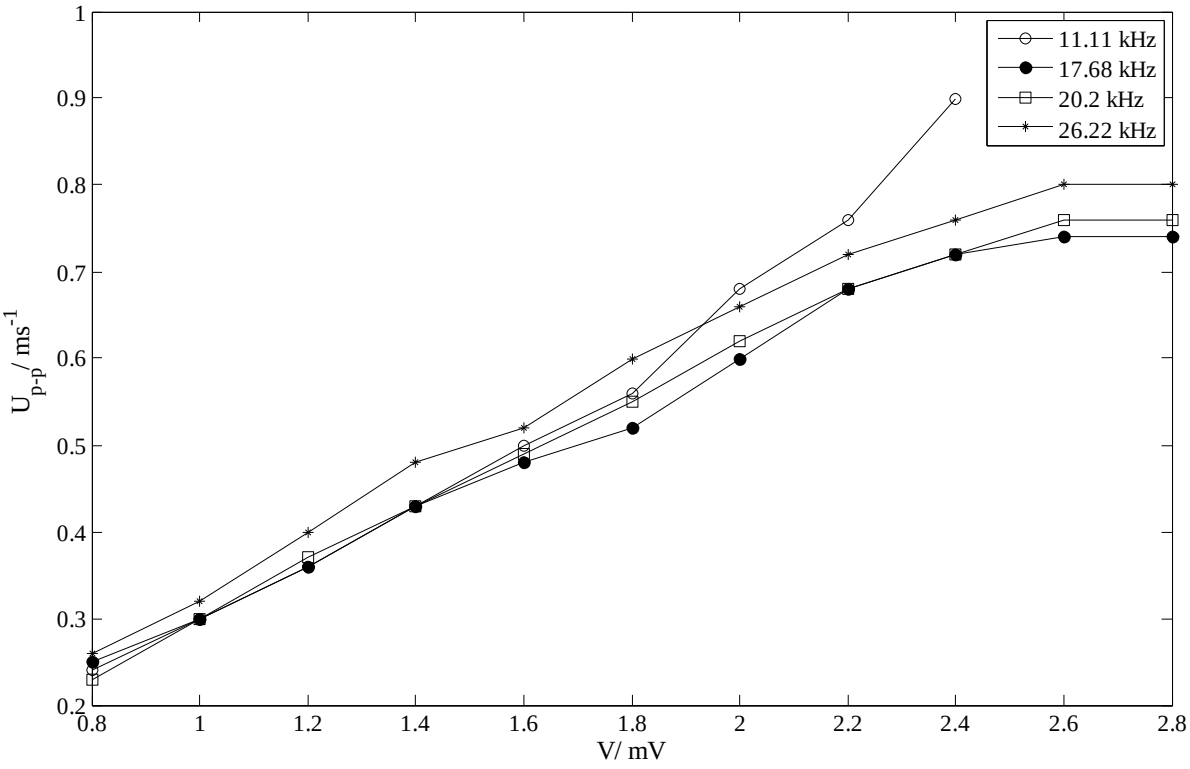

Figure 5-3: Variation of peak to peak base velocity, U, as function of input voltage signal, V, from signal generator.

The majority of the resonating frequencies show consistent linearly varying peak base velocities with input voltage, up to a peak velocity of 0.74 ms^{-1} (Fig. 5.3). Thus all runs were carried out within this base velocity envelope to ensure linearity and control of input parameters. The base frequencies, loading conditions and velocity amplitudes used for experiments are shown in the table 5.1.

e. Preliminary results

Runs with different numbers of grains at different frequencies and base velocities were carried out (see table 5.1 for details). Figure 5.4 shows the velocity distributions as a function of height for 3 cases. Previous investigations have shown that a Gaussian distribution is a reasonable estimate of the velocity distributions for bulk granular behaviour (Huntley, Martin et al. 2007). Therefore, we proceed similarly and the results are post-processed by fitting a Gaussian distribution at each vertical data location and determining the mean velocity and the granular temperature from the first and second moments.

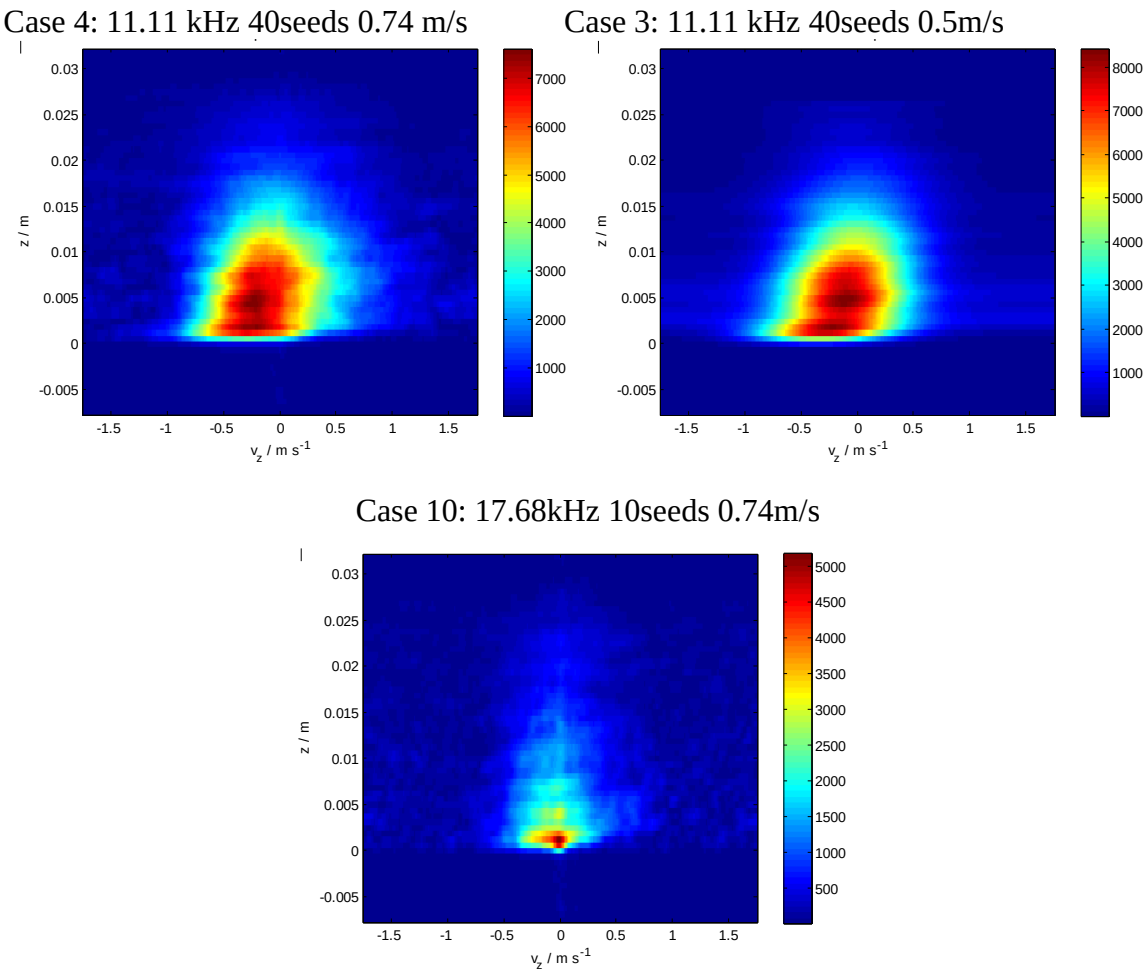

Figure 5-4: Vertical component of mean velocity along the axial direction for three cases as labelled.

An initial inspection of the data shown in Fig. 5.4 shows that near to the base the mean velocity is negative. This is unexpected, but is a result of the finite integration time of the NMR spectroscope and the high instantaneous velocities of the particles near to the base

(Huntley, Martin et al. 2007). It is suspected that the mean collision time near the base is of the order of scanning duration of NMR. Thus the data acquired in this region cannot be regarded as reliable as in other parts of the cell

However moving away from base the mean velocity of the distributions starts to move towards zero. To give an idea of the behaviour of the distributions as we move away from the base, Fig. 5.5 shows the typical velocity distributions at three heights with fitted Gaussian distributions. The fitted distributions are rather good considering the nature of the flow, but some deviations are seen in the tail regions particular for the distribution closest to the base (z = 4 mm). The higher velocity population at the positive end of the velocity distribution is expected due to the presence of a few high energy particles that have just recently collided with the base and are moving away. In general the approaching particles have mean velocity and temperature different from the mean velocity and temperature of particles leaving base and use of a bimodal distribution is suggested in this region. However away from the base for instance at z = 8 and 16 mm the velocity distribution is very close to a Gaussian distribution.

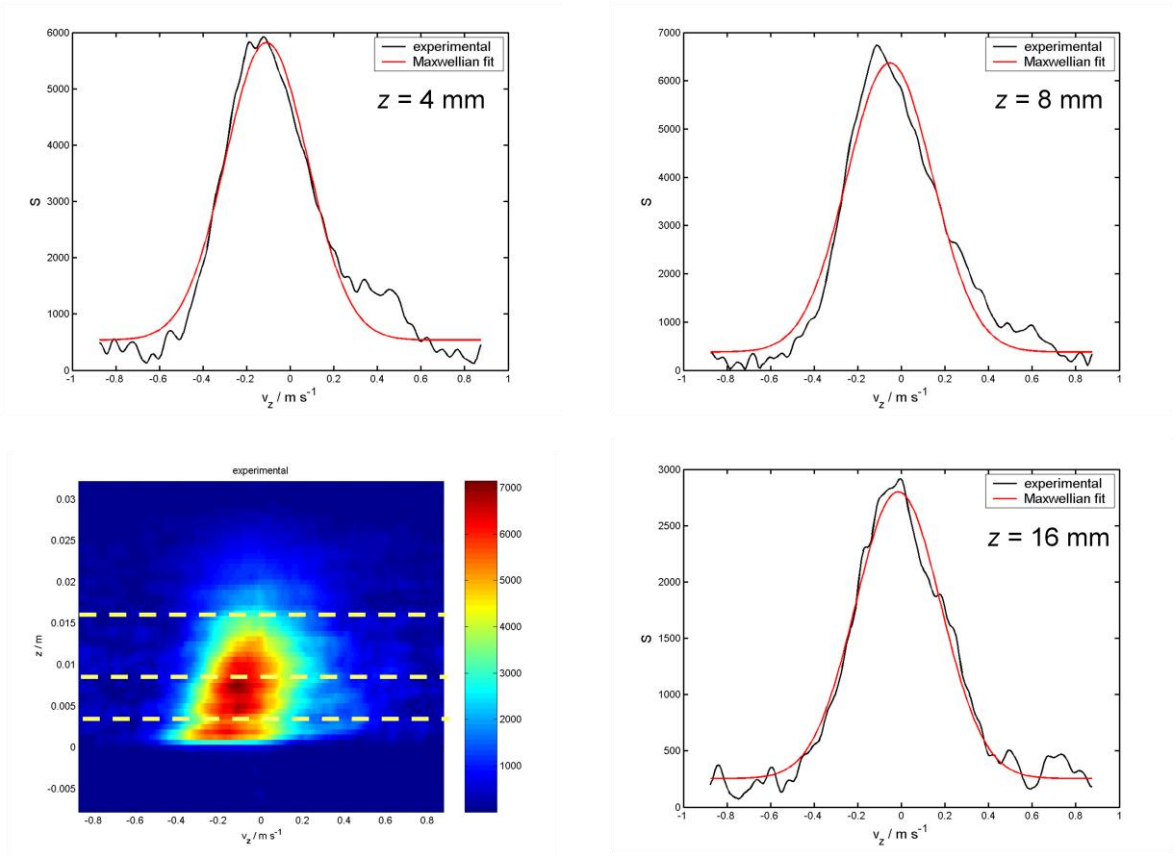

Figure 5-5: Experimental results for v_z for case 4 with fitted Gaussian at z = 4mm, 8mm and 16mm.

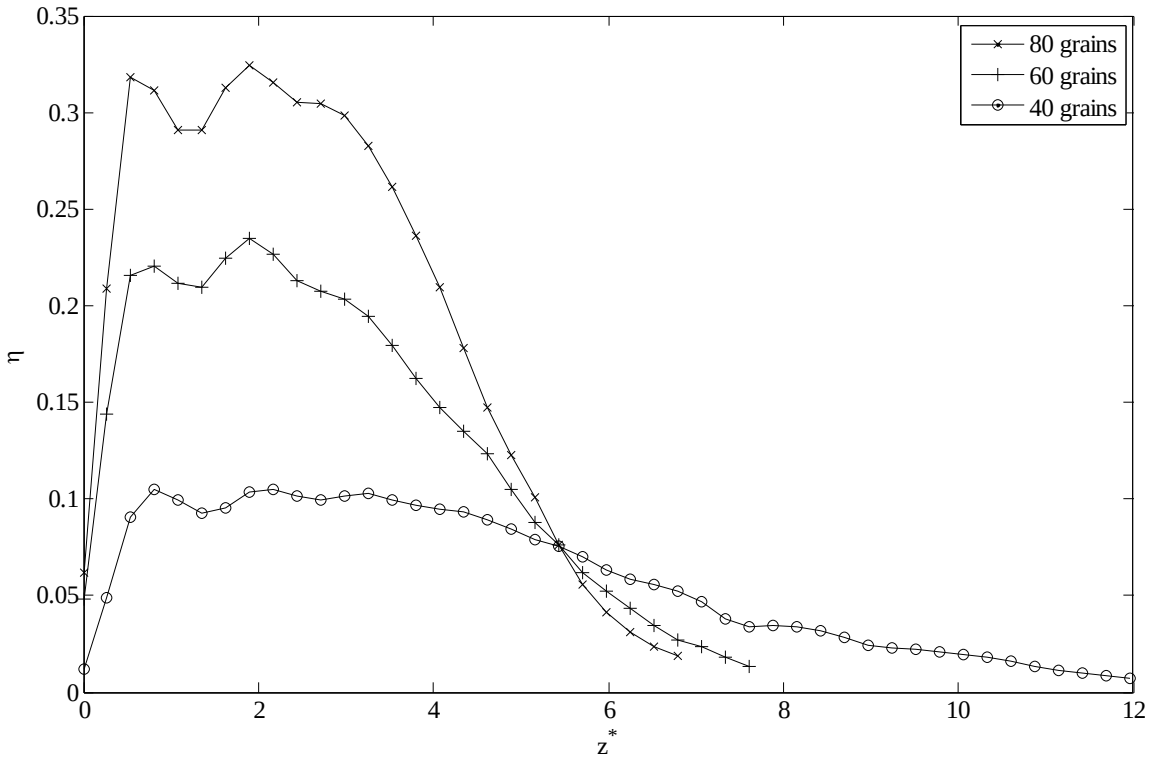

Figure 5-6: Time-averaged packing fraction for the same base velocities (0.74 m/s) for 80, 60 and 40 grains.

Apart from providing velocity distributions NMR also gives the profile for packing fraction along the height. The integral of intensity, S, of the signal is proportional to the packing fraction, and knowing the number of grains used in the experiment enables packing fraction profile to be obtained (Fig. 5.6). In the following sections we will discuss the behaviour of the distributions as a function of the experimental parameters, but first we will discuss the details of the inputs and operations of the MD simulations and hydrodynamic models.

5.3. MD simulations

In this chapter both event driven hard sphere as well as soft sphere MD simulations are employed to see the effects of high frequency agitation and test the assumption of binary and instantaneous collisions. A summary of input parameters and important details of both the hard sphere and soft sphere MD simulations relevant to the work presented in this chapter follows.

a. MD simulations-Hard Sphere

We follow the procedure for generating event driven MD simulations described in Section 2.2. The ensemble averaged results for granular temperatures and packing fractions are obtained using the recorded history of each of the grain during the course of the simulation. Experimentally determined (Section 5.2 c) mean values of coefficients of restitutions were used as an input into the hard sphere based MD simulations. To generate an initial configuration, particles were inserted sequentially and randomly in the cylinder without overlap. A preliminary run was performed typically for 10^6 total collisions in order to allow the system to reach the stationary non equilibrium state. The collision rule and data acquisition details can be found in Chapter 2 and 4.

b. MD simulations-Soft Sphere

The soft sphere code is based upon the normal force law developed by Kuwabara and Kono (Kuwabara, Kono 1987) as given by

$$F_n = \tilde{k}_n \delta^{3/2} + \gamma_n \delta^{1/2} \frac{d\delta}{dt} \quad \textbf{(5.1)}$$

where F_n is the contact force between colliding bodies and δ is the deformation produced during collision (Kuwabara, Kono 1987). The input parameters for the soft sphere model includes the grain stiffness $\tilde{k}_n$ and damping coefficient γ_n. Mean values for the coefficient, $\tilde{k}_n$, were calculated for mustard seeds using a low force compression test based on the Hertzian contact law (Johnson. 1987),

$$F = \tilde{k}_n \delta^{\frac{3}{2}}. \quad \textbf{(5.2)}$$

The compressive tests used anvils made of PEEK material in order to replicate grain-base interaction. The damping coefficient γ_n, was calculated using Eq. 5.1 constrained against the condition of the coefficient of restitution. The equation solves for the value of γ_n for the collision of two identical grains having approach and return relative velocities equal to the observed mean velocities in the experimental cell. The force law of Eq. 5.1 calculated the force which resulted in an effective coefficient of restitution while the damping coefficient was varied in order to obtain convergence at the fixed time-step of 1×10^{-7} s that was used in all the soft sphere simulations discussed in this thesis. The resulting coefficients for all collision types (grain-grain, grain-base and grain-sidewall) are presented in table 5.2. A feature of this treatment of the collision dynamics is that the

coefficient of restitution is velocity dependent. As an illustration the coefficient of restitution for grain-base collisions is plotted for various incident relative speeds in Fig. 5.7.

Table 5-2: Summary of force law coefficients.

Collision	e	$\widetilde{k}_n$ (N m$^{-3/2}$)	γ_n
Grain-Grain	0.66	5.60e6	25
Grain-Wall	0.74	1.45e7	48
Grain-Base	0.70	1.47e7	58

5.4. Hydrodynamic simulations

Both the steady state hydrodynamic model (Chapter 3) and the time varying hydrodynamic model (Chapter 4) are employed here to simulate the high frequency excited bed, using appropriate respective boundary conditions with the two constitutive relationships summarized in Chapter 3. Initially hydrodynamic results are verified against the hard sphere based MD simulations. This is followed by comparison against the results of soft sphere MD simulations and experiment.

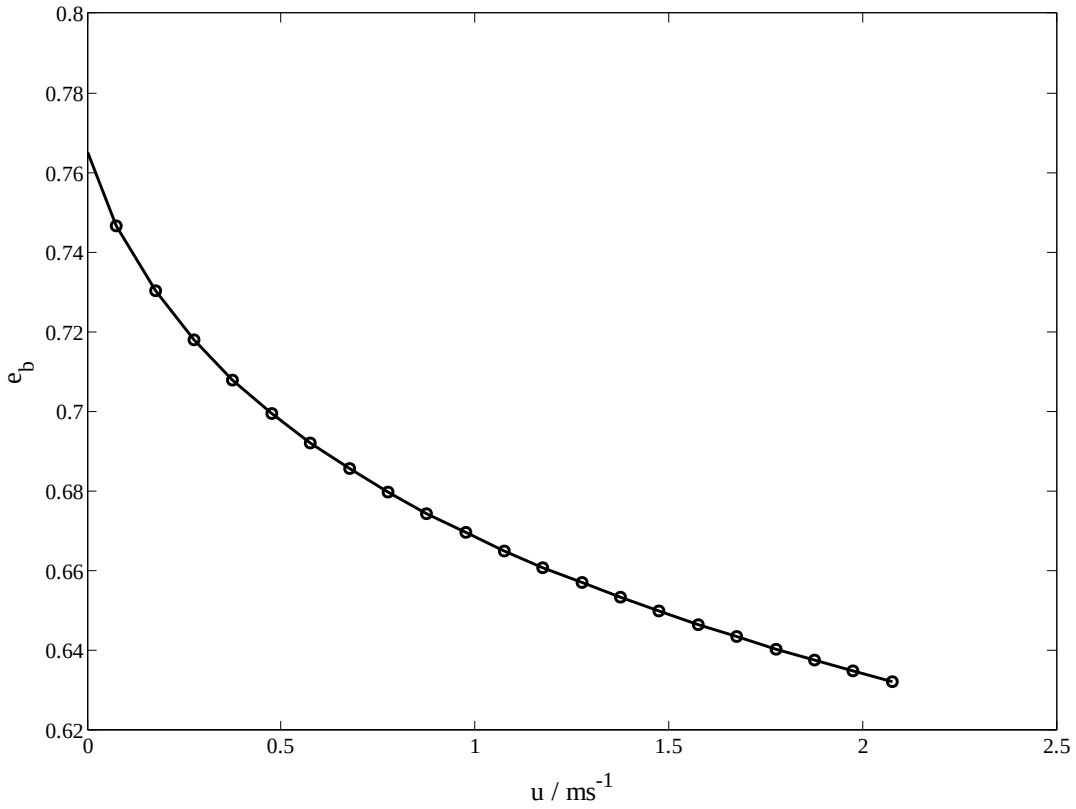

Figure 5-7: Variation of grain-base coefficient of restitution, e_b, as function of incident relative velocity, u.

5.5. Results

a. Comparison of ED MD simulations and hydrodynamic models

Initially we compare results for the average temperature profile predicted by hydrodynamic models with those predicted by event driven MD simulations. Both hydrodynamic models and event driven MD simulations employ the same assumption of binary instantaneous collisions that are a consequence of hard spheres. In order to validate the time dependent hydrodynamic models we make comparisons against the results of both the steady state model (SSH-Jenkins) and MD simulations and results, integrated over the cell radius, are presented in Fig. 5.8, 5.9 and 5.10 for the case of 80, 60 and 40 grains respectively, at an 11.1 kHz base frequency. The packing fractions for all three cases are compared in Fig. 5.11.

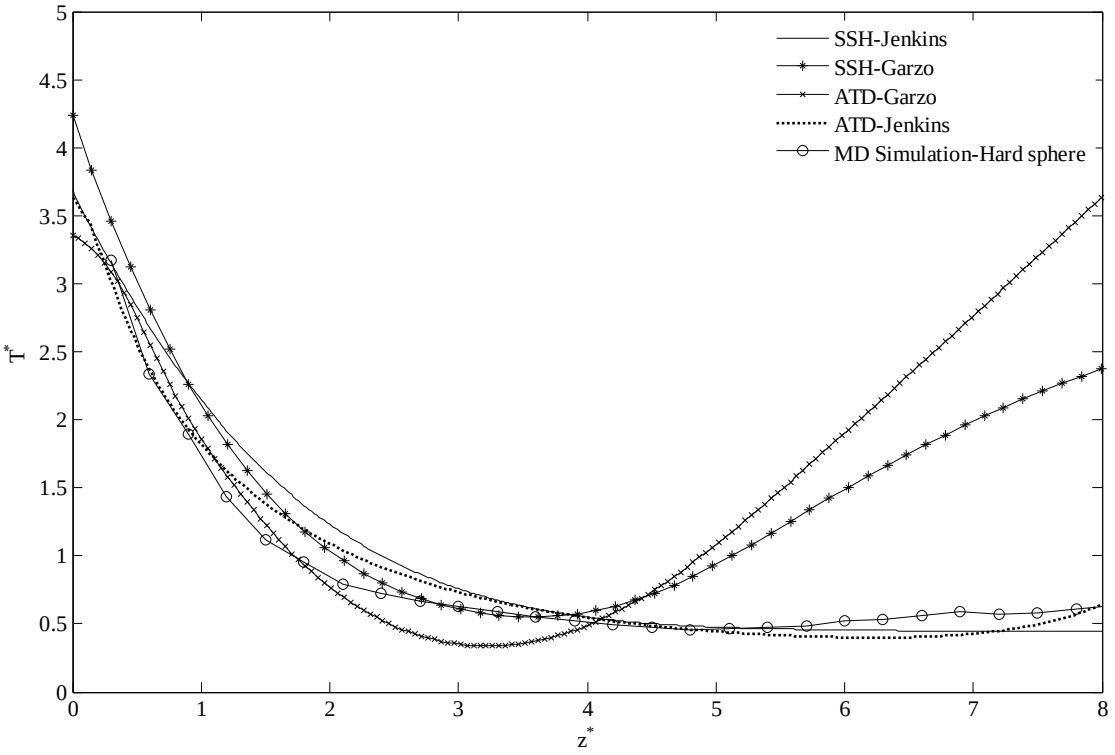

Figure 5-8: Variation of time averaged/steady state granular temperatures (T*) as the function of non-dimensional height (z*) for the case of 80 grains at 11.11 kHz.

It is evident that the time dependent model shows reasonable agreement in estimating the granular temperature in all the three cases. In all the cases ATD-Garzo predicts a lower minimum temperature and higher temperature upturn when compared to the SSH-Garzo. The results from ATD-Jenkins show reasonable agreement with SSH-Jenkins and MD simulations in most part of the cell. Despite being limited to near elastic flows SSH-

Jenkins and ATD-Jenkins show good agreement with MD simulations in all the cases. Slight discrepancies between the time varying models and steady state models are expected as the results for time-dependent model results are time averaged as opposed to steady state results for SSH. We anticipate that ATD-Garzo would predict a higher temperature upturn compared to SSH-Garzo due to a combination of density gradient term and viscous activity in the bulk (see Chapter 4 for details).

b. Comparison of the predictions of soft sphere MD simulations, experimental results and hydrodynamic models

Figure 5.12-5.14 show the granular temperature profiles for time dependent and steady state hard sphere based models, SSM-Jenkins and ATD-Jenkins, in comparison with soft sphere MD simulations and experimental findings. Significant discrepancies in the granular temperatures profiles can be observed amongst the experimental findings and hydrodynamic results in all the cases. It is evident that the predictions of the soft sphere MD simulations and the experimental results are close for $z^* < 4$, while the hard sphere based hydrodynamic models on the other hand show substantially higher granular temperature profiles in this region.

At 11.1 kHz the time period associated with the base vibration is of the order of the 10^{-5} s. The typical contact duration for two colliding spheres made of similar mechanical properties to mustard grains is 66 μs (Johnson 1987). The apparent lack of separation in these timescales suggests that the assumption of binary instantaneous collisions at the base may not hold at these vibration frequencies.

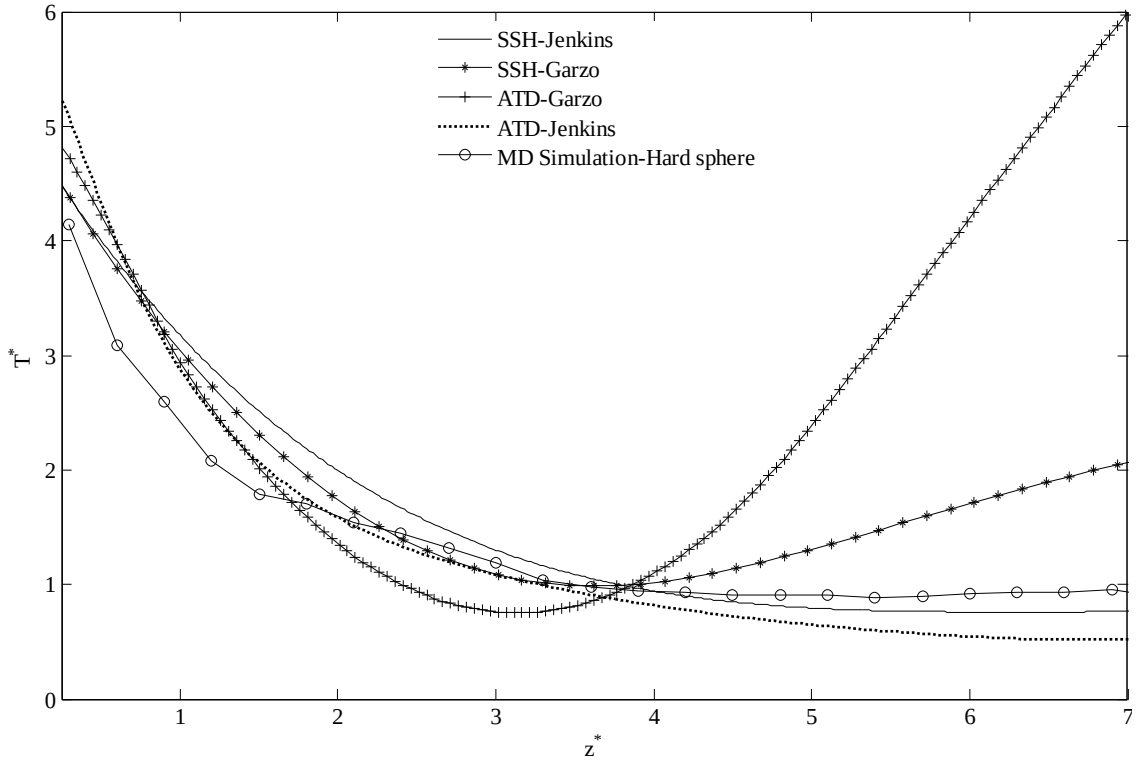

Figure 5-9: Variation of time averaged/steady state granular temperature (T*) as the function of non-dimensional height (z*) for the case of 60 grains at 11.11 kHz.

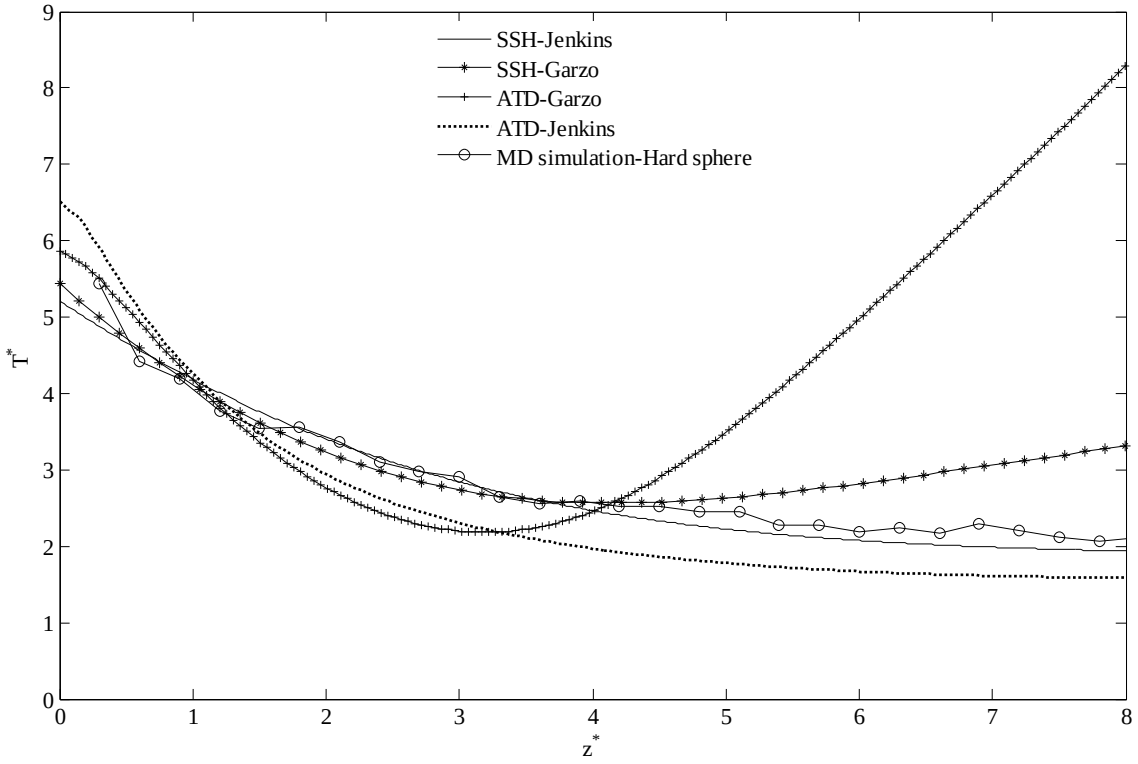

Figure 5-10: Variation of time averaged/steady state granular temperature (T*) as the function of non-dimensional height (z*) for the case of 40 grains at 11.11 kHz.

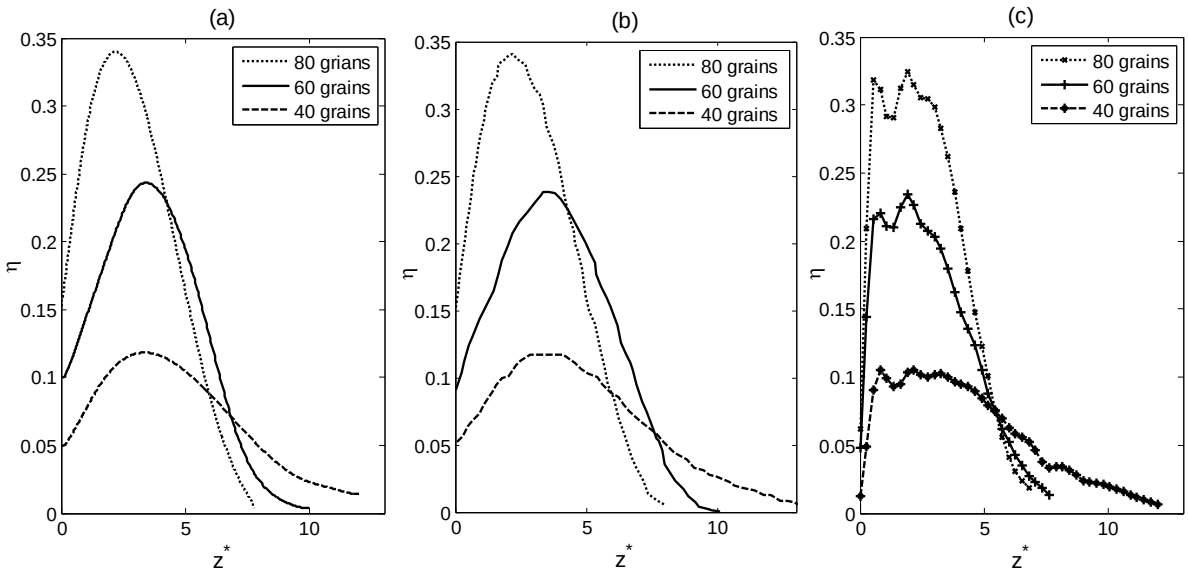

Figure 5-11: Comparison of time averaged packing fraction (η) as the function of non-dimensional height (z*) for the case of 80, 60 and 40 grains at 11.11 kHz. (a) ATD-Garzo, (b) ATD-Jenkins and (c) Experimental-NMR.

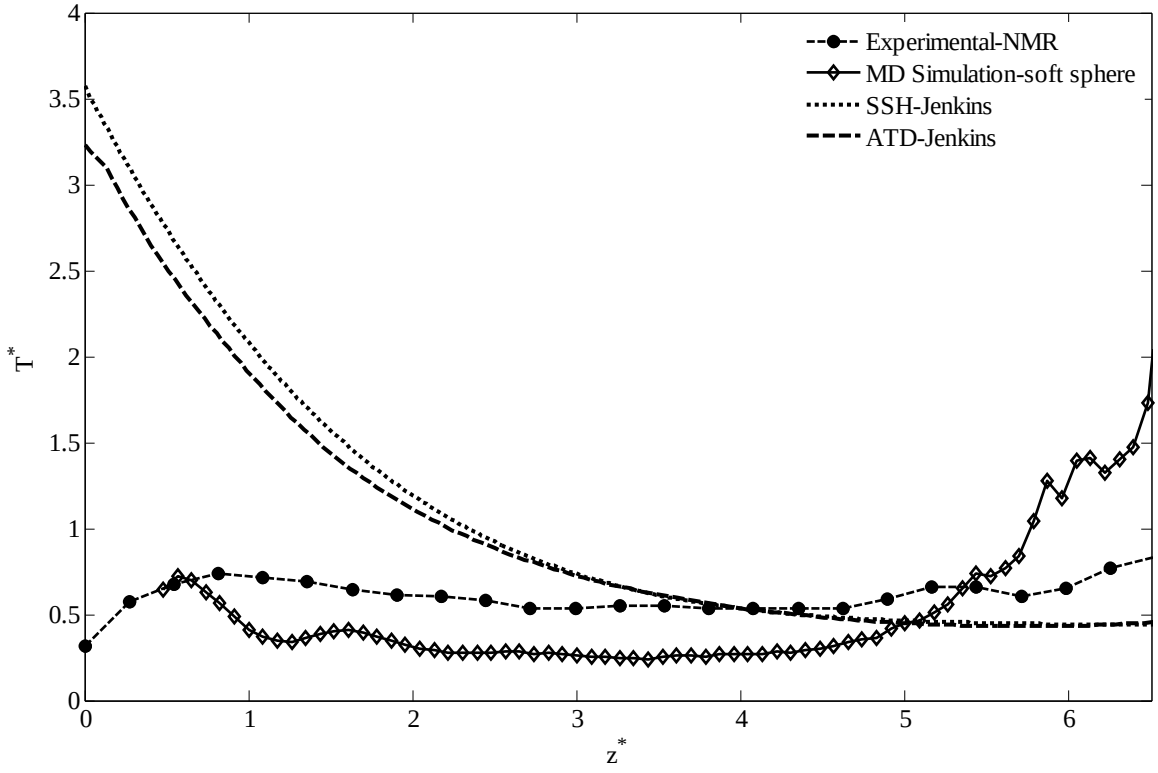

Figure 5-12: Granular temperature (T*) as the function of non-dimensional height (z*) for the case of 80 grains at 11.11 kHz compared against NMR and MD soft sphere results.

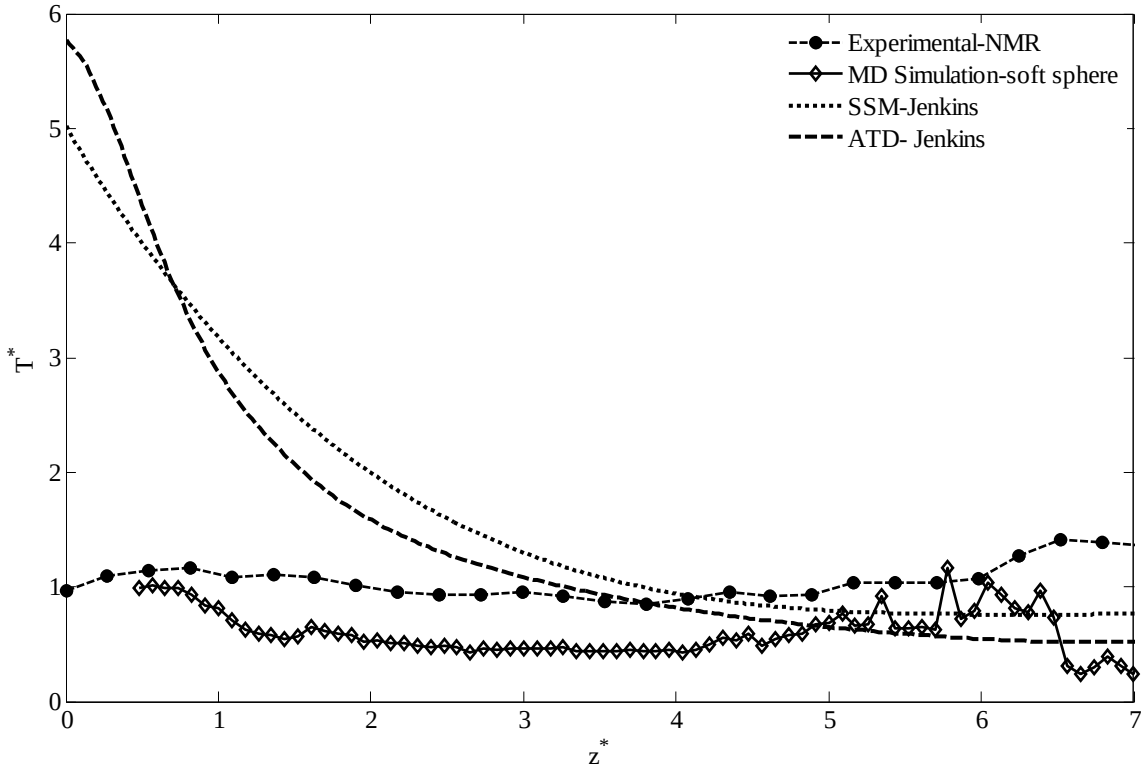

Figure 5-13: Granular temperatures (T*) as the function of non-dimensional height (z*) for the case of 60 grains at 11.11 kHz compared against NMR and MD soft sphere results.

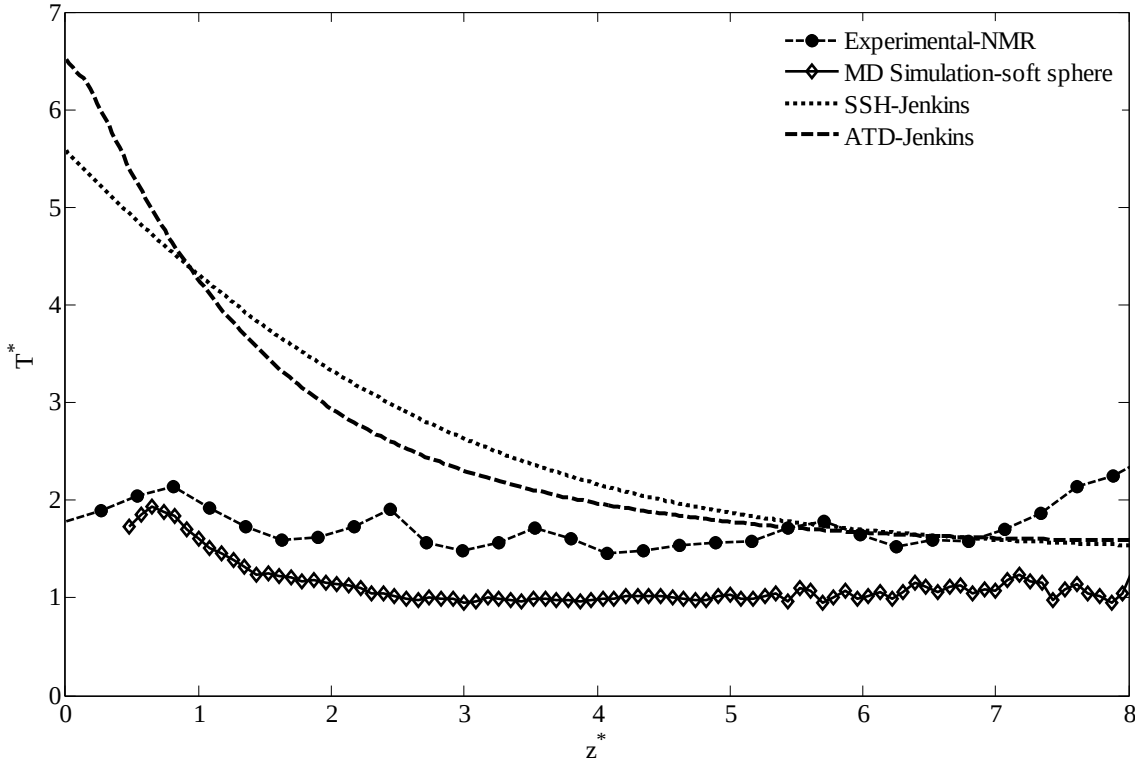

Figure 5-14: Granular temperatures (T*) as the function of non-dimensional height (z*) for the case of 40 grains at 11.11 kHz compared against NMR and MD soft sphere results.

5.6. Discussion

a. Vibrating base-heat flux boundary condition

The analytical foundation of the boundary conditions proposed and used in modelling granular beds has largely been developed on the argument of instantaneous binary collisions. Conditions for a steady state of heat flux and momentum balance have successfully been developed (Warr, Huntley 1995, Richman 1993, Jenkins, Louge 1997, Kumaran 1998) and implemented in hydrodynamic models (Viswanathan, Wildman et al. 2006, Martin, Huntley et al. 2005). One particularly effective model used in a number of simulations was developed by Richman (Richman 1993) for bumpy walls and simplifies rather neatly for the limiting case of a flat smooth vibrating wall. The results from the Richman method should be directly comparable with Warr's findings (Warr, Huntley 1995) in the limits of high frequency excitation. In this latter work, Warr and Huntley showed detailed calculations of the energy transfer from a vibrating boundary to a granular gas. From the mean change in velocity squared of the particles following a collision they numerically evaluated the energy transfer integral, I_e for a given base velocity magnitude. I_e was then related to the heat flux through (Martin, Huntley et al. 2005),

$$J_b = \frac{3m\eta G}{d^3(2\pi)^{3/2}}\left(\frac{m}{T}\right)^{1/2} I_e \qquad \textbf{(5.3)}$$

where J_b is the base heat flux and T_o is the base temperature (Richman 1993). The Warr and the Richman methods of calculating the heat flux agree, particularly at lower base velocities and higher base granular temperatures (Martin, Huntley et al. 2005). Kumaran also proposed expressions for the base heat flux in vibrated beds (Kumaran 1998), resulting in the following expression for $I_{e,}$ in non-dimensional form

$$I_e^* = 4T_o(1+e)^2V^2 + 2(e^2-1)T_0. \qquad \textbf{(5.4)}$$

Although this method is relatively easy to implement, it does allow for the possibility of energy extraction from the bed, and as a consequence we do not consider it in this work.

As the base velocity increases, however, the predictions of the three base heat flux models start to grow. Figure 5.15 shows the calculation of the energy integral for each of the formulations. We see that at high temperatures (high base velocity), Warr model is comparable with Richman's calculations, but that at low base temperatures (low base

velocity) there are substantial discrepancies. Thus for all practical calculations in this work, we use the Richman boundary conditions only. However none of the above mentioned models predict the energy flux has a dependence on the frequency of excitation and only scale with the base velocity.

This is important since the discrepancy between the predicted temperature profiles in Figs. 5.12-5.14 suggests the assumptions of frequency independent, instantaneous collisions are not holding. One test of the base heat fluxes for realistic particles is to employ soft sphere MD simulations, keeping a constant base velocity (0.74 m/s), and to vary the frequency. The results of this test are shown in Fig. 5.16, where we plot the heat fluxes against the frequency and compare the predictions of the hydrodynamics and the soft-sphere simulation. The figure shows that, in all the loading situations, that the theoretical prediction of the heat flux generally agrees with that found in the soft-sphere simulation until frequencies of the order of 5 kHz are reached. At frequencies in excess of this, the heat flux determined from the simulations starts to decrease rapidly and reduces to zero at around ~20 kHz. As we have noted, at these high frequencies, the duration of collisions are of the same order as the period of oscillation, in which case the base starts to act more and more as a static plate, and the heat transferred to the particles drops off. Clearly, under these conditions, one can no longer rely on the assumptions and consequences of instantaneous and binary collisions. To demonstrate this, we show a typical trajectory of a particle in collision with the base for different base frequencies (Fig. 5.17). As the frequency is increased from 5k Hz to 50k Hz (a-c) the particle consumes more and more cycles of the base during its typical collision. This leads to the reduction of energy heat flux from the predicted values as the grains spend more time relative to the base consuming energy in localized deformations. With further increase in frequency the grain sees the base oscillating back and forth during a typical collision and the net transfer of momentum to the particle is near to zero. The consequence of this is that as we increase the frequency, we observe the particles become less and less fluidised (Fig. 5.17 and 5.4). Clearly, at near ultra-sonic frequencies, heat flux conditions such as those proposed by Richman are no longer appropriate and conditions that take into account the collision duration are required.

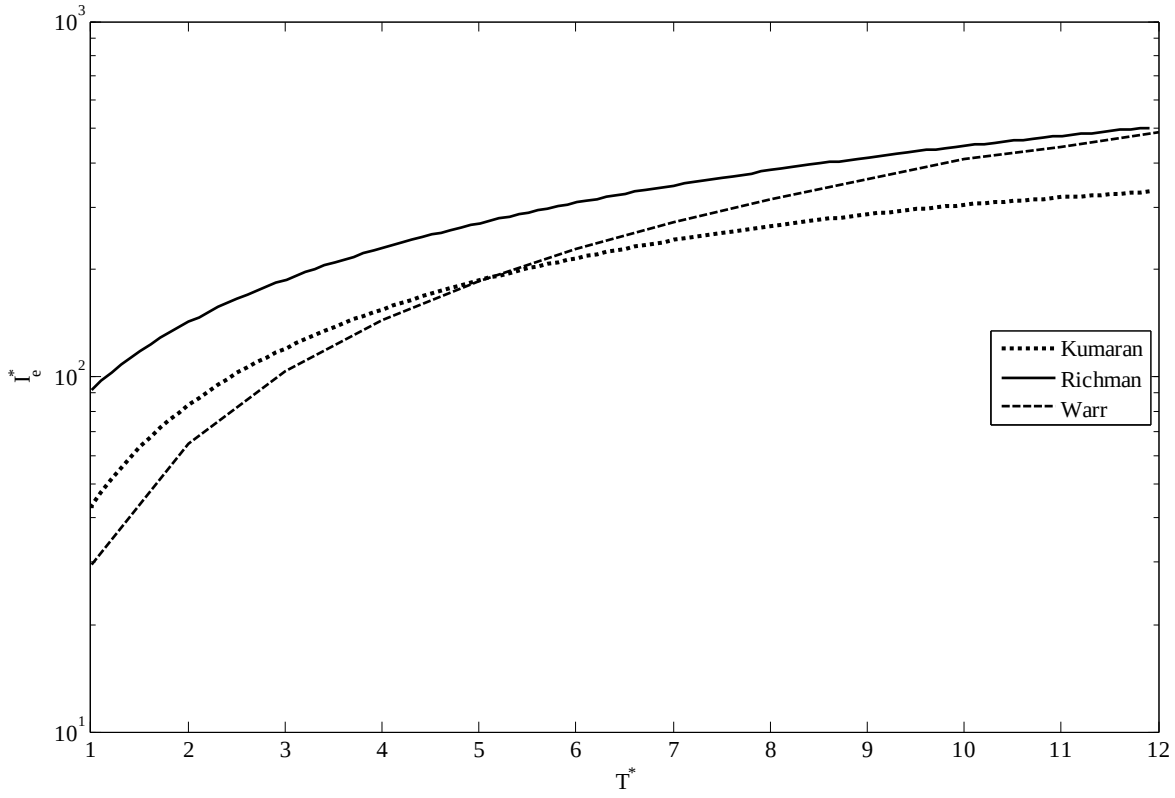

Figure 5-15: Non-dimensional heat flux energy integral (log scale) against granular temperature (T*) at non-dimensional base velocity (V_b^* = 1.74) for Richman (Richman 1993)**, Warr** (Warr, Huntley 1995) **and Kumaran** (Kumaran 1998)**.**

Interestingly Fig. 5-16 shows that there are deviations in the heat flux predictions from those predicted by Richman (Richman 1993) even at low frequencies (less than 5 kHz). The maximum difference between Richman and soft sphere simulation predictions lies within 5% for the cases of 20 and 40 grains. For 60 grains, it increases to 10% for 60 grains and around 12% for 80 grains at an instant. We would perhaps expect the discrepancies to grow with the number of particles since the assumption of instantaneous, binary collisions will start to weaken as the collision frequency increases.

In summary, we can see that the classical model for treating the heat flux at the base of a vibrating base is reasonable up to frequencies of the order of the 5 kHz (for our particular combination of material parameters), despite some discrepancies at low frequencies. At frequencies in excess of 5 kHz, consideration needs to be given on how to incorporate the effects of the collision duration into the predictions of heat flux.

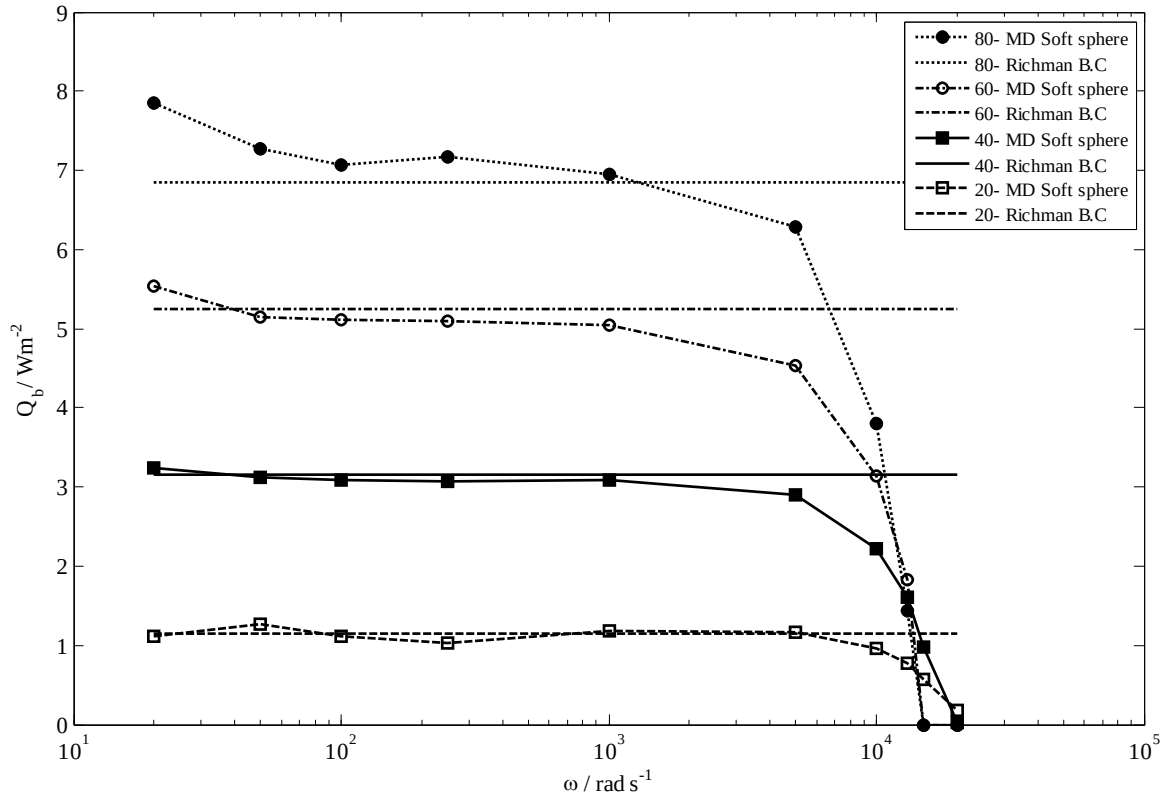

Figure 5-16: Base heat flux, Q_b, variation with frequency for hard sphere verses the soft sphere MD simulations at different loading conditions.

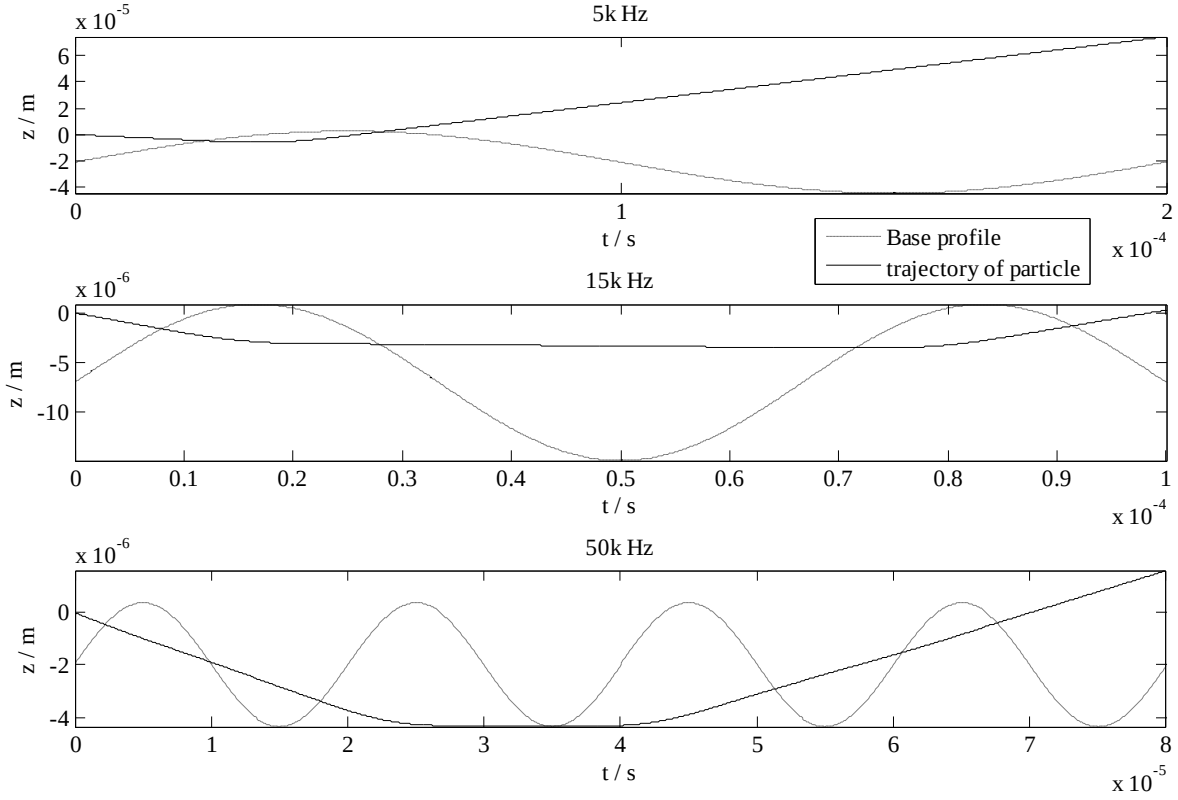

Figure 5-17: Trajectory of a colliding particle with base profile at different base frequencies.

b. Bulk physics

We saw in the previous section that there are important boundary effects due to the lack of separation between the collision duration and vibration timescales. In order to examine whether our proposed hydrodynamic model is able to capture bulk physics, it is necessary to control the heat flux at the base rather than leave it as part of the solution. To achieve matching of the heat fluxes at the bottom, we tuned the hydrodynamic heat flux at the base to that of the hard-sphere simulations. In addition, we modified the vibration amplitude of the base in the soft-sphere simulations to match these heat fluxes. In the case of the soft-sphere MD simulations this was done by varying the peak velocity to 1.33 times the actual value of the base with vibrating frequency at 11.1 kHz. Figures 5.18 to 5.20 show that at same base heat fluxes the bulk physics is generally same as that predicted by hydrodynamic models and MD hard sphere simulations.

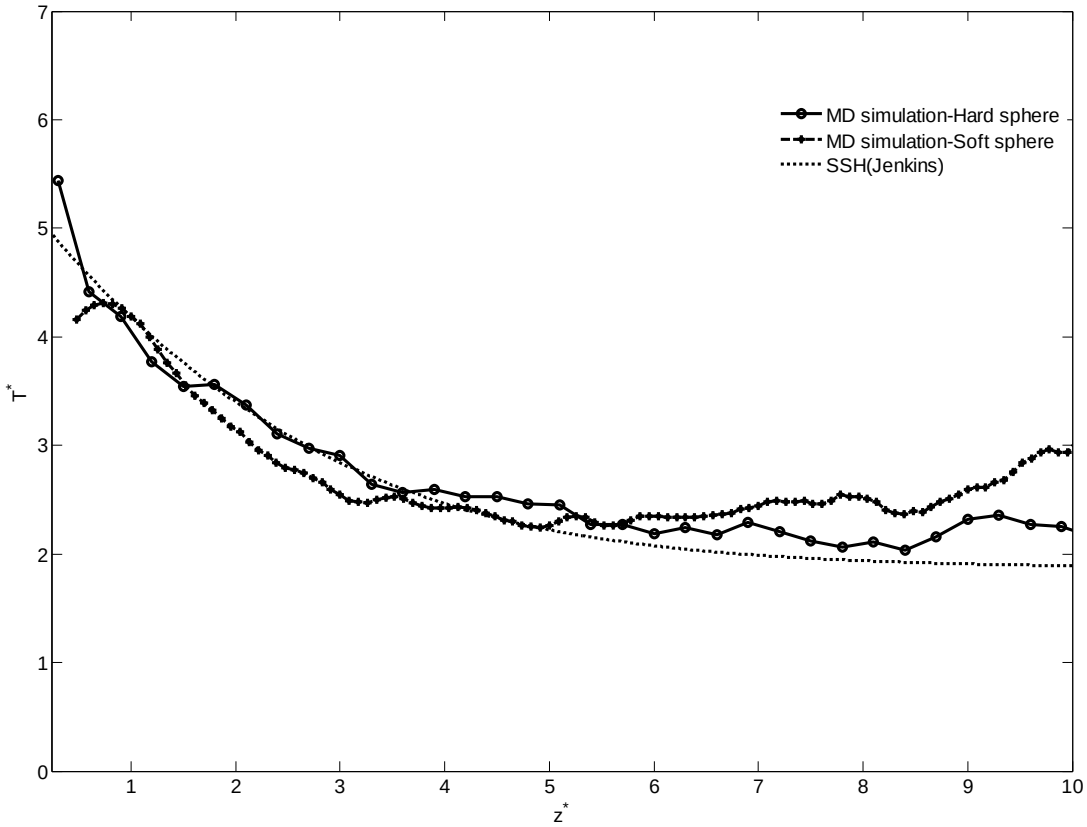

Figure 5-18: At 40 grains, comparison of the granular temperatures at steady state for MD simulations (hard and soft spheres) and SSH(Jenkins).

In the cases of 40 and 60 grains the bulk physics is well predicted by hydrodynamic model but there are discrepancies in the case of 80 grains. In hard sphere MD simulations and hydrodynamic models the calculations are carried out using a fixed coefficient of restitution, on the other hand the soft sphere model uses an elastic modulus along with

damping coefficient as inputs, which allows the restitution coefficient to change with the velocity, as shown in Fig. 5.7. In the case of 80 grains, the mean velocity is expected to be lower than in the case of 40 grains which results in an increase in the coefficient of restitution in the bulk. This increase in coefficient of restitution will result in comparatively less dissipation per collision, and thus will result in a relatively higher temperature compared to that observed in a system with particles of fixed coefficient of restitution. These results suggest that at least for relatively dilute systems, that the despite the boundary conditions suffering from a lack of separation of timescales, the bulk behaviour is predicted by hard-sphere models beyond the 5 kHz vibration frequencies.

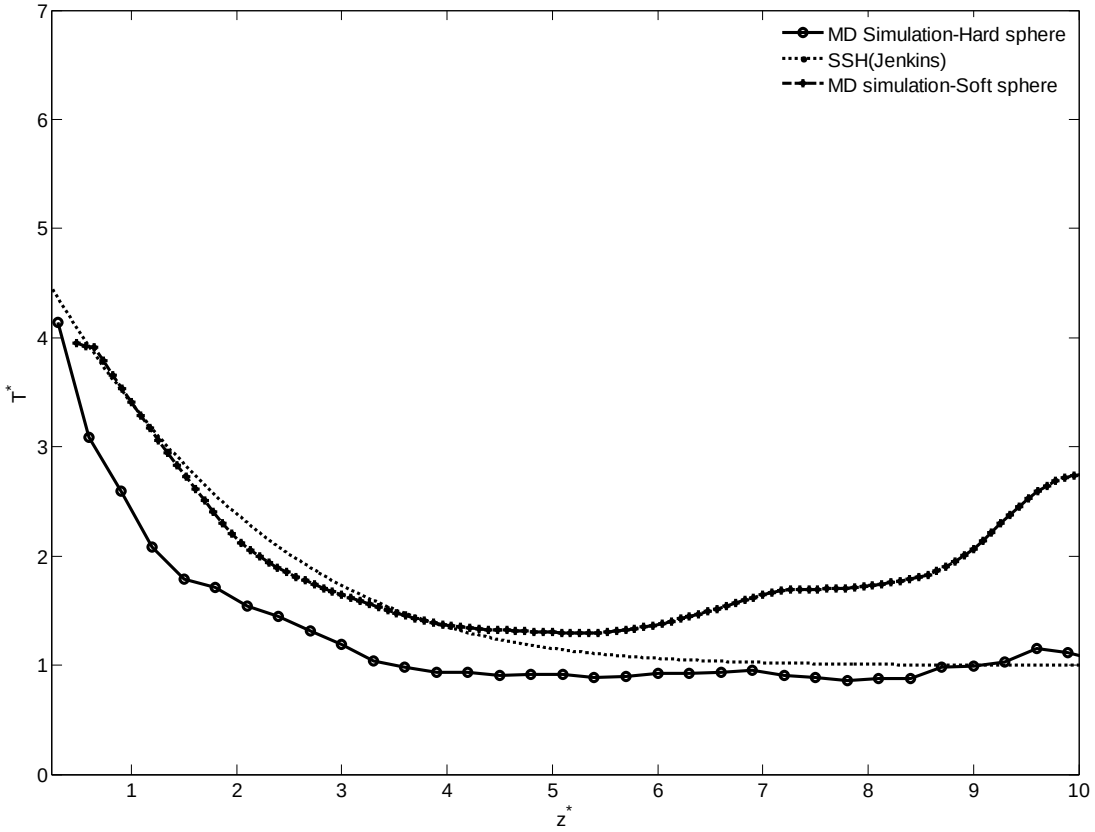

Figure 5-19: At 60 grains, comparison of the granular temperatures at steady state for MD simulations (hard and soft spheres) and SSH(Jenkins).

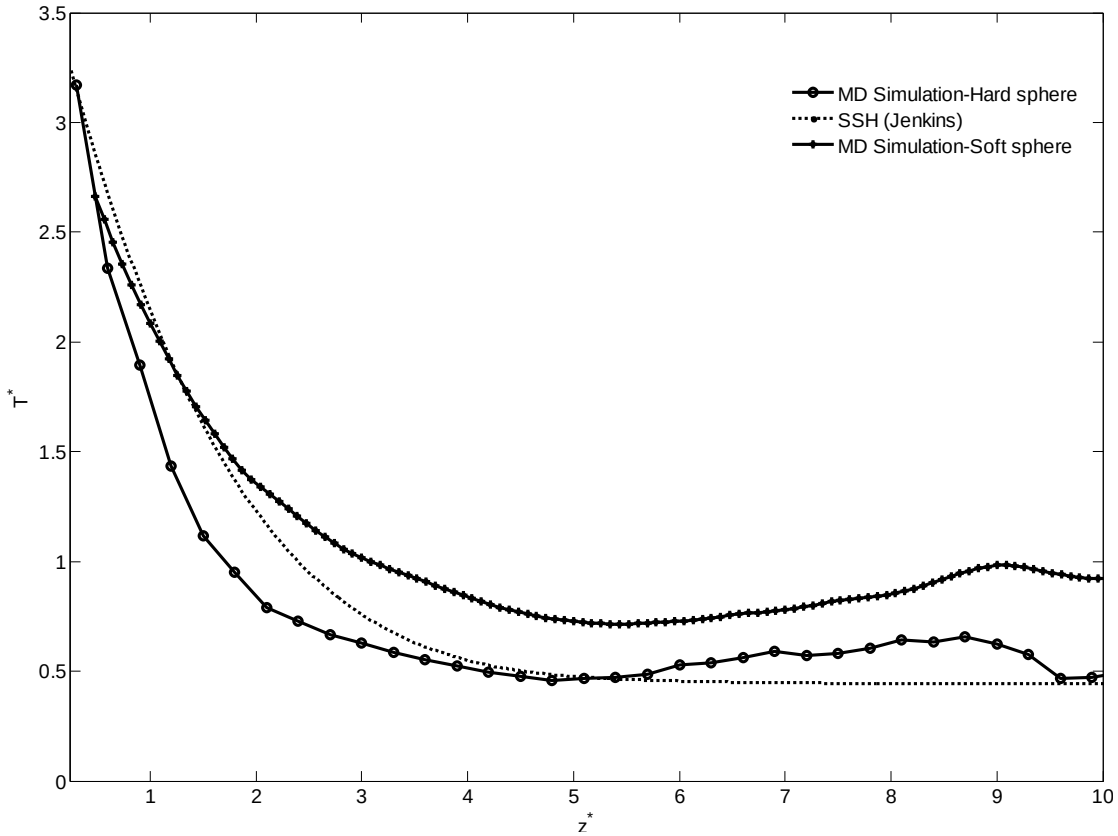

Figure 5-20: At 80 grains, comparison of the granular temperatures at steady state for MD simulations (hard and soft spheres) and SSH(Jenkins).

c. Effect of frequency on bulk physics

Alongside base heat flux variation with frequency, it is also important to show how the variation of frequency of the base vibration affects the bulk granular temperature. In the previous chapter we examined in detail the behaviour of a granular bed at low frequencies while in the previous sections of this chapter we have considered the steady state physics of a granular bed at higher frequencies. At elevated frequencies, apart from grain-base interaction and associated reduction of heat flux, the bulk physics is reasonably well described by hard sphere based models, and we restrict ourselves to hard sphere simulations for these analyses. Here we consider a case of reasonably dense bed with 60 grains. The rms base velocity amplitude is kept at $V_b^* = 1.17$ while frequency is varied from 55 Hz to 11 x 10^3Hz using original theoretical heat flux boundary condition.

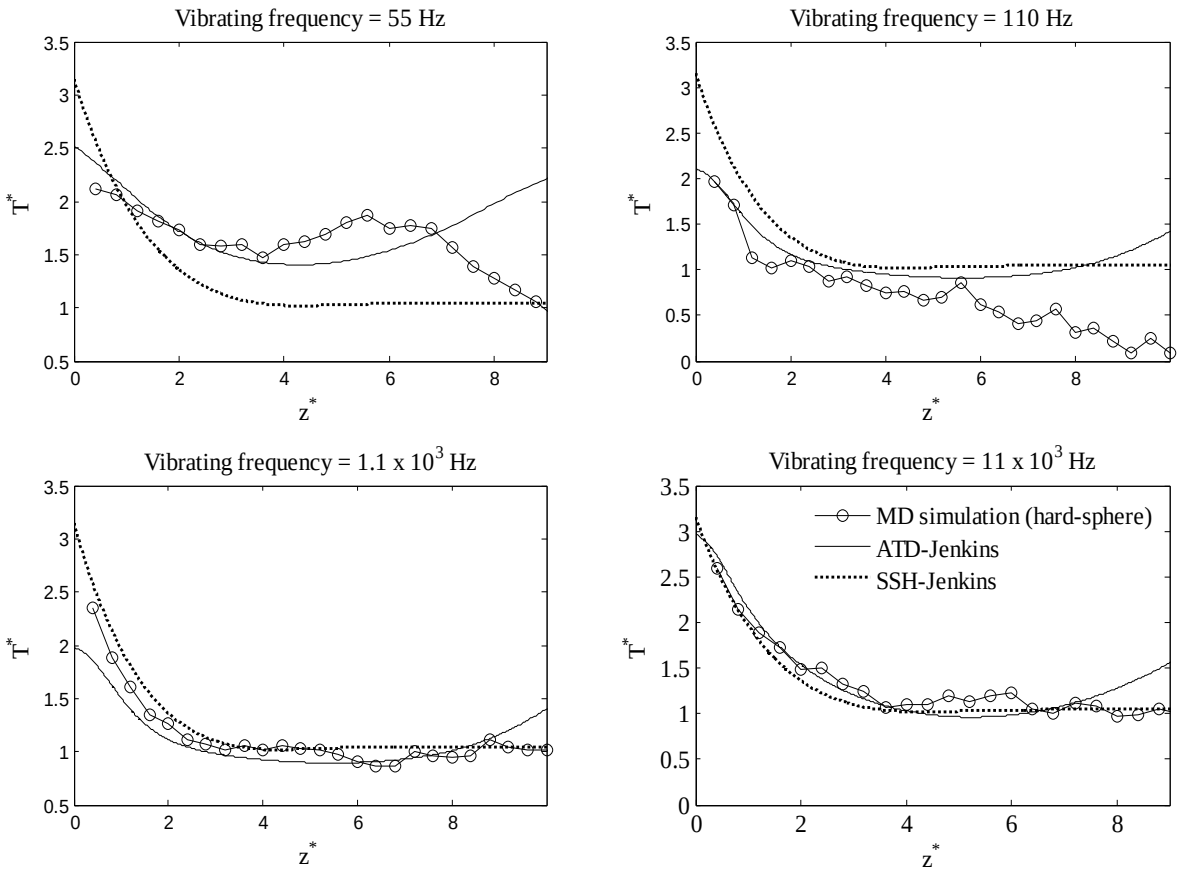

Figure 5-21: Granular temperature T* as a function of height z*, comparing ATD-Jenkins and SSH-Jenkins against hard sphere MD simulations. *N* = 80 grains, with an rms base velocity of V_b^*=1.17. The frequencies of vibration vary from 55 Hz to 11 kHz.

In Fig 5.21 we compare the granular temperature profiles obtained from hard-sphere MD simulations against the predictions of ATD-Jenkins and SSH-Jenkins. We choose ATD-Jenkins and SSH-Jenkins to highlight the bulk temperature behaviour with the upturn without the contributions of the density gradient term of ATD-Garzo. As one expects, the steady state predictions are independent of the frequency, but we can see from the time dependent simulations that there is a small dependence on frequency at low frequencies, but that importantly, the hard sphere simulations agree well with the time dependent hydrodynamic model. The MD simulation data is not sufficiently reliable at the highest altitudes to say with confidence whether the small upturn is observed in the system. This small increase in temperature near the top of the cell can be observed at all frequencies but because this occurs with close proximity of this phenomenon to the location of the limits of hydrodynamic applicability, probing this effect has proved difficult (the hydrodynamic limits decreases from $z^* = 7.4$ at 55 Hz to $z^* = 6.5$ at 11k Hz due to variation of mean temperature (Martin, Huntley et al. 2005)).

When vibration frequency of the base is decreased we see two effects. Firstly we see that the granular temperature of the particles near to the base goes down. Secondly, we see that the asymptotic temperature increases. These effects are somewhat expected, since as we have seen in the last chapter, at low frequency phenomena such as wave propagation can become prominent. This comparison underlines the importance of developing the axi-symmetric time-varying model along with steady state models. At the other end of the frequency spectrum, we anticipate that a steady state model may be appropriate, since wave propagation may not feature strongly.

5.7. Summary

We have demonstrated that the frequency of vibration has a strong effect on the fluidization behaviour of granular gas under a range of loading conditions. At high frequencies, experimental observations and soft sphere MD simulations showed remarkably different granular temperature profiles when compared to hard sphere based hydrodynamic models and event driven MD simulations. It was identified that the lack of separation in timescales at the base led to a collapse in heat flux at high frequencies of vibration. When focussing on hard sphere models, we saw good agreement between them, but it was evident that at low frequencies, time dependent effects became important. Analysing the bulk behaviour independently from the boundary conditions showed that at high frequencies, hard sphere models were able to capture the behaviour well. In the next chapter we combine the two frequency regions by the introduction of low frequency signal with the high frequency to study the effect of low frequency changes to the high frequency stimulation has on the bed behaviour.

Chapter 6 The behavior of granular beds fluidized using a modulated vibration signal

6.1. Introduction

In the two previous chapters we considered both high and low frequency vibrations and their respective influences on the granular physics at similar base velocities. At low frequency the granular bed showed granular temperature variations with the phase of the base while at high frequency the bed attains a steady state feature, whilst at the same time a considerable and unexpected reduction in the base heat flux is seen. The idea then arises that combining low frequency and high frequency base driving could enable us to observe both the time scales interacting in a single granular bed, giving rise to complex new phenomena. In this chapter we propose, therefore, to consider a granular gas driven by high frequency vibrations, modified through the application of a low frequency amplitude modulation.

We use two forms of amplitude modulations. The high frequency signal is at 11.1 kHz while the modulating low frequency signal is of two types. The first type is a square wave whilst in the second case a sine wave form profile is used. The square wave modulation is studied using MD simulations with the results compared against phase resolved NMR experimental findings. Later we extend the analysis to a sinusoidal amplitude modulation signal using MD simulation and time dependent hydrodynamic model. For all MD simulation analysis in this chapter we use a soft sphere based model in order to include the effect of heat flux reduction at high frequency (see Section 5.6 for details).

In this chapter we give a brief overview of the wave forms used in the analysis. We then go on to describe the experimental setup for NMR and the details of the MD simulations. Finally, we compare the experimental results to the predictions of the MD simulations.

6.2. Vibration profiles

The carrier signal is a high frequency vibration signal operating at 11.1 kHz modulated with a low frequency signal. The low frequency signal is of two types generating two resultant amplitude wave form sequences.

a. Square wave modulation

The first sequence was obtained through amplitude modulation with a square wave at 20 Hz using two levels of duty cycles resulting in two signals of the form as shown in Fig. 6.1. The two duty cycle levels are at 20% and 40% respectively, generating signals with the higher amplitude for 20% (DC20) and 40% (DC40) part of the 20 Hz cycle and the rest at lower amplitude. A typical signal type is shown in Fig. 6.1 for the part of the signal where there is a transition from high amplitude to low amplitude. The ratio of high to low amplitudes of the two regions is kept at 50% with the maximum higher amplitude of 0.23 m s^{-1}(see Fig. 5.3 for base velocity and voltage signal relationship). This ratio of 50% is used to ensure sufficient "jump" in the base amplitude to influence the bed dynamics.

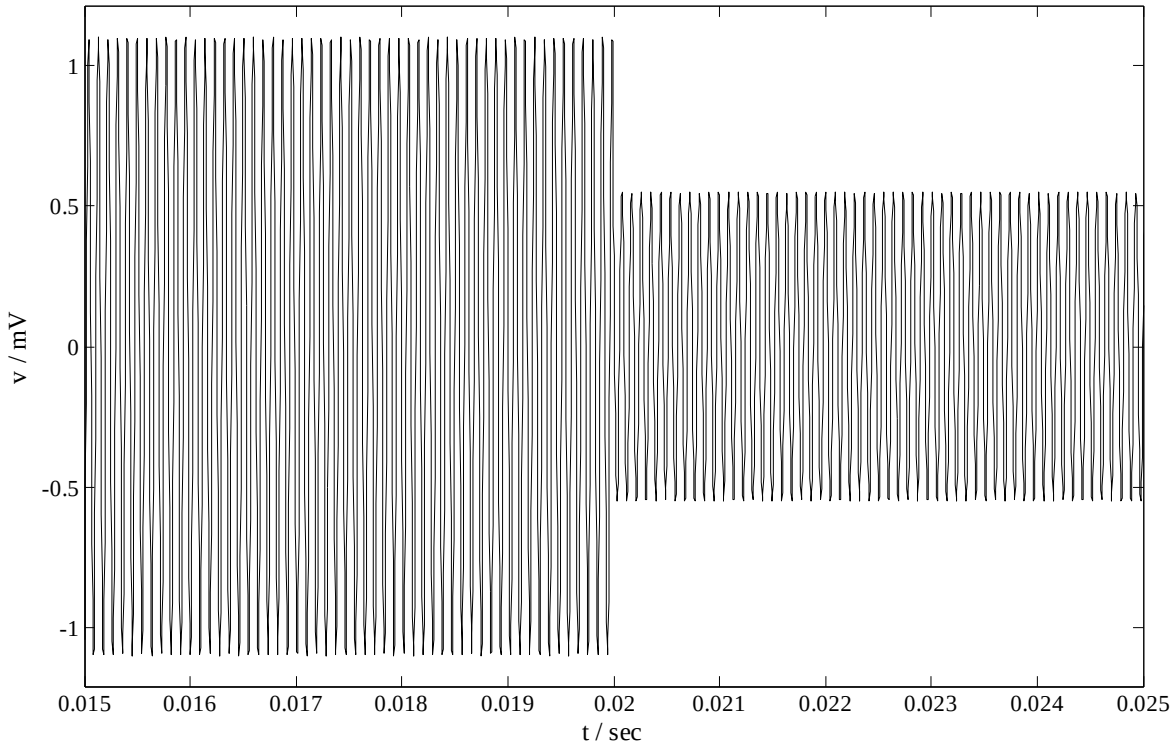

Figure 6-1: Part of the modulated voltage, v, signal for 20 Hz signal and 40% duty cycle ('DC40') with carrier signal at 11.1 kHz showing the transition from high amplitude voltage to low amplitude voltage.

b. Sinusoidal wave modulation

The second form of modulated signal produces a sinusoidal base amplitude generating a signal of the form shown in Fig. 6.2. The 40 Hz low frequency sine wave signal allows a smooth transition from low to high amplitude and vice versa. This form of signal is useful

to monitor smooth transitions in the bed. The maximum base amplitude of this signal is kept at 0.37 m s^{-1}.

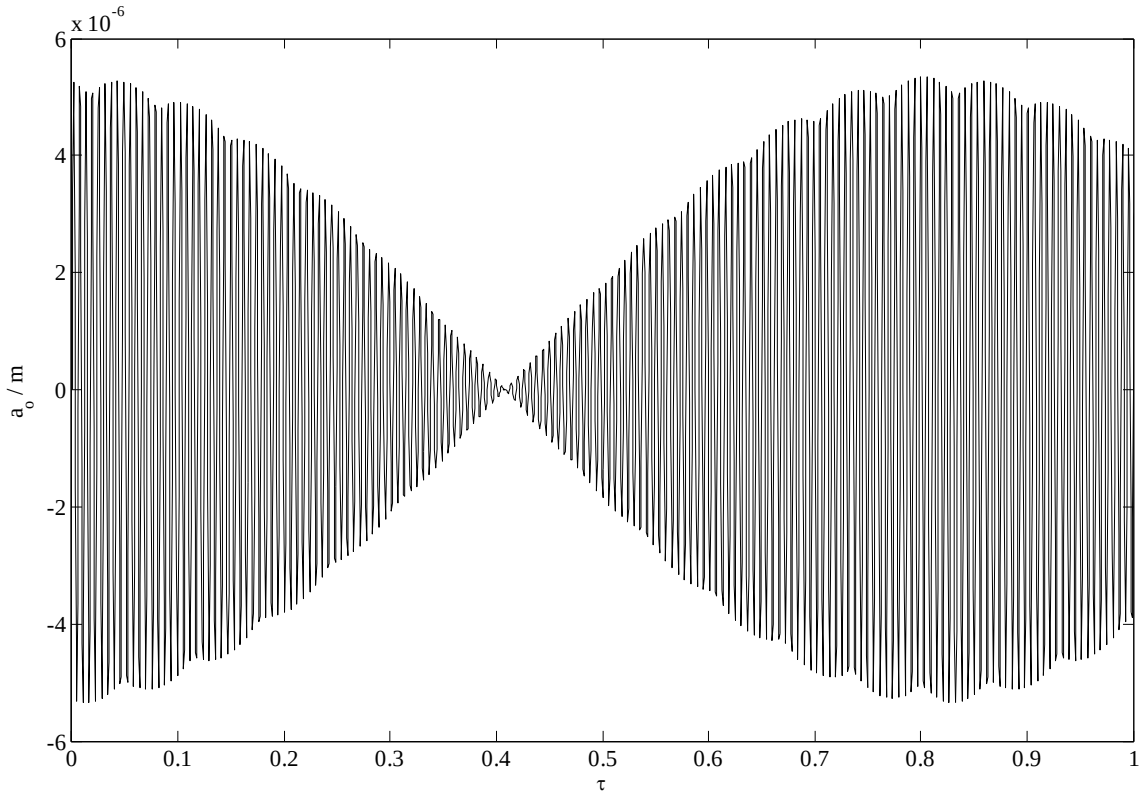

Figure 6-2: Sinusoidal base amplitude, a_o, signal for 40 Hz with carrier signal at 11.1 kHz showing the transition from high amplitude to low amplitude with $\tau = t * \sqrt{g/d}$.

6.3. Experimental setup using NMR

The experimental system of NMR spectroscope, ultrasonic exciter and granular material specification are same as those described in Section 5.2. The main difference in these experiments is the phase resolved monitoring of granular cell at the low frequency cycle. In this case, the NMR spectroscope is triggered at parts of the cycle that allow the greatest insight into the changes in the bed behaviour. For the experimental work, we use only the square wave modulated signal. The cycle shown in Fig 6.1 has three important components: the high amplitude, transition from high to low amplitude and low amplitude part. Our interest is in observing the response of the granular bed just before transition, shortly after the change from high to low amplitude and then some time after the transition. To achieve this, the NMR spectroscope is triggered at the three times (TR1, TR2, TR3) given in Fig. 6.3.

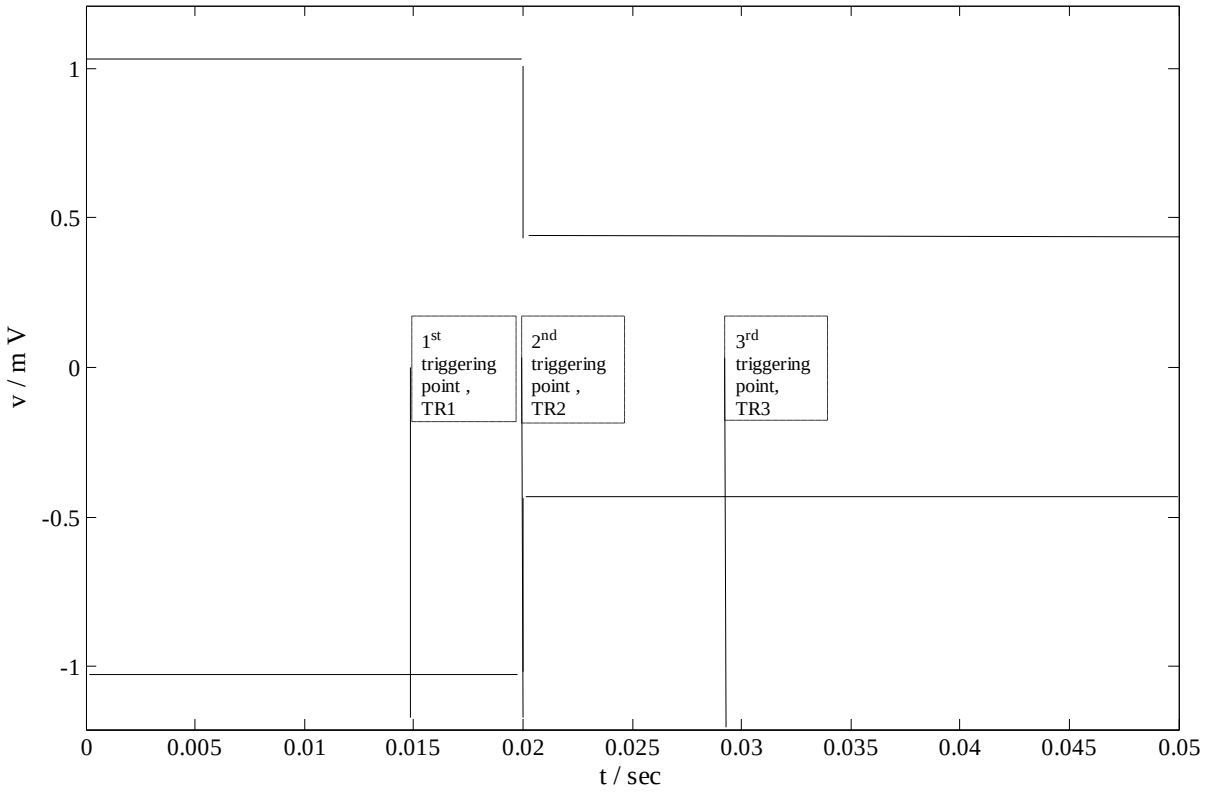

Figure 6-3: Three observation points in a schematic 20 Hz cycle at DC40, TR1 near the tripping edge, TR2 after the edge and TR3 at 8.0 ms after TR2.

These experiments are performed using 20 mustard seeds and we employ two different duty cycles, DC20 and DC40. To ensure that fluidisation was observed at the low amplitude, 20 grains were used in all the experiments.

6.4. MD simulations

Molecular dynamics simulations enable us to resolve the complete dynamics of the bed at all time scales. Here we only use soft sphere molecular dynamics simulations since we have shown in Chapter 5 that hard sphere MD has difficulty in describing base-particle interactions during high frequency driving. The characteristics of the grains such as mass, size, stiffness and damping coefficients as well as the granular cell dimensions, are the same as described in Chapter 5. For the signal modulated by a square wave 20 grains are used to match the experimental setup.

In the case of the sinusoidal wave form, results are reported for 60 grains producing a dilute to moderately dense granular gas. We take the case of 60 grains in order to establish the regions of hydrodynamic applicability comparable for the hydrodynamic model. With 60 grains the results produced in Chapter 5 showed a reasonable match between MD simulations and hydrodynamic models(see Figs. 5.9 and 5.21 for instance).

In both cases the system was initialized with a random distribution of particles ensuring non-interference between the grains within the simulation cell. In order to observe the dynamic effect progressing in a sequence, simulations were allowed to run at low amplitude until a steady state was achieved using 10^6 total number of collisions. Thereafter the amplitude modulation was introduced.

6.5. Results and discussion

a. Square wave modulation

The experimentally determined distribution of vertical velocities at the three triggering points shown in Fig. 6.3 at 20% and 40% duty cycle (DC20 and DC40) are shown in Figs. 6.4 and 6.5 respectively. It can be noticed that the level of fluidization is significantly low. Apparently no major differences amongst the vertical velocity distributions are visible at the three observation points (TR1, TR2 and TR3). However a detailed comparison for the second moment of the velocity distribution is presented a little later in the section.

The information relating the packing fraction profiles at TR1, TR2 and TR3 are determined by the method described in Section 5.2 and are shown in Fig. 6.6 and Fig. 6.7 for DC20 and DC40 respectively. As one might anticipate, the greater duration of the high amplitude part of the duty cycle in DC40 compared to DC20 leads to a relatively expanded bed for DC40. Moreover Figs. 6.6 and 6.7 show expansion of the granular bed for both DC20 and DC40 from the 1^{st} monitoring point (TR1) to the 3^{rd} monitoring point (TR3). For both the cases the value of the highest packing fraction observed in MD simulations decreases from TR1 to TR3 with its location moving away from the base. Especially Fig. 6.7 shows that the results for packing fraction profiles match well with experimental trends at TR2 and TR3 for DC40. In spite of the fact that TR3 lies in the lower part of the amplitude modulation (see Fig. 6.3) we observe a slightly expanded granular bed at this point compared to TR1. This suggests that a lag exists between the bed response and the amplitude modulation. However experimental results show very little difference in the packing fraction profiles from TR1 to TR3 in both the cases.

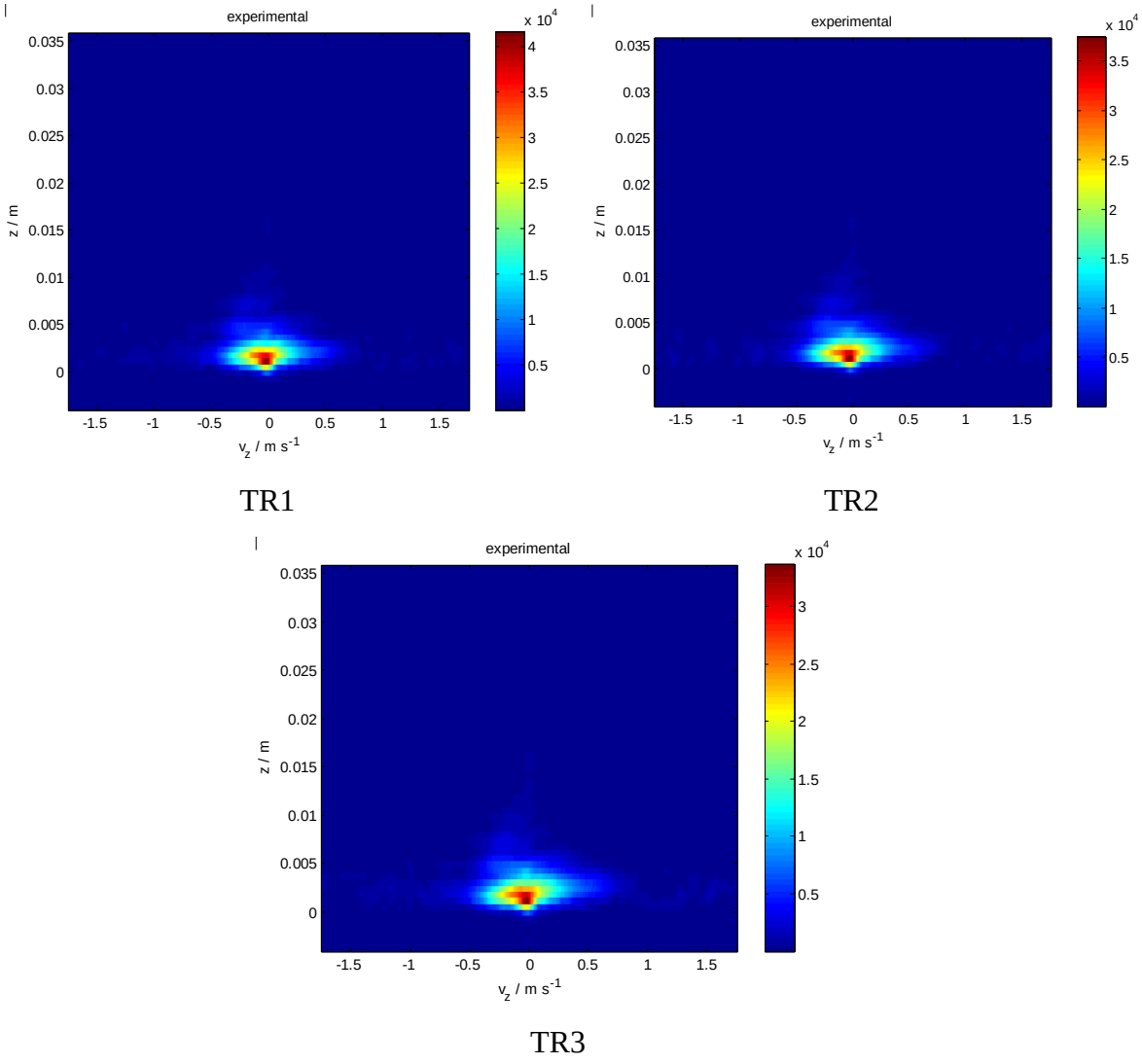

Figure 6-4: Vertical velocity distributions for three observation points (TR1, TR2 and TR3) in 20 Hz cycle with 20% duty cycle square wave modulation, DC20.

The vertical velocity distributions of Fig. 6.4 and 6.5 are approximated with Gaussian distributions, using the method described in Section 5.2. For the case of DC20 and DC40, the comparison of granular temperatures at TR1, TR2 and TR3 are plotted in Figs. 6.8 and 6.9 respectively. Although quantitative deviations can be observed amongst the predictions of granular temperatures, qualitatively the predictions are similar especially at TR2 and TR3 for both DC20 and DC40. In both cases MD simulations suggest an increase of mean granular temperature of the bed from TR1 to TR3. The increase of temperature from TR1 to TR3 suggests a similar lagging trend in the gas behaviour as observed for the packing fraction profiles. With the increase of base amplitude during the duty cycle an expansion in the bed is likely to occur. However the heat transfer in the bulk does not occur instantaneously and a delay or lag is the collective bed response is expected. MD simulations show the expansion and contraction of the bed during the cycle while experimental results show little evidence of such expansion.

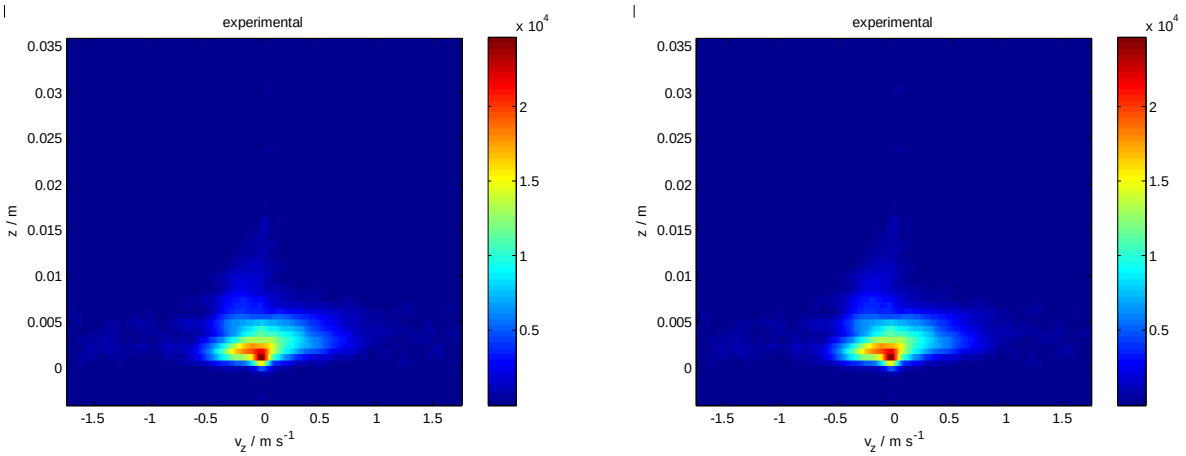

TR1 TR2

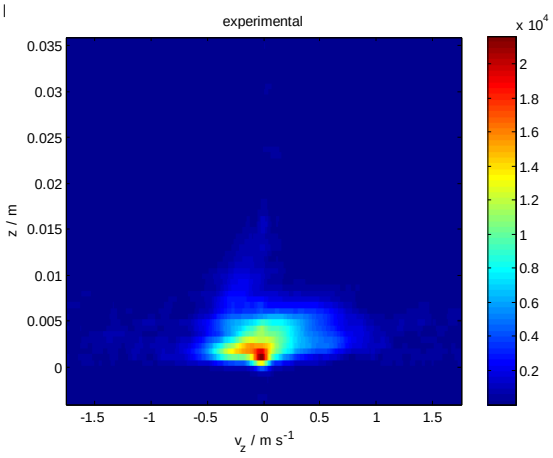

TR3

Figure 6-5: Vertical velocity distributions for three observation points (TR1, TR2 and TR3) in 20 Hz cycle with 40% duty cycle square wave modulation, DC40.

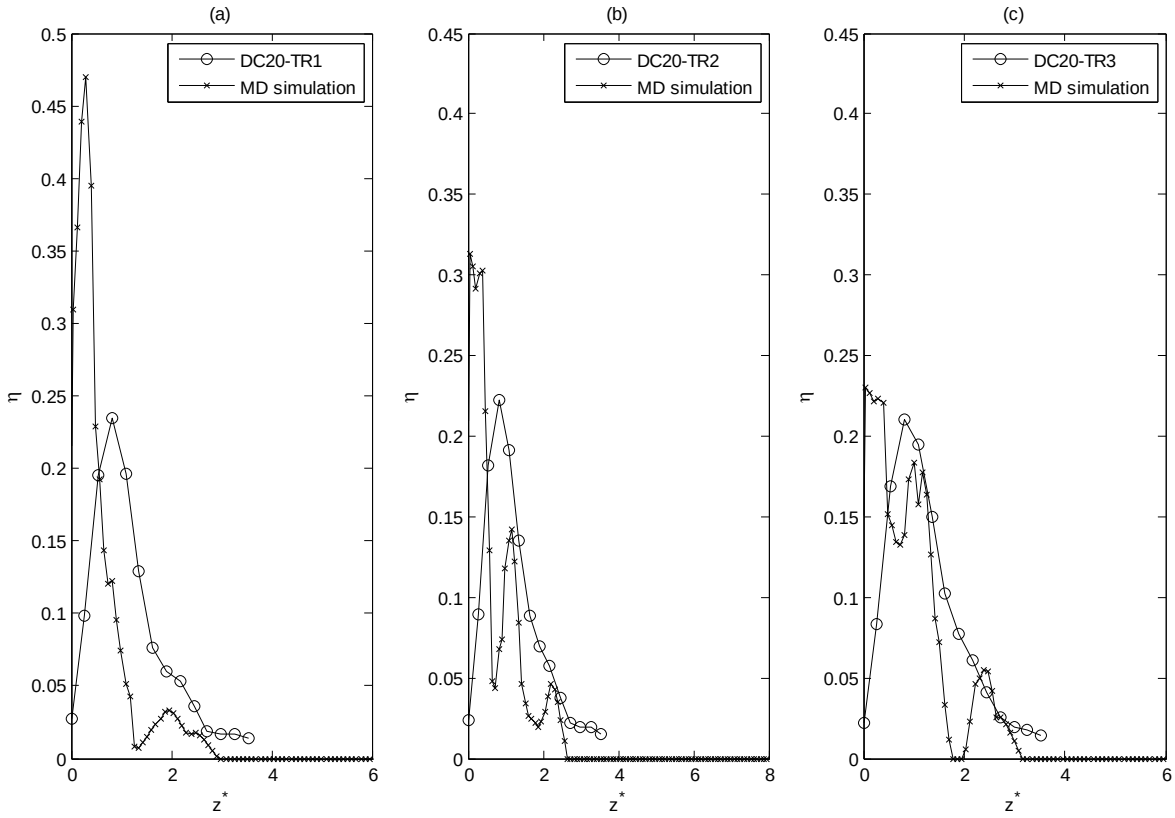

Figure 6-6: Packing fraction profiles as function of non-dimensional vertical height for DC20 at TR1 (a), TR2 (b) and TR3 (c).

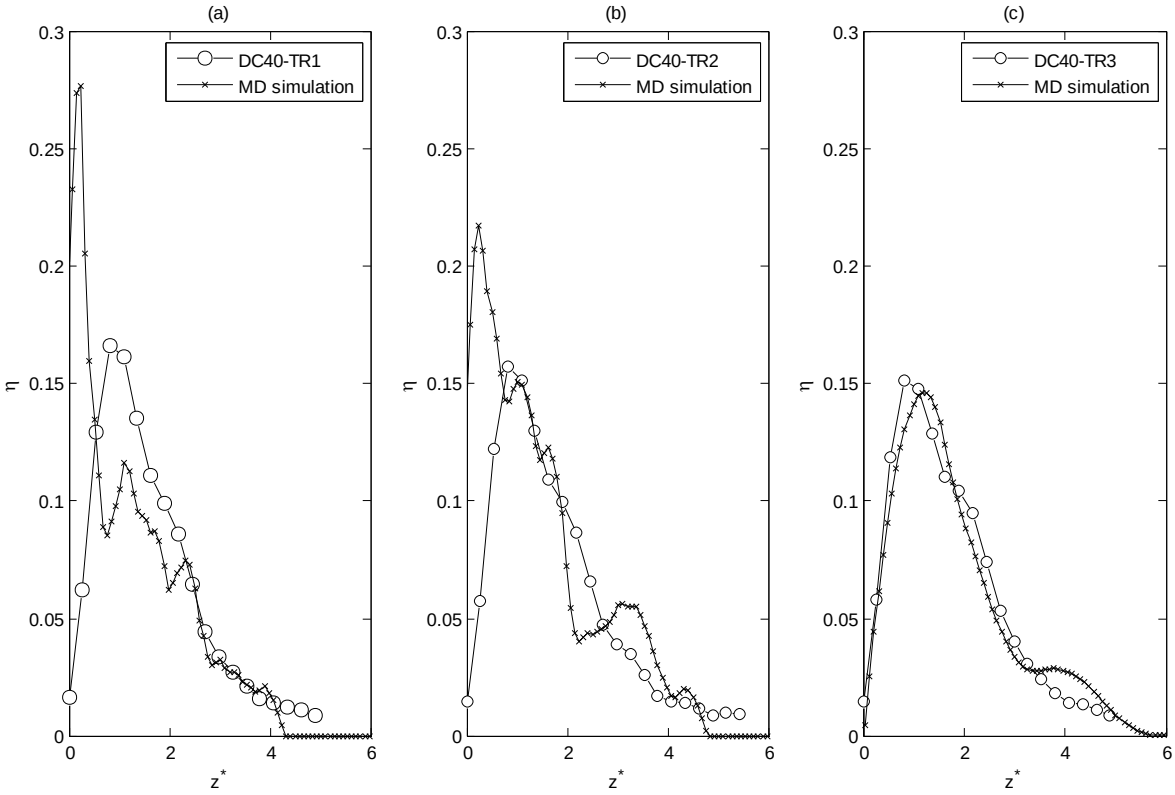

Figure 6-7: Packing fraction profiles as a function of non-dimensional vertical height for DC40 at TR1 (a), TR2 (b) and TR3 (c).

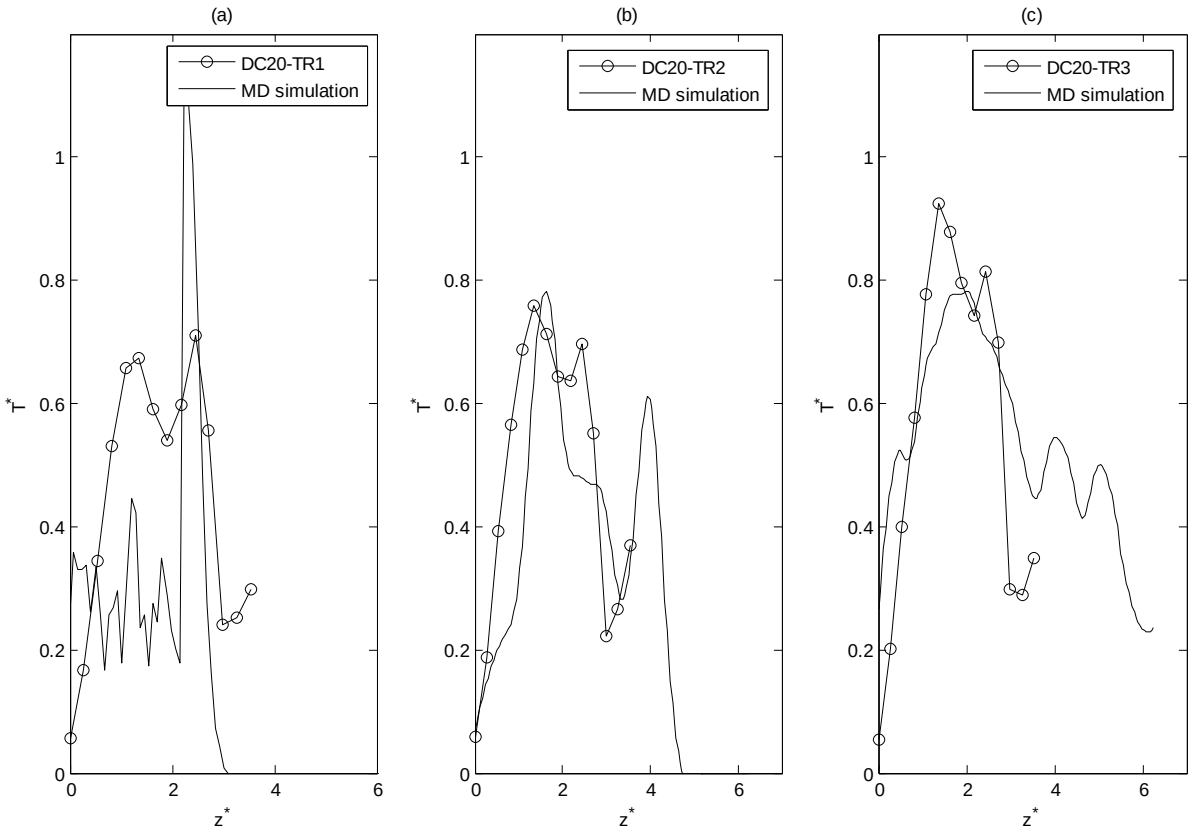

Figure 6-8: Granular temperature profiles as a function of non-dimensional vertical height for DC20 at TR1 (a), TR2 (b) and TR3 (c).

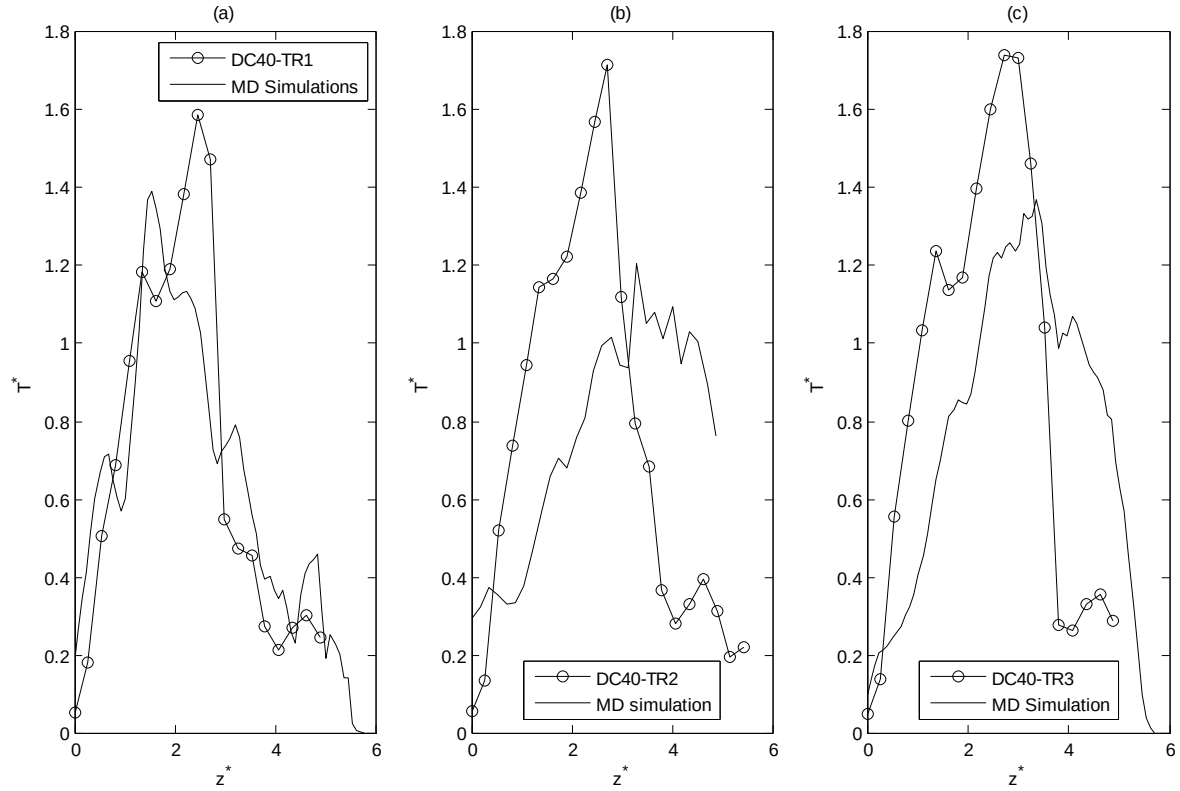

Figure 6-9: Granular temperature profiles as function of non-dimensional vertical height for DC40 at TR1 (a), TR2 (b) and TR3 (c).

With at least qualitative agreement between the experiment and the simulations, we can take advantage of the soft-sphere simulations to investigate the variation of bed dynamics over the course of a complete duty cycle. The total kinetic energy of the bed is shown in Fig. 6.10 with the schematic variation of amplitude of the driving vibration shown at the bottom for reference. For $t < 0$ the granular bed is allowed to achieve steady state at the peak base velocity of 0.115 m s^{-1}. At $t > 0$ one can see clearly that the bed shows considerable variation throughout the modulated cycle with the total kinetic energy somewhat out of phase with the driving amplitude. The energy builds up in the system as the amplitude is increased for 40% of the 20 Hz cycle and then a drop leading to a cooling stage occurs after the amplitude is reduced to half. Similar behaviour continues for the following cycles as shown in Fig. 6.11.

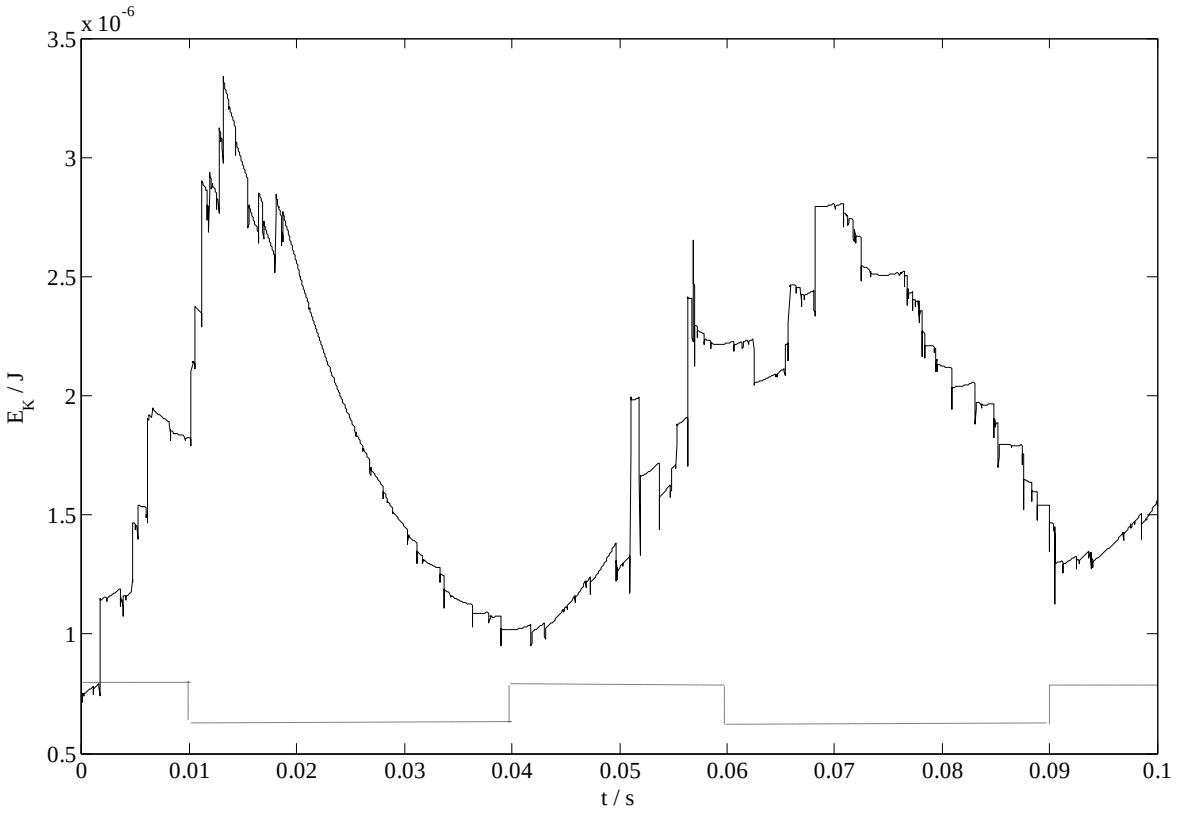

Figure 6-10: Total kinetic energy of the cell, E_k, at the introduction of modulated vibration signal for 20 grains at DC40.

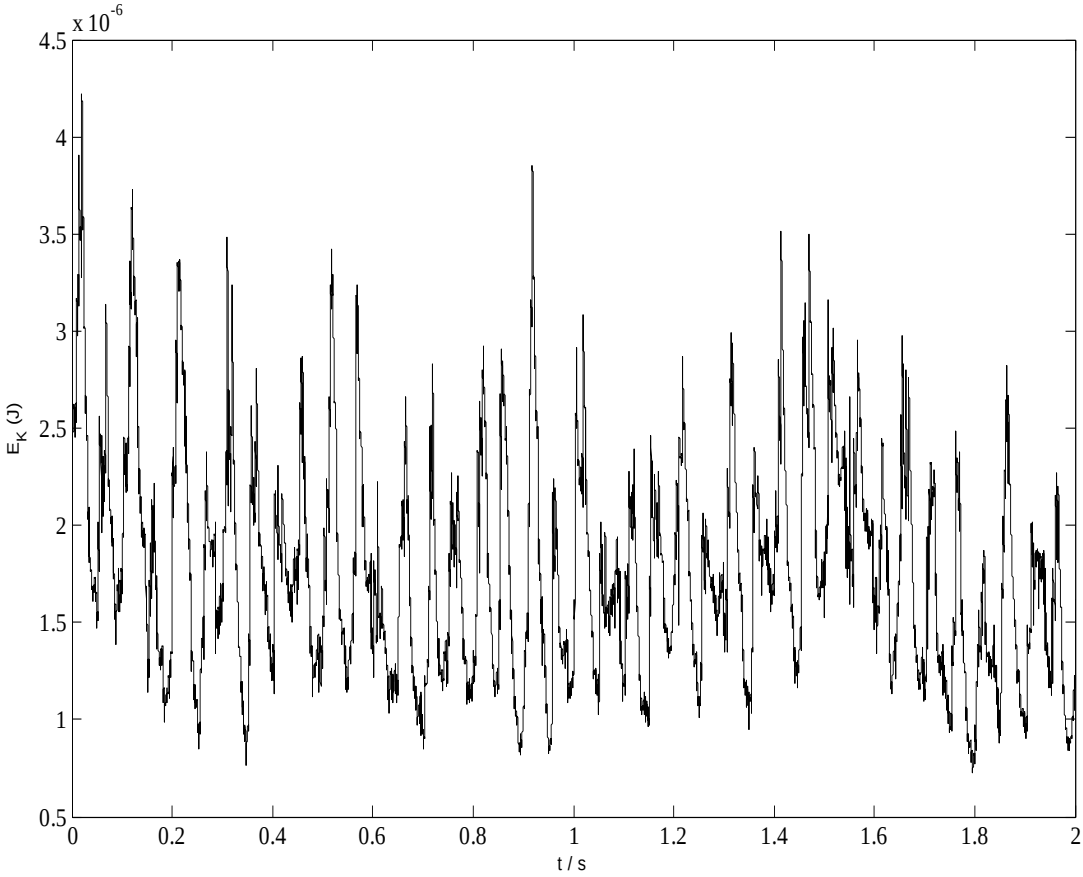

Figure 6-11: Time varying fluctuations observed in total kinetic energy of vibrated bed for 20 grains at DC40.

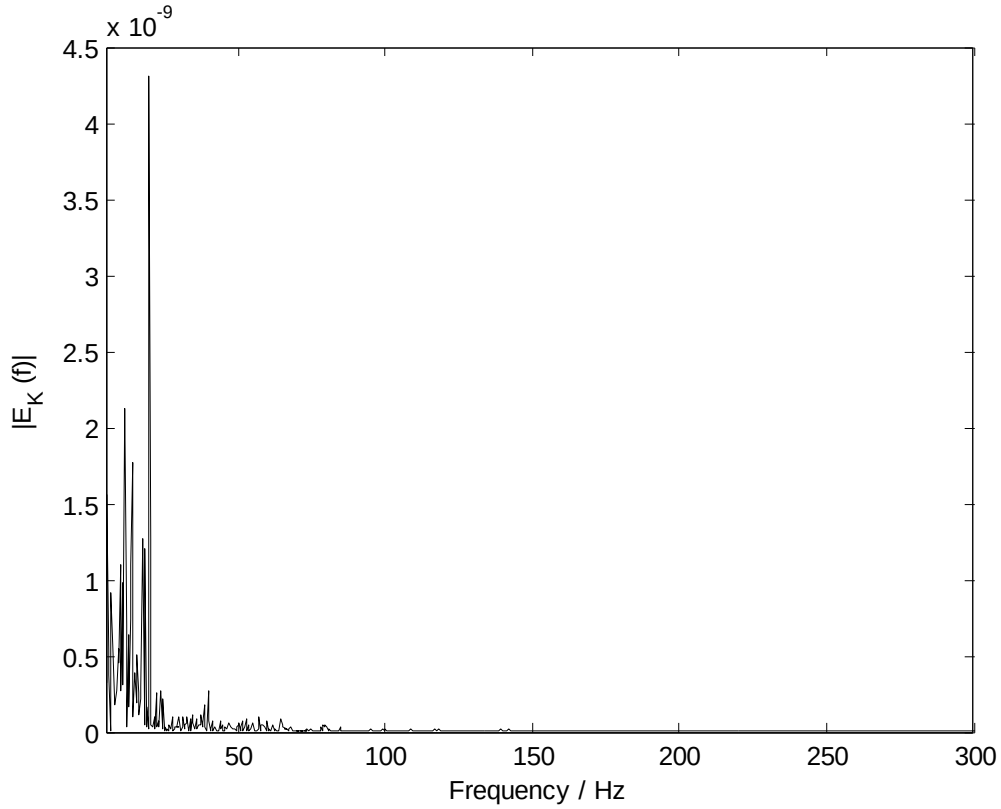

Figure 6-12: Fast Fourier transform of the total kinetic energy of vibrated bed for 20 grains at DC40.

Since it is apparent from Fig. 6.11 that amplitude of the response of the bed varies with time, we performed a fast Fourier transform (FFT) on the data to determine the dominant frequencies. An FFT of a time series of the total kinetic energy of length 2 seconds and sampling interval 10^{-5} seconds was carried out. Figure 6.12 shows the single sided amplitude spectrum of the total kinetic energy. Above 100 Hz, we do not observe any significant features, and restrict the figure to the range 0 to 300 Hz. We observe a distinct peak at 19.67 Hz with additional low frequency peaks near 10 Hz. For DC40 the time duration for high amplitude signal is 0.05 sec (20 Hz) and the FFT spectrum shows a distinct peak in the region associated with this frequency. Interestingly no significant amplitude appeared for the high frequency carrier signal (11.1 kHz) of the base. As noted earlier (see Section 5.6), at this high frequency, the duration of collisions are of the same order as the period of base oscillation, in which case no wave like perturbation in the bulk can be transmitted at this frequency.

i. Effect of frequency

It is apparent that the high frequency component of the base does not influence the granular bed while the influence of the 20 Hz signal is visible in the frequency spectrum. The total kinetic energy of the bed (Fig. 6.11) shows a distinct peak every time it experiences the higher amplitude signal. As the system runs further (Fig. 6.11), slight fluctuations appear in the mean kinetic energy pattern. It is expected that the variations observed with time (cyclic lag) in the Fig. 6.10 may cause slight deviations in granular behaviour from one cycle to another especially if the lag is of the order of the duty cycle.

A reasonable estimate of the time lag for the granular material in the limit of a near elastic dilute granular gas can be modelled by neglecting the energy loss through dissipation. The transient one dimensional heat transfer in the media can be modelled as,

$$\eta \frac{dT}{dt} + \frac{d}{dz}\left(\kappa \frac{dT}{dz}\right) = 0 \qquad \textbf{(6.1)}$$

where κ is the thermal conductivity of gas in the dilute limit (Chapman, Cowling 1991),

$$\kappa = \frac{75}{64\, d^2}\sqrt{\frac{T}{\pi}} \qquad \textbf{(6.2)}$$

Initially the gas is at a constant temperature $T_0$with a dilute packing fraction profile given as,

$$\eta = \eta_0 e^{-zg/T_0} \quad \textbf{(6.3)}$$

At time t_1 the base temperature is raised to T_1, causing the spatial averaged total energy of the system (E_K^*) to increase with time until the elastic gas acquires the uniform temperature T_1. The variation of total energy of the system is shown in Fig. 6.13 (a) where the energy rise follows a trend of the form of Ae^{-bt} where $1/b$ is the time constant or lag time. An estimate of $1/b$ for a 70% increase in total energy at a unit temperature rise is 0.015 s for the case of a typical DC40 cycle.

Table 6.1 shows the phase angles, computed from the Fourier coefficient at the dominating frequencies appearing in Fig. 6.12, indicating a phase lag of 2.55 *rad* at 20 Hz with respect to the phase of the driving signal. The phase lag is equivalent to 0.0219 s lag time for the case of DC40. It can also be noticed that the actual time lag for DC40 is slightly higher than the duty cycle of the excitation wave suggesting the possibility of the bed expansion even after the heat flux at the bed is varied. However the model for the estimation of lag time is a reasonable approximation given the highly inelastic nature of the granular flow.

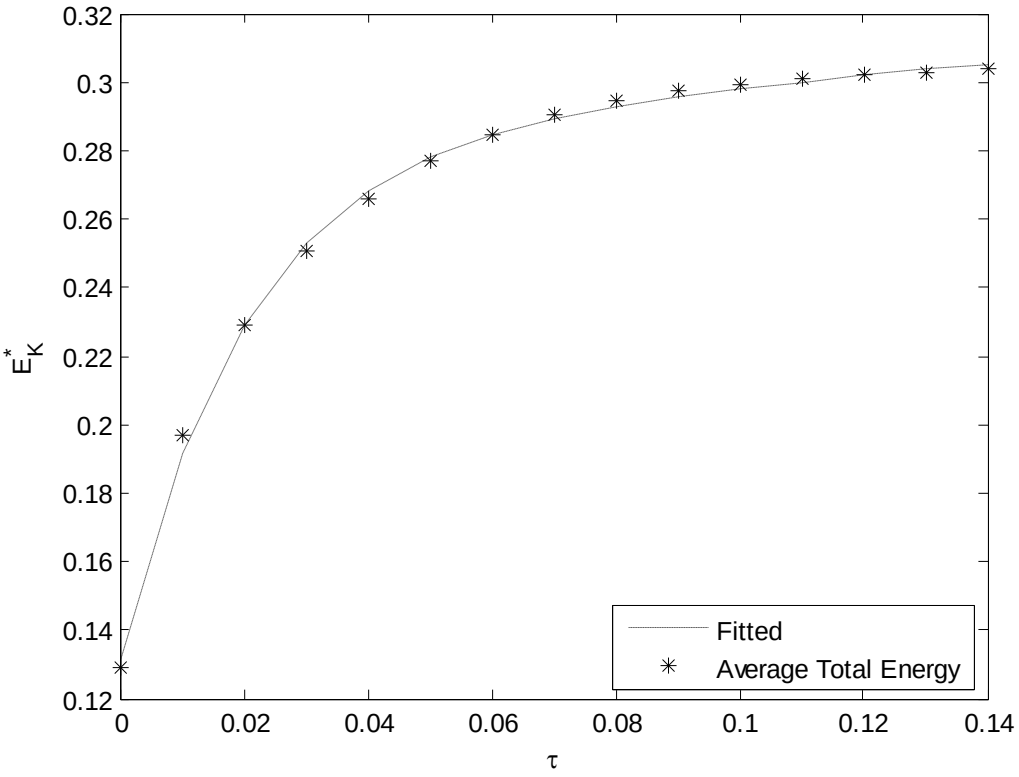

Figure 6-13: Theoretical energy increase in granular cell for a unit increase in temperature.

One may also anticipate low frequency effects such as wave propagation (see Chapter 4) to appear in the bed physics as the granular gas responds to the amplitude of the base. The generation of fluctuation pulse due to amplitude variation is seen at 20 Hz (see Fig. 6.11). The square wave modulation in particular carries a sudden change of amplitude due to the prescribed duty cycle. The sudden change might only act as a trigger for the kinetic energy fluctuation however the considered system is significantly dilute and difficult to track the localized variations. Therefore in the next section we study by MD simulations a relatively dense system excited by a traceable smooth amplitude transition at moderate base driving velocities. This enables us to track the localized hydrodynamic variations over the course of the low frequency cycle.

b. Sinusoidal wave modulation

The second form of amplitude modulation as introduced in Section 6.2 was modelled using soft sphere MD simulations. A total of 60 grains was used to obtain more than a single layer of grains at rest, and at an appropriate driving velocity this enables us to compare the predictions with the hydrodynamic models. Here results are presented for the total kinetic energy in the granular cell vibrated with a sinusoidal modulated signal. The fluctuations in the kinetic energy with time are seen in Fig. 6.14. In order to highlight the base phase the profile of the base amplitude is also shown in Fig. 6.14. It can be noticed that MD simulations show a slight lag similar to one observed in square wave modulation. This is particularly visible during the second wave shown in Fig. 6.14; MD simulations show a peak in total energy at a point where the base amplitude is significantly low in this region.

If the long time behaviour of the kinetic energy is observed for MD simulations fluctuations and variations (see Fig. 6.15) reminiscent of those observed in Fig. 6.11 are seen. For comparison, a FFT of a trace of 2 seconds, 10^{-5} seconds interval was performed. The FFT of the energy fluctuations (Fig. 6.16) show peaks similar to those observed for the square wave modulation. Energy fluctuation for smooth transition signal shows signature of the forcing frequency in the form of a peak at 40 Hz.

Table 6-1: Phase angles of the vibrated bed at the dominating frequencies for 20 grains for DC40

Frequency / Hz	Phase angle / rad
10.3	-1.715
20.1	2.55
40.05	1.627

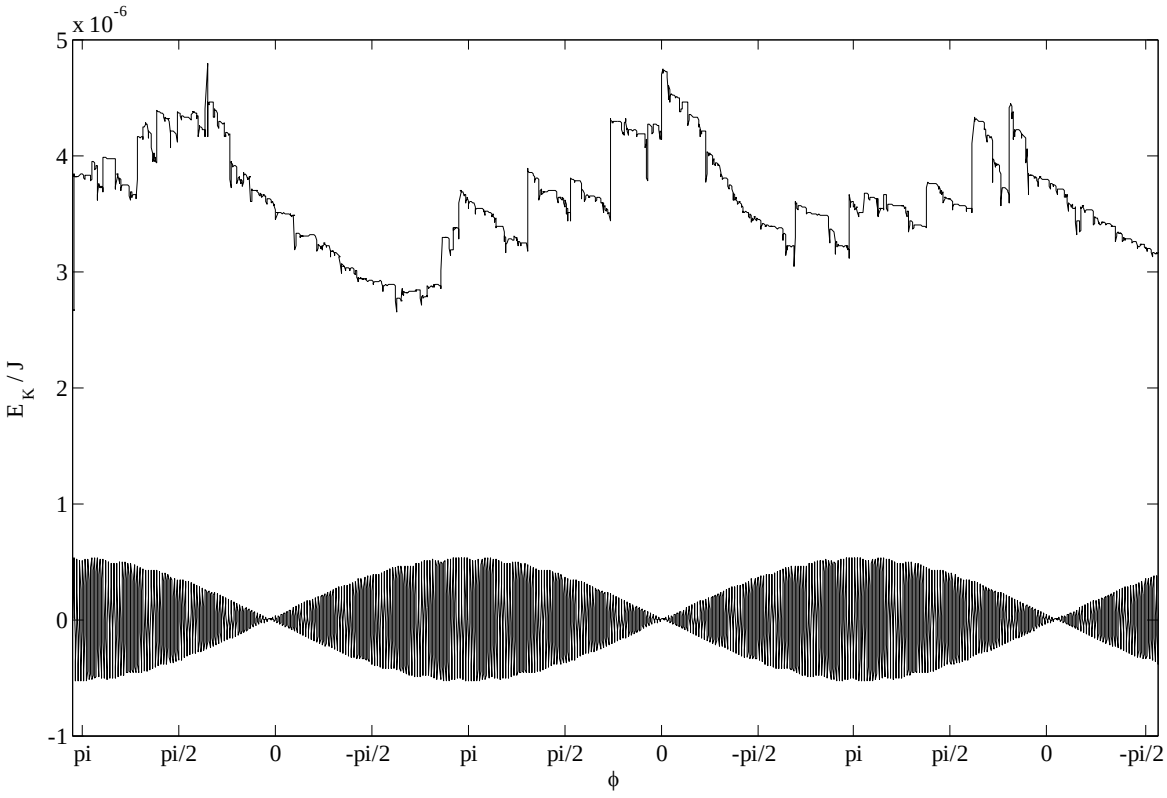

Figure 6-14: Cyclic variation of total heat flux fluctuations for MD simulations.

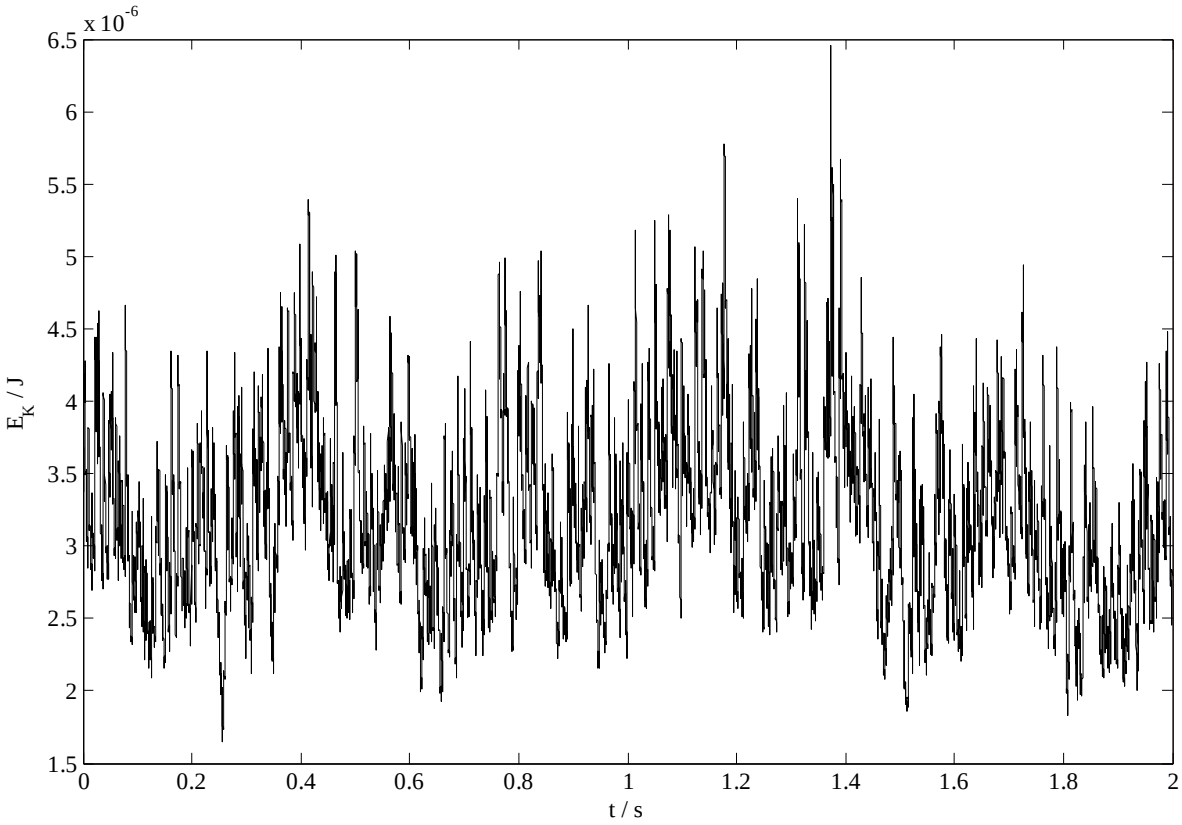

Figure 6-15: Total heat flux fluctuations with time for sinusoidal wave form using MD simulations for 60 grains.

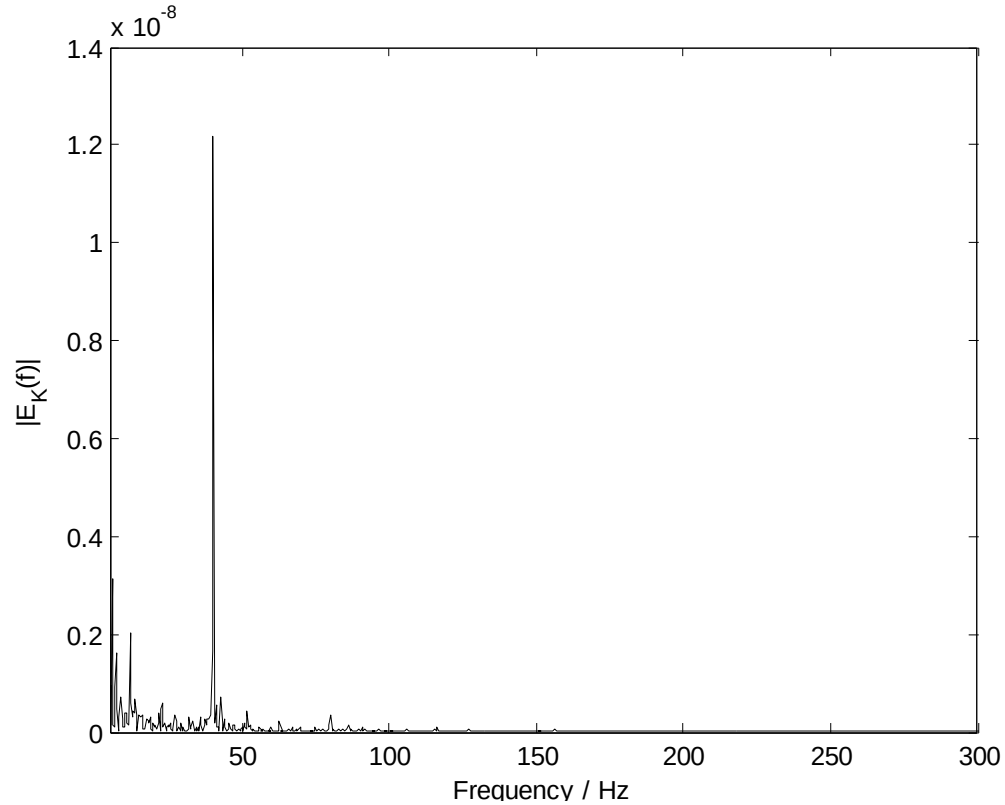

Figure 6-16: FFT of the total kinetic energy of the bed for 60 grains with sinusoidal modulation.

The pattern of Fig. 6.14 shows a trend similar to the one seen in Fig. 6.10 for the square wave modulation. The total energy increases from its minimum to maximum value reaching its peak value with a lag compared to the duty cycle and then follows with a decreasing smooth profile. Interestingly, in Fig. 6.14 we see that after the total energy has reached a maximum and it decays towards the minimum, the higher frequency oscillations are diminished until the energy increases once more.

i. Bulk behavior

To analyze the behaviour of bulk in correspondence with the low frequency cycle, Fig. 6.17 (c) shows the plots of granular temperature in vertical direction, T_z^*, at 8 equally spaced phase locations of the cycle using MD simulations. The broken horizontal lines indicate the local reference for each phase location starting from the top. Plots of without modulation low frequency (at 40 Hz) and high frequency (at 11.1k Hz) excitations are also shown in Fig. 6.17 (a) and (b) respectively at the same rms base velocity of $V_b^* = 1.71$ with 60 grains. The low frequency excitation (without modulation), Fig. 6.17 (a), shows a strong wave propagation in the bulk while the high frequency excitation indicates no notable fluctuation over the course of the base phase (Fig. 6.17 (b)). The modulated sinusoidal signal (Fig. 6.17 (c)) shows fluctuation of granular temperature on a pattern similar to Fig. 6.17 (a) but with significantly lower amplitude.

A reduction in the heat flux at the high frequencies of excitation is shown in Fig. 5.16 due to lack of separation of time scales between base motion and grain-base contact duration (see Section 5.6 for details). Since the carrier signal in the modulated wave is at a high frequency (11.1k Hz) this results in a overall reduction of heat flux. However the steadiness in the bed physics seen at high frequency (Fig. 6.17(b)) is disturbed due to the low frequency amplitude modulation cycle as seen in the fluctuation of granular temperature (see Fig. 6.17 (c)).

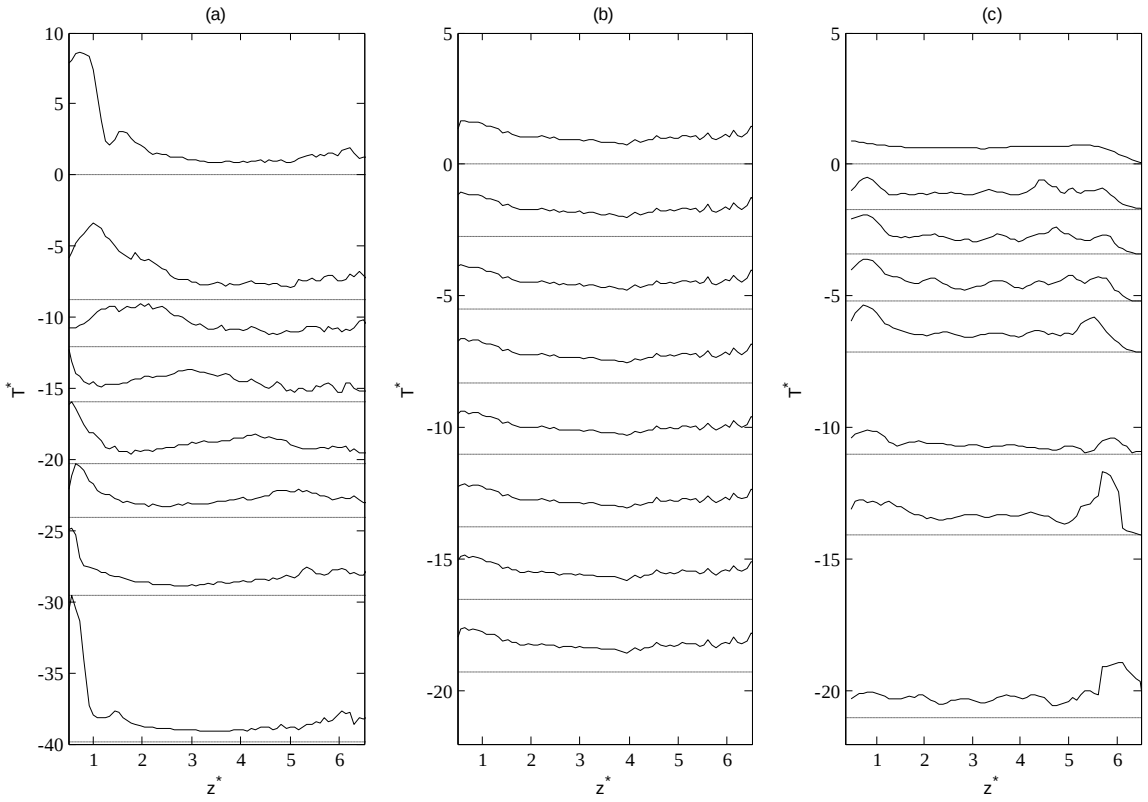

Figure 6-17: Phase resolved granular temperature as a function of height for (a) 40Hz excitation; (b) 11.1k Hz excitation; (c) modulated sinusoidal wave with broken lines show the local reference.

In the next step the rms heat flux at the base for modulated sinusoidal wave is increased to match the rms heat flux transmitted at low frequency vibration at 40 Hz. This enables us to compare the results with the hard sphere based time dependent hydrodynamic models (ATD-Garzo and ATD-Jenkins). By tuning the amplitude of vibration to 1.45 times V_b^*, the resultant phase resolved vertical granular temperature is shown in Fig. 6.18 (c) along with ATD-Garzo results Fig. 6.18 (a) and ATD-Jenkins Fig. 6.18 (b). The sinusoidal modulation force is introduced in to momentum balance (Eq. 3.1) using the method described in Section 4.2 enabling the base boundary to be modelled as non-moving. Both ATD-Garzo and ATD-Jenkins indicate the generation and movement of similar wave motion as seen in Fig. 6.18 (c). MD simulations show qualitatively similar trends in the bulk as seen in ATD-Garzo and ATD-Jenkins. ATD-Garzo (Fig. 6.18(a)) predicts a considerably higher temperature upturn at all phase locations for z* > 4.0 compared to Fig. 6.18 (c). A detailed discussion on the cause of larger upturn for ATD-Garzo can be found in Sections 3.6 and 4.4. Figure 6.17 (a) and 6.18 (c) are reproduced in Figure 6.19 for a direct comparison. Interestingly the behaviour shown in Fig. 6.19 (a) is qualitatively similar to Fig. 6.19 (b) in the sense that the generation of wave-like effect is seen with the low frequency component of the modulated signal. We anticipate some differences in the

granular temperature especially near the base (z* < 2) due to different patterns and nature of the waves. However the bulk behaviour (Fig. 6.19 (b)) shows the propagation of pulse over the course of the cycle similar to the one seen in Fig. 6.19 (a).

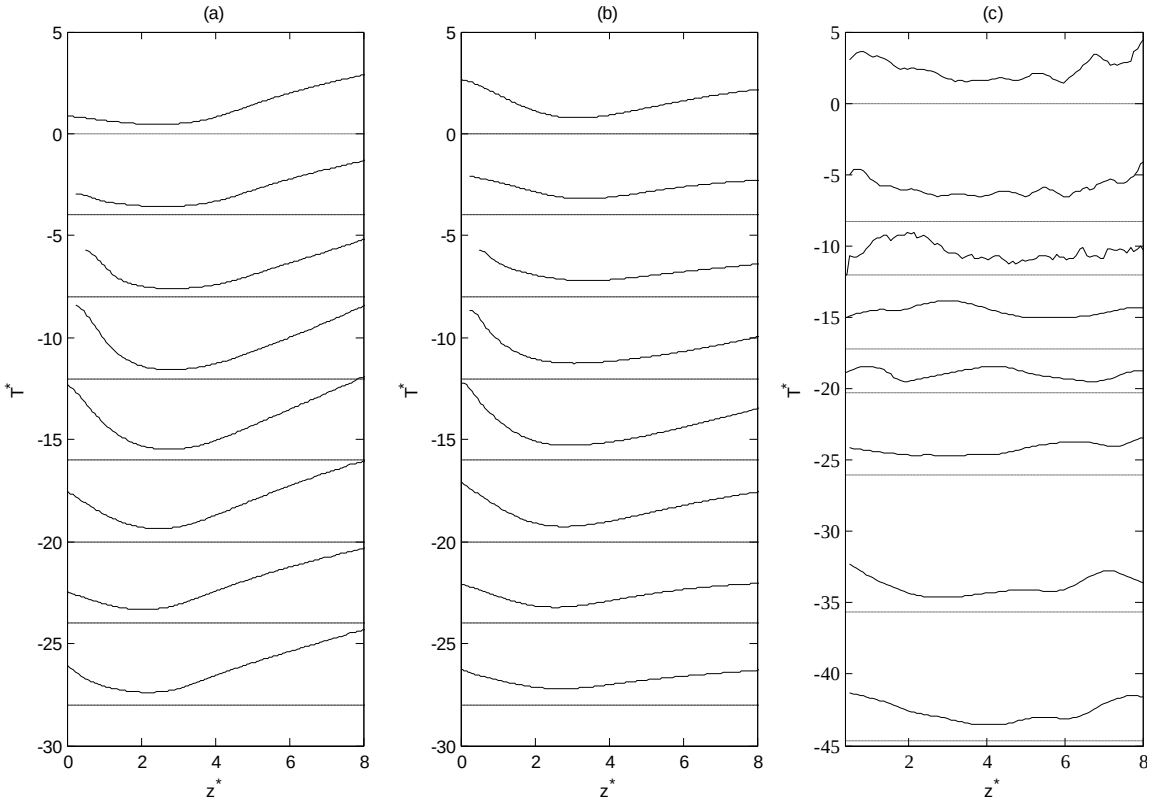

Figure 6-18: Phase resolved granular temperature as a function of height for (a) ATD-Garzo; (b) ATD-Jenkins; (c) modulated sinusoidal wave at 1.45 times V_b^*.

It can be concluded that the effect of low frequency amplitude variations in the high frequency signal results in temporal variations in the bed physics in an otherwise steady granular bed. The effect of the high frequency carrier is to reduce the amplitudes of fluctuations in the granular temperature due to the limited heat flux yet the effect of low frequency amplitude variation appears on a cyclic basis. Upon fixing the heat flux the phase resolved behaviour indicates relatively stronger wave motion in the granular bed and comparison with the time dependent models show reasonable agreement. This indicates that the low frequency vibration leads to generate time varying behaviour of granular gas in a vertically vibrated bed.

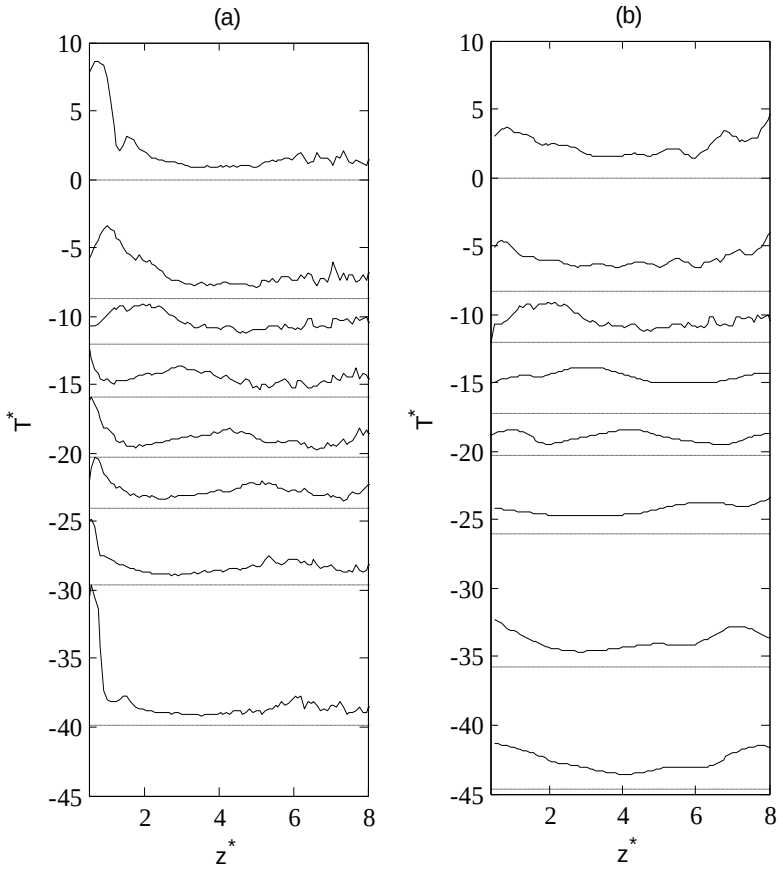

Figure 6-19: Phase resolved granular temperature as a function of height for (a) 40Hz excitation; (b) modulated sinusoidal wave at 1.45 times V_b^*.

6.6. Summary

This chapter is focused on the combined effects of low and high frequency vibrations in a single bed. Although the signal is primarily at high frequency, the bed shows the effect of the low frequency modulating signal. In MD simulations the bed dynamics fluctuate due to the amplitude modulation in a cyclic fashion and generate wave-like patterns in the bed over the course of each cycle. However the strength of the wave is reduced due to the limited heat flux at the base. By tuning the heat flux at the base the results show wave propagation in a fashion similar to the non-modulated low-frequency case. Time-dependent hydrodynamic models show a reasonable qualitative comparison to MD simulations results in the phase-resolved behaviour of the granular bed. It is expected that with the different types of modulation schemes, duty cycles, amplitude ratios and wave forms, further patterns in the bed will be observable.

Chapter 7 Scaling in granular flows

7.1. Introduction

In previous chapters we have shown hydrodynamic predictions for temporal and spatial variations of granular flows under different operating conditions and compared them with experimental results and MD simulations. Tests of two sets of constitutive relationships showed reasonable agreement, though with some deviations between the two descriptions. The hydrodynamic solutions generally capture key scaling relations that demonstrate the broad trends of behaviour that granular flows follow. Identification of important parameters and their scaling will not only help us in our understanding of flow physics but will also direct our modelling approaches. In granular flows some of the scalings can be obtained relatively simply through dimensional analysis (Turner, Woodcock 1990, Sunthar, Kumaran 1999), but those do not usually reflect higher order effects that might be present, and are unable to reveal any temporal or spatial correlations in the system.

In this chapter we try to identify and test the scaling parameters that govern the behaviour of granular flow in a simplified system. We consider a case of a time independent vibrated bed with smooth nearly elastic hard spheres, shaken vertically in the presence of gravity. By neglecting the viscous effects the system is completely described with three constitutive relationships for thermal conductivity, dissipation and pressure. A key test will be made of recently proposed scaling relationships (Kumaran, Wildman et al. unpublished), which in the asymptotic limits predict the scaling of state variables in a vibrated system. This simplified configuration of constitutive relationships reveals important correlations but still needs testing and validation.

In this chapter we introduce the newly identified form of constitutive relationships along with the form of non-dimensionalisation. This is followed by validation of the model solved using finite element methods against the predictions of hard sphere MD simulations. Later the predicted correlations are tested using MD simulations in the limits identified by the non-dimensional parameters followed by discussion and conclusions.

7.2. Steady state model

The steady state configuration for one dimension, incompressible and inviscid system of granular particles in a vibrated bed in presence of gravity reduces to balances of momentum and energy,

$$\frac{dp}{dz} + \rho g = 0 \quad \textbf{(7.1)}$$

$$\frac{d}{dz}\left(\kappa \frac{dT}{dz}\right) - Q = 0 \quad \textbf{(7.2)}$$

where p, κ and Q can be expressed as constitutive relations for pressure, thermal conductivity and dissipation in a rescaled form. The idea is to recast the relationships for identical smooth spherical particles of unit mass in a form where they are functions of granular temperature and packing fraction ($\eta = \pi d^3 \rho / 6m$) only. The first step is to divide Eq. 7.1 and 7.2 by the particle mass *m*. Next we introduce the following re-scaled variables $p' = \frac{p}{m}, \rho' = \frac{\rho}{m}, \eta = \frac{\pi d^3 \rho'}{6}$, $\kappa' = \frac{\kappa}{m}$ and $\gamma = \frac{Q}{m}$. For scale of notational convenience we now drop the primes and write $p = p', \rho = \rho'$, and $\kappa = \kappa'$. This yields

$$\frac{dp}{dz} + \eta g = 0 \quad \textbf{(7.3)}$$

$$\frac{d}{dz}\left(\kappa \frac{dT}{dz}\right) - \gamma = 0 \quad \textbf{(7.4)}$$

The relationships for pressure, thermal conductivity and dissipation are given below,

$$p = p_c T \quad \textbf{(7.5 a)}$$

$$\kappa = \kappa_c \left({}^{T^{1/2}}/_{d^2} \right) \quad \textbf{(7.5 b)}$$

$$\gamma = \gamma_c \left({}^{(1-e^2)\, T^{3/2}}/_{d^4} \right) \quad \textbf{(7.5 c)}$$

where p_c, κ_c and γ_c are functions of packing fraction, η, granular temperature *T* and pair distribution function, χ in non-dimensional form. For low to moderately dense system, the relationships for p_c, κ_c and γ_c as given below

$$p_c = \frac{\eta(1+4\eta\chi)}{\left(\pi d^3/6\right)} \quad \textbf{(7.6)}$$

$$\kappa_c = \frac{75}{64\sqrt{\pi}\chi}\left(1 + \frac{12\eta\chi}{5}\right)^2 + \frac{72\eta^2\chi}{\pi^{3/2}} \quad \textbf{(7.7)}$$

$$\gamma_c = \frac{72}{\pi^{3/2}} \eta^2 \chi \qquad \textbf{(7.8)}$$

with $\chi = \frac{2-\eta}{2\,(1-\eta)^3}$.

In the dilute limit, the effect of the pair distribution function is reduced and p_c, κ_c and γ_c are reduced to simple relationships. For further analysis in this chapter all the following relationships are scaled using the mass of particle and not shown for particles with unit mass.

7.3. Definition of non-dimensional parameters

a. Identification of length scales

Apart from the particle diameter, other characteristic length scales can be identified in granular flows (Kumaran, Wildman et al. unpublished). In the limit of nearly elastic particles the dissipation term γ is negligible. In such a case by solving Eq. 7.1 and 7.2, the leading order density in terms of number density per unit area *N* is given by

$$\rho = \frac{Ng}{T} e^{-\frac{gz}{T}}. \qquad \textbf{(7.9)}$$

This shows that by assuming *T* as constant the density decreases with a length scale of T/g. Figure 7.1 shows the decreasing profile of density in the limit of an elastic gas.

The other length scale associated with the granular temperature can be obtained by comparing the conduction and dissipation terms in the heat balance (see Eq. 7.2) (Kumaran 2000a). Conduction rate is proportional to $T^{3/2}/d^2 z_L^2$ where z_L is the length at which the temperature varies, while the energy dissipation rate is proportional to $\rho^2 d^2 T^{3/2}(1-e^2)$. A balance between the two is achieved when $z_L = 1/\left(\rho d^2 \sqrt{1-e^2}\right)$.

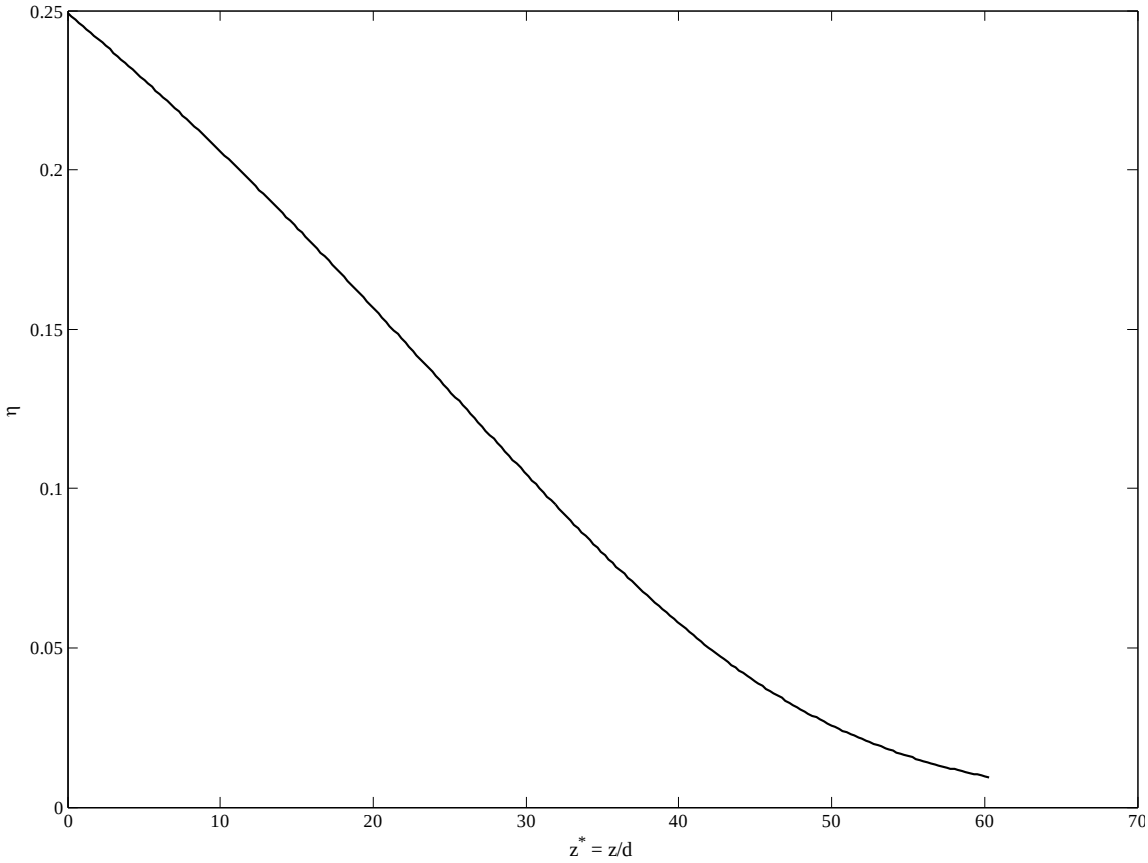

Figure 7-1: Packing fraction profile for an elastic gas at constant temperature.

b. Non-dimensional parameters

The length scales identified in previous section can be used to scale the state variables. The length scale associated with z_L is $d/\sqrt{1-e^2}$ and it is appropriate to define the non-dimensional height as

$$z^* = z/d/\sqrt{1-e^2} \quad \textbf{(7.10)}$$

and the non-dimensional temperature is scaled as

$$T^* = T/\left(\frac{gd}{\sqrt{1-e^2}}\right) \quad \textbf{(7.11)}$$

7.4. Comparison of length scales

A comparison of the two length scales defined in section 7.3 leads to three scenarios. First when the $\frac{T}{g} \ll \frac{1}{\rho d^2\sqrt{1-e^2}}$, second when $\frac{T}{g} \gg \frac{1}{\rho d^2\sqrt{1-e^2}}$ and in between the two extremes when $\frac{T}{g} \approx \frac{1}{\rho d^2\sqrt{1-e^2}}$. Detail on these cases are discussed below.

In the regime where the length scale associated with the decay of the density profile is much shorter than the length scale associated with z_L, then the inequality $\frac{T}{g} \ll \frac{1}{\rho d^2\sqrt{1-e^2}}$ is true. The density decreases quickly owing to a larger rate of conduction compared to dissipation rate. If the temperature at the base of the vibrated bed is at T_0, then the mass balance condition requires the density at the base to be $\rho = \frac{Ng}{T_0}$. Inserting the value of base density and temperature, T_0, leads to the condition where $N^* = Nd^2\sqrt{1-e^2} \ll 1$. For such a situation to occur either the base velocity has to be sufficiently high or the granular gas is near to an elastic gas.

In the second regime of the conduction length scale being much smaller than the ballistic length $\frac{T}{g}$ thus $\frac{T}{g} \gg \frac{1}{\rho d^2\sqrt{1-e^2}}$. For such case it can be shown that $N^* = Nd^2\sqrt{1-e^2} \gg 1$. In this regime the granular material has large packing fraction and this situation exists at low driving velocities and/or high bulk dissipation. An analytical solution cannot be obtained in the limit of high dissipation with large near base density due to the non-linear pair distribution function. The third scenario exists between the two limits when the conduction length is of the order of ballistic length. In both regimes different combinations of variations of N^* are possible depending upon the intensity of the base driving. Base driving can be non-dimensionlised as a Froude number, where $Fr = \frac{\langle V^2 \rangle}{gd}$.

By using these non-dimensional parameters, $N^*$and Fr, through an asymptotic analysis it is proposed that in the above mentioned limits characteristic scaling relationships exist between the state variables (Kumaran, Wildman et al. unpublished). A number of the predictions for the scaling relationship are given in table 7.1 and the following sections we will test them through solving the hydrodynamic equation set and through molecular dynamics simulations.

Table 7-1: Scaling relationships for state variables under different limits.

State variable	N^*<<1	N^*>>1
T_0^*	$\frac{Fr^2}{(1-e^2)N^*}$	Fr
$\frac{T_0^*}{T_\infty^*}$	1	N^*
η_0		N^*/Fr
η_{max}		N^*/Fr
$T^{*'}$	N^{*2}	N^*
z_{max}^*		Fr/N^*

7.5. Non-dimensional form of hydrodynamic model and boundary conditions

Using the non-dimensionalisation of Eq. 7.10 and 7.11 the hydrodynamic model described in the set of Eq. 7.1 and 7.2 can be recast into dimensionless form such that

$$\frac{dp_c T^*}{dz^*} + \eta = 0 \qquad \textbf{(7.12)}$$

$$\frac{d}{dz*}\left(\kappa_c \sqrt{T^*}\frac{dT^*}{dz^*}\right) - \gamma_c {T^*}^{3/2} = 0 \qquad \textbf{(7.13)}$$

The equation set (Eq. 7.12 and 7.13) requires three conditions to generate the solution. The first one is that the number of particles in the bed is fixed and secondly that the heat flux condition at the vibrating base is specified and finally, there is zero heat flux at $z^* = \infty$. The mass conservation for such a system is specified by

$$\int_0^\infty \eta \, dz^* = N^* \frac{\pi}{6} \qquad \textbf{(7.14)}$$

where N^* is given in section 7.4 with N is the number of particles per unit area. Using heat flux relationship developed by Richman (Richman 1993), the temperature gradient for elastic base is given by

$$\frac{dT^*}{dz^*} = \frac{C_\phi \eta_o}{\kappa_c} Fr \qquad \textbf{(7.15)}$$

where η_0 is the base packing fraction and C_ϕ is a constant in the limit of a dilute bed. The value of C_ϕ scales the heat flux at the base and a detailed estimation of the form of C_ϕ in a

moderately dense bed is required. In the following sections we will determine the form of C_ϕ from numerical simulation.

7.6. Numerical simulation

a. Hydrodynamic simulations

The hydrodynamic model of Eq. 7.12 and 7.13 is solved along with the boundary conditions given by Eqs. 7.14 and 7.15 using the multiphysics solver COMSOL. Using COMSOL user defined PDE modules and its boundary sets, the problem is solved for different loading conditions and driving velocities through the finite element method. The PDE module of COMSOL allows introduction of differential equations in generalized form on a specified domain. The boundary conditions can be specified on each side/end of the domain.

Here we used a one dimensional domain with a unit thickness. Equation 7.12 and 7.13 form two sets of PDE modules utilizing constitutive relationships defined as scalar variables. The pressure equation is introduced using an additional PDE module. The heat flux at the top boundary of the domain is specified as zero. The heat flux at the base is specified by Eq. 7.15 while the coefficient C_ϕ is estimated from MD simulations. The steady-state solution is obtained using non-linear GMRES solver to a drop tolerance of 10^{-6}. Further details on solution technique and COMSOL can be seen in Chapter 3 and COMSOL theory manual (COMSOL 2007).

a. MD simulations

Hard sphere MD simulations were also performed to validate the findings of hydrodynamic simulations and to determine C_ϕ. These simulations used the model described in Chapter 2, using elastic side walls with no upper surface. In order to study the scaling behaviour only as the function of hydrodynamic variables particles of unit diameter having unit mass under influence of unit gravity for MD simulations. The base-particle coefficient of restitution was kept at unity to minimize any effects due to the inelasticity of the base. The motion of the base made it difficult to correctly obtain value of packing fraction and temperature at the base, and thus, the values of temperature and packing fraction at the base are estimated through an extrapolation of the data on the first three grid points adjacent to the base. The first grid point next to the base was placed at half particle

diameter. The distance between the grid points was varied from half a particle diameter to a maximum of one particle diameter.

The initial configuration of the cell uses a random distribution of grains in the simulation cell, which is then run for a total of 10^6 number of collisions. Evaluation of granular temperature and packing fraction is obtained through ensemble averaging over 10^6collisions. Complete detail on the working of MD simulations, collision dynamics and data collection can be found in Chapter 2 and 3.

7.7. Results and discussion

a. Validation at varying N^* and Froude number

In order to validate the new form of hydrodynamic model (Eq. 7.12 and 7.13) we compare the results with hard sphere MD simulations. Results are compared for a range of *Fr* and *N**. The range for *N** is varied from 0.3 to 10 and *Fr* is varied from 0.25 to a maximum of 361. In this section we present results for *N** = 0.3, 1.0, 2.0 and 3.0 at different *Fr* to demonstrate the comparison in a dilute to moderately dense granular bed. The systematic variations of *Fr* with *N** and the bed scaling behaviour is presented forthcoming sections. Figures 7.2 and 7.3 show the variations of granular temperatures and packing fractions as the function of scaled heights for *N** = 0.3 at *Fr* = 0.25. Good agreement can be seen amongst the predictions of MD simulations and hydrodynamic model in most part of the cell. With increase of *N** to 1.0 (fig. 7.4 and 7.5) the agreement amongst the two is still reasonable but differences appear near base and towards the peak packing fraction region. The discrepancies becomes much clearer at higher values of N* = 2.0 and 3.0 (see fig. 7.6-7.9) with the maximum error near the peak packing fraction region rises to 25% for *N** = 3.0 at *Fr* = 36.0.

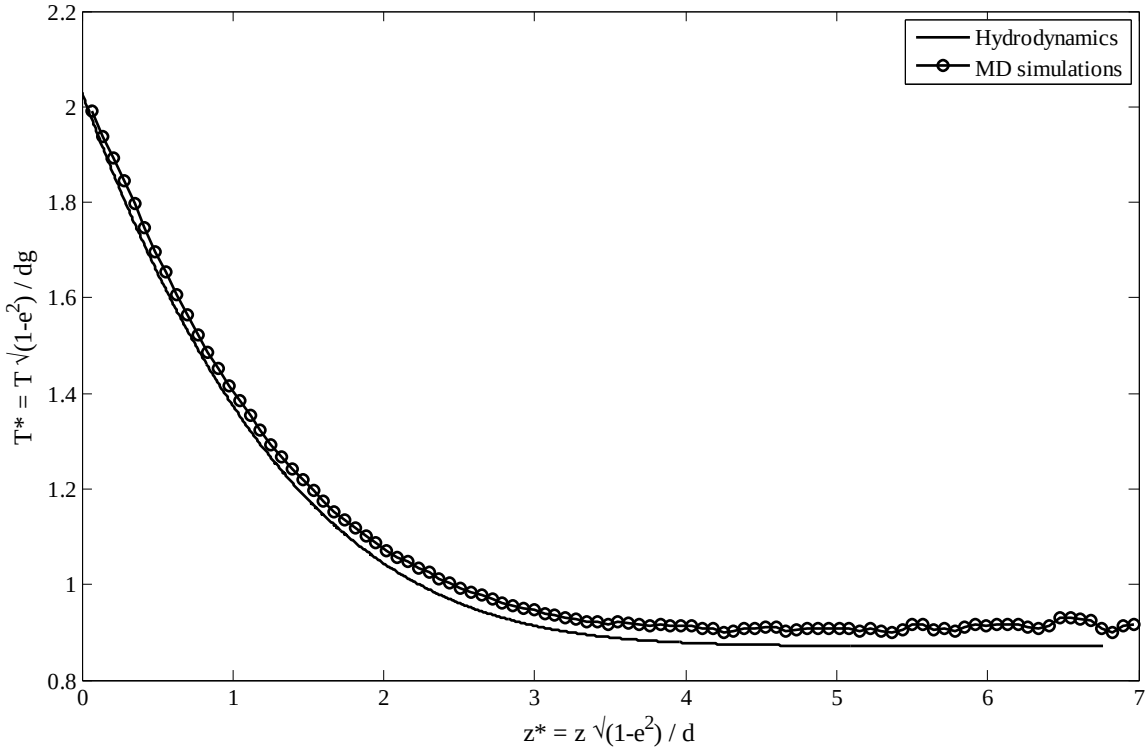

Figure 7-2: Scaled granular temperature as the function of scaled height for $N^* = 0.3$ at $\mathbf{Fr} = 0.25$.

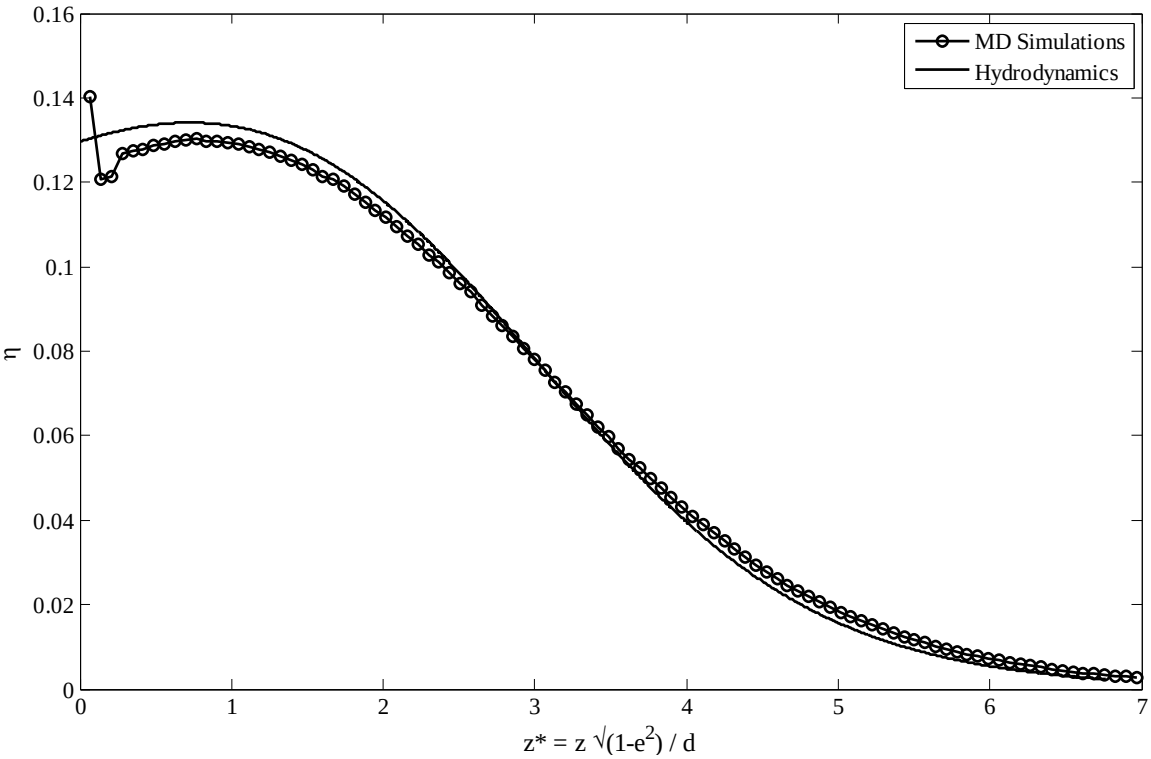

Figure 7-3: Packing fraction as the function of scaled height for $N^* = 0.3$ at $\mathbf{Fr} = 0.25$.

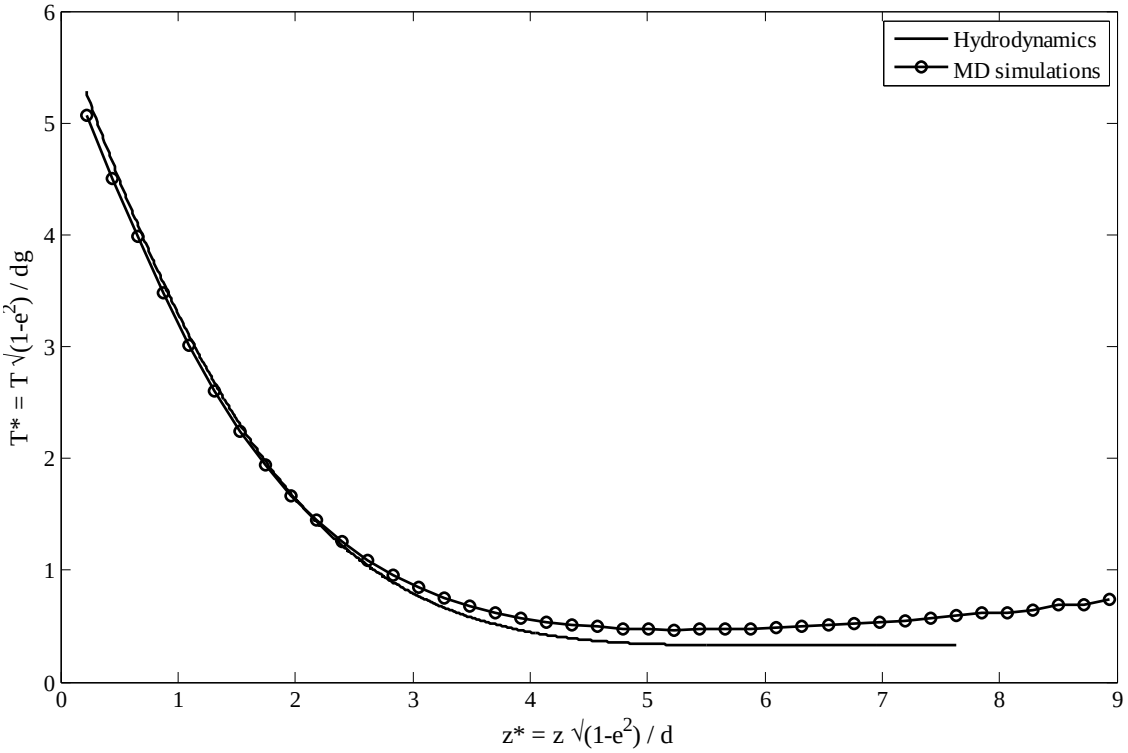

Figure 7-4: Scaled granular temperature as the function of scaled height for $N^* = 1.0$ at Fr $= 4.0$.

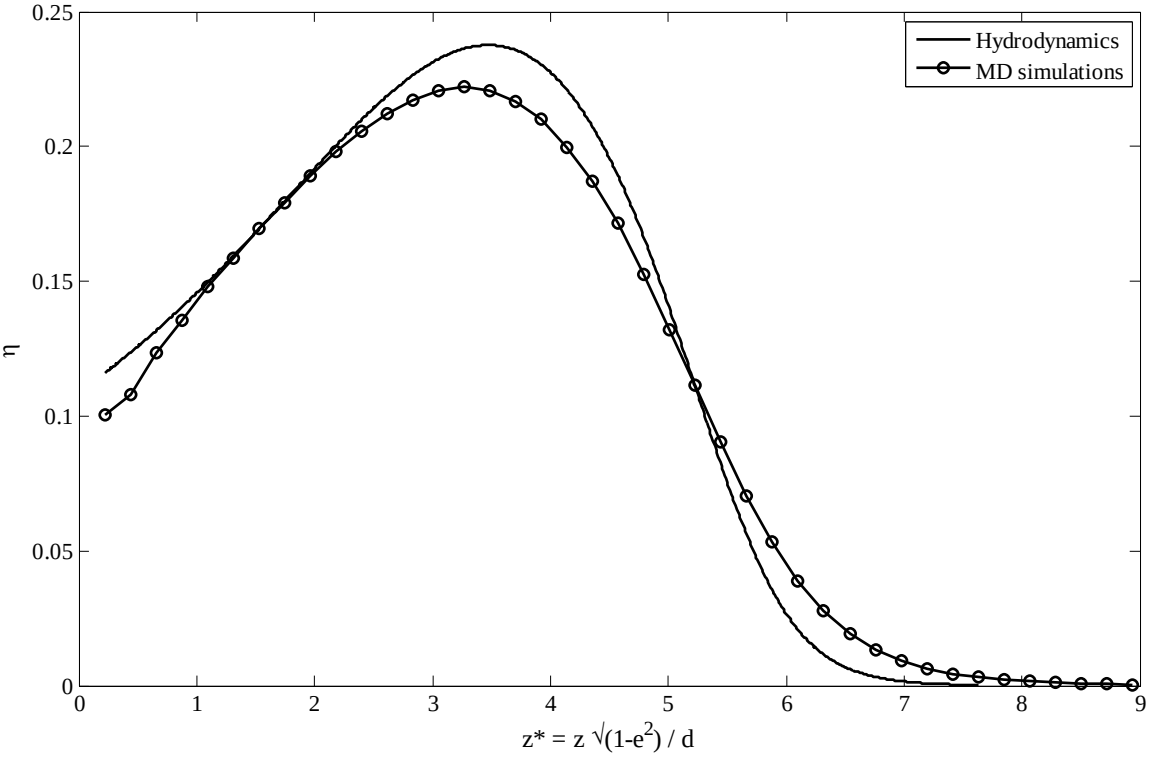

Figure 7-5: Packing fraction as the function of scaled height for $N^* = 1.0$ at Fr $= 4.0$.

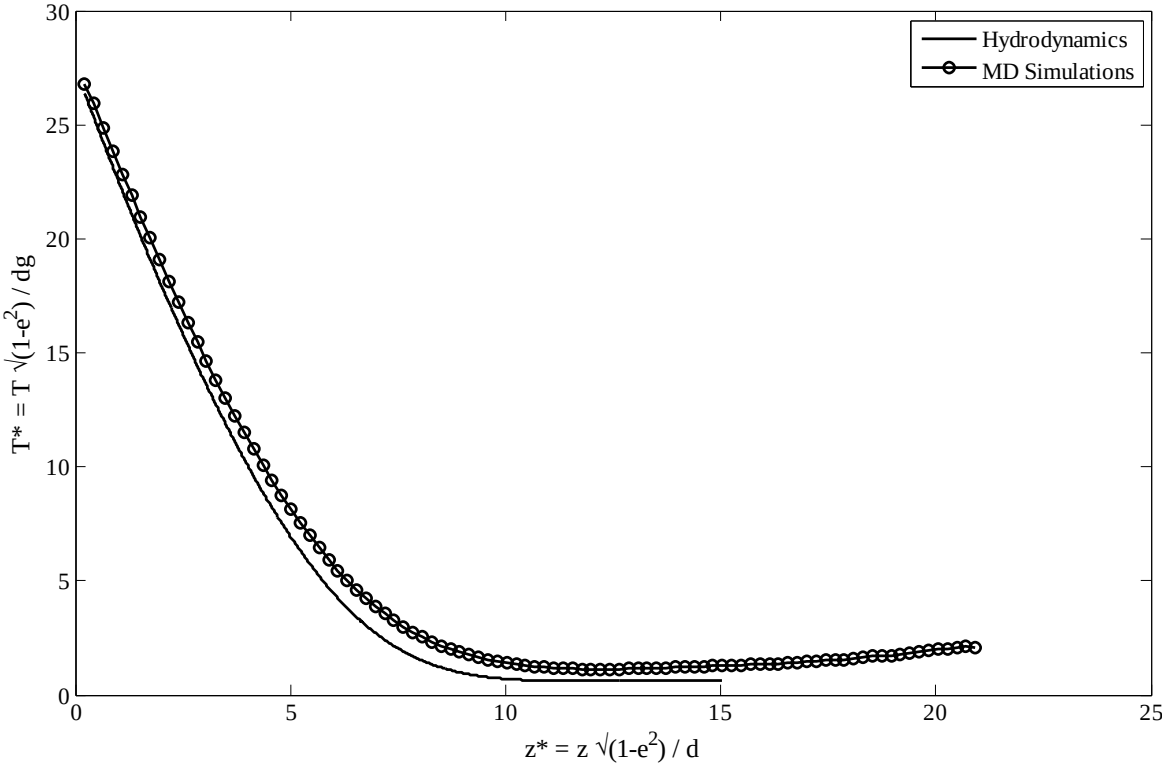

Figure 7-6: Scaled granular temperature as the function of scaled height for $N^* = 2.0$ at Fr $= 25.0$.

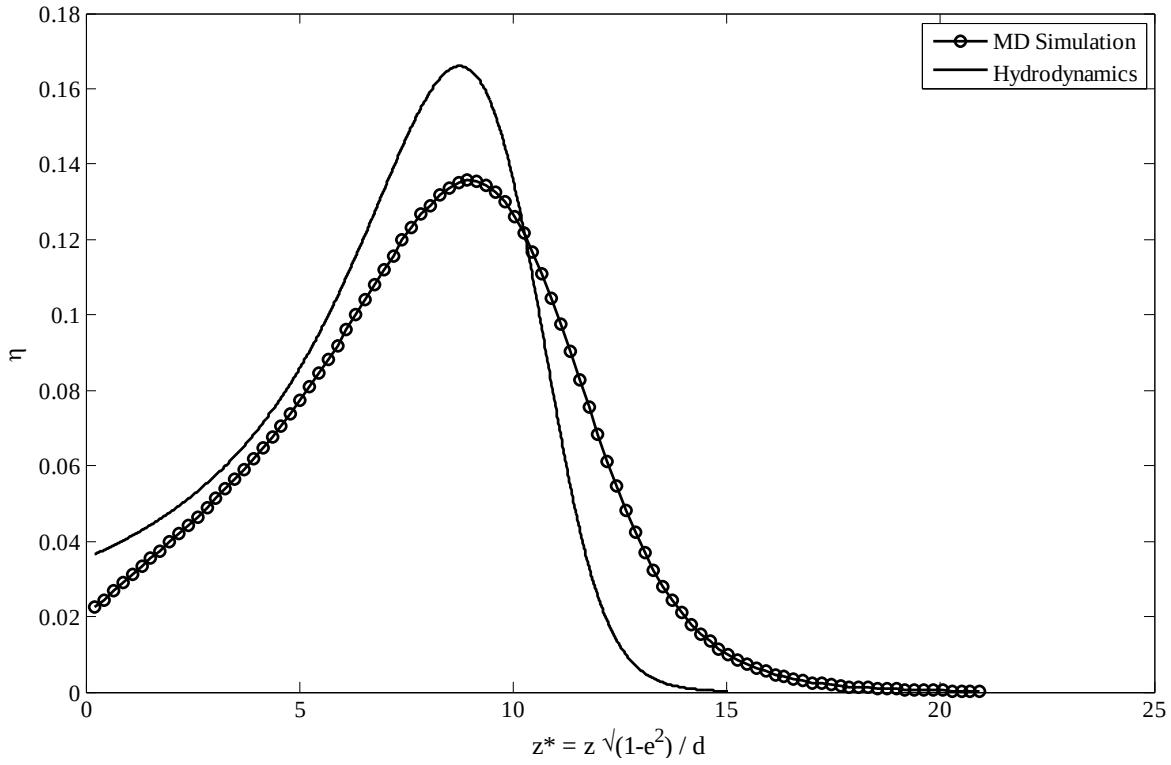

Figure 7-7: Packing fraction as the function of scaled height for $N^* = 2.0$ at Fr $= 25.0$.

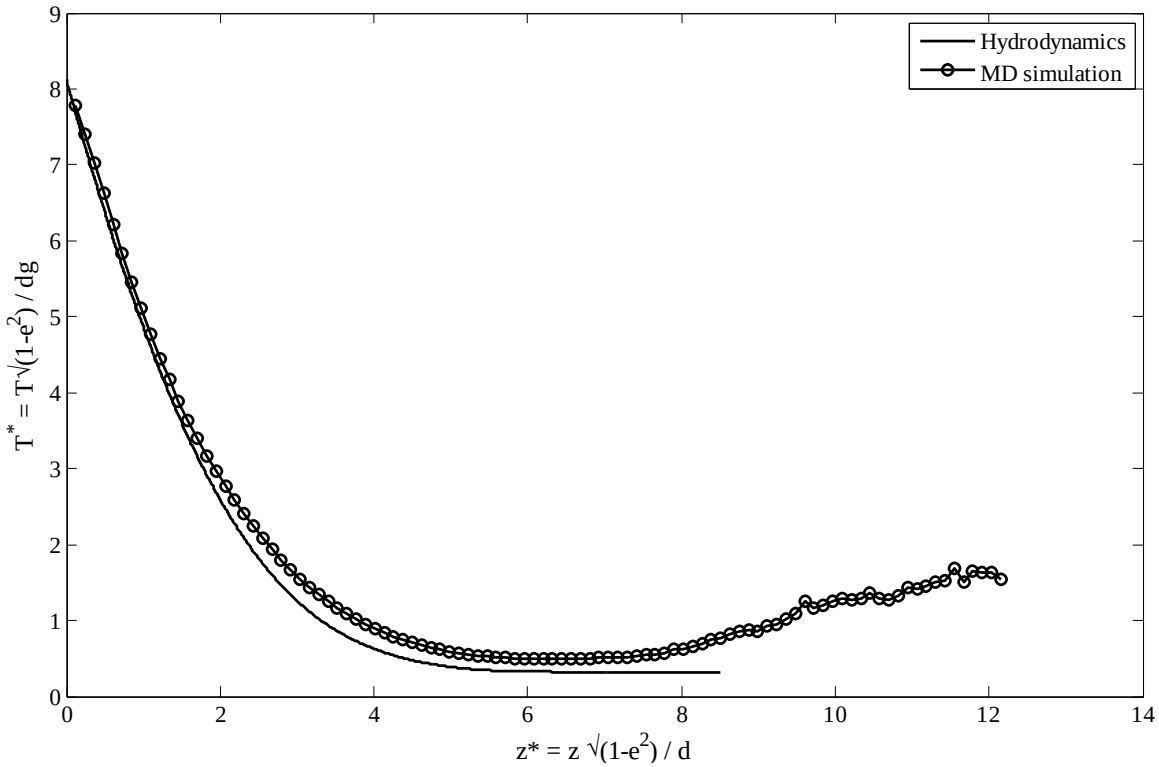

Figure 7-8: Scaled granular temperature as the function of scaled height for $N^* = 3.0$ at $Fr = 36.0$.

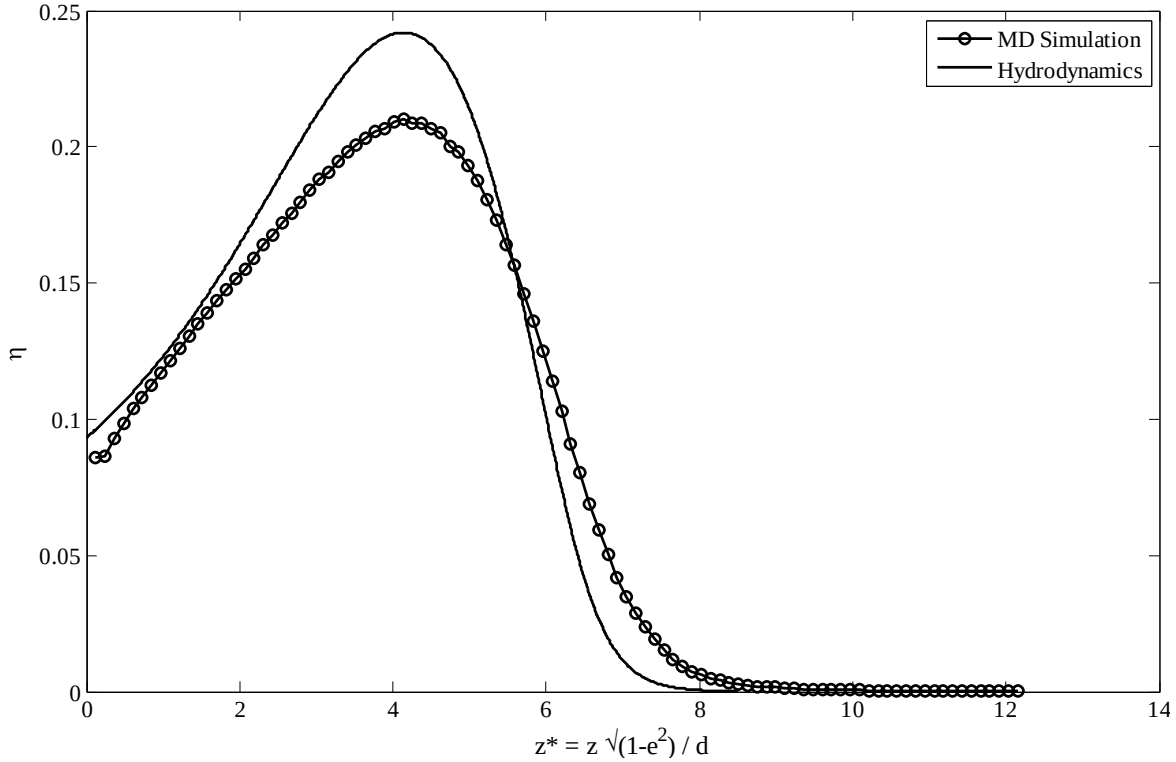

Figure 7-9: Packing fraction as the function of scaled height for $N^* = 3.0$ at $Fr = 36.0$.

As it can be noticed that the discrepancy starts to increase as N^* is increased. The comparison becomes more substantial as the loading increases i.e., $N^* >> 1.0$. At $N^* > 3.0$,

the temperature profiles are no longer comparable as shown in fig. 7.10 with similar order of deviations can be seen for packing fraction profiles in fig. 7.11.

A fundamental parameter in describing flows is the state law that links the state variables together. This is often described in the form $^{p}/_{T} = f(\eta)$, and is a key test. In fig 7.12 we plot $^{p}/_{T}$ against η with the state law given in Eq. 7.3 shown for comparison. It can be seen that the state law follows the MD simulation predictions up to $\eta < 0.30$. At higher packing fractions deviations starts to become apparent. Figure 7.12 also shows the behaviour of equation of state using two other forms of pair distribution functions different from the Eq. 7.8. These are adopted from Lun et al (Lun, Savage et al. 1984) and Garzo & Dufty (Garzo, Dufty 1999) respectively. Both models also predict reasonable agreement up to $\eta < 0.30$ but experience deviations at higher packing fractions. It can be concluded that discrepancy in the state equation is expected to be larger with higher loadings i.e., $N^* > 3.0$ leading to deviations in granular temperature predictions from MD simulations. Based on fig. 7.2-7.9 the prediction of hydrodynamic model below $N^* < 3.0$ are in reasonable agreement with MD simulations. In next section the bulk behaviour of bed is shown with systematically varying $N^* < 3.0$ and *Fr*.

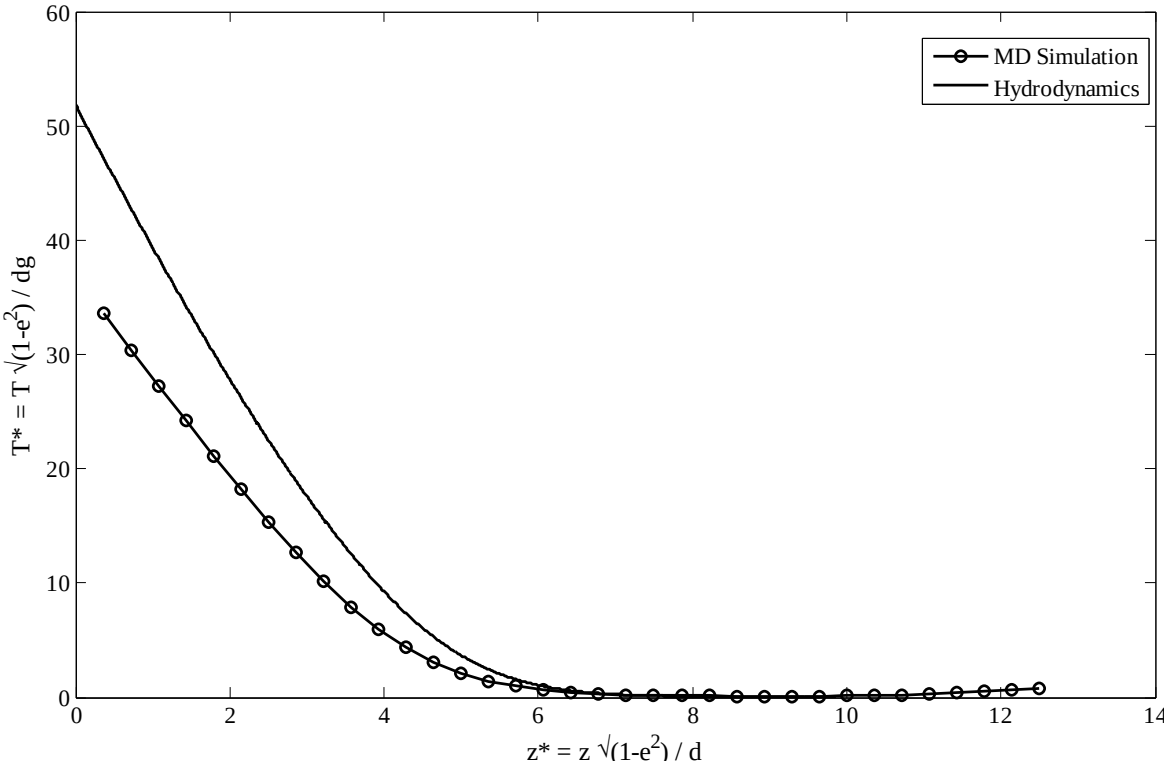

Figure 7-10: Scaled granular temperature as the function of scaled height for $N^* = 3.7$ at Fr = 36. 0.

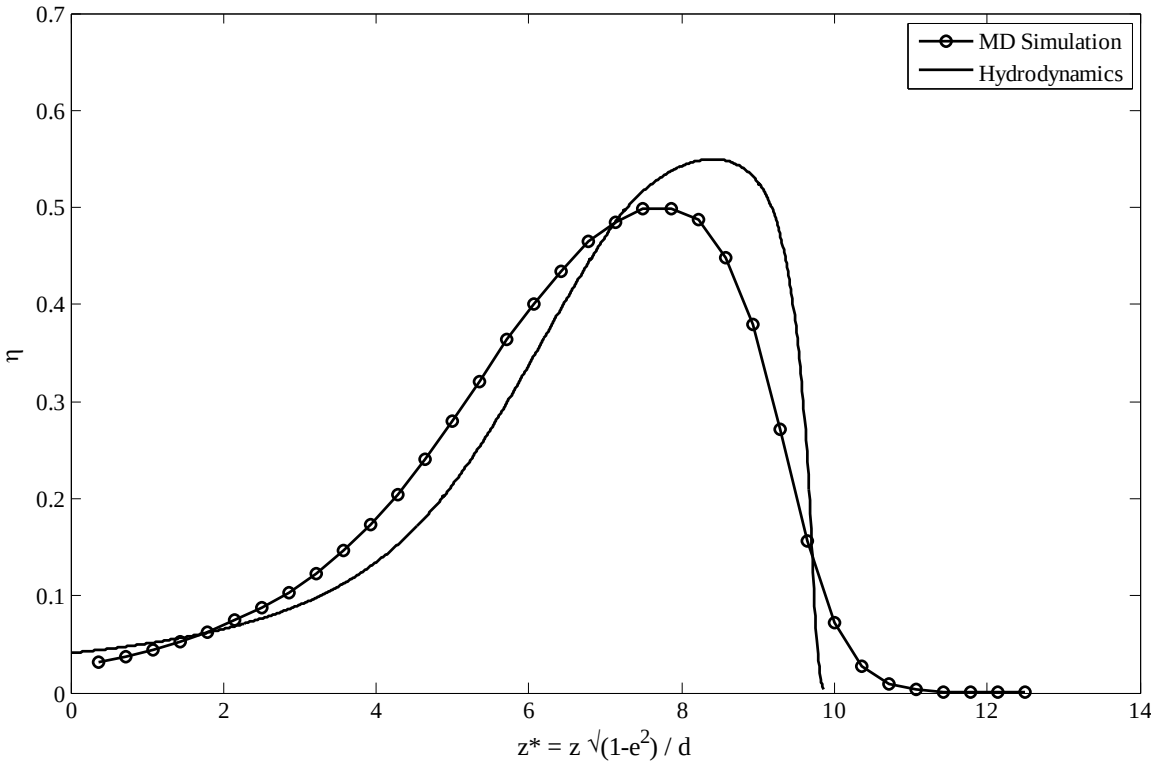

Figure 7-11: Packing fraction as the function of scaled height for $N^* = 3.7$ at $Fr = 36.0$.

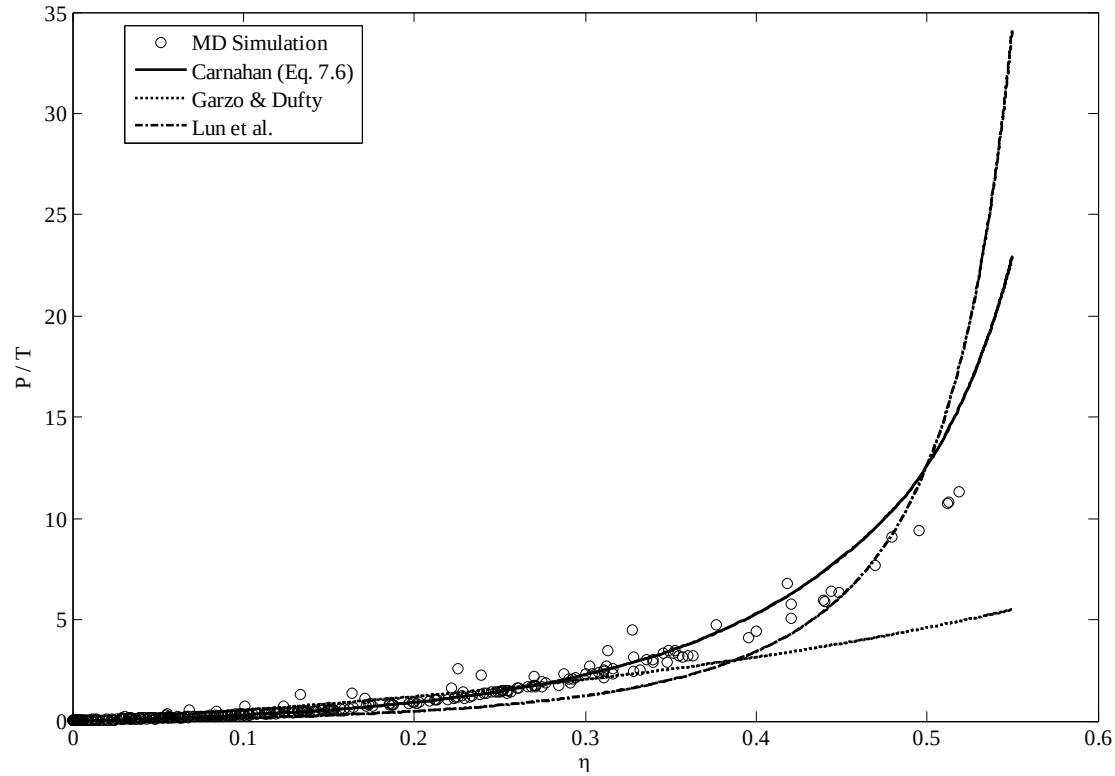

Figure 7-12: Pressure to temperature ratio verses packing fraction for MD simulations, Carnahan Eq. 7.6, Garzo & Dufty and Lun et al.

b. Effect of *N** and *Fr*

Here we consider two cases, (a) variation of loading (*N**) at large values of *Fr* and (b) variation of loading (*N**) at small values of *Fr*. The packing fraction profiles and granular temperatures for both cases are plotted in fig. 7.13 and 7.14 for a range of *N** from 1.37 to 3.12 with *Fr* varied from 36.0 to 1.44 respectively. At high values of Fr, we see that (fig. 7.13) the trend is for the bed to form a "block" of packed material at the top of the bed, the position of which moves towards the base as *N** is increased. Clearly, the shape of the density profile in the cell depends strongly on the value of *N** at high Fr.

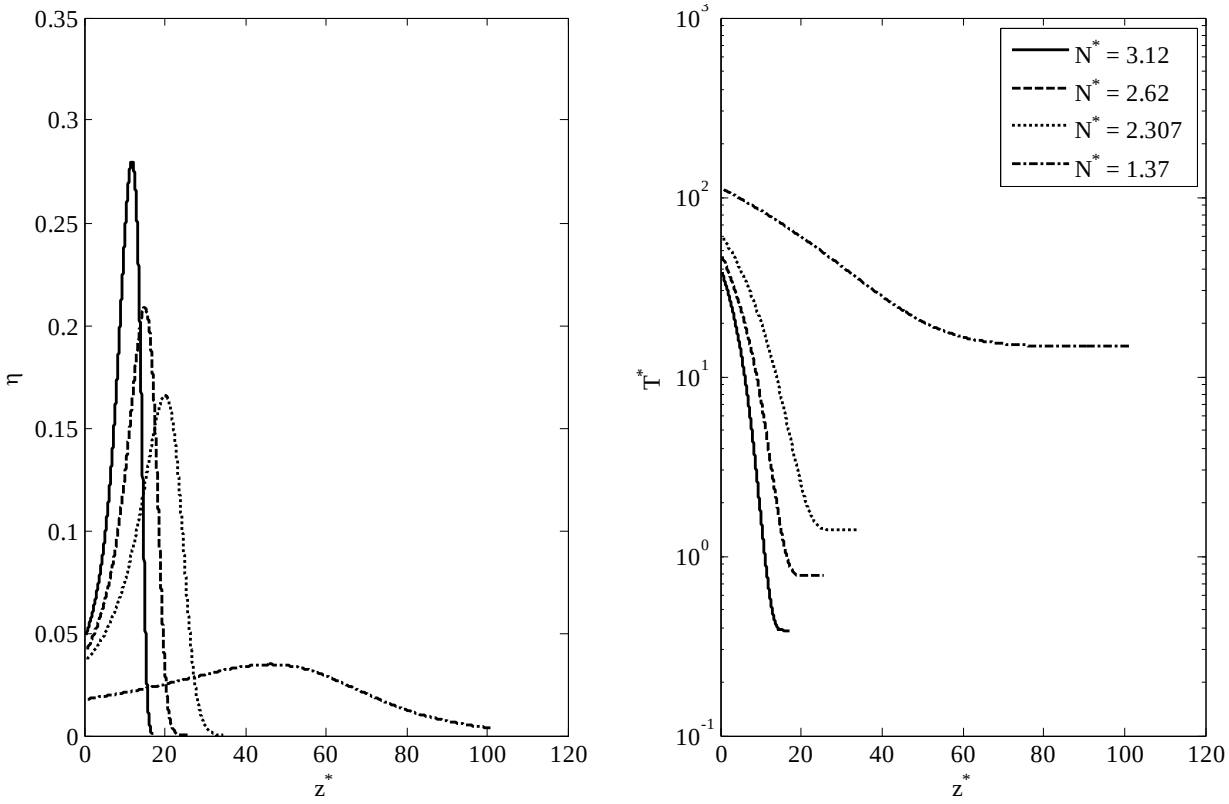

Figure 7-13: (a) Packing fraction and (b) scaled temperature as the function of loading N* for same driving velocity (Fr = 36.0).

The temperature profile is typical for high *Fr* and low *N** but as *N** is increased the striking result that the granular temperature rapidly goes to near zero is observed, suggesting very high bulk dissipation. At heights above the maximum density increase, a large decrease in packing fraction occurs with near to zero temperature gradient. Usually the region with low temperature gradients is considered dilute having high velocity grains with a lesser number of collisions. On the other hand, at *N**>>1.0, the region with very low temperature gradients is shifted towards the region of high density having very low temperatures (see fig. 7.10 and 7.11). The hydrodynamic model predicts a rapid decrease in packing profile after density hump to balance mass alongside pressure temperature state

equation relationship. Whereas MD simulations show no such abrupt decrease while having low granular temperature (see Fig. 7.11 at $z^* \geq 8$). In this region the equation of state shows deviations from the MD simulations.

The behaviour at low *Fr* is quite different. We see that as we increase *N** the peak in density is not so pronounced and that its movement towards the base is not so strong. For the case *N** <<1.0, a nearly elastic gas, the density decreases exponentially from peak base density due to nearly constant temperature profile. As *N** is increased, the absolute value of the temperature is reduced, but we do not observe the characteristic reduction in *T** to near zero. In fig 7.13b we see that the ratio of T_0/T_∞ is of the order ~10, whilst in fig 7.14b

we see a much lower ratios. In figure 7.15 we show the variation in the packing fraction and temperature for a fixed *N** = 2.0 and varying *Fr*. The behaviour of the packing fraction and granular temperature is somewhat reminiscent of that shown in fig. 7.13. However near the base the temperature decreases and the packing fraction increases significantly with the reduction of *Fr*. At lower values of *Fr*, the heat flux at the base is reduced resulting in lesser granular temperatures and higher packing fractions near the base.

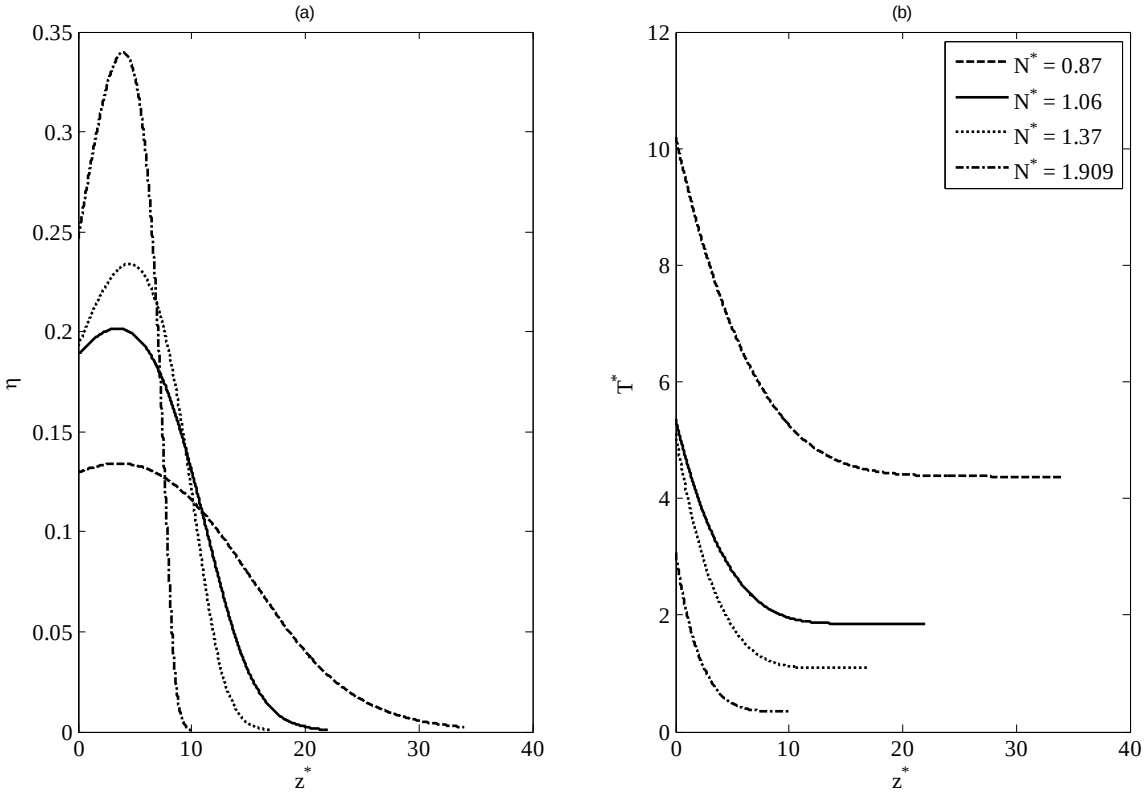

Figure 7-14: (a) Packing fraction and (b) scaled temperature as the function of loading N* for same driving velocity (Fr = 1.44).

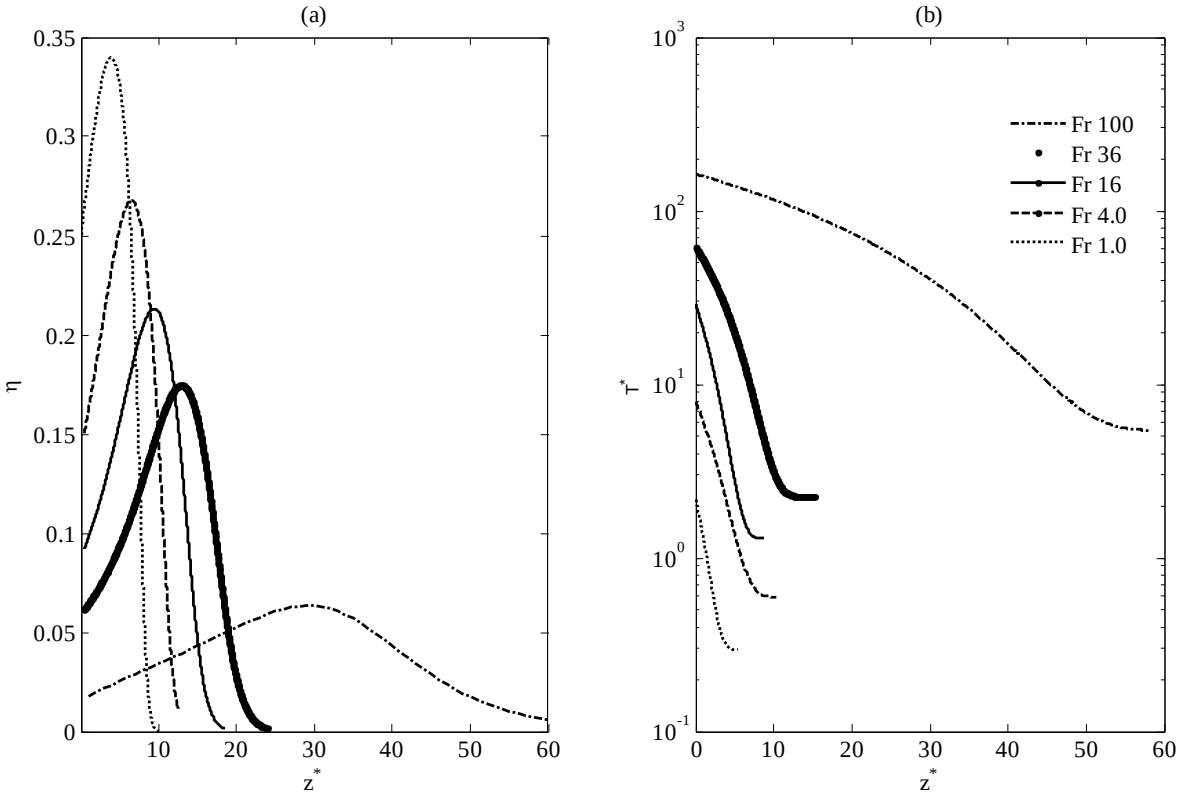

Figure 7-15: (a) Packing fraction and (b) scaled temperature as the function of *Fr* for same loading condition (N* = 2.0).

7.8. Characterization of the heat flux

In Eq. 7.15, the term C_ϕ was left undetermined. It is possible to determine this function using the MD simulations if we rearrange Eq. 7.15 thus,

$$C_\phi = \frac{J_b^*}{\eta_o}\frac{1}{Fr} \qquad \textbf{(7.16)}$$

where J_b^* is the heat flux at the base and η_o is the base packing fraction, we can see that the right hand side of the equation can be determined through MD simulations. It seems likely that C_ϕ will be a function of base density (Kumaran, Wildman et al. unpublished). Therefore, if we plot C_ϕ as a function of packing fraction for different values of the coefficient of restitution *e*, we can specify the form of C_ϕ. In our analysis we assume a form of $C_\phi = (1 + a\eta\chi)$ with *a* as constant. Figures 7.16 to 7.18 show the variation of C_ϕ as seen in the MD simulations alongside fitted curves. The fitted form shows good agreement and suggest that the dependence on the base density is close to that specified, at least within the range of packing fractions tested. We see a small downward trend in *a* as the coefficient of restitution is reduced, with *a* = 5.97, 5.31 and 4.14 for *e* = 0.98, 0.85 and 0.70 respectively.

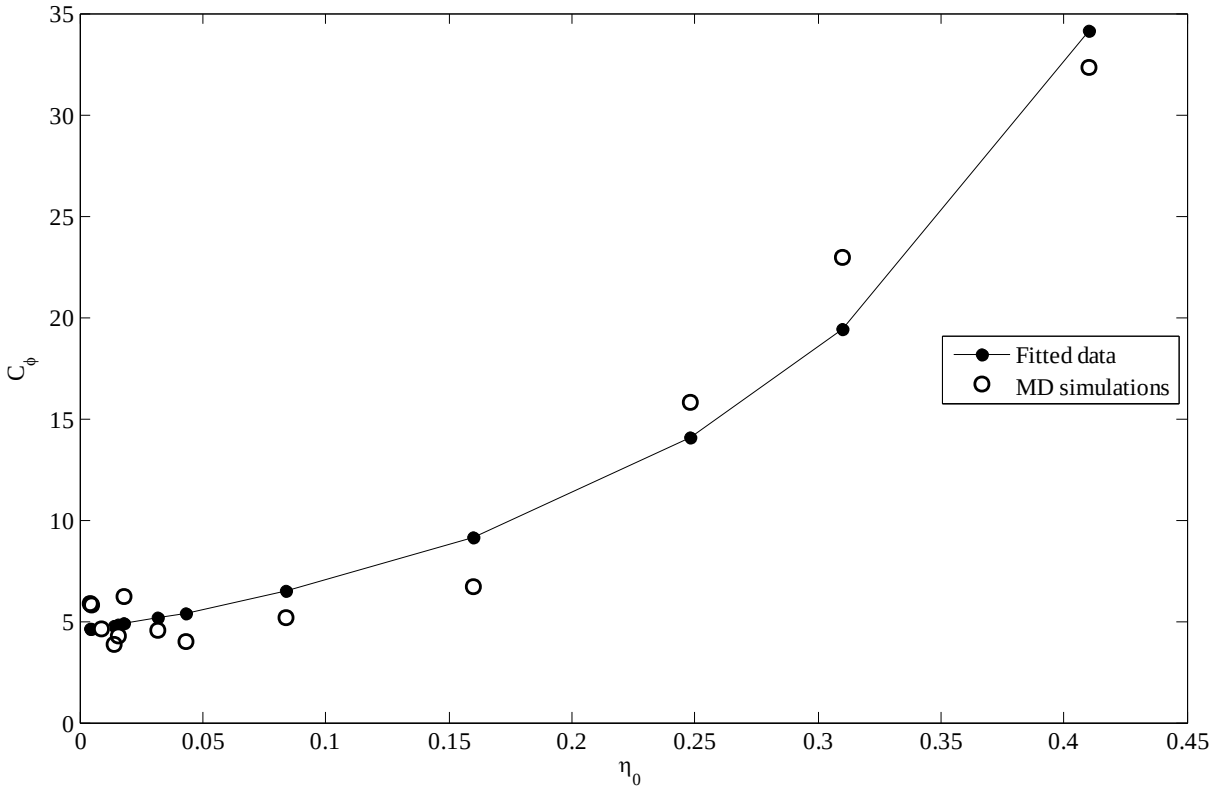

Figure 7-16: Variation of C_ϕ as the function of base packing fraction for e = 0.70.

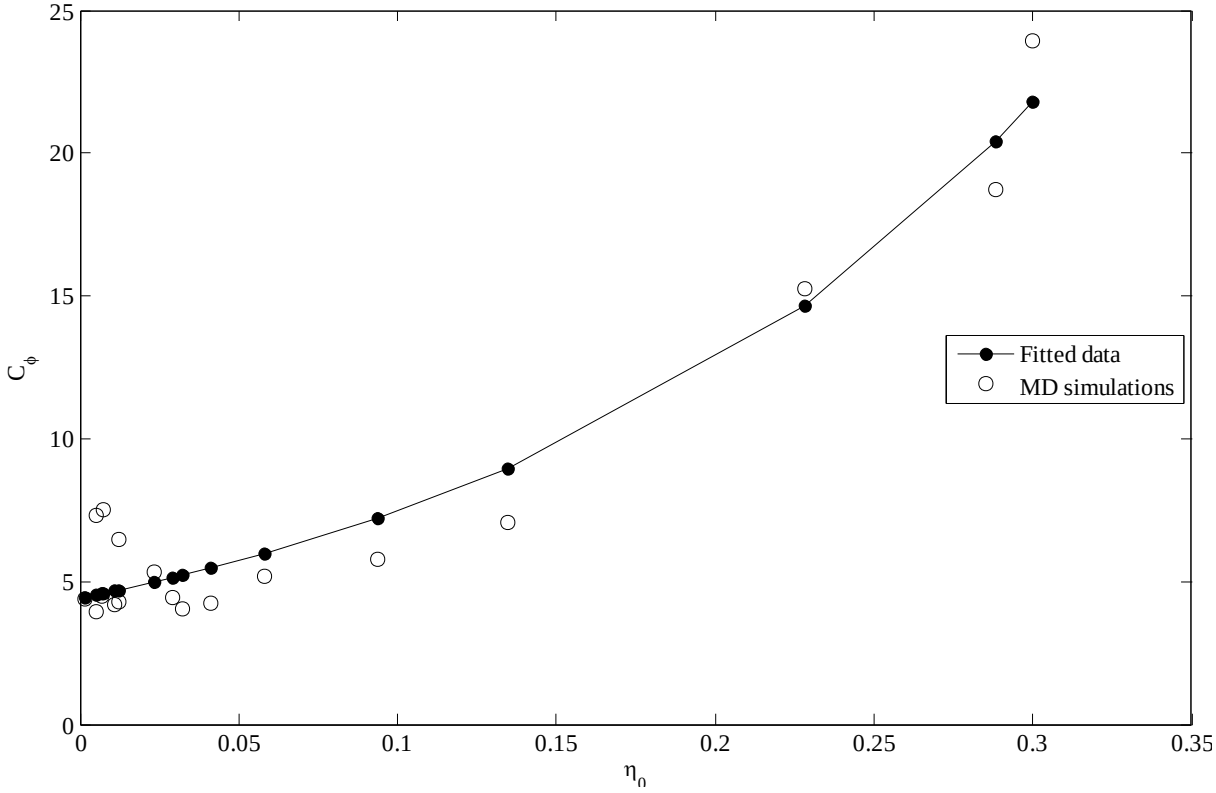

Figure 7-17: Variation of C_ϕ as the function of base packing fraction for e = 0.85.

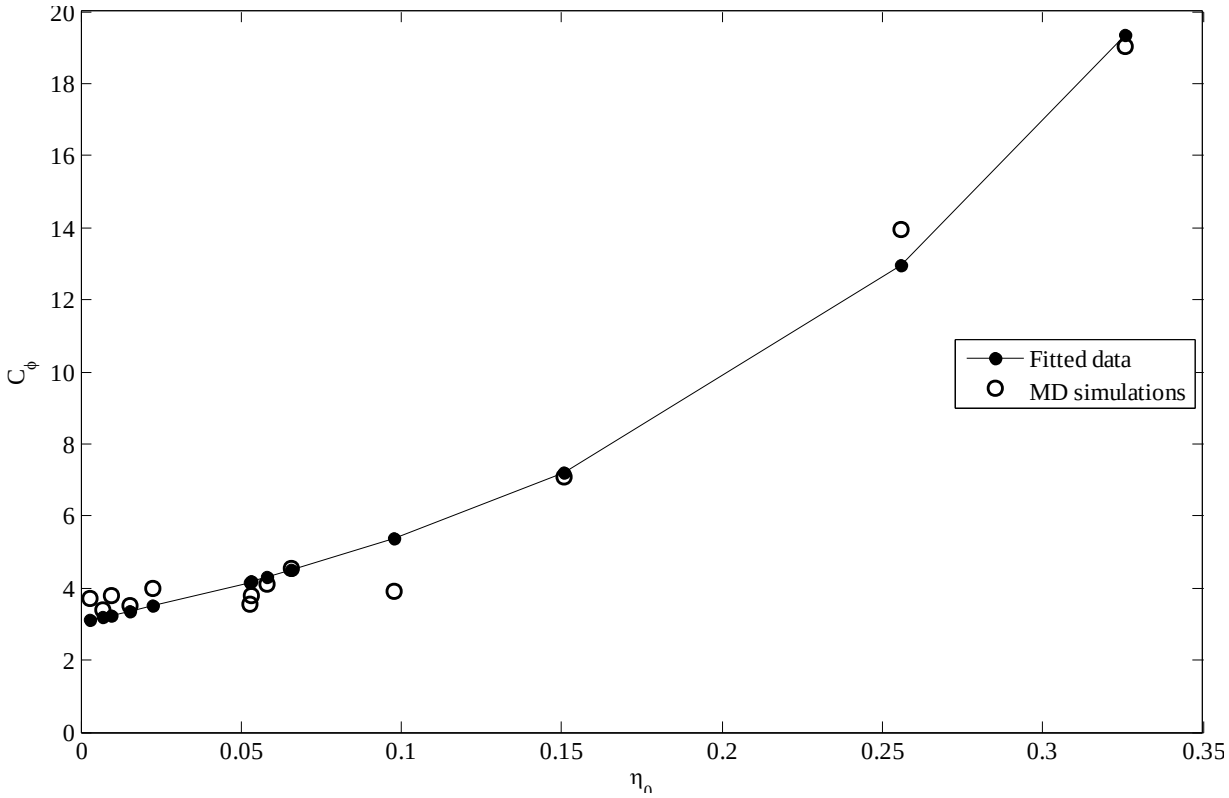

Figure 7-18: Variation of C_ϕ as the function of base packing fraction for e =0.98.

7.9. Scaling relationships

In previous sections we have established the influence of *Fr* and *N** on the bed behaviour; in this section we will examine the scaling of the state variables using MD simulations and compare our results to the predictions in table 7.1. Where predictions involve parameter estimation at the base, we extrapolate to $z^* = 0$ from the local $z^* > 0$ behaviour. Difficulties in calculating the temperature gradient $T^{*\prime}$ in the bulk and then extrapolating mean that the scaling of this parameter was not tested.

a. Scaling for T_o

The temperature at the base, T_o, is expected to scale as $\frac{V^2}{N^*(1-e^2)}$ for small *N** and as *Fr* for large *N**. Therefore, we plot in Fig. 7-19 the variation of T_o with $\frac{V^2}{N^*(1-e^2)}$ whilst in Fig. 7.20 we show the variation of T_o with *Fr* for *N** 0.3, 1.0, 3.0 and 10.0. Figure 7.19 shows that at low *N** that a scaling of T_o with $\frac{V^2}{N^*(1-e^2)}$ is a reasonable approximation. At $N^* \geq 1.0$ we see that T_o scales well with *Fr* through a function of the form of $m \times Fr$, where $m = f(N^*)$ shown in Fig. 7.21. Figure 7.20 indicates that the theoretical predictions are

reasonable, and the physics depends strongly on *Fr* and *N**. The dependence of base temperature T_0 on *N** is not predicted but it scales the value of m for *N**≥1.0. However in Fig. 7-20 some scatter from the master trend line can be observed resulting from the fluctuation of the value of *m* especially at higher values of *N**.

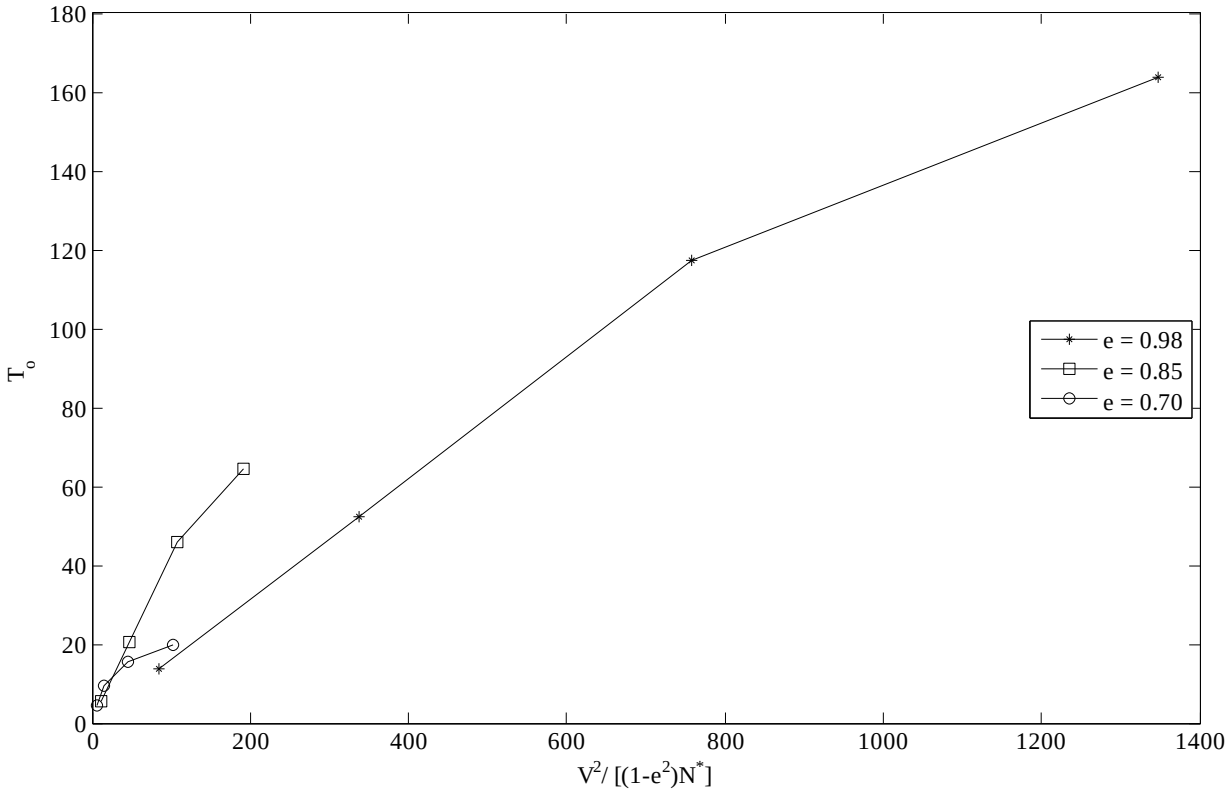

Figure 7-19: Base temperature for N* = 0.3 at varying $V^2/(N^*(1-e^2))$ and e.

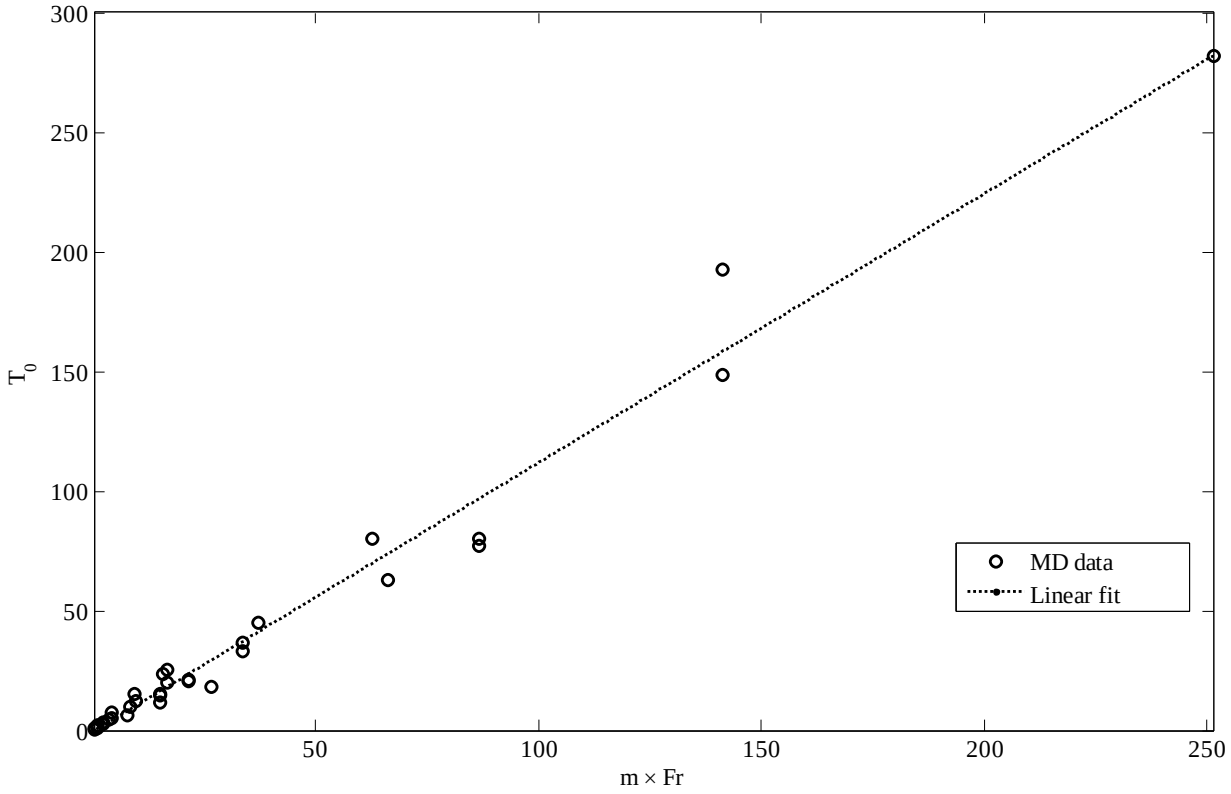

Figure 7-20: Base temperature, T_0, for N^* = 1.0, 3.0 and 10.0 at varying m x Fr.

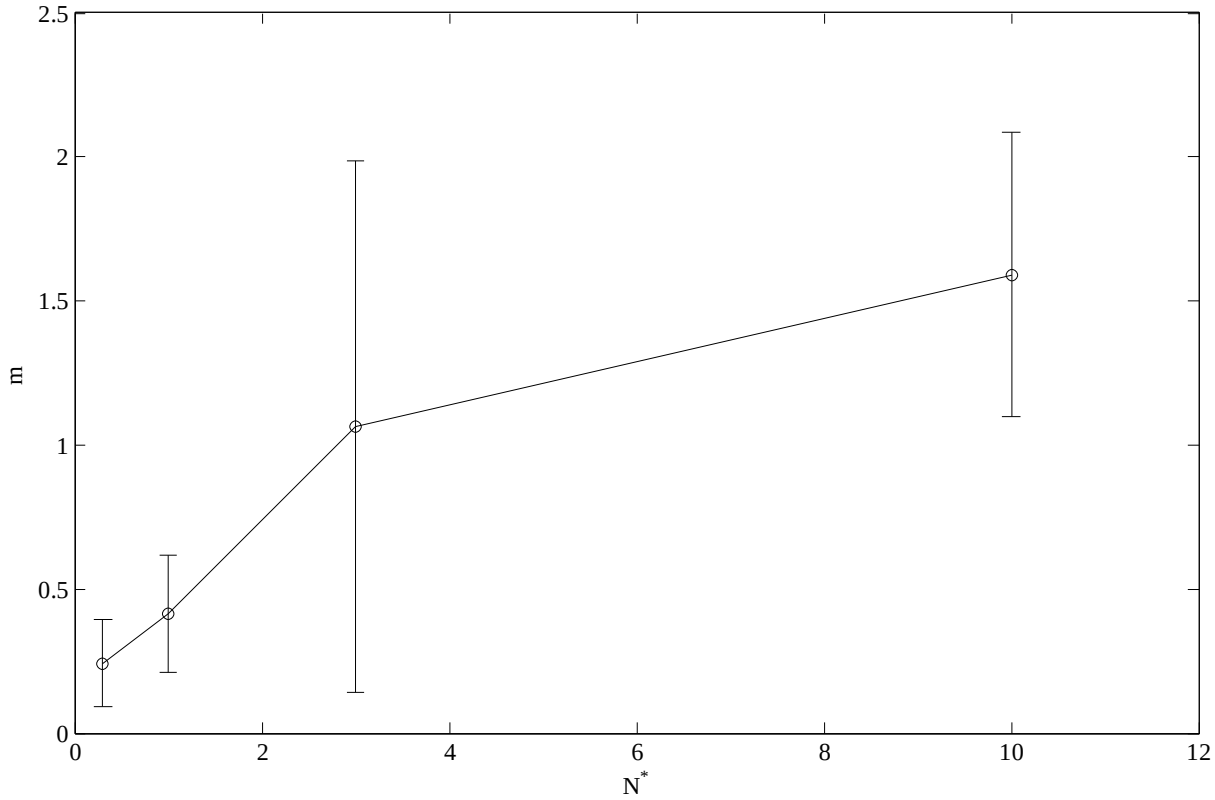

Figure 7-21: Value of m as the function of N^*.

b. Scaling for $\frac{T_0}{T_\infty}$

The ratio of base temperature and the asymptotic, high altitude temperature is expect to scale as 1 for small N^* and N^* for large N^*. At $N^* << 1.0$, the Fig. 7.22 shows the ratio is almost constant and close to 1.0 as expected irrespective of *Fr* and *e*, though there appears to be a slight *Fr* dependency at small *Fr*. With $N^* << 1.0$, the gas is a near elastic one so a flat temperature profile is expected. While for $N^* > 1.0$, the ratio is expected to scale with N^*. In Fig. 7.23 the variation of $\frac{T_0}{T_\infty}$ is shown against N^* along with mean values and deviations. We see an mean increasing trend with the increase of N^*. However high scatter in the value of $\frac{T_0}{T_\infty}$ at each N^* can be seen primarily linked with the variation of *Fr*. The scatter is significantly large for $N^* >> 1.0$. At $N^* >> 1.0$ the dissipation is expected to increase and large temperature ratios are expected at sufficient base driving. It is observed in section 7.7 that at high *Fr*, the asymptotic temperature, T_∞, decreases significantly close to zero (see Fig. 7.13(b)) and the resultant $\frac{T_0}{T_\infty}$ is strikingly higher compared to the low *Fr* case (see Fig. 7.14(b)). As stated earlier a weak dependence on *Fr* exists for the base to asymptotic temperature ratio at $N^* << 1.0$. However for $N^* > 1$ it is expected the likely trend is of the form of $\frac{T_0}{T_\infty} \approx f(Fr) \times N^*$. At low *Fr* and higher packing fraction, an exact form of the relationship cannot be deduced at $N^* >> 1.0$ and in this region the theoretical predictions are likely to be less applicable.

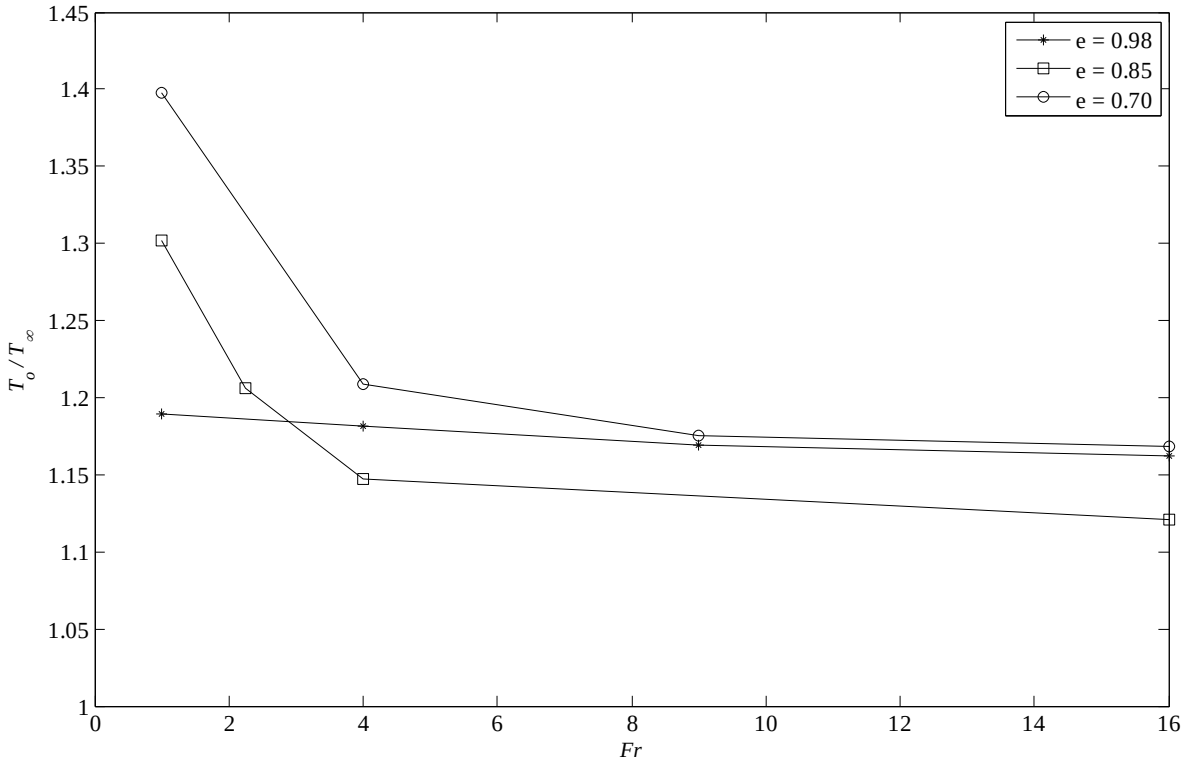

Figure 7-22: Ratio of Base temperature, T_0, to Asymptotic temperature, T_∞, for N* = 0.3.

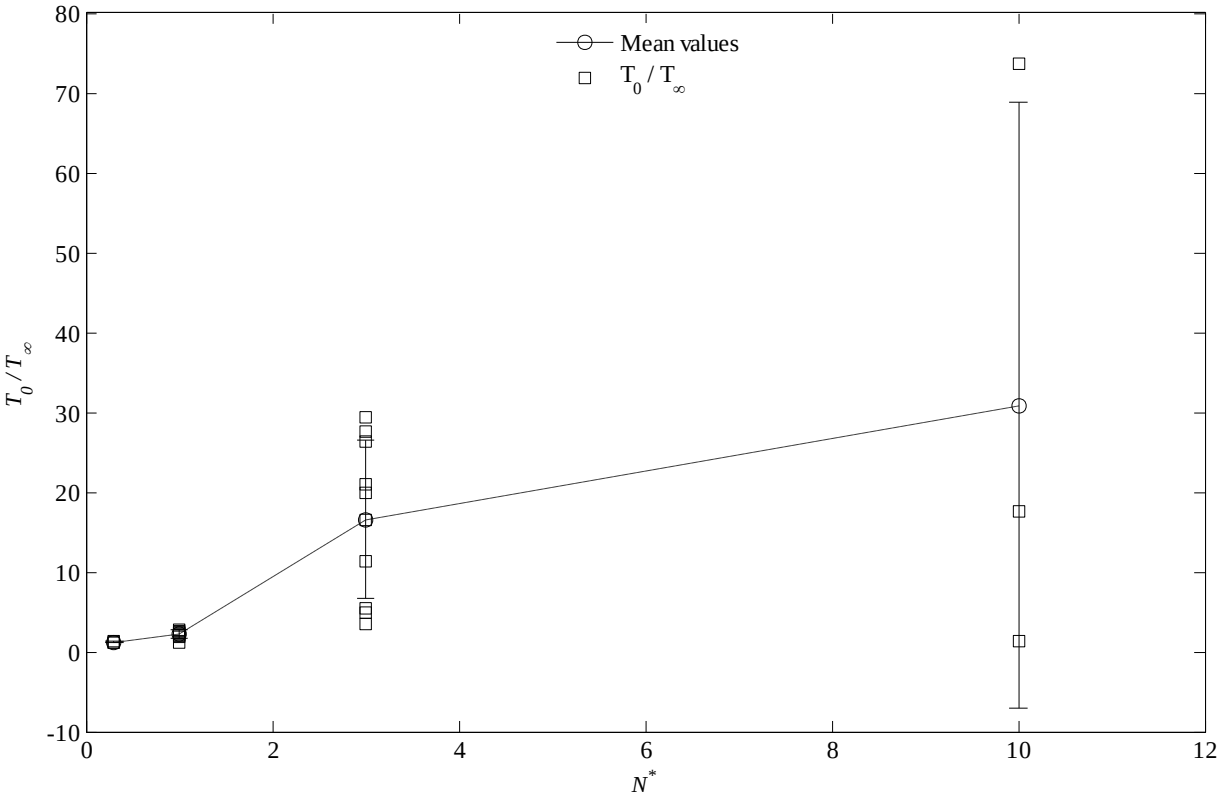

Figure 7-23: Ratio of Base temperature to minimum temperature for *Fr* = 1.0 with varying *N.**

c. Scaling for η_0

In Fig. 7.24 we show the variation of packing fraction at the base, η_o, with the ratio *N*/Fr*. For all values of *N*/Fr* < 1.0 in Fig. 7.24, an increasing trend can be observed as expected. The cluster shows a consistent trend generating a master scaling pattern at lower values of *N** or high values of *Fr* especially with packing fractions less than 0.2. At higher values of $\frac{N^*}{Fr} > 1.0$ still an increasing trend is seen while the packing fraction at the base, η_o, is more than 0.20. It can be seen that the expected trend is observed with the $\frac{N^*}{Fr}$.

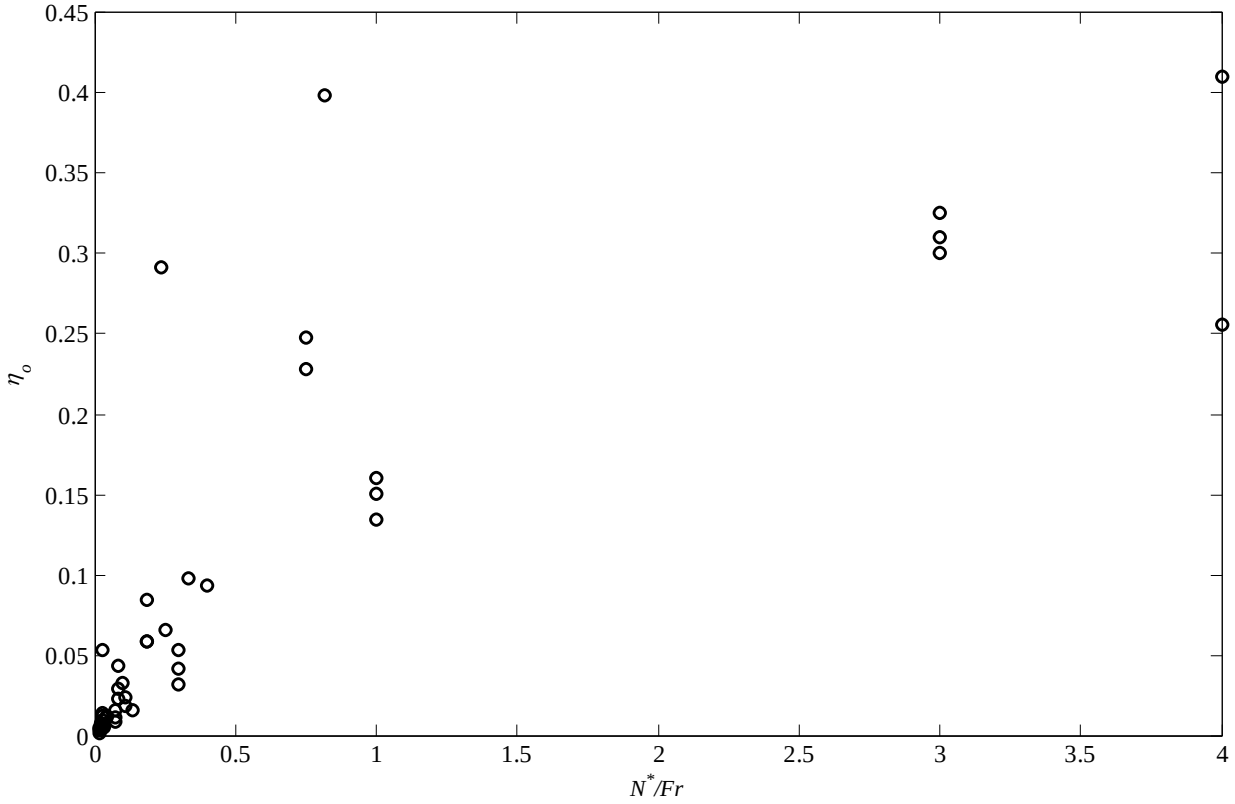

Figure 7-24: Base packing fraction at varying ratio of N*/Fr .

d. Scaling for η_{max}

Figures 7.25 shows the variation of peak packing fraction, η_{max}, with the *N*/Fr*. For all values of *N*/Fr* in Fig. 7.25, an increasing trend can be observed as expected. Especially for $\frac{N^*}{Fr} < 0.5$ the monotonically increasing trend is observed with the appearance of three identifiable clusters can be seen. Each of these three separate clusters has an identical coefficient of restitution for all of its values. Starting from the bottom with *e* = 0.98, 0.85 and 0.70 to the top such that the least elastic corresponds to the maximum packing fraction. This highlights an indirect dependence of η_{max} on *e*. While for $\frac{N^*}{Fr} > 1.0$, the trends are no

longer linear and dependency on *e* becomes less significant. For $\frac{N^*}{Fr} >> 1.0$ i.e., at low *Fr* or high value of *N** with high peak packing fractions the predicted are expected to deviate from the MD simulations.

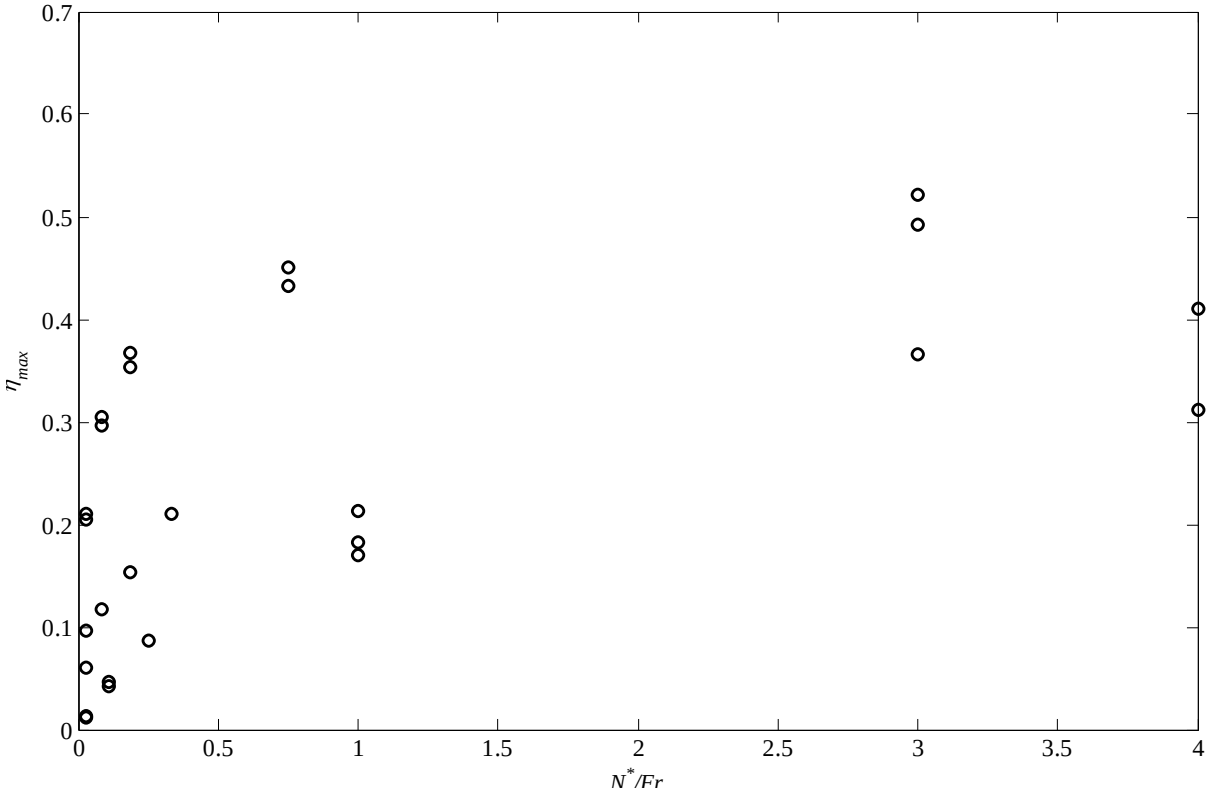

Figure 7-25: Peak packing fraction for *N = 0.3, 1.0, 3.0 and 10.0 at varying ratio of N*/Fr .**

e. Scaling for z^*_{max}

We anticipate that at large *N** values, z^*_{max} will scale as *Fr/N**. Figures 7.26 to 7.29 show z^*_{max} plotted against as *Fr / N** for progressively larger values of *N**, plus also show how the coefficient of restitution influences the scaling. In all cases for $N^* \geq 1$ we see that this scaling holds for *Fr* large, but where *Fr* is small, we see a non-linear dependence on *Fr/N**. One reason for this is that the system is weakly fluidised at low *Fr*, and as we saw in Figs.7.10 that at high densities, the simple hydrodynamic description begins to break down. In addition, we see that scaling itself is only weakly influenced by e, but that the absolute value is, suggesting that the coefficient of restitution becomes progressively less important as one increases the driving.

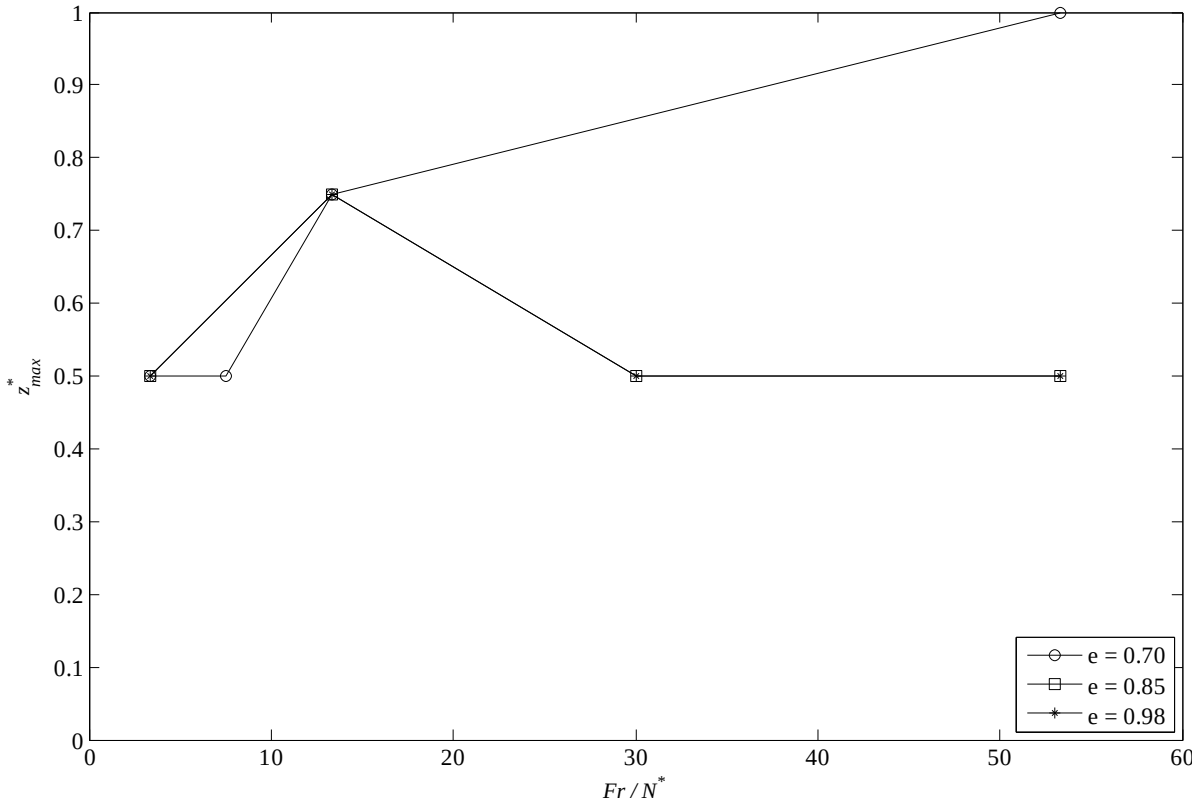

Figure 7-26: Location of Peak packing fraction for N* = 0.3 at varying ratio of *Fr/N with e.**

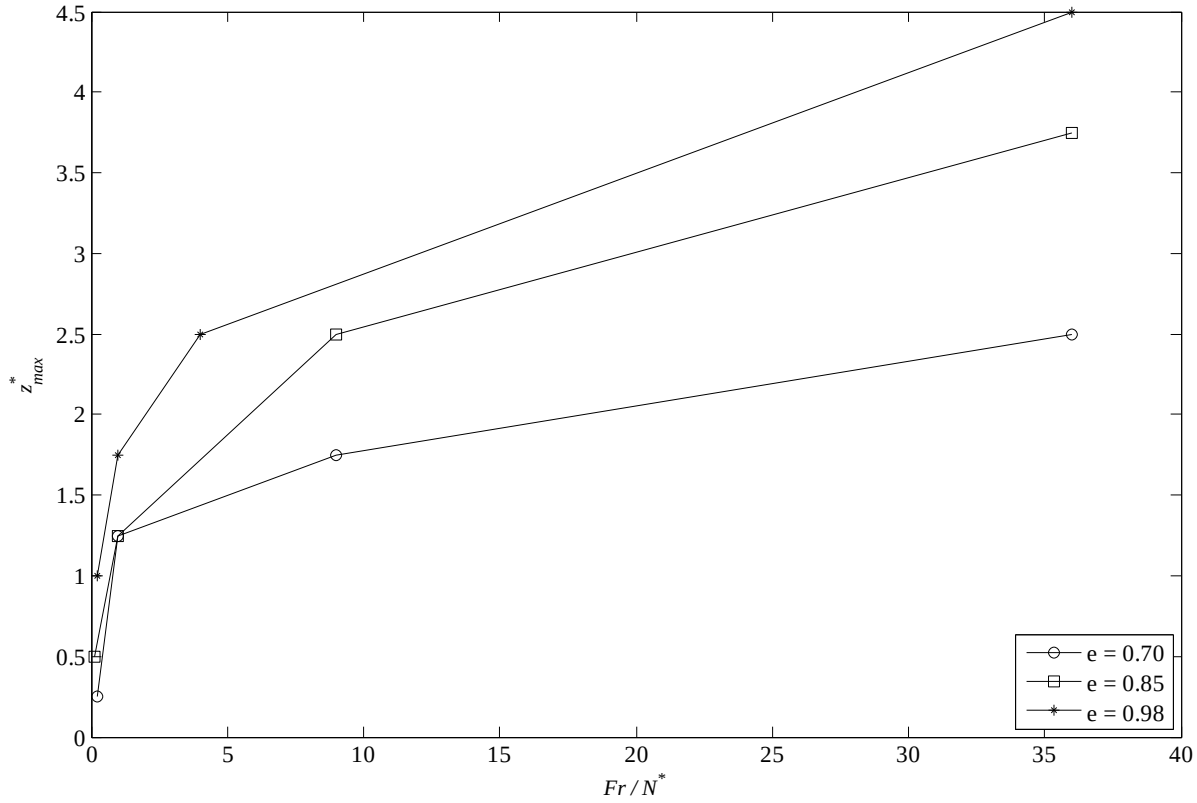

Figure 7-27: Location of Peak packing fraction for *N =1.0 at varying ratio of *Fr/N** with e.**

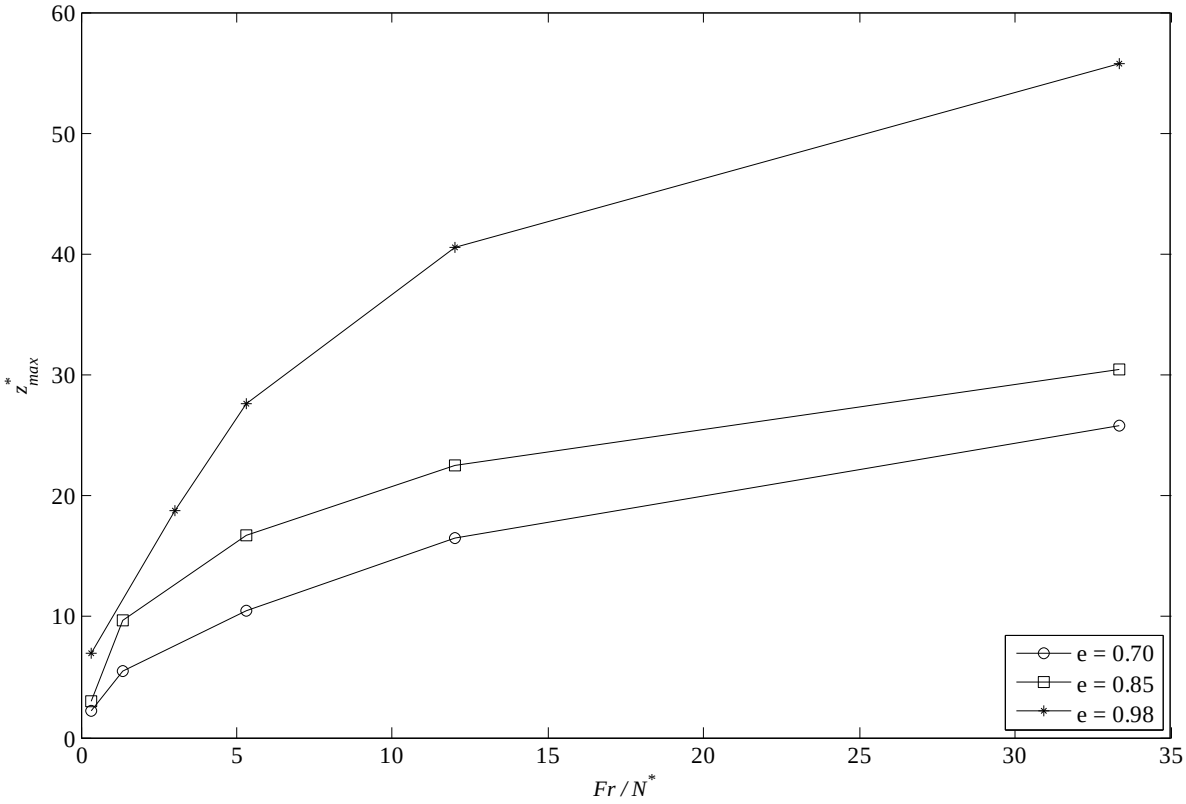

Figure 7-28: Location of Peak packing fraction for *N = 3.0 at varying ratio of *Fr/N** with e.**

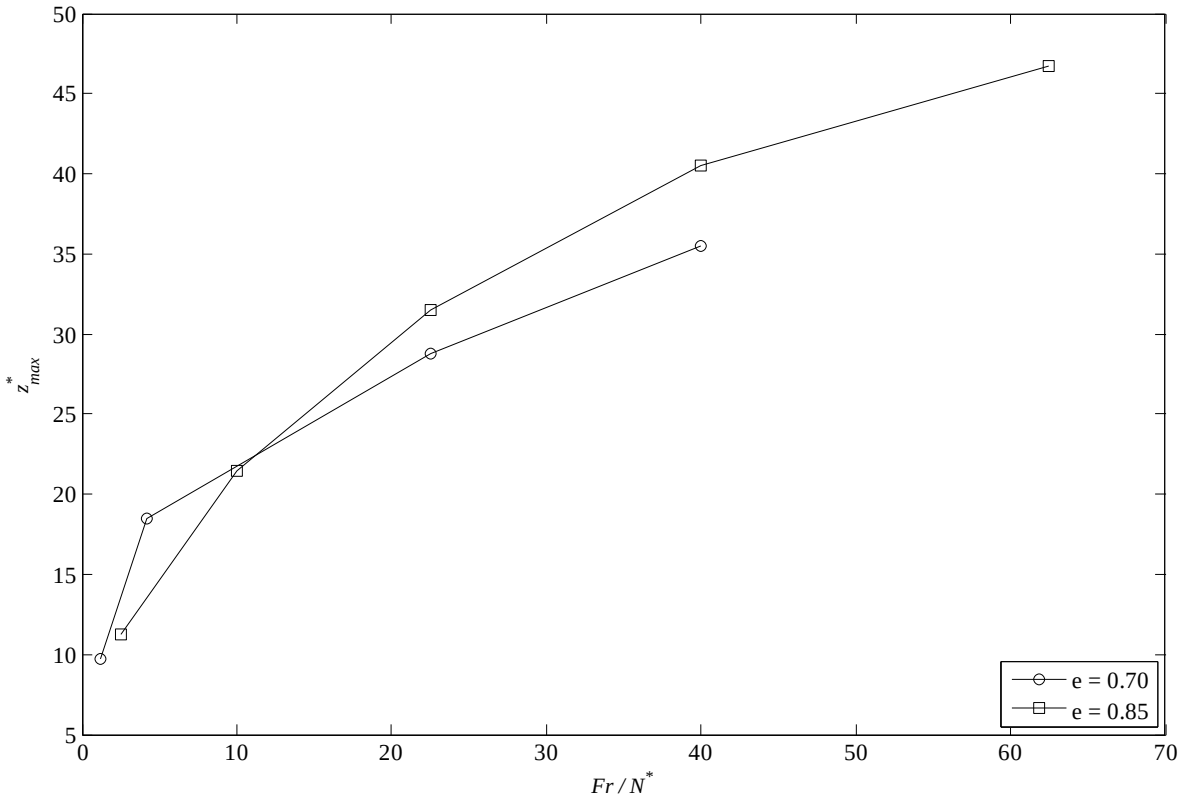

Figure 7-29: Location of Peak packing fraction for *N = 10.0 at varying ratio of *Fr/N** with e.**

The analysis presented in this chapter indicates the importance of the two parameters *Fr* and *N** and their scaling with steady bed physics. In general the predicted scaling relationships of table 7.1 are observed for the dilute limit case especially for base temperature, T_0, base packing fraction, η_0, and temperature ratios, $\frac{T_0}{T_\infty}$. With the introduction of moderately to high density granular bed the trends start to change and deviations from the predicted scaling appear to occur. The non-linearity is clearly visible in the bulk behaviour as seen in the trends of peak packing fractions, η_{max}, and their locations, z^*_{max}.

At *N**<<1.0, i.e., when the length of conduction is larger than the dissipation length, we expect the peak packing fractions very close to the base and $\frac{T_0}{T_\infty} \sim 1.0$. In Fig. 7.26 we observe z^*_{max} within one particle diameter while Fig. 7.22 shows the almost constant base to asymptotic region temperature ratio. For *N**>>1.0 the predicted scaling behaviour depends upon the base driving *Fr*. We observe that the peak packing fraction, η_{max}, their locations, z^*_{max},and the base packing factions, η_0, show the increasing trend in the limit $\frac{N^*}{Fr} < 1.0$ thereby at high *Fr* or low values of *N** the general trend exists. Interestingly the predictions of T_0 is significantly consistent for *N**>>1.0 with additional dependence on *N** is predicted linked through the factor *m*. However at low *Fr* or higher values of *N** the packing fractions are expected to increase and the effect of dilute limit scaling is less likely to be observed as seen in the case of $\frac{T_0}{T_\infty}, \eta_{max}$ and z^*_{max}. Apart from predicted scaling unexpectedly weak additional dependence on the coefficient of restitution has been observed in few of the cases.

It can be concluded that the scaling are observed in general with expected deviations are seen in the conditions of low *Fr* and high *N**. At high *N** the peak packing fraction is significantly high due to moderately to dense bed loading conditions and at low *Fr* the bed is not sufficiently fluidized. This suggests that the model begins to fail to capture the main physics of the system under these conditions. The main reason for this is that the model is proposed for dilute nearly elastic system, and we have seen in Chapters 3-5, that the exact physics of the granular bed is far more complex and requires additional constitutive relationships and modifications to the current coefficients. This model does, however, set the basis for describing the main scalings for vibrofluidized granular beds, and in the future we anticipate that effects of further inelasticity and enhanced density could be incorporated.

7.10. Summary

This chapter showed that by non-dimensionalisation of the length scale using $d/\sqrt{1-e^2}$, two prominent parameters can be developed, N^* and Fr. The newly formed non-dimensional model is solved shows good agreement with MD simulations especially at lower values of N^* and deviates progressively for $N^* >> 1.0$. For $N^* > 3.0$, the predictions of nature of the constitutive relationships differs significantly from MD simulations indicating dense gas higher order effects. The parameters of N^* and Fr also exhibit scaling behaviour in the dilute regime for characteristics granular quantities. The results included here are based on near elastic model and the exact physics of the granular bed is far more complex, however, this sets the basis for describing the general scalings for vibrofluidized granular beds.

Chapter 8 Conclusion and future recommendations

8.1. Summary of conclusions

This dissertation is focused on the mechanics of granular flows from the aspect of evaluation and study of the constitutive relationships. Spatial and temporal aspects of the dry mono-dispersed granular flows in vibrated beds are studied through experimental techniques, kinetic theory based particle level and continuum order models. We showed a complete solution of Navier-Stokes order hydrodynamic model with comparison of two sets of constitutive form for steady-state as well as time varying nature validated against the results of experiments and MD simulations. Together these constitutive relationships cover majority of monodisperse granular flows in general and particularly the model proposed by Garzo and Dufty (Garzo, Dufty 1999) covers wide range of inelasticity in dissipative granular flows. All hydrodynamics simulations are carried out within the commercially available modules of mercantile finite element method CFD package COMSOL. Although we have discussed granular flows in vibrated beds, the solution methods and applicability of the proposed hydrodynamic models are not limited and the conclusions drawn here are applicable for general granular behaviour under similar flow conditions. The model, solution technique and the implementation methods used in this dissertation can be utilized with appropriate geometric and boundary condition modifications to solve similar granular flow problems. This work is a small step towards the commercialisation of general granular flow module in multiphysics environment equipped with latest validated mathematical models.

In this dissertation we started with the validated steady state hydrodynamic model, developed by Vishwanathan (Viswanathan, Wildman et al. 2006) with near elastic constitutive relations (SSM-Jenkins), it was extended to cover broader range of inelastic granular flows using constitutive relationships proposed by Garzo and Dufty (Garzo, Dufty 1999) (SSM-Garzo). Validation for the steady state case in a vibrated bed was completed through comparison of the results for SSM-Garzo against those for SSM-Jenkins and PEPT experimental data, and showed that SSM-Garzo agrees well with SSM-Jenkins model in the dilute regime. Upon validation both models were extended to obtain a time-dependent solution at various loading conditions and frequencies of excitation. To our knowledge the complete time dependent solution of the ATD-Garzo model has not been reported in the literature prior to this dissertation.

Time dependent models showed the influence of base frequency on the characteristics of granular flow. At low frequencies of excitation both time dependent models, ATD-Jenkins and ATD-Garzo, successfully described the dynamic as well as time averaged nature of the vibrofluidized bed, and compared reasonably well with MD and experimental results. We observed the appearance of strong rolling and wave propagation and showed a link between the cyclic increase in the granular temperature with the viscous effects. The hydrodynamic results especially for ATD-Garzo showed a reasonable match with the MD simulations as a function of time. A qualitative matching behaviour was also seen with the experimental results. However at high frequencies (near ultrasonic) the lack of separation in the timescales between grain-base interaction and the base time period led to a collapse in the heat flux making the hard sphere based model inappropriate for the boundary condition estimation at these frequencies. Using a soft sphere model based MD simulations we demonstrated that the frequency of vibration has a strong effect on the fluidization behaviour of granular gas. However analysing the bulk behaviour independently from the base boundary condition showed that at high frequency, hard sphere based models were able to capture the steady state behaviour reasonably well for the cases considered in this dissertation.

Further analysis using the combination of both low and high frequency vibrations in a granular gas through amplitude modulations demonstrated the presence of low frequency wave propagation in the granular cell. The physics of the gas remained somewhat unaffected by the high frequency excitation. However the strength of the wave-like temperature fluctuations in the bulk was significantly reduced due to restricted heat flux from the base at high frequency. Analyzing the bulk behaviour independently from the heat flux boundary condition showed that both time-dependent hydrodynamic models (ATD-Jenkins & ATD-Garzo) predicted a reasonable qualitative comparison with MD simulations results in the phase-resolved granular temperature. Importantly the nature of the wave propagation in the bulk qualitatively resembled the wave motion caused by the low frequency non-modulated excitation. This highlights that the wave motion in the granular gas is a dynamic influence caused by the low frequency vibration of the granular bed.

In general the bulk physics was reasonably well predicted by both hydrodynamic formulations. Using a simplified hydrodynamic model key parameters were identified that demonstrate the broad trends of behaviour the granular flows follow. A one-dimensional

steady state model suitable for near elastic dilute limits proposed key scalings with slightly different non-dimensionalisation method. Despite having a number of simplifications the non-dimensional form of constitute relationships in the model showed good agreement with MD simulations especially in the dilute to moderate dense granular bed however at high loading, N^*, and low driving, Fr, the model failed to capture main physics due to complex nature of flow at high bed densities.

Testing of the predicted scalings using hard sphere based MD simulations showed validity in the dilute to moderate loading conditions though the influence of packing fraction and coefficient of restitution were noted in some of the cases. This model does, however, set the basis for describing the main scalings for vibrofluidized granular beds, and in the future we anticipate that effects of further inelasticity and enhanced density could be incorporated.

8.2. Future recommendations

The hydrodynamic model and the constitutive relationships used in this thesis describes wide-ranging three dimensional time dependent mono-dispersed granular flows. They are simulated in a vibrated bed for the purpose of validation and the understanding of flow physics in a controlled shear-free environment. In general these validated models can be used to simulate complex granular physics in different geometries using the same implementation technique with appropriate modifications. We expect that in near future further application of these models will be made for simulating high shear rate and complex granular flows in different geometries and operating conditions.

The multiphysics environment of COMSOL software facilitates the use of modules of different branches of physics and chemical engineering together in a single solution. This allows direct implementation of the granular flow module, developed in this dissertation, as a multiphysics module with ease. COMSOL also allows the possibility of extending the granular module to include latest developments of the mathematical models. Different constitutive formulations and forms of boundary conditions have been proposed to describe mono, bi and poly-disperse granular flows e.g., (Garzo, Dufty et al. 2007) for multiphase environments. We expect that in the near future different granular flow models and boundary conditions will be implemented within the broader framework proposed in this research work.

This dissertation highlighted the time dependent influence of frequency of base motion on the fluidization levels and the physics of granular gas. The failure of instantaneous collision models for the prediction of heat flux is expected at high frequencies of base vibration however the limiting values of base frequency could vary with the variation of the material properties of the participating granular media. The contact duration of the grain with base surface varies with the material properties of interacting surfaces. We expect that for different types of surfaces a general relationship could be developed between heat flux and the product of frequency and contact duration, ωT_c, where T_c is the contact duration between grain and the surface. Such a trend shall enable us in determining the limit of applicability of hard sphere based models for high frequency vibrated beds. We recommend extensive experimental testing of different material combinations to obtain such trend.

The influence of multiple frequencies through amplitude modulation has already shown interesting time varying features in granular gas. With the help of modulation we expect temporal as well as spatial variations in the granular gas. It is expected that with the different types of modulation schemes, duty cycles, amplitude ratios and wave forms, further patterns in the bed will be observable. From the perspective of theoretical understanding of instability initiation and propagation in the granular flows, amplitude modulation gives a new dimension to contemplate. We recommend further experimentation and extensive numerical simulations with types of modulation schemes and amplitudes to study different phenomena such as granular flow initiation, bulk perturbation propagation and pattern formations.

The non-dimensionalisation of constitutive relationships and the governing equations highlighted key scaling nature in granular flow. However the model used in this study is simplified and it has also been established in this dissertation that a complete description of granular flow is more complicated especially as the dissipation of media increases. It is recommended that the proposed model and the non-dimensionalisation shall be extended to include appropriate constitutive relations for a Navier-Stokes order description of granular flows. The flow characteristics and scaling shown in this study is only studied in one dimension while Chapters 3 and 4 highlighted significant radial variations linked with the influence of dissipative side boundary wall. We recommend further investigation of these models in realizable systems using numerical simulations and experiment.

Reference

ALAIN, B., EMMANUEL, T. and MATTHIEU, H.E., 2005. Granular gases: dynamics and collective effects. *Condens.Matter*, **17**, S2429.

BAXTER, G.W. and BEHRINGER, R.P., 1990. Cellular automata models of granular flow. *Phys.Rev.A,* **42**(2), 1017-1020.

BIZON, C., SHATTUCK, M.D., SWIFT, J.B., MCCORMICK, W.D. and SWINNEY, H.L., 1998. Patterns in 3D Vertically Oscillated Granular Layers: Simulation and Experiment. *Phys.Rev.Lett.,* **80**(1), 57-60.

BOUGIE, J., MOON, S.J., SWIFT, J.B. and SWINNEY, H.L., 2002. Shocks in vertically oscillated granular layers. *Phys. Rev. E,* **66**(5), 051301.

BREY, J.J., DUFTY, J.W., KIM C. S. and SANTOS, A., 1998. Hydrodynamics for granular flow at low density. *Phys. Rev. E,* **58**(4), 4638-4653.

BREY, J.J., DUFTY, J.W. and SANTOS, A., 1999. Kinetic Models for Granular Flow. *Journal of Statistical Physics,* **97**(1), 281-322.

BREY, J.J., DUFTY, J.W., KIM, C.S. and SANTOS, A., 1998. Hydrodynamics for granular flow at low density. *Phys.Rev.E,* **58**(4), 4638-4653.

BUG, A.L.R. and BERNE, B.J., 1987. Shaking-induced transition to a nonequilibrium state. *Phys.Rev.Lett.,* **59**(8), 948.

CARNAHAN, N.F. and STARLING, K.E., 1969. Equation of State for Nonattracting Rigid Spheres. *The Journal of Chemical Physics,* **51**(2), 635-636.

CHUNG, T., 2002. Computational Fluid Dynamics. Cambridge University Press.

CLEUREN, B. and EICHHORN, R., 2008. Dynamical properties of granular rotors. *Journal of Statistical Mechanics: Theory and Experiment,* **2008**(10), P10011.

COMSOL, 2007. COMSOL, Theory manual.

COSTANTINI, G., MARCONI, U.M.B. and PUGLISI, A., 2008. Noise rectification and fluctuations of an asymmetric inelastic piston. *EPL (Europhysics Letters),* **82**(5), 50008.

COSTANTINI, G., MARINI BETTOLO MARCONI, U. and PUGLISI, A., 2007. Granular Brownian ratchet model. *Phys.Rev.E,* **75**(6), 061124.

DING, J. and GIDASPOW, D., 1990. A bubbling fluidization model using kinetic theory of granular flow. *AICHE Journal,* **36**(4), 523-538.

DURAN, J., 2000. Sands, Powders, and Grains: An Introduction to the Physics of Granular Materials. XIII edn. Springer.

ESHUIS, P., VAN DER WEELE, K., LOHSE, D. and VAN DER MEER, D., 2010. Experimental Realization of a Rotational Ratchet in a Granular Gas. *Phys.Rev.Lett.*, **104**(24), 248001.

EVESQUE, P., 1992. Shaking dry powders and grains. *Contemporary Physics*, **33**(4), 245-261.

FALCON, WUNENBURGER, R., EVESQUE, P., FAUVE, S., CHABOT, C., GARRABOS, Y. and BEYSENS, D., 1999. Cluster Formation in a Granular Medium Fluidized by Vibrations in Low Gravity. *Phys.Rev.Lett.*, **83**(2), 440-443.

FARKAS, Z., TEGZES, P., VUKICS, A. and VICSEK, T., 1999. Transitions in the horizontal transport of vertically vibrated granular layers. *Phys.Rev.E*, **60**(6), 7022-7031.

FEYNMAN, R.P., LEIGHTON, R.B. and SANDS, M.L., 1989. The Feynman lectures on physics / Feynman, Leighton, Sands. Addison-Wesley, Redwood City, Calif.

GALVIN, J.E., DAHL, S.R. and HRENYA, C.M., 2005. On the role of non-equipartition in the dynamics of rapidly flowing granular mixtures. *J. Fluid Mech.*, **528**(1), 207.

GALVIN, J.E., HRENYA, C.M. and WILDMAN, R.D., 2007. On the role of the Knudsen layer in rapid granular flows. *Journal of Fluid Mechanics*, **585**(1), 73.

GARZO, V. and DUFTY, J.W., 1999. Dense fluid transport for inelastic hard spheres. *Phys.Rev.E*, **59**(5), 5895-5911.

GARZO, V., DUFTY, J.W. and HRENYA, C.M., 2007. Enskog theory for polydisperse granular mixtures. I. Navier-Stokes order transport. *Phys. Rev. E (Statistical, Nonlinear, and Soft Matter Physics)*, **76**(3), 031303.

GARZO, V., HRENYA, C.M. and DUFTY, J.W., 2007. Enskog theory for polydisperse granular mixtures. II. Sonine polynomial approximation. *Phys. Rev. E (Statistical, Nonlinear, and Soft Matter Physics)*, **76**(3), 031304.

GOLDHIRSCH, I., 2003. Rapid Granular Flows. *Annual Review of Fluid Mechanics*, **35**(1), 267-293.

GOLDSHTEIN, A., KAMENETSKY, V., POTAPOV, A., SHAPIRO, M., CAMPBELL, C. and DEGANI, D., 2002. Hydrodynamics of rapid granular flow of inelastic particles into vacuum. *Granular Matter*, **4**(3), 115-127.

GOLDSHTEIN, A. and SHAPIRO, M., 2006. Mechanics of collisional motion of granular materials. Part 1. General hydrodynamic equations. *J. Fluid Mech.*, **282**(1), 75.

GOLDSHTEIN, A., SHAPIRO, M., MOLDAVSKY, L. and FICHMAN, M., 2006. Mechanics of collisional motion of granular materials. Part 2. Wave propagation through vibrofluidized granular layers. *J. Fluid Mech.*, **287**(1), 349.

HAFF, P.K., 1983. Grain flow as a fluid-mechanical phenomenon. *J. Fluid Mech.*, **134**(1), 401.

HILL, K.M., CAPRIHAN, A. and KAKALIOS. J, 1997. Bulk Segregation in Rotated Granular Material Measured by Magnetic Resonance Imaging. *Phys. Rev. Lett.,* **78**, 50-53.

HRENYA, C.M., GALVIN, J.E. and WILDMAN, R.D., 2008. Evidence of higher-order effects in thermally driven rapid granular flows. *J. Fluid Mech.,* **598**(1), 429.

HUAN, C., YANG, X., CANDELA, D., MAIR, R.W. and WALSWORTH, R.L., 2004. NMR Experiments on a Three-Dimensional Vibrofluidized Granular Medium. *Phys. Rev. E,* **69**.

HUNTLEY, J.M., MARTIN, T.W., MANTLE, M.D., SHATTUCK, M.D., SEDERMAN, A.J., WILDMAN, R.D., GLADDEN, L.F. and HALLIWELL, N.A., 2007. NMR measurements and hydrodynamic simulations of phase-resolved velocity distributions within a three-dimensional vibrofluidized granular bed. *Proceedings of the Royal Society A: Mathematical, Physical and Engineering Sciences,* **463**(2086), 2519-2542.

JENKINS, J.T. and RICHMAN, M.W., 1985a. Grad's 13-moment system for a dense gas of inelastic spheres. *Archive for Rational Mechanics and Analysis,* (4), 355.

JENKINS, J.T. and RICHMAN, M.W., 1985b. Kinetic theory for plane flows of a dense gas of identical, rough, inelastic, circular disks. *Physics of Fluids,* **28**(12), 3485-3494.

JENKINS, J.T. and SAVAGE, S.B., 1983. A theory for the rapid flow of identical, smooth, nearly elastic, spherical particles. *J. Fluid Mech.,* **130**(1), 187-202.

JENKINS, J.T. and LOUGE, M., 1997. On the flux of fluctuation energy in a collisional grain flow at a flat, frictional wall. *Physics of Fluids,* **9**(10), 2835-2840.

JENKINS, J.T. and RICHMAN, M.W., 2006. Boundary conditions for plane flows of smooth, nearly elastic, circular disks. *J. Fluid Mech.,* **171**(1), 53.

JOHNSON, K.L., 1987. Contact Mechanics. Cambridge University Press.

JOHNSON, P.C., NOTT, P. and JACKSON, R., 1990. Frictional–collisional equations of motion for participate flows and their application to chutes. *J. Fluid Mech.,* **210**(1), 501-535.

JULIAN TALBOT, ALEXIS BURDEAU and PASCAL VIOT, 2010. An exact analysis of a class of granular motors in the Brownian limit. Research paper edn. *Phys. Rev. E.*

KHAIN, E. and MEERSON, B., 2003. Onset of thermal convection in a horizontal layer of granular gas. *Phys.Rev.E,* **67**(2), 021306.

KUMARAN, V., 2008. Dense granular flow down an inclined plane: from kinetic theory to granular dynamics. *J. Fluid Mech.,* **599**(1), 121.

KUMARAN, V., 2006a. The constitutive relation for the granular flow of rough particles, and its application to the flow down an inclined plane. *J. Fluid Mech.,* **561**(1), 1.

KUMARAN, V., 2006b. Granular flow of rough particles in the high-Knudsen-number limit. *J. Fluid Mech.,* **561**(1), 43.

KUMARAN, V., 2004. Constitutive relations and linear stability of a sheared granular flow. *J. Fluid Mech.,* **506**(1), 1.

KUMARAN, V., 2000a. Kinetic theory for a vibro-fluidized bed. *J. Fluid Mech.,* **364**(1), 163.

KUMARAN, V., 2000b. Velocity distribution function for a dilute granular material in shear flow. *J. Fluid Mech.,* **340**(1), 319.

KUMARAN, V., 1998. Temperature of a granular material fluidized by external vibrations. *Phys.Rev.E,* **57**(5), 5660-5664.

KUWABARA, G. and KONO, K., 1987. Restitution Coefficient in a Collision between Two Spheres. *Japanese Journal of Applied Physics,* **26**(Part 1, No. 8), 1230-1233.

LIU, C.H. and NAGEL, S.R., 1993. Sound in a granular material: Disorder and nonlinearity. *Phys. Rev. B.,* **48**(21), 15646.

LIU, C.H. and NAGEL, S.R., 1992. Sound in sand. *Phys. Rev. Lett.,* **68**(15), 2301.

LUDING, S., CLEMENT, E., RAJCHENBACH, J. and DURAN, J., 1996. Simulations of pattern formation in vibrated granular media. *EPL (Europhysics Letters),* **36**(4), 247-252.

LUN, C.K.K., SAVAGE, S.B., JEFFREY, D.J. and CHEPURNIY, N., 1984. Kinetic theories for granular flow: inelastic particles in Couette flow and slightly inelastic particles in a general flow field. *J. Fluid Mech.,* **140**, 223-256.

MAKSE, H.A., BALL, R.C., STANLEY, H.E. and WARR, S., 1998. Dynamics of granular stratification. *Phys.Rev.E,* **58**(3), 3357-3367.

MARSHALL, J.S., 2009. Discrete-element modeling of particulate aerosol flows. *J.Comput.Phys.,* **228**(5), 1541-1561.

MARTIN, T.W., HUNTLEY, J.M. and WILDMAN, R.D., 2005. Hydrodynamic model for a vibrofluidized granular bed. *J. Fluid Mech.,* **535**(1), 325.

MCNAMARA, S. and LUDING, S., 1998. Energy flows in vibrated granular media. *Phys.Rev.E,* **58**(1), 813-822.

MEER, D.V.D., REIMANN, P., WEELE, K.V.D. and LOHSE, D., 2004. Spontaneous Ratchet Effect in a Granular Gas. *Phys. Rev. Lett.,* **92**, 184301.

MONTANERO, J.M., GARZO, V., SANTOS, A. and BREY, J.J., 2000. Kinetic theory of simple granular shear flows of smooth hard spheres. *J. Fluid Mech.,* **389**(1), 391.

MONTANERO, J.M., SANTOS, A. and GARZÓ, V., 2007. First-order Chapman–Enskog velocity distribution function in a granular gas. *Physica A: Statistical Mechanics and its Applications,* **376**, 75-93.

NEDDERMAN R. M., 1992. Statics and kinematics of granular materials. Cambridge University Press.

PAK, H.K. and BEHRINGER, R.P., 1993. Surface waves in vertically vibrated granular materials. *Phys. Rev. Lett.,* **71**(12), 1832.

PAOLOTTI, D., BARRAT, A., MARINI BETTOLO MARCONI, U. and PUGLISI, A., 2004. Thermal convection in monodisperse and bidisperse granular gases: A simulation study. *Phys.Rev.E,* **69**(6), 061304.

RAMIREZ, R., RISSO, D. and CORDERO, P., 2000. Thermal Convection in Fluidized Granular Systems. *Phys.Rev.Lett.,* **85**(6), 1230-1233.

RAMREZ R. and SOTO R., 2003. Temperature inversion in granular fluids under gravity. *Physica A,* **322**, 73-80.

REIMANN, P., 2002. Brownian motors: noisy transport far from equilibrium. *Physics Reports,* **361**(2-4), 57-265.

RERICHA, E.C., BIZON, C., SHATTUCK, M.D. and SWINNEY, H.L., 2001. Shocks in Supersonic Sand. *Phys. Rev. Lett.,* **88**(1), 014302.

RICHMAN M.W. and MARTIN R.E., 1992. Confined, Granular Flows induced by identical, parallel, vibrating boundaries, Engineering Mechanics (Proc. of the Ninth ASCE Engineering Conference), May 24-27, **92**.

RICHMAN, M.W., 1993. Boundary conditions for granular flows at randomly fluctuating bumpy boundaries. *Mechanics of Materials,* **16**(1-2), 211-218.

SAVAGE, S.B. and SAYED, M., 1984. Stresses developed by dry cohesionless granular materials sheared in an annular shear cell. *J. Fluid Mech.,* **142**(1), 391-430.

SELA, N. and GOLDHIRSCH, I., 2000. Hydrodynamic equations for rapid flows of smooth inelastic spheres, to Burnett order. *J. Fluid Mech.,* **361**(1), 41.

SELA, N. and GOLDHIRSCH, I., 1998. Hydrodynamic equations for rapid flows of smooth inelastic spheres, to Burnett order. *J. Fluid Mech.,* **361**(1), 41.

SERERO, D., GOLDHIRSCH, I., NOSKOWICZ, S.H. and TAN, M.L., 2006. Hydrodynamics of granular gases and granular gas mixtures. *J. Fluid Mech.,* **554**(1), 237.

SERNA, S. and MARQUINA, A., 2005. Capturing shock waves in inelastic granular gases. *J.Comput.Phys.,* **209**(2), 787-795.

SERRELI, V., LEE, C., KAY, E.R. and LEIGH, D.A., 2007. A molecular information ratchet. *Nature,* **445**(7127), 523-527.

SHÄFER, J., DIPPEL, S. and WOLF, D.E., 1996. Force Schemes in Simulations of Granular Materials. *J.Phys.I France,* **6**(1), 5-20.

SHEN, H.H. and HOPKINS, M.A., 1988. Stresses in a rapid, simple Shear Flow of granular materials with multiple grain sizes. *Particulate Science and Technology: An International Journal,* **6**(1), 1.

SOTO, R., MARESCHAL, M. and RISSO, D., 1999. Departure from Fourier's Law for Fluidized Granular Media. *Phys. Rev. Lett.,* **83**(24), 5003-5006.

STEVENS, A.B. and HRENYA, C.M., 2005. Comparison of soft-sphere models to measurements of collision properties during normal impacts. *Powder Technology,* **154**(2-3), 99-109.

SUNTHAR, P., 2001. *Characterisation and Analysis of a Vibro-fluidised Granular Material,* PhD thesis, Department of Chemical Engineering Indian Institute of Science Bangalore, India.

SUNTHAR, P. and KUMARAN, V., 2001. Characterization of the stationary states of a dilute vibrofluidized granular bed. *Phys.Rev.E,* **64**(4), 041303.

SUNTHAR, P. and KUMARAN, V., 1999. Temperature scaling in a dense vibrofluidized granular material. *Phys.Rev.E,* **60**(2), 1951-1955.

TORQUATO, S., 1995. Nearest-neighbor statistics for packings of hard spheres and disks . *Phys. Rev. E,* **51**(4), 3170-3182.

TURNER, M.C. and WOODCOCK, L.V., 1990. Scaling laws for rapid granular flow. *Powder Technology,* **60**(1), 47-60.

VAN DER WEELE, K., 2008. Granular gas dynamics: how Maxwell's demon rules in a non-equilibrium system. *Contemporary Physics,* **49**(3), 157.

VISWANATHAN, H., WILDMAN, R.D., HUNTLEY, J.M. and MARTIN, T.W., 2006. Comparison of kinetic theory predictions with experimental results for a vibrated three-dimensional granular bed. *Physics of Fluids,* **18**(11), 113302.

VISWANATHAN. H, SHEIKH, N.A., WILDMAN, R.D. and HUNTLEY, J.M., submitted for publication. Convection in vibrated granular beds. *J. Fluid Mech., 2011*.

WARR, S. and HUNTLEY, J.M., 1995. Energy input and scaling laws for a single particle vibrating in one dimension. *Phys. Rev. E,* **52**(5), 5596-5601.

WARR, S., HUNTLEY, J.M. and JACQUES, G.T.H., 1995. Fluidization of a two-dimensional granular system: Experimental study and scaling behavior. *Phys. Rev. E,* **52**(5), 5583-5595.

WARR, S. and HANSEN, J.-., 1996. Relaxation of local density fluctuations in a fluidized granular medium. *EPL (Europhysics Letters),* **36**(8), 589-594.

WILDMAN, R.D., HUNTLEY, J.M. and PARKER, D.J., 2001. Convection in Highly Fluidized Three-Dimensional Granular Beds. *Phys. Rev. Lett.,* **86**(15), 3304-3307.

WILDMAN, R.D. and PARKER, D.J., 2002. Coexistence of Two Granular Temperatures in Binary Vibrofluidized Beds. *Phys. Rev. Lett.,* **88**(6), 064301.

WILDMAN, R.D., HUNTLEY, J.M. and HANSEN, J.-., 1999. Self-diffusion of grains in a two-dimensional vibrofluidized bed. *Phys. Rev. E,* **60**(6), 7066.

WILDMAN, R.D., HUNTLEY, J.M. and PARKER, D.J., 2001. Granular temperature profiles in three-dimensional vibrofluidized granular beds. *Phys.Rev.E,* **63**(6), 061311.

WILDMAN, R.D., MARTIN, T.W., HUNTLEY, J.M., JENKINS, J.T., VISWANATHAN, H., FEN, X. and PARKER, D.J., 2008. Experimental investigation and kinetic-theory-based model of a rapid granular shear flow. *J. Fluid Mech.,* **602**(1), 63.

WILDMAN, R.D., MARTIN, T.W., KROUSKOP, P.E., TALBOT, J., HUNTLEY, J.M. and PARKER, D.J., 2005. Convection in vibrated annular granular beds. *Phys.Rev.E,* **71**(6), 061301.

XIAOYU YANG and CANDELA, D., 2000. Potential Energy in a Three-Dimensional Vibrated Granular Medium Measured by NMR Imaging. *Phys. Rev. Lett.*, **85**, 298-301.